Fall 1999

The influence of high performance matrices on fracture behavior of concrete

Pusit Lertwattanaruk
New Jersey Institute of Technology

ABSTRACT

THE INFLUENCE OF HIGH PERFORMANCE MATRICES ON FRACTURE BEHAVIOR OF CONCRETE

by
Pusit Lertwattanaruk

Modification of cement matrices by the addition of micro particle pozzolanic materials such as silica fume and fly ash is known to improve the strength of concrete, but its contributions to fracture behavior remains unclear. In this study, the influence of replacing cement by silica fume and fly ash on the cement matrix-coarse aggregate interfacial bond, compressive stress-strain behavior and fracture behavior of concrete is investigated.

While the linear elastic fracture mechanics (LEFM) concept is not appropriate for concrete, a non-linear fracture model based on the load vs. load-line deflection and the load vs. crack-mouth-opening displacement (CMOD) responses of the three-point bend tests on notched beams is proposed and validated. Instead of using the LEFM based Two-Parameter Fracture Model that cannot adequately describes fracture processes in concrete, the proposed model is capable of generating the load vs. crack growth curve and the fracture resistance curve, and seems to be more appropriate for studying fracture behavior of concrete.

Incorporating silica fume in concrete mixture is found to have many beneficial effects on cement matrix-coarse aggregate interface, but less likely to improve the toughness of the cement matrix itself. The enhanced interfacial bond due to silica fume produces a more homogeneous concrete, which is responsible for the high strength, but

more brittle concrete. It is shown that improving interfacial bond has positive effect on the pre-peak fracture behavior of concrete (e.g. the critical energy release rate, G_C), but does not necessarily improve the overall fracture behavior (e.g. the fracture energy, G_F, and the brittleness).

In this study, coal fly ashes were fractionated into various size ranges by the air classifier method. It is found that replacing cement by very fine fly ash (with average particle size less than 3 microns) can enhance both the toughness of cement matrix and the interfacial bond, which results in high strength and less brittle concrete. The coarser fly ashes, which are porous and less reactive, are shown to enhance the interfacial bond, but produce brittle cement matrix. By reducing the particle size of fly ash, incorporating fly ash in cement matrix can improve both the strength and brittleness of concrete.

THE INFLUENCE OF HIGH PERFORMANCE MATRICES ON FRACTURE BEHAVIOR OF CONCRETE

by
Pusit Lertwattanaruk

A Dissertation
Submitted to the Faculty of
New Jersey Institute of Technology
In Partial Fulfillment of the Requirements for the Degree of
Doctor of Philosophy

Department of Civil and Environmental Engineering

January 2000

APPROVAL PAGE

THE INFLUENCE OF HIGH PERFORMANCE MATRICES ON FRACTURE BEHAVIOR OF CONCRETE

Pusit Lertwattanaruk

Dr. Methi Wecharatana, Dissertation Advisor — Date
Professor of Civil and Environmental Engineering, NJIT

Professor Edward G. Dauenheimer, Committee Member — Date
Professor of Civil and Environmental Engineering, NJIT

Dr. C. T. Thomas Hsu, Committee Member — Date
Professor and Associate Chairman of Civil and Environmental Engineering, NJIT

Dr. Dorairaja Raghu, Committee Member — Date
Professor of Civil and Environmental Engineering, NJIT

Dr. Rajendra Navalurkar, Committee Member — Date
Structural Engineer, URS GREINER WOODWARD CLYDE, Inc., New York

BIOGRAPHICAL SKETCH

Author: Pusit Lertwattanaruk

Degree: Doctor of Philosophy

Date: January 2000

Undergraduate and Graduate Education:

- Doctor of Philosophy in Civil Engineering
  New Jersey Institute of Technology, Newark, NJ, 2000

- Master of Science in Civil Engineering
  New Jersey Institute of Technology, Newark, NJ, 1995

- Bachelor of Engineering in Survey Engineering
  Chulalongkorn University, Bangkok, Thailand, 1992

Major: Civil Engineering

Presentations:

Pusit Lertwattanaruk (1996), "Recycled Concrete as Aggregate for Concrete Production," Graduate Seminar, Department of Civil and Environmental Engineering, Department of Civil and Environmental Engineering, New Jersey Institute of Technology, Newark, New Jersey, November 9.

Pusit Lertwattanaruk (1999), "Influence of High Performance Matrix on Fracture Behavior of Concrete," Graduate Seminar, Department of Civil and Environmental Engineering, Department of Civil and Environmental Engineering, New Jersey Institute of Technology, Newark, New Jersey, November 17.

This dissertation is dedicated to my parents and all parents
who spare no pain to see their children in the path of education.

ACKNOWLEDGMENT

I wish to express my sincere gratitude to my advisor, Professor Methi Wecharatana, for his guidance, encouragement and valuable suggestions throughout the course of this research.

Special thanks go to my committee members, Professor Edward G. Dauenheimer, Professor C. T. Thomas Hsu, Professor Dorairaja Raghu and Dr. Rajendra Navalurkar for their constructive evaluation and suggestions.

The opportunity and financial assistance received over the course of this study from the Department of Civil and Environmental Engineering is gratefully appreciated. Also, special thank goes to Mr. Allyn Luke, assistant to the Chairman for Laboratories, for his efforts and assistance with experimental equipment in the High Performance Concrete Laboratory.

Appreciation is expressed to Dr. Walairat Bumrongjaroen and Dr. Manaskorn Rachakornkij who provided suggestions and expertise for equipment in the Fly Ash Laboratory.

I wish to thank Ms. Peeranuch Sukatassanee for her understanding and moral support during the writing of this dissertation.

Finally, I wish to express my love to my family for their constant encouragement and understanding throughout my life.

TABLE OF CONTENTS

TABLE OF CONTENTS
(Continued)

Chapter **Page**

TABLE OF CONTENTS
(Continued)

Chapter **Page**

TABLE OF CONTENTS
(Continued)

Chapter **Page**

LIST OF TABLES

Table **Page**

LIST OF TABLES
(Continued)

Table **Page**

LIST OF FIGURES

Figure **Page**

LIST OF FIGURES
(Continued)

Figure **Page**

LIST OF FIGURES
(Continued)

Figure **Page**

LIST OF FIGURES
(Continued)

Figure **Page**

LIST OF FIGURES
(Continued)

Figure **Page**

LIST OF FIGURES
(Continued)

Figure **Page**

LIST OF FIGURES
(Continued)

Figure **Page**

LIST OF FIGURES
(Continued)

Figure **Page**

LIST OF FIGURES
(Continued)

Figure **Page**

LIST OF FIGURES
(Continued)

Figure **Page**

LIST OF FIGURES
(Continued)

Figure **Page**

CHAPTER 1

INTRODUCTION

1.1 General

Tensile capacity of concrete is commonly known to be very small in comparison with its compressive strength. To enhance the tensile property of concrete, reinforcement of various kinds are widely used. Metallic, synthetic, and glass fibers were added to cement matrices to make high performance fiber reinforced cement composites (HPFRCC). Another alternative is to improve the density of cement matrices. This was made possible by the addition of micro particles of pozzolanic materials such as micro silica and fly ash either as cement replacement or additives. These additives tend to increase the bond strength between mortar paste and coarse aggregate, enhancing fracture behavior of concrete. While it is generally believed that pozzolanic and packing effect are the two key contributions enhancing the strength and durability of the cement composites, much remains unclear for each of its specific contribution. Recently, several types of processed fly ashes and coal fly ash with finer grain size have been introduced to make low-cost high performance cement composites. These fly ash-cement matrices have different engineering characteristics that provide various degrees of pozzolanic and packing effect.

In this study, the influence of high performance matrices on the fracture behavior of concrete will be investigated. Dense cement matrices will be made by means of the addition of fine particles such as silica fume and fly ashes of various sizes to cement mixes. Physical and chemical compositions of each fine particle added will be correlated with the observed strength and fracture properties of the cement composites. A non-linear

fracture mechanics model will be developed to study the influence of high performance matrices on the enhancement of fracture behavior of concrete structures. Emphasis will be given to the experimental determination of various important fracture mechanics parameters and also to study the strength and the tensile behavior of high performance concrete members.

1.2 Research Significance

Several fracture mechanics approaches have been proposed to study the fracture behavior of concrete. These promising approaches primarily include the Fictitious Crack Model (FCM) by Hillerborg et al. (1976), the Two Parameter Fracture Model (TPFM) by Jenq and Shah (1985a), and the Size Effect Model (SEM) by Bazant and Kazemi (1988). Each of these models introduces some material fracture properties regardless of the structural geometry and the size. In order to use any of these models in practice, material fracture parameters have to be experimentally evaluated.

Fracture energy (G_F), a material property, is one of the very important parameters used in studying fracture behavior of concrete. It is the amount of energy required to extend a unit crack area through the material. If fracture energy is known then the overall fracture behavior of a structure can be predicted more accurately. The most widely used fracture mechanics model for analyzing concrete structures is the Fictitious Crack Model (FCM) proposed by Hillerborg (1976). To implement FCM, which requires Finite Element analysis, both the fracture energy and tensile strength of material need to be determined and incorporated. If these values are not accurately available the analysis for the fracture behavior and other fracture parameters will not be accurate.

The TPFM (Jenq and Shah, 1985a) proposes to use the stress intensity factor (K_{IC}) and the critical crack tip opening displacement ($CTOD_C$) as material fracture parameters. According to RILEM TC 89-FMT (1990), only one size of the three point bend specimen is needed for measuring the values of K_{IC} and $CTOD_C$. However, the testing procedure requires an unloading at the peak load. To achieve a stable unloading after the peak load a closed loop testing system is usually required, making the proposed testing method somewhat restrictive to most practical engineering testing laboratories.

Survey of numerous fracture energy tests by using three-point bend tests on notched beams based on the RILEM TC 50-FMC (1985) method indicates that the load line deflection measurement is strongly affected by the support conditions. The crack mouth opening displacements on the other hand are not to be affected by the test setups in any way. Based on this fact, Kim (1996) recently found a more reliable method for evaluating the fracture energy of concrete by using the relationship between the load-line deflection (LLD) measurement and the crack mouth opening displacement (CMOD) measurement.

In this study, the concept of LLD and CMOD relationship is adopted to develop a fracture mechanics model. A non-linear fracture mechanics model is proposed to study the fracture behavior of concrete in terms of the applied load and the fracture parameters as functions of crack growth. The proposed fracture mechanics model can be implemented by experimentally obtaining the load measurement versus the corresponding LLD and CMOD from the three-point bend tests on notched beams. For the proposed model, it is not necessary to perform the direct tension test to obtain the tensile strength of material or to apply the time-consuming Finite Element Method as

required by the Fictitious Crack Model (FCM). Furthermore, by using the proposed model, the material fracture parameters as mentioned in the Two-Parameter Fracture Model (TPFM) and other fracture parameters can be obtained without requiring a stable unloading at the peak load, which is difficult to accurately execute during the test.

At present, numerous studies on influence of fine particles such as fly ash and silica fume on strength and fracture behavior of concrete have been reported. But the effect of size and fineness of fine particles on fracture behavior of concrete have not yet been investigated. Several researchers (Hillerborg et. al. 1976, Petersson 1981, Gopalaratnam and Ye 1991, Navalurkar 1996) studied the performance of concrete based on the Fictitious Crack Model (FCM). The FCM depends heavily on the tensile strength and the criterion crack opening displacement (w_c) of material, which are obtained only by the direct tension test, or otherwise, have to be assumed, in order to apply the Finite Element Model to study fracture behavior of concrete structure. If the value of tensile strength is not accurate, the FCM will not provide the true characteristics of concrete. Other groups of researchers investigated the performance of concrete using the fracture parameters G_F, K_{IC} and $CTOD_C$ according to RILEM (1990) recommendations. The parameters K_{IC} and $CTOD_C$ are derived based on the Linear Elastic Fracture Mechanics (LEFM) concept, which is not suitable for the non-linear behavior of concrete.

In this study, the proposed non-linear fracture mechanics model is applied to study the effect of size and fineness of micro-particles on the enhancement of fracture behavior of concrete. Among the properties investigated are crack growth responding to the applied load, and fracture properties such as fracture toughness and brittleness of concrete.

1.3 Objectives of Present Study

The primary objective of this study is to determine the influence of high performance matrices on fracture behavior of concrete. Fine particles such as micro silica, and coal fly ash were used as cement replacement to produce high performance concrete matrices. Studies on mechanical and fracture mechanics properties of concrete in enhancing compressive and flexural strength, fracture behavior, and brittleness of concrete material and structure were carried out by varying the type and size of these micro-particles. In order to accomplish the above objective, the present research is divided into four phases as follows:

1. To propose a non-linear fracture mechanics model based on the Three-Point Bend Tests on Notched Beams (RILEM 1985, 1990) to study fracture behavior of concrete by neither performing the direct tension test nor applying the Finite Element Method as required by the Fictitious Crack Model (Hillerborg et al. 1976).
2. To develop an experimental program to evaluate the effect of high performance matrices incorporating fine-particle pozzolans with various size ranges on the basic mechanical properties and fracture behavior of concrete.
3. To implement the proposed model to study fracture behavior of concrete and to determine the fracture mechanics parameters related to the Two-Parameter Fracture Model (e.g. critical crack growth and fracture toughness) without performing the difficult unloading and reloading as outlined in the Fracture Mechanics of Concrete Test Methods (RILEM 1990).
4. To verify the performance of the proposed fracture mechanics model by comparison with other test data and the fracture mechanics models of other researchers.

CHAPTER 2

LITERATURE REVIEW

2.1 Overview of Normal Concrete Characteristics

Concrete is a heterogeneous and inelastic material. It consists of aggregate, an essentially homogenous and elastic material, and cementitious mortar, an inelastic material. Therefore, its behavior is complicated by the interaction of the constituents. In general, the mechanical properties of cement-based materials like concrete are influenced by 1) the chemical composition, the microstructure, and the pore geometry of the cementitious materials; 2) the properties of aggregate, and 3) the nature of the cement paste-aggregate bond. Particularly, the nature of the various interfaces between different phases in concrete (e.g. between the cement mortar and aggregate) and the associated interfacial properties significantly influences the global properties of composite materials like concrete. Load transfer between the phases of concrete is depended on and affected by, the degree of contact and cohesive bond at the interface or interfacial transition zone (ITZ). Stress concentration appears in this zone because two materials meet with considerable difference in stiffness. The rather low strength of the ITZ contributes to the fact that cracks are most likely to appear in this region.

Numerous studies have been performed at the micro-level of concrete regarding the interfacial transition zone. In these studies the chemical bond between the hardened cement paste (HCP) and aggregates is emphasized. Overviews on the subject are for example given by Mindess (1987, 1994) and Struble et al. (1980). The micro-structure of the ITZ is characterized by the accumulation of hexagonal calcium hydroxide, $Ca(OH_2)$,

compounds, causing the porous structure of the ITZ. Figure 2.1 shows the microstructure of interface between coarse aggregate and cement mortar with fly ash in the composites. The actual transition between the HCP and the aggregate particles is created by the chemical bond. It may be clear, however, that the actual failure mechanism not only depends on the chemical bonding, but also on the strength of the constituents.

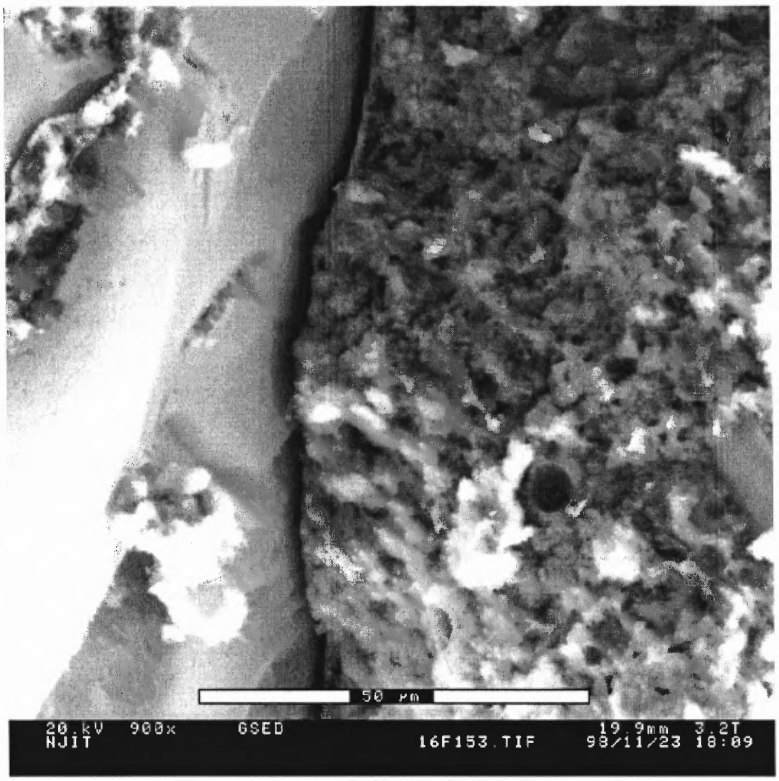

Figure 2.1 Scanning Electron Micrograph (showing interface between cement matrix and coarse aggregate)

More recent works in this field were carried out by Lee et al. (1992,1994) and Buyukozturk (1993) who adopted the linear elastic fracture mechanics (LEFM) concept to study interface fracture in concrete. Two modes of failure are distinguished for interface cracking. For weak interface, cracks tend to follow the interface, and crack deflection occurs. Contrarily, while for tough interface, penetration of crack into the

aggregate occurs. They also demonstrated that the fracture toughness of the interfacial zone is the most important factor in determining whether crack and deflection or crack penetration should be expected. In the model they proposed, crack deflection was more likely to occur for decreasing interfacial toughness, with respect to the toughness of the mortar matrix. Porosity, for example, therefore stimulates crack deflection. Next to the interfacial toughness, also the energy release of the deflected crack and the maximum energy release rate of the penetrated crack play an important role. They concluded that in high strength concrete, the increased compactness and the reduction of the thickness of the interfacial zone improve the transfer of stresses from the cement paste to the aggregate, allowing more contribution of the aggregate in resisting applied load. In general, strong interface enhances the strength, stiffness and durability of concrete.

Ductility in concrete may be related to the fact that bond cracks may not form at the same time as mortar cracks. This time lag between the formation of bond cracks and the formation and propagation of mortar cracks affects the deformation capability of concrete before failure. Furthermore, cracking scenarios in interfacial regions, such as aggregate debonding and transgranular cracking, strongly influence the post-peak behavior. Since the interfacial transition zone is generally weaker than both the mortar matrix and the aggregates, it seems obvious that cracking is observed first in this region.

The effect of these bond cracks (preceding to failure of the specimen) on the stress-strain curve is given in Figure 2.2. Microcracks in the interfacial transition zone are already noticed at about 25% of the peak-load (Strubel et a. 1980), and are reflected by the slightly non-linear behavior of the stress-strain response. Just before the peak stress is reached strong non-linearity is caused by the growth of mortar matrix cracks, implying

that the matrix strength is mainly responsible for the global strength of the concrete. Scholer (1967) demonstrated that the concrete strength is mainly affected by the mortar matrix strength. Hsu et al. (1963) confirmed this, and showed that the ultimate load is hardly effected by bond strength. In other studies performed by Chen and Wang (1987), Wu et al. (1987) and Wu and Zhou (1987) they concluded that the tensile strength increases considerable by the interface bond strength. As soon as matrix-cracks start propagating, macro-cracks are formed and debonding of the aggregate becomes of less importance. However, the final crack-path is already fixed at this point, and is mainly determined by the cracks in the interfacial transition zone.

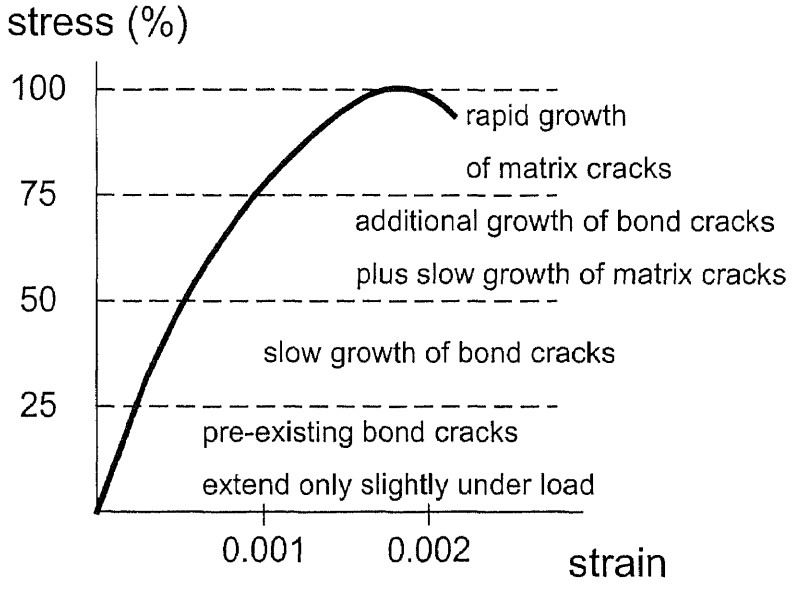

Figure 2.2 Typical Stress-Strain Response for Concrete in the Pre-Peak Regime, and the Relation to Micro-Cracking in the Material. (Strubel, Skalny, and Mindess, 1980)

As widely known, mechanical properties of any material, including cementitious materials are assumed to be controlled by its microstructure. At the microstructure level, cement paste is a heterogeneous mixture of variety of crystalline (e.g. calcium silicate hydrate, C-S-H) and quasi-crystalline (e.g. calcium hydroxide, $CaOH_2$) phases and pores of different sizes and shapes. Pores are essential components of cement paste and can be modified by changing the particle size distribution of cement or ultra fine fillers such as fly ash, affecting the overall behavior of cementitious material.

2.2 High Performance Fly Ash Concrete

2.2.1 Effects of Fly Ash in Concrete

Fly ash has been widely used to replace part of cement in concrete due to the fact that it behaves like a pozzolan for concrete. *Pozzolan*, as defined by ASTM C-593, is "a siliceous or alumino-siliceous material that in itself possesses little or no cementious value but that in finely divided form and in the presence of moisture will chemically react with alkali and alkaline hydroxides at ordinary temperatures to form or assist in forming compounds possessing cementitious properties".

Chemical composition and physical properties of fly ash are believed to be primary factors affecting the strength and durability of concrete with fly ash. During the hydration Portland cement produces an excess of lime that is released to the pore spaces. It is presence of this lime that allows the reaction between the silica components in fly ash (as a pozzolana) and calcium hydroxide (an excess of lime in cement environment) to produce additional calcium silicate hydrate (C-S-H). This process stabilizes the concrete, reduces permeability, and makes the interfacial transition zone (between aggregate and

mortar matrix) denser. Fine particles of ash also fill the voids in between cement grains and aggregates, which further densifies the matrix. These two phenomena seem to occur simultaneously and so integrated that a clear distinction on the contribution from each factor is rather impossible. The morphology of fly ash hydrates is suggested to be denser than that of cement (Lam et al. 1998).

Previous studies (Langley 1989) revealed that high volume fly ash concrete generally have higher modulus of elasticity, lower shrinkage and creep, as compared to the Portland cement concrete having equivalent compressive strength. This is because the unreacted fly ash particles have higher modulus of elasticity than the cement hydration products. Ahmed et al. (1995) found that the fracture parameters (e.g. the critical stress intensity factor, K_{IC}) are directly effected by changes in the porosity of cement paste. Furthermore, unlike the compressive strength, K_{IC} is independent with hydration time and increases rapidly at early ages, then reaches a plateau at about 10 days. Lam et al., (1998) found that low volumes of fly ash improved the tensile strength of concrete and had positive effects on the interfacial bond between the paste and the aggregates. High volume of fly ash showed slightly lower tensile strength, but higher values of crack tip opening displacement and final mid-span deflection in the fracture tests. Their work also showed that improving interfacial bond between the paste and the aggregate had positive effects on fracture toughness (or the critical stress intensity factor, K_{IC}), but did not necessarily produce higher fracture energy (G_F) values.

It should be noted that general perception was the different amount of fly ash used in concrete mix modified the performance of concrete. However, at this moment none has yet demonstrated how the size of fly ash influences the fracture behavior, ductility and

durability of concrete structures. Without this definitive, qualitative and conclusive information, fly ash will not be attractive to concrete and construction industry.

2.2.2 Chemical Activity of Fly Ash in Concrete

The principal product of the reactions of fly ash with alkali and calcium hydroxide in concrete is essentially the same as that of the hydration of Portland cement which is to form calcium silicate hydrate (C-S-H). Silicon dioxide in fly ash reacts with lime (e.g. alkali and calcium hydroxide) from the hydration process of cement produces additional C-S-H gel. The amount of heat evolved as a consequence of the reactions in concrete is usually reduced when fly ash is used as a portion of the cementitious material in concrete. The rate of early heat evolution is reduced in these cases and the time of maximum rate of heat evolution is retarded.

All cement particles in the paste of concrete do not essentially take part in hydration. The hydration usually starts from the finest cement particles (Neville 1983). The hydrated cement envelopes unreacted cement particles resulting in the reduction of the rate of hydration. Even after a long time large amounts of unhydrated cement may remain in the paste. When fly ash is incorporated in the paste, these particles act as nuclei for the hydration reaction, thus generating more hydrated products than otherwise. The hydration reaction of fly ash is known to be essentially the same as that of Portland cement, but occurs very much slower than that of Portland cement (Berry and Malhotra 1980). This is primarily due to the inert glassy phase of fly ash and possibly the availability of calcium hydroxide that only starts after one or two weeks producing the alkalinity of the pore water high enough to dissolve the fly ash (Fraay et al. 1989). This

continued reaction results in continuous strength development beyond 28 days. Thus the 28-day compressive strength cannot be accepted as a good indicator of the strength capacity of fly ash concrete.

2.2.3 Classification of Fly Ash

ASTM C-618 defines fly ash into two classes: Class F and Class C. Class F fly ash is usually produced by burning anthracite and bituminous coal which is often found in the North-East region of the United States of America. Class C fly ash is normally produced by burning sub-bituminous coal and lignite, which is available along the West Coast. The separation of fly ash into two classes reflects differences in composition, which affect cementitious and pozzolanic properties. Class C fly ash usually has cementitious properties in addition to pozzolanic effect, while Class F fly ash is rarely cementitious when mixed with water alone.

2.2.4 Chemical Composition of Fly Ash

The main chemical compositions of fly ash are SiO_2, Al_2O_3, and Fe_2O_3. Wide ranges exist in the amounts of these three principal constituents: SiO_2 (25 to 60 percent), Al_2O_3 (10 to 30 percent) and Fe_2O_3 (5 to 25 percent). Class F fly ash normally has a CaO content less than 10% and the sum of the oxides of SiO_2, Al_2O_3, and Fe_2O_3 not less than 70%. Class C fly ash usually has the CaO content of 10% or higher with the sum of the above mentioned oxides not less than 50%, and is believed to be more cementitious than Class F fly ash.

Fly ashes used in concrete typically have less than 6 percent loss on ignition (LOI). The principal active constituent of Class F fly ash is siliceous or alluminosilicate glass. The principal active constituent in Class C fly ash is calcium alumino-silicate glass. Carbon content is not usually determined directly, but is often assumed to be approximately equal to the loss on ignition (LOI), however, ignition loss will also include decomposition of hydrates or carbonates that may be present in the fly ash.

2.2.5 Particle Shape and Size Distribution of Fly Ash

Particle size and shape characteristics of fly ash are dependent upon the source and uniformity of the coal, the degree of pulverization prior to burning, the combustion environment (temperature level and oxygen supply), uniformity and load of combustion, and the type of collection system used: mechanical separators, bag filters, or electrostatic precipitators. The majority of fly ash particles are glassy, solid or hollow and spherical in shape. Hollow empty spheres are called cenospheres. Spheres that contain smaller particles of ash are known as plerospheres. The remaining fly ash particles are translucent to opaque, slightly to highly porous, and vary in shape from rounded to elongated.

Individual particles of fly ash range in size from less than 1 micron to greater than 1 mm. Older power plants where mechanical separators are used, the fly ash is coarser than in more modern plants which use electrostatic precipitators or bag collectors. It should be noted that even from the same boiler the particle size may vary when fly ash is collected from front and rear precipitators. For fly ash suitable for concrete the majority of the particles pass the No. 325 sieve (45 microns). Fineness of fly ash has a significant influence on its performance in concrete (Jaturapitakkul 1993). The finer the particle size

of fly ash, the larger are the surface area, which in many cases correlates with higher reactivity of fly ash in concrete.

Many researchers have observed direct correlation between fineness of fly ash and the strength development of fly ash concrete. Utika et al. (1991) showed that as percentage of finer particles ranging from diameters of 1 to 20 microns increases, the corresponding strength gain is notable. Similar results have also been reported by Giergiczny and Werynska (1989). They found that 0-20 microns fraction brought about the highest strength increase in the mortar as compared to the 20-40, 40-60, and those greater than 60 microns. Bumrongjaroen (1999) studied the properties of ground and air-classified fly ashes on mortar. They found that by grinding fly ash, the fineness increased and consequently the ground fly ash substantially improved the strength and workability of concrete. Most of these studies seem to conclude that finer fly ashes tend to perform better because the finer fractions not only reduce the voids but also allow the hydration and pozzolanic reactions to proceed more rapidly.

2.3 Fracture Mechanics Parameters

2.3.1 Linear Elastic Fracture Mechanics (LEFM)

Fracture mechanics deals with the mechanical responses of a flawed or a cracked body subjected to the application of forces or stresses. For certain cracked configurations subject to external forces, it is possible to derive closed-form expressions for the stresses in the body, assuming isotropic linear elastic material behavior. Westergaard (1939) and Irwin (1957) were among the first to publish such solutions. If we define a polar

coordinate axis with the origin at the crack tip, which is assumed as a sharp point (see Figure2.3), the stress field in any linear elastic cracked body can be shown as

$$\sigma_{ij} = \left(\frac{k}{\sqrt{r}}\right) f_{ij}(\theta) + \sum_{m=0}^{\infty} A_m r^{\frac{m}{2}} g_{ij}^{(m)}(\theta) \tag{2.1}$$

where σ_{ij} is the stress tensor, r and θ are defined in Figure 2.3, k is a constant, and f_{ij} is a dimensionless function of θ. The solution for any given configuration contains a leading term that is proportional to $1/\sqrt{r}$. As r approaches zero, the leading term approaches infinity, but the other terms remain finite or approach zero. Equation 2.1 describes a stress *singularity*, since stress is asymptotic to the crack tip (r = 0). In reality, fracture stresses at the crack tip are finite because the crack tip radius is finite; not a sharp point as assumed in the closed-form solution. Also, materials go through inelastic and/or plastic deformation due to high stress concentration region near the crack tip, which is called *fracture process zone*.

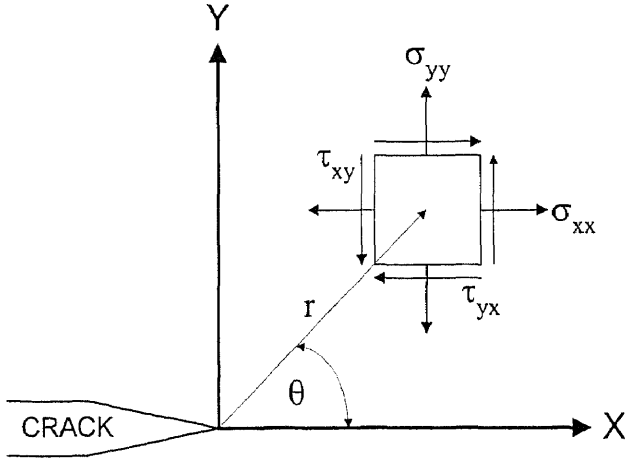

Figure 2.3 Definition of the coordinate axis ahead of a crack tip.
The Z direction is normal to the page.

Fracture behavior can be classified into three basic types (see Figure 2.4), each associated with a local mode of deformation. Mode I, or the opening mode, where the principal load is applied normal to the crack plane, tends to open the crack. Mode II, or sliding mode, corresponds to in-plane shear loading and tends to slide one crack face with respect to the other. Mode III, or the tearing mode, refers to out-of-plane shear. A cracked body can be loaded in any one of these modes, or a combination of two or three modes. In the field of fracture mechanics, only Mode I is of major interest because Mode II and III have been relatively less important in fracture testing and application except for testing of adhesive joints.

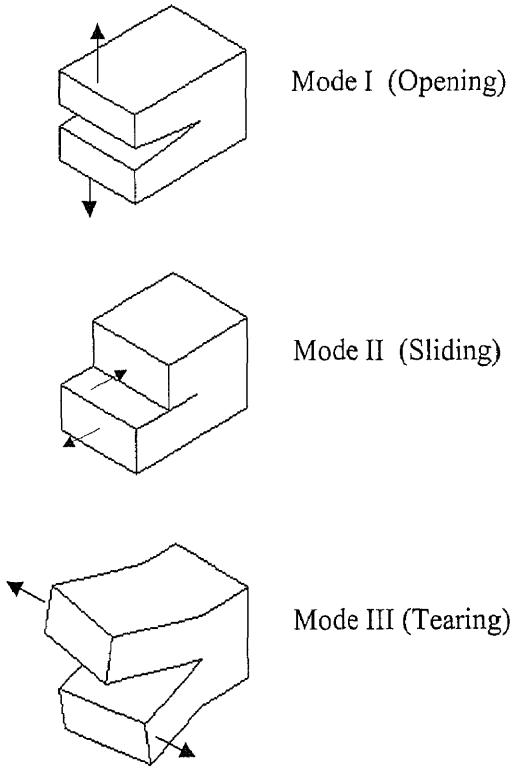

Figure 2.4 Three Basic Types of Fracture Behavior

It is convenient at this point to replace k in Equation 2.1 by the *stress intensity factor*, K, where $K = k\sqrt{2\pi}$. The stress intensity factor is usually given as subscript to denote the mode of fracture; i.e., K_I, K_{II} or K_{III}. Thus the stress field (σ_{ij}^I) in the vicinity of a crack tip in an isotropic linear elastic material for Mode I can be written as

$$\lim_{r\to o} \sigma_{ij}^I = \frac{K_I}{\sqrt{2\pi r}} f_{ij}^I(\theta) \tag{2.2}$$

where K_I is the stress intensity factor for Mode I.

Since the applied loading in Mode I is perpendicular to the crack plane, all stress components at all locations of a linear elastic body must increase in proportional to the remotely applied stress (σ). According to Equation 2.2, the stress intensity factor (K_I) has the dimension of $stress \times \sqrt{length}$, and the only relevant length scale is the crack size (a). Therefore the relationship between K_I and the global condition can be written in the closed-form solution as follows:

$$K_I = \sigma\sqrt{\pi a} f(a/w) \tag{2.3}$$

where a is the crack length, σ is the applied external stress and $f(a/w)$ is a function of the ratio of the crack length to the thickness, w, in the crack plane. $f(a/w)$ for a number of practical configurations are reported by Tada, Paris and Irwin (1985).

The K_I factor is a LEFM parameter because it is assumed that the material is linearly elastic, isotropic, and homogeneous. Most cementitious materials are neither linear elastic, isotropic nor homogeneous, and thus modification of LEFM or non-linear fracture mechanics models are needed to predict the fracture behavior of concrete.

2.3.2 Critical Stress Intensity Factor

Crack propagation will occur when the combination of stress and strain (stress intensity) reaches a critical value commonly referred to as the *critical stress intensity factor*, K_{IC}. This value is also referred to as the material *fracture toughness*, which describes the ability of a material to deform plastically and to absorb energy before and during rupture.

The critical stress intensity factor is usually determined from the measured peak load, the initial notch depth and related specimen geometry. A number of investigators have produced the quite different results for K_{IC} in concrete specimens depending on specimen geometry and size. The results of these experiments show that when fracture toughness is evaluated from notched beam specimens using conventional linear elastic fracture mechanics a significant size effect is observed (Francois 1984). This size effect has been attributed to the nonlinear stable crack growth (or the development of fracture process zone) that occurs prior to the peak load. Such an approach is analogous to applying linear elastic K_I equations to metal specimens that exhibit significant plasticity prior to failure. Microcracking, slow crack growth and a large size process zone ahead of the traction-free cracks are all independent characteristics inherent to the inhomogeneous composition of concrete.

In order to apply the fracture mechanics concept to concrete, the microcraked zone (or fracture process zone) must be incorporated into the analysis. For a three-point bending beam test (RILEM 1985, 1990), in the region between the proportional limit and peak load, the process zone gradually grows until it reaches the full size. After the peak, the process zone shifts upwards as the microcrack grows but the size of the process zone remains unchanged unless a confinement due to specimen configuration is encountered.

If fracture toughness is a material property, its value should be a constant, regardless of the specimen or the notch size.

Kim (1996) proposed the method to determine K_{IC} for various notch depths and beam sizes taking into consideration of the process zone. He showed K_{IC} to be constant until the initial notch depth ratio (*notch depth/beam depth*) is 0.5 where it seemed to drop. The reason for this is the ligament of the beam has become so small that the process zone reaches the compression zone of the beam before it is fully developed. Therefore, the load cannot be increased further so the corresponding K_{IC} value is smaller than those of other notch sizes.

2.3.3 Energy Release Rate

Due to inaccurate estimation of fracture stress by the stress concentration approach in the linear elastic fracture mechanics theory (i.e., infinite stresses at the crack tips), Griffith (1920) established an energy based criterion for crack initiation or growth. According to the First Law of Thermodynamics, when a system goes from a non-equilibrium state to equilibrium, there will be a net decrease in energy. In 1920 Griffith applied this idea to the formation of a crack. A crack can form (or an existing crack can grow) only if such a process causes the total energy to decrease or remain constant. Thus the critical conditions for fracture can be defined as the point where crack growth occurs under equilibrium conditions, with no net change in total energy. The Griffith energy balance for an incremental in the crack length, *da*, under equilibrium conditions can be expressed as follows:

$$\frac{dF}{da} = \frac{dW}{da} + \frac{dU}{da} = 0 \qquad (2.4a)$$

or

$$-\frac{dU}{da}=\frac{dW}{da} \tag{2.4b}$$

where F is the work done by the external force, W is the energy required to create new surface (or for crack growth) and U is the internal strain energy.

In 1957, Irwin (1957) proposed the *energy release rate*, G, or sometimes referred to as the *crack driving force* which is a measure of the energy available for an increment of crack extension. The strain energy release rate has the dimension of energy per unit crack surface where the crack surface is the product of unit thickness and unit crack extension, and can be expressed as:

$$G=\frac{dU}{Bda} \tag{2.5}$$

where B is the thickness of crack surface.

The energy required for crack propagation is denoted by R or G_R, which is called *crack resistance*. R or G_R is defined as the energy required to generated a unit crack area, and can be expressed as:

$$R=\frac{dW}{Bda} \tag{2.6}$$

To illustrate stable or unstable crack extension, a plot of R versus crack extension is called a *resistance curve* or *R curve*, and the corresponding plot of G versus crack extension is the *driving force curve*. The cracked body is unstable with further crack growth because the rate of change in driving force exceeds the slope of the R curve.

The conditions for stable crack growth can be expressed as follows:

$$G=R \tag{2.7a}$$

and

$$\frac{dG}{da} \leq \frac{dR}{da} \tag{2.7b}$$

Unstable crack growth occurs when

$$\frac{dG}{da} \geq \frac{dR}{da} \tag{2.8}$$

where $\frac{dG}{da}$ is the slope of the crack driving force and $\frac{dR}{da}$ is the slope of the resistance curve or R curve.

2.3.4 Critical Strain Energy Release Rate

The critical strain energy release rate, G_C, is directly related to the measured peak load, and also implies to the stability of crack growth described previously. At the peak load from a test for fracture mechanics parameters, G_C can be expressed as

$$G_C = G_{\text{(at peak load)}} = R_{\text{(at peak load)}} \tag{2.9}$$

Based on linear elastic fracture mechanics (Broek 1982), it is commonly known that the relationship between K_I and G can be expressed as

$$G = \frac{K_I^2}{E'} \tag{2.10}$$

where $E' = E$ for plane strain condition, $E' = E/(1-\upsilon^2)$ for plane stress condition, E is the Young's modulus and υ is the Poisson's ratio.

Also as shown in Equation 2.10, the critical strain energy release rate, G_C, can be expressed in terms of the critical stress intensity factor, K_{IC} as

$$G_C = \frac{K_{IC}^2}{E'} \tag{2.11}$$

since G_C is closely related to K_{IC}.

2.3.5 Fracture Energy

The fracture energy, G_F, has a physical meaning similar to the critical strain energy release rate, G_C. However, unlike the determination of G_C which is directly related to the peak load, the fracture energy is determined from the work needed to completely separate the specimen into two halves. The value of G_F should be calculated using direct uniaxial tensile tests. But, due to the difficulties in performing a direct uniaxial tensile test, Petersson (1980a, 1980b) has described in detail how G_F is determined from three-point bend test on notched beams. Later, the determination of the fracture energy of mortar and concrete by means of three-point bend tests on notched beams was proposed by RILEM (1985). From the load versus deflection curve obtained in a stable condition, the fracture energy is calculated from the following equation.

$$G_F = \frac{W_0 + mg\delta_0}{A_{lig}} \tag{2.12}$$

where W_0 is the energy represented by the area under the load-deflection curve, m is the mass of the specimen, g is the gravity acceleration, δ_0 is maximum deflection of the beam at failure, A_{lig} is area of uncracked ligament, and $mg\delta_0$ represents the energy supplied by the weight of the beam.

2.4 Nonlinear Fracture Mechanics for Concrete

2.4.1 Phenomenological Aspects

Although cementitious materials such as mortar and concrete are often considered brittle, they are actually quasi-brittle materials that are tougher than most of the so-called advanced ceramics. Concrete derives its toughness from pre-critical cracking that

precedes ultimate failure. This pre-critical damage results in nonlinear stress-strain response and R curve behavior.

Initial attempts to apply traditional fracture mechanics to concrete were unsuccessful because these early approaches were based on linear elastic fracture mechanics (LEFM) and failed to take account of the process zone that forms in front of macroscopic cracks. In general, there are two types of non-linearity, ductile, as exhibited by metals, and non-ductile, as exhibited by ceramics, glass and concrete. Compared to the ductile materials, in which most of the non-linear zone undergoes plastic hardening, the fracture process zone in concrete is large and occupies nearly the entire non-linear zone.

The formation of a fracture process zone in concrete, together with two idealizations of the process zone is schematically illustrated in Figure 2.5. Microcracks form ahead of a macroscopic crack, which consists of a bridged zone directly behind the tip and a traction-free zone further behind the tip. The bridging is a result of the weak interface between the aggregates and the matrix. Normal concrete, when subjected to tensile loads, behaves elastically until about 40%-60% of its tensile strength. Pre-critical crack growth and microcracking have been observed to be the cause of non-linearity before the peak load. As loading increases, the process zone, which is the region ahead of a traction-free crack, starts developing, and forms one localized crack. After the peak load, the localized crack is still able to transfer decreasing levels of stresses as the crack widens because of aggregate interlocking and traction between cracked surface. In the other regions away from the process zone, the material simply unloads elastically. This localization of the deformation is referred to as the strain-softening behavior of concrete.

The process zone can be modeled as a region of strain softening (Figure 2.5b) or as a longer crack that is subjected to closure traction (Figure 2.5c).

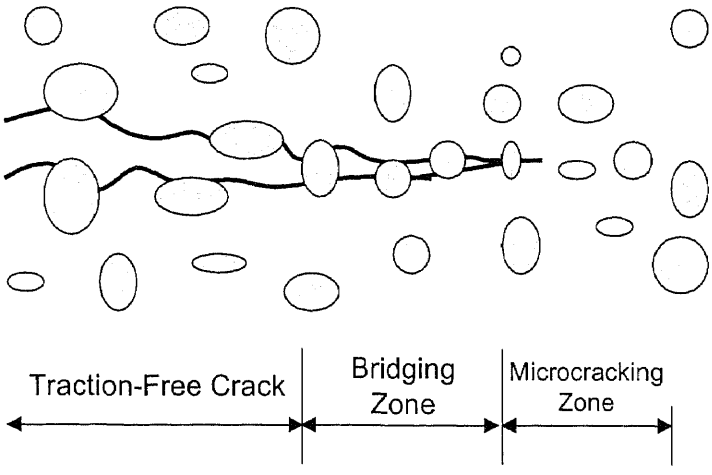

(a) Crack Growth in Concrete

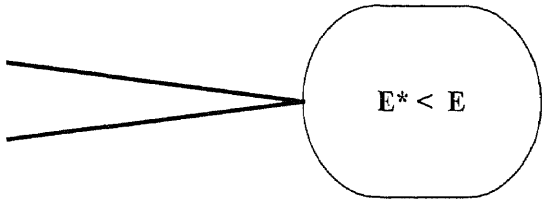

(b) Process Zone idealized as a zone of strain softening

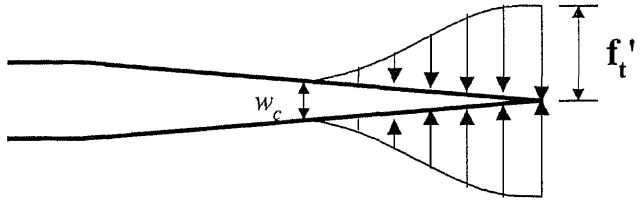

(c) Process zone idealized by closure tractions

Figure 2.5 Schematic Illustration of Crack Growth in Concrete, together with Two Simplified Models

Many nonlinear fracture models for the fracture process zone have been proposed. Three of the most well-known fracture models are the fictitious crack model (FCM) (Hillergborg et al. 1976), the crack band model (CBM) (Bazant and Oh 1983) and the two-parameter fracture model (TPFM) (Jenq and Shah 1985a, 1985b). These models are intended to incorporate the nonlinear behavior of concrete into the analysis of the fracture processing of concrete regardless of the structural geometry and the size. In order to use any of these models, material fracture parameters have to be experimentally evaluated.

2.4.2 Fictitious Crack Model (FCM)

Hillerborg, et al. (1976) proposed the fictitious crack model (FCM), also called a cohesive zone model, to incorporate the stress-softening behavior of concrete. Figure 2.6a illustrates the typical tensile response of concrete. The model assumes that the stress versus crack opening displacement (σ - w) behavior in the damage zone is a material property. After a small degree of nonlinearity caused by microcracking, the material reaches its tensile strength, $f_t^{'}$, and then strain softens. Once $f_t^{'}$ is reached, subsequent damage is concentrated in a local fracture process zone. Virtually all of the displacement following the maximum stress is due to the process zone (or the damage zone).

In the model, the length from the tip of the traction-free crack to the tip of the fracture process zone is called *fictitious crack length.* The traction-free crack tip begins to open when the tip of the process zone reaches the tensile strength, $f_t^{'}$. As the crack opens, closing traction based on the amount of opening are introduced across the process zone (See Figure 2.5c). When the tip of the traction-free crack reaches a critical displacement, w_c, the closing traction across the tip drops to zero. Assuming that the closure stress, σ,

and the traction-free crack opening displacement, w, are uniquely related, the fracture energy, G_F is defined as the area under the σ - w curve (see Figure 2.6b).

$$G_F = \int_0^{w_c} \sigma dw \tag{2.13}$$

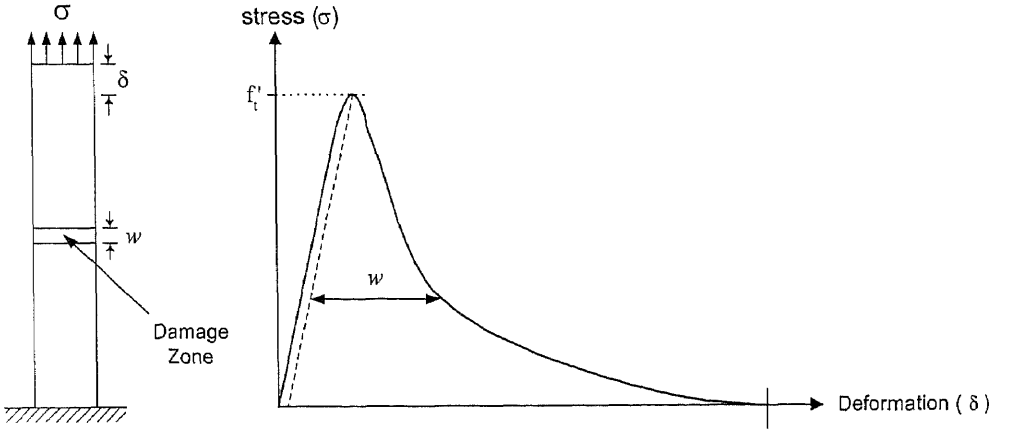

(a) Typical Tensile Response of Concrete
From a Uniaxial Direct Tension Test

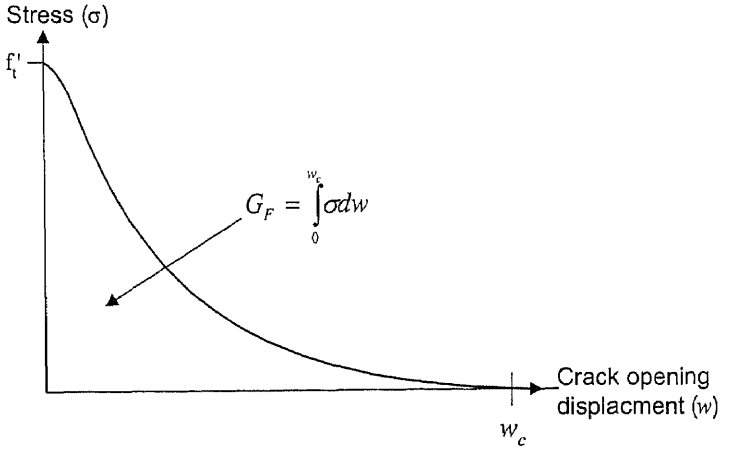

(b) Typical Stress versus Crack Opening Displacement Response

Figure 2.6 Typical Fracture Parameters (f_t', w_c and G_F) Required to Implement the Fictitious Crack Model

The fracture parameters are completely characterized by two parameters G_F and f_t'. The finite element analysis is necessary to implement the model to predict fracture responses of concrete members. The values obtained by the model are quite sensitive to the uniaxial tensile strength and the critical crack opening displacement, which are not easy to determine. Although the actual G_F should be determined from a direct uniaxial tensile test, due to the difficulty of conducting the direct tensile test most researchers accept the indirect method using the three-point bending beam test (RILEM 1985). The model has been shown to correctly predict the experimentally observed size effects for notched and unnotched beam specimens. But it has been pointed out that the fracture parameters from notched beams were specimen size dependent because the process zone produced during fracture of concrete were often quite large, and interaction between the process zone and free boundary could influence the fracture behavior. Therefore, the dimension of the test specimen must strictly adhere to the recommended requirements.

Based on the results of Kim (1996), it was found that specimens with span to depth ratio of 4 were easy to handle and produced more reliable data (less scatter). The RILEM (1985) beam size has a span to depth ratio of 8, is relatively heavier and difficult to handle during testing. Recently, Kim (1996) further developed the method to improve the measurement of fracture energy, and also found the appropriate beam specimen configurations, which have the notch depth to beam depth ratio equal to or less than 0.4, that yield more reliable values of the fracture parameters. Kim's results (Kim 1996) showed that when the notch depth to beam depth ratio was too high, the fracture process zone for the beam reaches the confinement of the compression zone before being fully developed and thus magnified the specimen size effect.

2.4.3 Two-Parameter Fracture Model (TPFM)

The two-parameter fracture model was developed by Jenq and Shah (1985a, 1985b). This model was derived under the special non-linear fracture models without using the complete concrete stress-strain ($\sigma - \varepsilon$) and stress-deformation ($\sigma - w$) softening relationship. It is based on the pre-peak nonlinear behavior of concrete. The linear elastic fracture mechanics (LEFM) principles are modified to approximately reflect the fracture behavior of concrete. Figure 2.7 shows the testing configuration and geometry of specimen required for implementing the model. The a_0 is the pre-notched crack length or the initial crack length. To achieve the tests for TPFM, a closed-loop testing system is usually required to obtain the stable load versus crack mouth opening displacement curve.

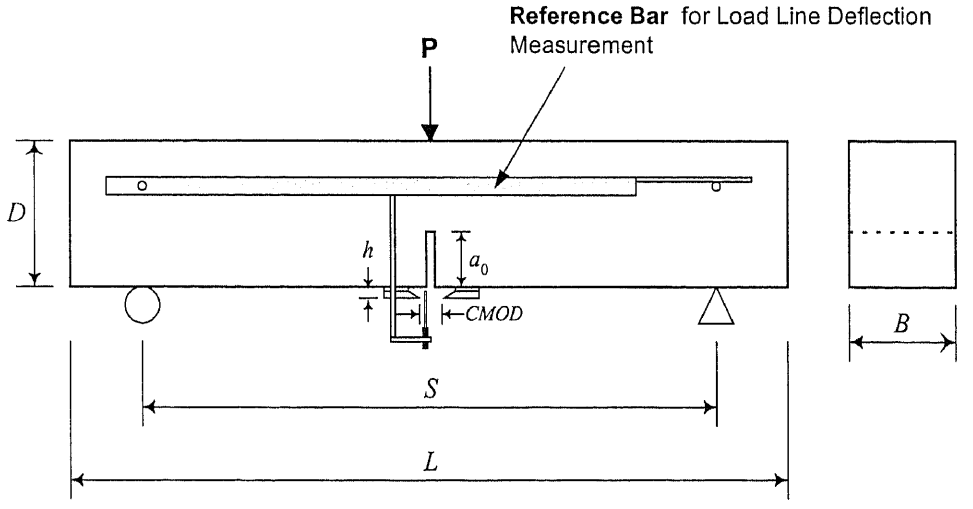

Figure 2.7 Testing Configuration and Geometry of Specimen for Three-Point Bend Tests on Notched Beams

P = load, L = specimen length, S = specimen loading span
D = beam depth, B = beam width, a_0 = initial notch depth
h = thickness of holder of clip gauge
$CMOD$ = crack mouth opening displacement

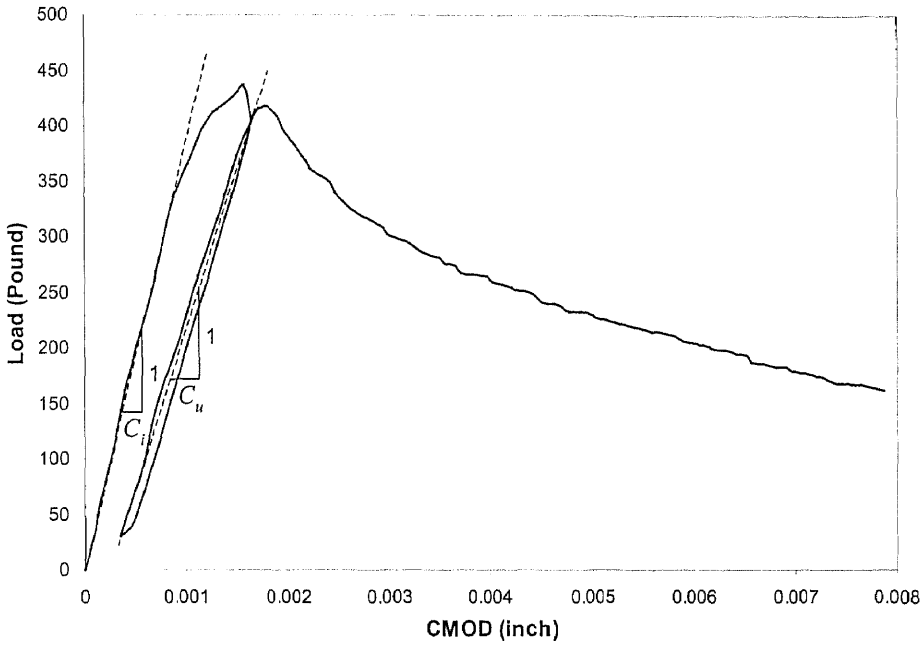

Figure 2.8 Typical Load vs. CMOD Plot from Three-Point Bend Tests

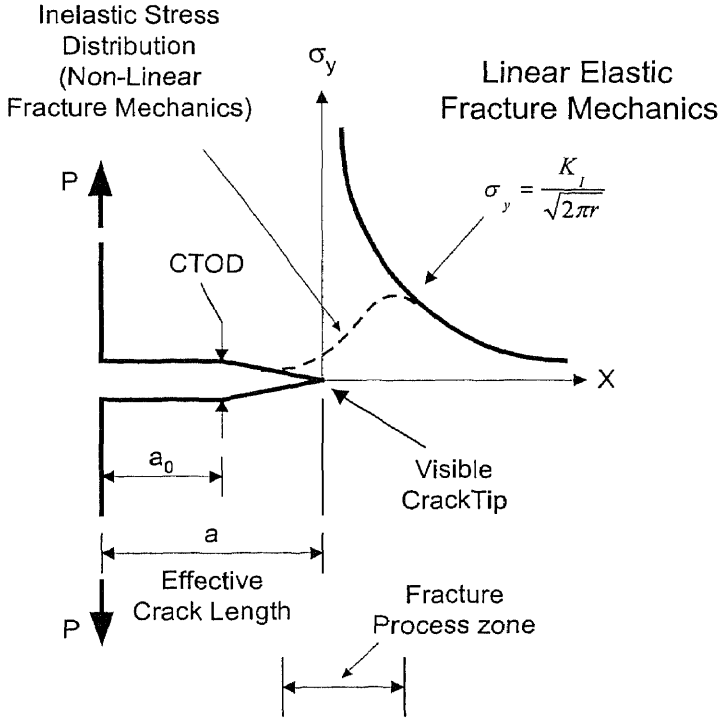

Figure 2.9 Effective Crack Length for the TPFM model

In general, the measurement of crack path in concrete is tedious. Furthermore cracks in concrete may not be traction free due to the effect of aggregate interlock. As a result, the experimental determination of the effective crack length at the peak load or so called *critical effective crack length*, a_c, on a specimen surface is not useful for determining the critical stress intensity factor, K_{IC}. An alternate method called the *compliance* technique is used to determine the critical effective crack length (a_c). Compliance is defined as the value of crack mouth opening displacement (*CMOD*) per unit load. For the three-point bend test on notched beams, C_i is the initial compliance at the beginning of loading, and C_u is the unloading compliance just after the peak load by performing unloading and reloading (See Figure 2.8). Using LEFM readily available relationship (Tada et al. 1985) between compliance (C_i and C_u) and specimen geometry, one can determine the critical effective crack length (a_c). Figure 2.9 shows the definition of the effective crack length (a) in the TPFM based on the LEFM concept without consideration of the fracture process zone for quasi-brittle materials such as concrete.

The critical effective crack length (a_c) calculated using the TPFM method depends on the size of the beam specimens, the compressive strength of concrete and on the strain rate (Jenq and Shah 1985a, 1985b). It is important to note that a_c reduces with increasing compressive strength and increasing strain rate. Note that for elastic perfectly brittle material, a_c approaches a_0. A decrease in the critical crack length of a_c generally implies increase in the brittleness of the composite (Shah 1990).

Since it was found that the value of a_c depends on the material properties and on the specimen's geometry, the value of a_c determined from one particular size cannot be used to predict fracture behavior for beams of other sizes. To overcome this problem,

Jenq and Shah (RILEM, 1990) proposed to use the critical crack tip opening displacement at the peak load, $CTOD_C$, as a fracture parameter. Their measurements showed that $CTOD_C$ was essentially independent of the size and geometry of specimens. The available LEFM equations are used to calculate $CTOD_C$ from the compliance measurements. Since the parameters in TPFM are directly determined from LEFM formulae, crack tip singularity is automatically incorporated in the model. Therefore K_{IC} calculated based on peak load and the corresponding a_c, and $CTOD_C$ become the two parameters that characterize the fracture toughness of concrete.

Based on the load-CMOD curve, the brief procedure involved in the calculation of the two parameters K_{IC} and $CTOD_C$ for three-point bend specimens (See Figure 2.7) proposed by the RILEM Technical Committee 89-FMT (1990) is as follows:

The Young's Modulus (E) is determined from the initial compliance C_i by using an empirical equation:

$$E = \frac{6Sa_0V(\alpha)}{C_iD^2B} \tag{2.14}$$

where S = Specimen loading span; B = width of the beam; D = depth of the beam

$\alpha = \frac{(a_0 + h)}{(D + h)}$; a_0 = initial notch depth; h = thickness of holder of clip gauge

$$V(\alpha) = 0.76 - 2.28\alpha + 3.78\alpha^2 - 2.04\alpha^3 + \frac{0.66}{(1-\alpha)^2}$$

C_i = the initial compliance experimentally determined from the load-CMOD curve

The critical effective crack length (a_c) is calculated by using E from Equation 2.14 and by knowing the unloading compliance C_u. Using the iteration process, a_c is found when the following empirical equation is satisfied:

$$E = \frac{6Sa_c V(\alpha)}{C_u D^2 B} \tag{2.15}$$

where a_c = the critical effective crack length

C_u = the unloading compliance at 95% of peak load (experimentally determined)

The critical stress intensity factor (K_{IC}), after which a_c is known, is calculated by using the following relationship.

$$K_{IC} = \frac{3(P_{max} + 0.5W)S\sqrt{\pi a_c}F(\alpha)}{2D^2 B} \tag{2.16}$$

where $F(\alpha) = \frac{1.99 - \alpha(1-\alpha)(2.15 - 3.93\alpha + 2.7\alpha^2)}{\sqrt{\pi}(1+2\alpha)(1-\alpha)^{3/2}}$

$\alpha = \frac{a_c}{D}$; P_{max} = the measured maximum load; $W = W_0 \frac{S}{L}$

W_0 = self-weight of the beam and L = length of beam

Finally, the critical crack tip opening displacement ($CTOD_C$) is calculated using the following equation.

$$CTOD_C = \frac{6P_{max} Sa_c V(\alpha) f(\alpha, \beta)}{ED^2 B} \tag{2.17}$$

where $f(\alpha,\beta) = \{(1-\beta)^2 + (1.081 - 1.149\alpha)(\beta - \beta^2)\}^{1/2}$; $\alpha = \frac{a_c}{D}$ and $\beta = \frac{a_0}{a_c}$

In the two parameter fracture model, the maximum applied load (peak load) and the corresponding slope of the unloading-reloading portion of the load-CMOD curve (used to calculate C_u) are experimentally determined. With known specimen geometry and Young's Modulus, the critical effective crack length (a_c) can be determined using

LEFM formulae. It should be noted that an iterative procedure is needed to calculate a_c. Once a_c is calculated, K_{IC} and $CTOD_C$ can be obtained.

In addition, based on linear elastic fracture mechanics (Broek 1982) the critical strain energy release rate (G_C) can be related to the critical stress intensity factor (K_{IC}) as

$$G_C = \frac{K_{IC}^2}{E'} \tag{2.18}$$

where $E' = E$ for plane stress condition; $E' = \frac{E}{(1-\upsilon^2)}$ for plain strain condition

E = Young's modulus; υ = Poisson's ratio.

CHAPTER 3

PROPOSED NON-LINEAR FRACTURE MECHANICS MODEL FOR CONCRETE

3.1 Introduction

For the Fictitious Crack Model, a constitutive relationship in terms of stress versus crack opening displacement, which is only obtained by performing the direct tensile testing, is required to obtain the fracture energy (G_F) and the tensile strength of material. Also the finite element analysis is needed to implement the model. The direct tensile testing for concrete is very difficult to operate, and requires special closed-loop testing equipment. There are not many laboratories where the direct tensile test can be performed. Therefore, most researchers use the assumed value of tensile strength of material to implement the model. Due to the fact that the model is very sensitive to the tensile strength, if the assumed value does not well represent the actual tensile response of the material, the model will not accurately predict the fracture behavior of the structure.

In the case of the Two-Parameter Fracture Model (TPFM), the critical effective crack length (a_c) is calculated from LEFM formulae using the measured critical crack-mouth-opening displacement ($CMOD_C$) and the measured peak load. Unloading at after approximately 95% of the peak load, which needs a special testing effort, is required to obtain the $CMOD_C$. In case that the unloading is relatively late after the peak load, an overstated $CMOD_C$ could be obtained. To achieve a stable unloading a closed-loop testing system is usually required that thus restricts the application of the TPFM. Furthermore, only two parameters, the critical stress intensity factor (K_{IC}) and the $CMOD_C$, represent the fracture behavior of material. Therefore the material responses to

crack growth cannot be obtained from the model. Researchers (Gopalaratnam and Ye 1991, Ratnalert and Wechartana 1989) showed that the TPFM did not give a good indication of material fracture properties.

In this study, by adopting the concept of the relationship between load line deflection (LLD) and crack mouth opening displacement (CMOD), which will be explained in more details later in Section 3.2, the proposed non-linear fracture mechanics model is developed. The proposed model can be implemented by experimentally obtaining the load measurement versus the corresponding LLD and CMOD from the three-point bend tests on notched beams (see Figure 3.1 for the test setup). For the proposed model, it is not necessary to perform the direct tension test or to apply any finite element analysis as required by the Fictitious Crack Model. Furthermore, by implementing the proposed model, the fracture behavior of material corresponding to crack growth, the fracture resistance curve, the brittleness of material and other important fracture parameters that are related to the Two Parameter Fracture Model can be obtained without performing any stable unloading at the peak load.

3.2 Bi-linear Relationship between Load-Line Deflection (LLD) and Crack-Mouth-Opening Displacement (CMOD)

The indirect method for obtaining fracture energy, G_F, suggested by RILEM (1985) requires the complete load versus load-line deflection (LLD) curve from the three-point bending beam test. It is difficult to obtain an accurate LLD due to the effects of the support crushing conditions. To obtain an accurate LLD, a special test setup, which eliminates the effect of support crushing, was developed. However, the measurement of crack-mouth-opening displacement (CMOD), which is not affected by the test setups in

any way, provided the more accurate results than the load-line deflection (LLD) measurement. Kim (1996) was the first to apply the relationship between CMOD and LLD to predict the fracture parameters (e.g. critical stress intensify factor) based on the LEFM formulae. He also found that the application of load-CMOD curve to determine the fracture energy is more reliable than that of load-LLD curve, which is commonly recommended by RILEM (1985). Navalurkar (1996) later investigated the method proposed by Kim (1996) to calculate the fracture energy based on the load-CMOD measurement, and also showed that the fracture energy calculated from the load-CMOD measurement is more reliable than the load-LLD measurement.

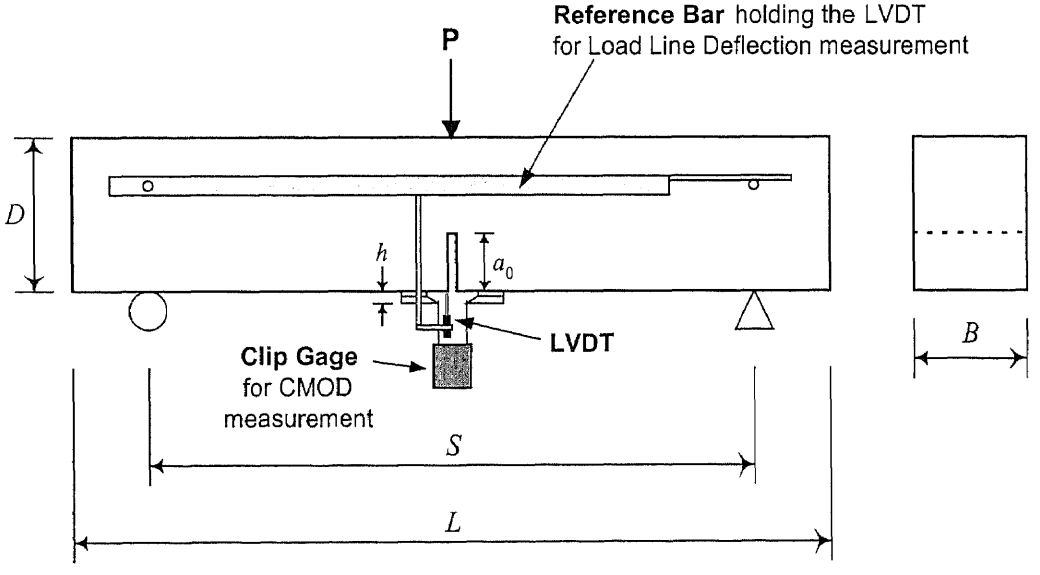

Figure 3.1 Test Setup Details for the Three Point Bend Tests on Notched Beams

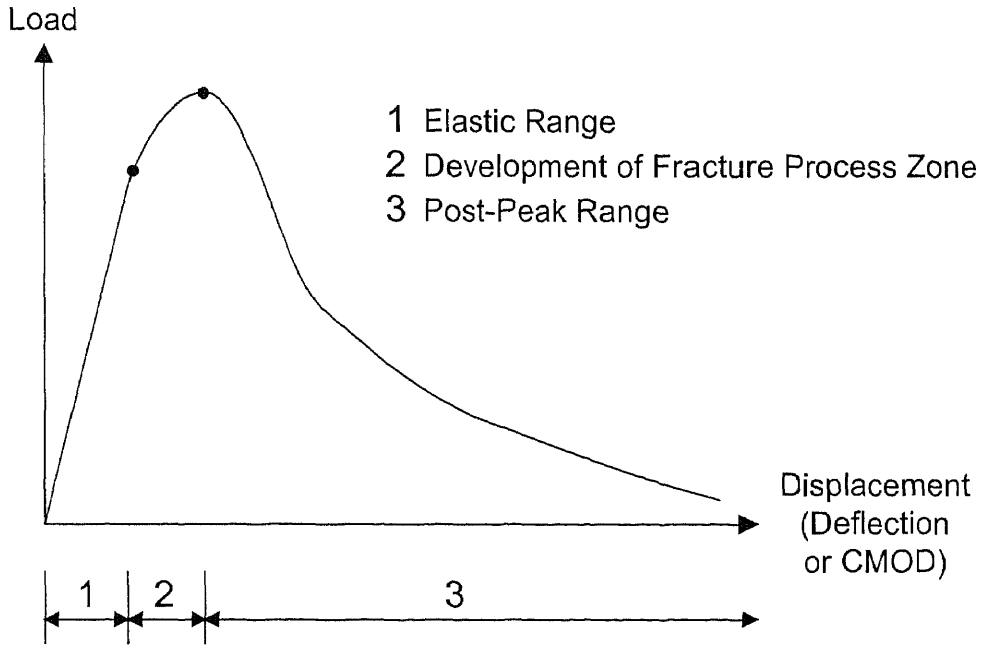

Figure 3.2(a) Typical Load - Displacement Response of Concrete

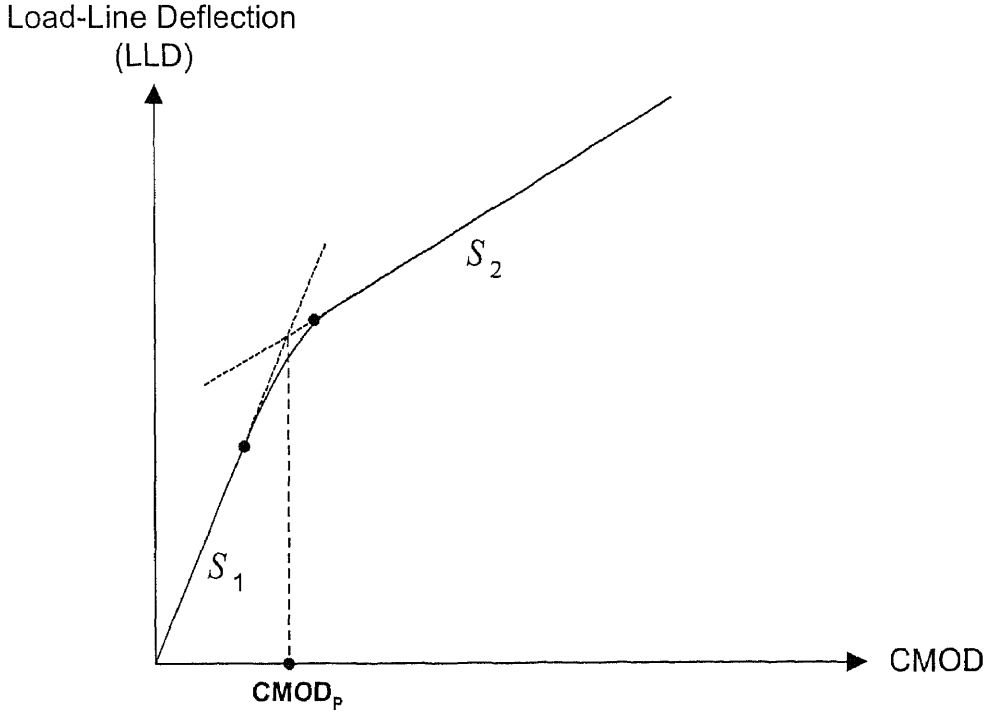

Figure 3.2(b) Relationship between Load-Line Deflection (LLD) and Crack-Mouth-Opening Displacement (CMOD)

Figure 3.2(a) illustrates a typical load versus displacement (LLD or CMOD) response. As seen in Figure 3.2(b), a typical relationship between accurately measured LLD and CMOD is bi-linear in shape. The initial slope S_1 is valid in the linear elastic portion of the load versus deflection responses. Near the peak load, the slope S_1 then gradually changes to S_2 during the formation of the fracture process zone, which is the nonlinear zone in the vicinity of the crack tip. At the peak load, the fracture process zone is fully developed, and produces traction-free cracked surface after which the specimen exhibits a linear relationship between LLD and CMOD with a constant slope S_2. The values of S_1 and S_2 can be experimentally evaluated. In Kim's study (1996) both the values of S_1 and S_2 were reported to be a material property.

3.3 Determination of Fracture Energy of Concrete

Based on the results reported by Navalurkar et al. (1999) that the fracture energy (G_F) obtained from the three-point-bend beam tests (recommended by RILEM 1985) in which the load-line deflections were measured accurately compared very well with the G_F obtained from the direct tension tests (recommended by Hillerborg 1976). They also validated that the G_F obtained from both of the experimental methods above mentioned can be considered as a material property, and since it was found to be independent of the type of test used for evaluating as well as the size of beam specimen.

Therefore, in this study, the fracture energy (G_F) is derived based on the three-point bend tests as recommended by RILEM (1985) with the special test setup (see Figure 3.1) to eliminate the effects of support crushing on the measurement of load-line deflections.

To derive the relationship for determining the fracture mechanics parameters from load versus CMOD response of a notched beam test (see Figure 3.1) the following assumptions are utilized:

1. Fracture energy, G_F, is a material property.
2. Fracture energy can be defined as the accumulation of the energy as the notched beam finally separates into two halves.
3. The fracture process zone is fully developed at the peak load, and when a crack propagates the size of fracture process zone does not change.

From the global energy balance concept, the work done by external load, F, at any instant of time Δt during the fracture process can be expressed as

$$F = W + U = \int_{\delta=0}^{\delta=\delta} P d\delta \tag{3.1}$$

where W = energy consumed in the fracture process zone for crack formation or crack growth (plastic energy), U = elastic strain energy, P = load acting on the beam and $d\delta$ = incremental load line deflection at the considered time, Δt.

The fracture energy of the cementitious material is generally defined as the amount of total energy absorbed during the fracture process divided by the fracture area, which can be expressed as

$$G_F = \frac{dF}{Bd\Delta a} = \frac{d(W+U)}{Bd\Delta a} \approx \frac{\int_{\delta=0}^{\delta=\infty} P d\delta}{B(D-a_0)} \tag{3.2}$$

where B = width of the beam, Δa = crack growth (See Figure 3.3), D = depth of the beam and a_0 = pre-notched crack length.

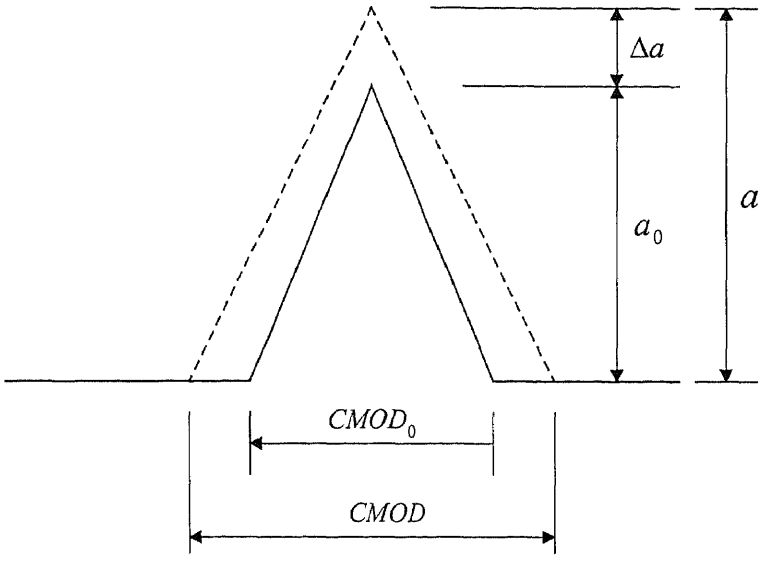

Figure 3.3 Relationship between CMOD and Crack Length (a)
$CMOD_0$ = CMOD at the beginning of the test
a_0 = initial notch length and Δa = crack growth

The incremental ratio of LLD to CMOD, $d\delta/dCMOD$, can be expressed using the chain rule as

$$\frac{d\delta}{dCMOD} = \frac{d\Delta a}{dCMOD}\frac{d\delta}{d\Delta a} \tag{3.3}$$

where $d\Delta a$ = incremental crack growth.

The energy needed to produce a small increment of load line deflection, dF is

$$dF = Pd\delta \tag{3.4}$$

where F = work done by external load and P = external load.

Substituting Equation 3.4 into Equation 3.3 gives

$$\frac{d\delta}{dCMOD} = \frac{d\Delta a}{dCMOD}\frac{dF}{Pd\Delta a} \tag{3.5}$$

Since $\frac{dF}{Bd\Delta a}$ is the fracture energy, G_F, Equation 3.3 changes to

$$\frac{d\delta}{dCMOD} = \frac{G_F B d\Delta a}{PdCMOD} \tag{3.6}$$

where B = the width of the beam.

From the typical three-point bend test on notched beams for determining the fracture energy, the relationship between LLD and CMOD ($d\delta/dCMOD$) is empirically found to be bi-linear as aforementioned. Then Equation 3.6 can be rewritten as

$$\left(\frac{d\delta}{dCMOD}\right) PdCMOD = G_F B d\Delta a \tag{3.7}$$

Integrating both sides of the Equation 3.7 within the same boundary condition gives

$$\left(\frac{d\delta}{dCMOD}\right)_1 \int_0^{CMOD_P} PdCMOD + \left(\frac{d\delta}{dCMOD}\right)_2 \int_{CMOD_P}^{CMOD} PdCMOD = G_F B \int_{\Delta a=0}^{\Delta a=\Delta a} d\Delta a \tag{3.8}$$

The first term on the left side of the above equation represents the linear elastic range of the load-CMOD curve, whereas the second term represents the post-peak response.

Integrating Equation 3.7 from time, $t = 0\,(\Delta a = 0)$, to time, $t = \Delta t\,(\Delta a = \Delta a)$, and using the definition of F from Equation 3.6 gives the following result at any time instant, Δt, as

$$G_F B \int_{\Delta a=0}^{\Delta a=\Delta a} d\Delta a = F = \int_{\delta=0}^{\delta=\delta} Pd\delta \tag{3.9}$$

Substituting Equation 3.9 into Equation 3.8 gives the relationship between the work done by external load (F) and CMOD as follows:

$$S_1 \int_0^{CMOD_P} PdCMOD + S_2 \int_{CMOD_P}^{CMOD} PdCMOD = G_F B \int_{\Delta a=0}^{\Delta a=\Delta a} d\Delta a = \int_{\delta=0}^{\delta=\delta} Pd\delta \tag{3.10}$$

where $S_1 = (d\delta / dCMOD)$ = the slope of LLD-CMOD curve in the linear elastic region and $S_2 = (d\delta / dCMOD)$ = the slope of LLD-CMOD curve in the post-peak region (or plastic region). The region between the linear elastic region and post peak region is approximated by extending the slope S_1 and S_2 till they intersect, as shown in Figure 3.2(b). The intersection of S_1 and S_2 is represented by $CMOD_P$ in Equation 3.10.

To calculate the fracture energy (G_F), which is the external energy needed to completely separate the notched beam specimen into two halves, the right side of Equation 3.2 is substituted into the Equation 3.10. Then the following relationship is obtained to calculate the G_F from the complete load-CMOD curves.

$$G_F B(D-a_0) = \int_{\delta=0}^{\delta=\infty} P d\delta = S_1 \int_0^{CMOD_P} P dCMOD + S_2 \int_{CMOD_P}^{\infty} P dCMOD \qquad (3.11)$$

Therefore the procedure for determining the fracture energy by using the load-CMOD curve can be briefly described as follows:

1. Determine the correlated constant S_1 and S_2 by relating accurately measured load line deflection (LLD) to crack-mouth-opening displacement (CMOD) of the beam.
2. G_F is determined by multiplying the correlated constants (S_1 or S_2) to the corresponding area under the load-CMOD curve as shown in the Equation 3.11.

3.4 Determination of Crack Growth in Concrete

It has been observed from fracture tests that the load-line deflection (LLD) measurements are strongly affected by the support conditions. The crack-mouth-opening displacements (CMOD), on the contrary, are not affected by the same support crushing conditions in anyway, and therefore are more reliable responses to crack growth than the load-line

deflection. Based on this finding, it is possible to relate the accurate deflection measurements to the crack-mouth-opening displacement measurements. It is therefore possible to use load and crack-mouth-opening displacement measurements to evaluate the fracture behavior of concrete structure. In this study, a method is developed using the load and crack-mouth-opening displacement responses to determine the fracture behavior and fracture parameters of concrete such as the load-crack growth response, the resistance curve, the critical crack growth and the critical energy release rate.

The phenomenon of slow crack growth prior to the peak load, which is caused by the growth of the fracture process zone in front of the crack tip, has long been noticed. Jenq and Shah (1985a, 1985b) proposed using the Linear Elastic Fracture Mechanics (LEFM) method to study the growth of fracture process zone by means of the critical effective crack length (a_c), which is defined as the sum of the initial notch length (a_0) and a stable crack growth (Δa) at the peak load.

In this study the crack growth (Δa) at any instant of time, Δt ($\Delta a = \Delta a$ and $\delta = \delta$), during the fracture process can be determined. By applying Equation 3.10, the relationship to determine the crack growth can be expressed as

$$G_F B \int_0^{\Delta a} d\Delta a = \int_0^{\delta} P d\delta = S_1 \int_0^{CMOD_P} P dCMOD + S_2 \int_{CMOD_P}^{CMOD} P dCMOD \tag{3.12a}$$

$$\Delta a = \frac{1}{G_F B} \int_0^{\delta} P d\delta = \frac{1}{G_F B} \left(S_1 \int_0^{CMOD_P} P dCMOD + S_2 \int_{CMOD_P}^{CMOD} P dCMOD \right) \tag{3.12b}$$

where G_F = the fracture energy and a material property.

From Equation 3.12b, the crack growth (Δa) at any instant of time can be determined by using either the load-CMOD curve or the load-deflection curve. If during a

given time instant, the fracture process zone has not been fully developed, or the peak load has not been reached, the second term of the load-CMOD equation will be zero. Therefore, the plots between the applied load (P) or flexural stress and the crack growth (Δa) at any instant of time can be obtained, representing the fracture behavior of structures. Figure 3.4 shows a typical load-crack growth response obtained by implementing the proposed model (see Equation 3.12b) into the load-displacement (accurately measured LLD or CMOD) response in the present study. The analytical results by the proposed model for all concrete specimens tested are presented and discussed in Chapter 5.

In applying the Two Parameter Fracture Model (TPFM) to the fracture of a given cracked concrete beam, the model can utilize the LEFM-based K_{IC} and the critical crack mouth opening displacement ($CMOD_C$) to predict only the maximum load and the critical crack growth (a_c) of the beam. Limited by its generality, the model is unable to predict other fracture behavior such as maximum deflection, or the overall fracture behavior of the member (including post-peak characteristics). However, the TPFM has been conventionally used, in large part, due to the difficulties encountered in making exact measurements of the load-line deflection as required by the more complicated models such as the Fictitious Crack Model (Hillerborg 1976). There have been many discrepancies for determining the area under the load-deflection curve without properly accounting for the support-crushing phenomenon. These problems can be eliminated by using the concept of the bilinear relationship between CMOD and deflection as proposed here in this study. Since the CMOD is unaffected by the support condition, and also directly related to the crack growth, the area under load-CMOD curve is more reliable

when used to determine the crack growth. With this process, the whole load-crack growth curve can be predicted (see Figure 3.4).

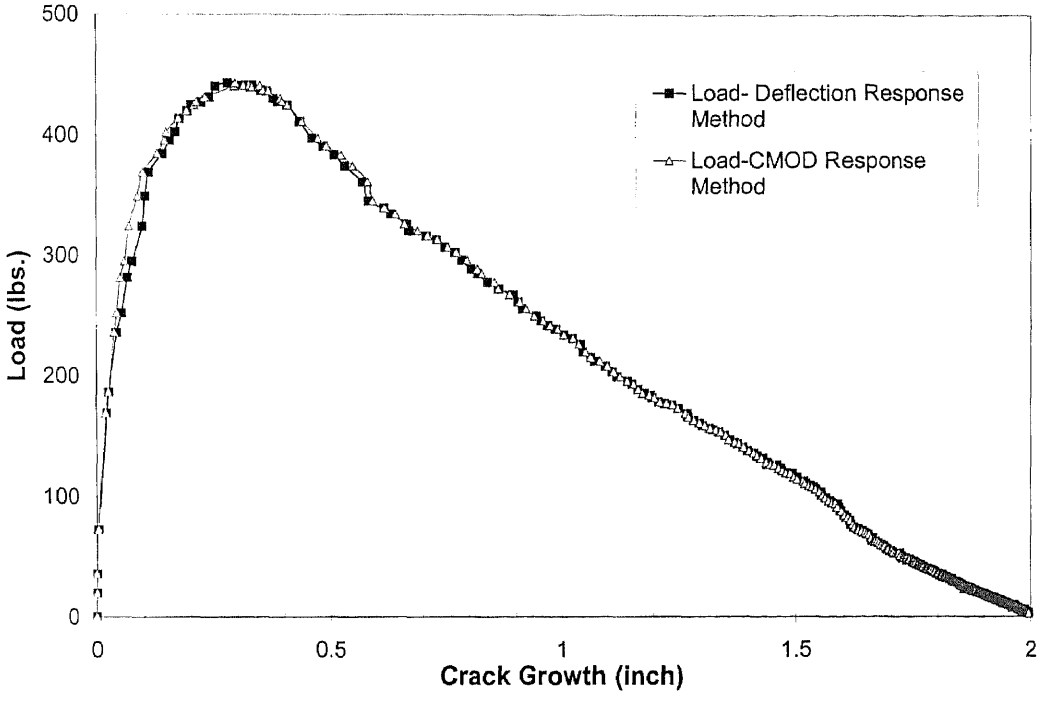

Figure 3.4 Typical Load-Crack Growth Response Obtained by the Proposed Model

Therefore the critical crack length, a_c, as defined by the Two-Parameter Fracture Model (TPFM) can be determined by using Equation 3.12b to obtain Δa at the peak load as follows:

$$a_c = a_0 + \Delta a_{\text{peak load}} \tag{3.13}$$

where a_0 = initial notch depth.

The a_c calculated from Equation 3.13 can be compared with those determined from the TPFM to investigate the performance of the proposed fracture mechanics model.

3.5 Determination of Fracture Resistance and Brittleness of Concrete

By realizing that during the fracture process, the material outside the fracture process zone is assumed to be linear elastic, whereas those inside the fracture process behaves nonlinear and inelastic (Hillerborg et al. 1976, Patersson 1981). For a three-point-bend beam test, the fracture process zone gradually grows until reaching its full size at the peak load. After the peak load, the process zone moves upwards as the microcrack grows, but the process zone size remains unchanged unless a confinement effect due to the compression zone is encountered. Furthermore no microcrackings will occur outside the fracture process zone, and thus the material outside of the process zone simply unloads elastically.

To derive a relationship for determining the fracture mechanics parameters from load-displacement (load line deflection or crack mouth opening displacement) responses of a three-point bending beam test the following assumptions are used:

1. The elastic components of both the load line deflection (δ_E) and crack mouth opening displacement ($CMOD_E$) can be calculated at any applied load by considering that the material unloads and reloads elastically with the constant initial stiffness K_i of the load-displacement (δ or CMOD) curve (Navalurkar 1996).
2. The ratios of the change of LLD to the change of CMOD in the pre-peak and post-peak phases during fracture process (S_1 and S_2) are constant and material properties.

The beam displacements either load line deflection or CMOD can be separated into two components, namely the elastic component and the plastic component occurring during crack propagation (see Figure 3.5). This phenomenon can be expressed as

$$\delta = \delta_E + \delta_P \tag{3.14a}$$

$$CMOD = CMOD_E + CMOD_P \tag{3.14b}$$

where δ and $CMOD$ = total load line deflection and total CMOD respectively;

δ_E and δ_P = elastic and plastic component of the load line deflection respectively;

$CMOD_E$ and $CMOD_P$ = elastic and plastic component of CMOD respectively.

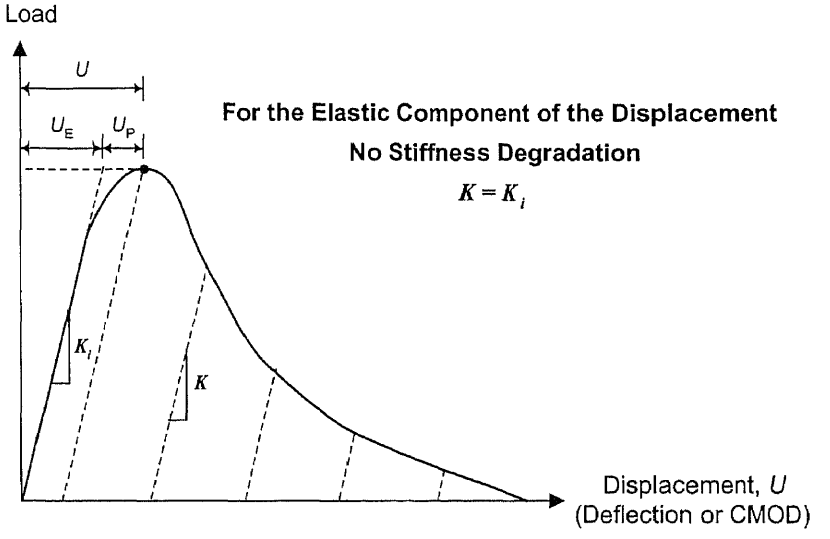

Figure 3.5 Assumption of Elastic Unloading-Reloading Behavior of the Elastic Component of the Displacement (Deflection or CMOD) (Navalurkar 1996)

The elastic component of the displacement can be determined by using the first assumption as listed above, or by performing cyclic tests as shown by Jenq and Shah (1985b). The elastic components of both load-line deflection and crack-mouth-opening displacement as a function of the total displacement are material properties (Jenq and Shah 1985b), and also used for determining the energy consumed in the fracture process zone to propagate the crack. Applying the concept that outside the fracture process zone the material behaves elastically along with the first assumption, the relationship between the elastic component of the displacements and the material stiffness can be expressed as

$$K_i^{\delta} = \frac{dP}{d\delta_E} \tag{3.15a}$$

$$K_i^{CMOD} = \frac{dP}{dCMOD_E} \tag{3.15b}$$

where K_i^{δ} and K_i^{CMOD} are the initial stiffness of the beam determined from the slope of the load-LLD curve and the load-CMOD curve respectively (before the start of the fracture process zone growth).

The energy required for propagating the crack at the crack tip (or the inelastic energy absorbed by the fracture process zone) can be obtained by considering the energy balance of a beam under bending at any instant as follows:

$$W = F - U \tag{3.16}$$

where W = energy consumed for crack propagation (plastic energy);

F = work done by external load (external energy) and U = elastic strain energy.

By knowing the elastic component of the displacement, the plastic energy (for crack propagation) can be determined by subtracting the elastic strain energy from the work done by external load (external energy). This phenomenon represented by the Equation 3.14a can be expressed in terms of the load-LLD relationship as:

$$W = \int_{\delta=0}^{\delta=\delta} P d\delta_P = \int_{\delta=0}^{\delta=\delta} P d\delta - \int_{\delta=0}^{\delta=\delta} P d\delta_E \tag{3.17}$$

During crack propagation, crack tip extension generally consumes some energy equal to W. The rate of change of W with respect to crack length (a), denoted by G_R, is termed *the fracture resistance* or *the strain energy release rate*. And, G_R can be expressed as:

$$G_R = \frac{1}{B}\frac{dW}{d\Delta a} = \frac{1}{B}\frac{d}{d\Delta a}(F - U) \tag{3.18}$$

where B = the width of the beam and Δa = crack growth or crack extension.

Rearranging the above equation gives

$$G_R B d\Delta a = dW = dF - dU \tag{3.19}$$

By integrating both sides of Equation 3.19 between $t = 0\,(\Delta a = 0 \text{ and } \delta = 0)$ and $t = \Delta t\,(\Delta a = \Delta a \text{ and } \delta = \delta)$, the G_R at any instant of time, Δt, can be expressed as:

$$G_R B \int_0^{\Delta a} d\Delta a = W = \int_0^{\delta} P d\delta - \int_{\delta=0}^{\delta=\delta} P d\delta_E \tag{3.20}$$

Using the relationship between the total deflection (δ) and its elastic component, and by substituting the elastic component of LLD (δ_E) from the Equation 3.15a into the Equation 3.20, this gives

$$G_R B \int_0^{\Delta a} d\Delta a = W = \int_0^{\delta} P d\delta - \int_{P(\delta=0)}^{P(\delta=\delta)} \frac{P dP}{K_i^{\delta}} \tag{3.21}$$

Rearranging Equation 3.21 leads to

$$G_R = \frac{1}{B\Delta a}\int_0^{\delta} P d\delta - \frac{1}{B\Delta a}\left[\frac{P^2}{2K_i^{\delta}}\right]_{P(\delta=0)}^{P(\delta=\delta)} \tag{3.22}$$

where Δa is the crack growth at any time instant previously derived in Equation 3.12b and K_i^{δ} is the initial stiffness of the beam determined from the slope of the load-LLD curve. Therefore, the fracture resistance or energy release rate at any time instant can be determined from the load-LLD curve using Equation 3.22.

The G_R can also be derived using the load-CMOD curve. By applying the correlated constants S_1 and S_2, which are the relationship between load-line deflection (LLD) and crack mouth opening displacement (CMOD) obtained from the beam tests, G_R can be obtained, by substituting the Equation 3.10 into Equation 3.20, as follows:

$$G_R B \int_0^{\Delta a} d\Delta a = \left[S_1 \int_0^{CMOD_P} PdCMOD + S_2 \int_{CMOD_P}^{CMOD} PdCMOD \right] - \int_{\delta=0}^{\delta=\delta} Pd\delta_E \tag{3.23}$$

From the bi-linear relationship between LLD and CMOD as described in Equation 3.7 through 3.10, the relationship between the incremental LLD and CMOD in the elastic region (before the fracture process zone fully developed) can be expressed as

$$d\delta_E = S_1 dCMOD_E \tag{3.24}$$

Substituting Equation 3.15b into Equation 3.24 gives

$$d\delta_E = S_1 \frac{dP}{K_i^{CMOD}} \tag{3.25}$$

Substituting Equation 3.25 into Equation 3.23 results to

$$G_R B \int_0^{\Delta a} d\Delta a = \left[S_1 \int_0^{CMOD_P} PdCMOD + S_2 \int_{CMOD_P}^{CMOD} PdCMOD \right] - S_1 \int_{P(\delta=0)}^{P(\delta=\delta)} \frac{PdP}{K_i^{CMOD}} \tag{3.26}$$

and by rearranging Equation 3.26,

$$G_R = \frac{1}{B\Delta a} \left[S_1 \int_0^{CMOD_P} PdCMOD + S_2 \int_{CMOD_P}^{CMOD} PdCMOD \right] - \frac{S_1}{B\Delta a} \left[\frac{P^2}{2K_i^{CMOD}} \right]_{P(\delta=0)}^{P(\delta=\delta)} \tag{3.27}$$

where Δa is the crack growth at any instant of time previously shown in Equation 3.12b and K_i^{CMOD} is the initial stiffness of the beam determined from the slope of the load-CMOD curve. Therefore, by knowing Δa , P, S_1, S_2 and the area under *P-CMOD* curve at any time instant, the G_R value can be obtained by using Equation 3.27.

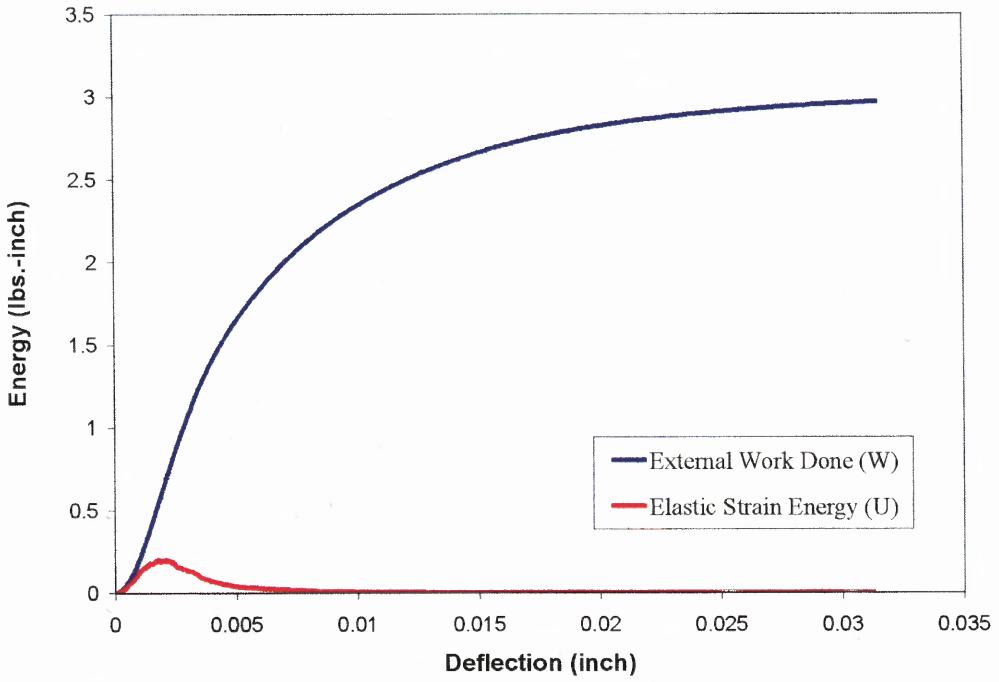

Figure 3.6 Typical Energy Absorption of Notched Beam during Bending Based on the Load-Deflection Response

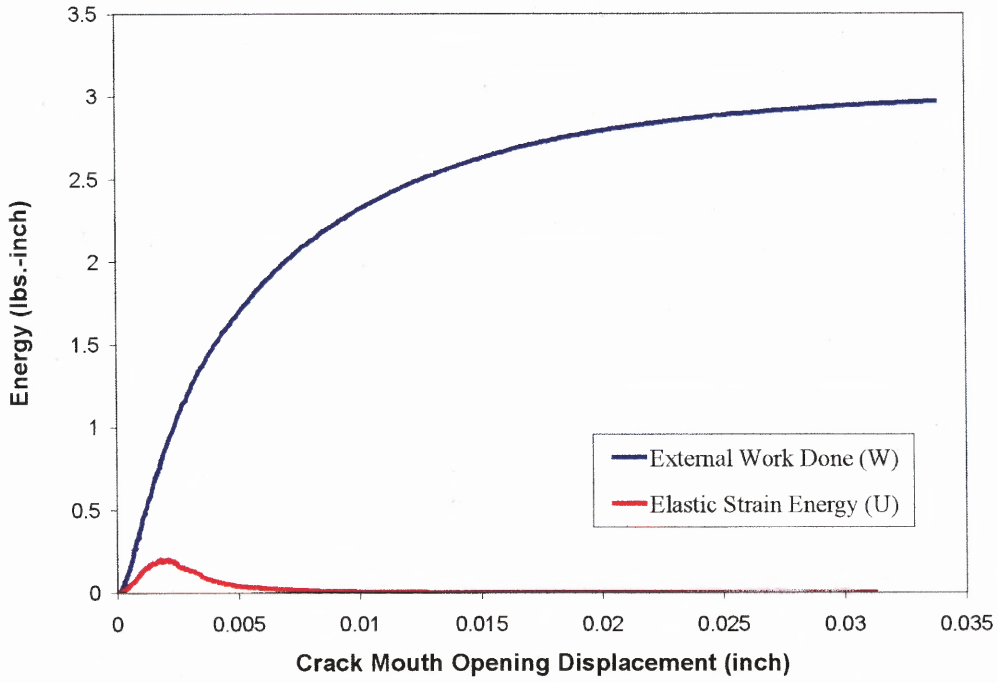

Figure 3.7 Typical Energy Absorption of Notched Beam during Bending Based on the Load-CMOD Response

Figure 3.6 shows the energy absorption of the notched beam during a bending test based on the load-accurately measured deflection response as expressed in Equations 3.16 and 3.20. Figure 3.7 shows the energy absorption during a bending test as derived from the load-CMOD response as expressed in Equations 3.16 and 3.23.

At the instant of unstable crack growth, G_R is called G_C, *the critical strain energy release rate*, which is a measure of fracture toughness. Therefore, for a three-point-bend beam test, G_C is equal to the value of G_R at the peak load, and can be calculated from Equations 3.22 and 3.27. The G_C value from this model can be compared with the relevant fracture parameters calculated from the Two Parameter Fracture Model (RILEM 1990).

A plot of energy release rate (G_R) versus crack extension (Δa) or crack length (a) is called a *Resistance Curve* or *R Curve*, which illustrates the material resistance to crack extension. The G_R value at any instant of time and the R curve can be determined by implementing the proposed model, substituting Equation 3.22 into the load-deflection response, or Equation 3.27 into the load-CMOD response. The concept of the energy release rate shown here previously has been discussed in details in Section 2.3.3.

Figure 3.8 shows typical R curves generated by the proposed model using Equation 3.27 with both the load-deflection and load-CMOD responses obtained from a bend beam test in this study. The R curves are the plot between the crack length (initial notch length $+\Delta a$) and its corresponding G_R value. The analytical results by the proposed model for all concrete specimens tested are presented in Chapter 5. Figures 3.9 (a) and 3.9 (b) show schematic R curves for ideally brittle materials and quasi-brittle materials such as concrete.

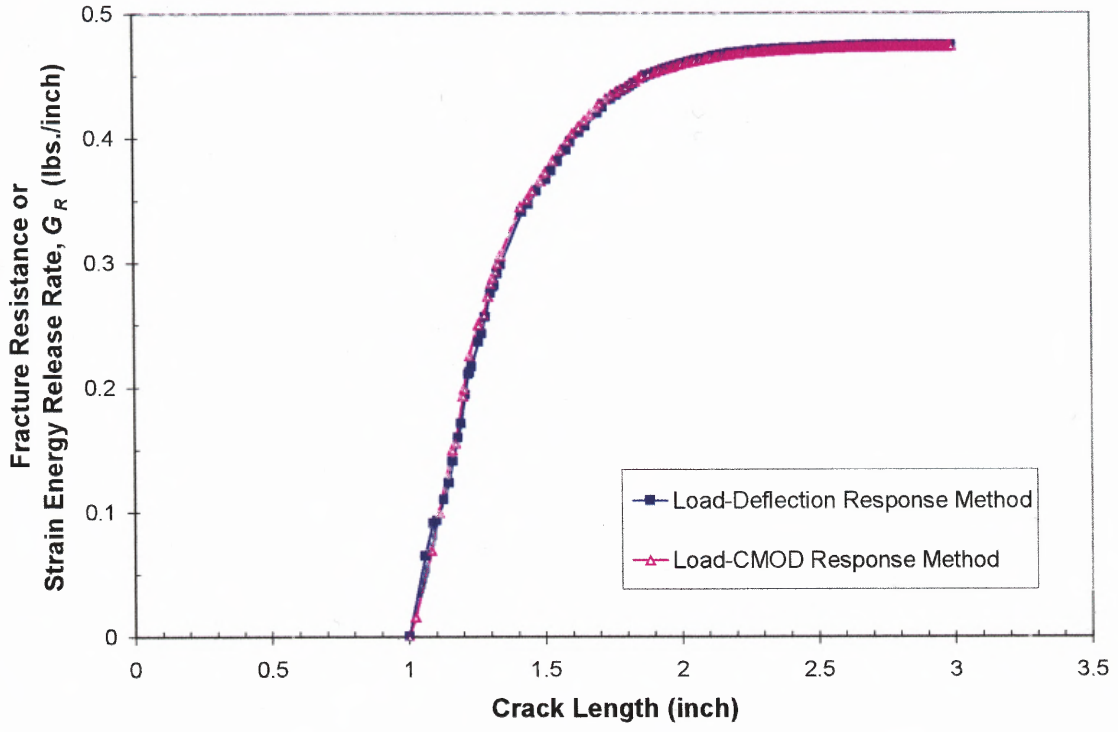

Figure 3.8 Typical Resistance Curve (*R* curve) in the Present Study

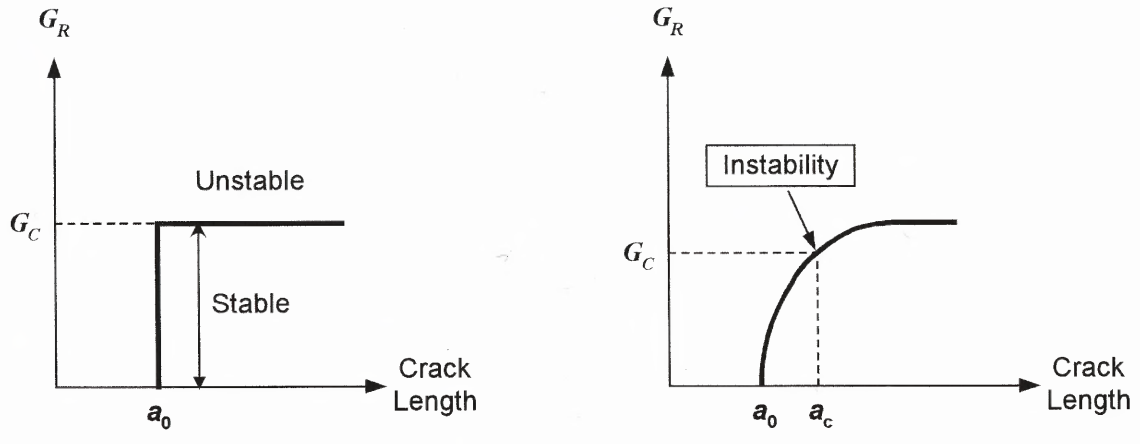

(a) Ideally Brittle Material

(b) Quasi - Brittle Material

Figure 3.9 Schematic *R* Curve Diagrams

The shape of the R curve depends on material behavior and, to a lesser extent, on the configuration of the cracked structure. The R curve for an ideally brittle material is rising with the infinite slope and becomes flat at the critical load for ideal brittle material, the sudden failure at peak load will occur. Propagation of the initial crack may mean catastrophic failure of the structure. For quasi-brittle material like concrete, the R curve is rising with the steep slope, and decreasing until reaching the flat slope. This phenomenon occurs due to the existence of crack arrest mechanism such as aggregate bridging resulting from the bond strength between cement matrices and aggregate. A plastic zone or fracture process zone at the crack tip increases in size as the crack grows. The external force must increase to maintain crack propagation. When the fracture process zone has fully developed, G_R will eventually reach stead-state values, and the R curve becomes flat with any further crack growth. Therefore the slope of the R curve when the fracture process zone fully developed can be used to indicate the ductility or brittleness of concrete materials.

In this study, the brittleness of the material is expressed by the slope of the R curve at the peak load, which can be expressed as

$$Brittleness\ Index = \frac{dG_R}{d\Delta a} \tag{3.28}$$

For a zero slope at the peak load, an ideally brittle material is obtained. In the case of quasi-brittle materials like concrete, the lesser the slope of R curve at the peak load, the more brittle the material becomes. However, for material with a steeper slope of R curve at the peak load, the less brittle the material behaves.

CHAPTER 4

EXPERIMENTAL PROGRAM

4.1 Introduction

This chapter describes the experimental program developed to study the influence of high performance matrices on fracture behavior of concrete. Fine particles such as silica fume and coal fly ash of various sizes were used as cement replacement to produce high performance concrete matrices. Sizes, fineness and chemical compositions of fine particles used in this study were investigated prior to mixing with concrete. The mechanical properties and the fracture behavior of concrete are among the main parameters to be studied. The scheme of work carried out in the present study is shown in Figure 4.1. The mechanical properties of concrete were carried out by means of uniaxial compression tests on cylinders and cubes. Test data obtained by performing three-point bend tests on notched beams were used to validate the Two-Parameter Fracture Model and the proposed fracture mechanics model, both of which yield fracture parameters that were used to study the fracture behavior of concrete and also to verify the proposed fracture model.

The data obtained from all tests of the experimental program were categorized into two major groups: the empirical results and the analytical values as determined by the proposed fracture models. The types of tests conducted in the experimental program are as follows: particle size distribution test of fly ash, compressive strength test of mortar, uniaxial compression test of concrete, and three-point bend test on notched beams. Details of the experimental programs are described in the following sections.

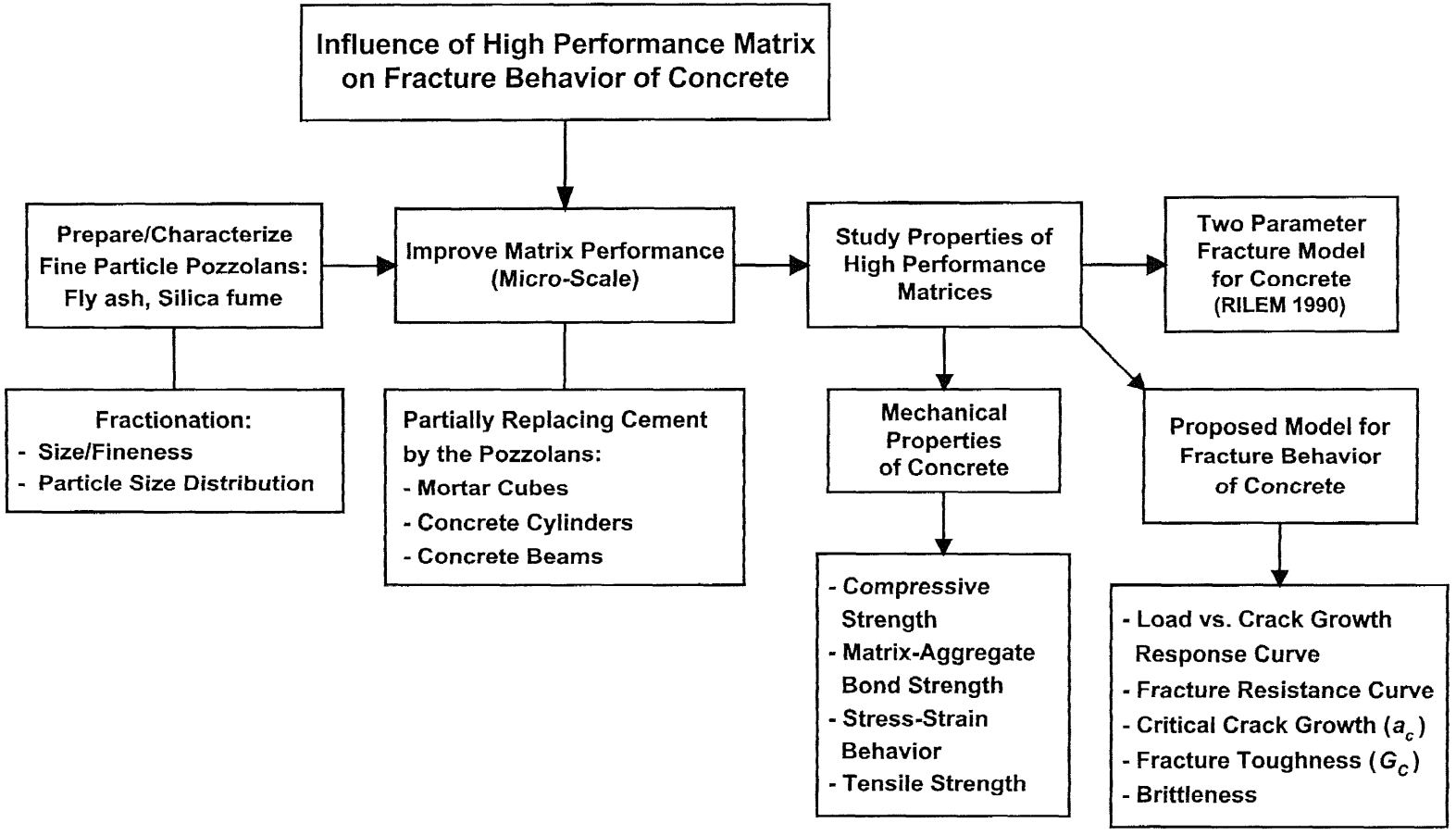

Figure 4.1 Scheme of Work of the Present Study

4.2 Materials

Materials used in this study are as follows:

1. Cement – A standard Portland cement type I conforming to ASTM C 150.
2. Sand – Local siliceous sand (river sand) passing through sieve No. 4 (opening size 4.75 mm) conforming to ASTM C 33.
3. Coarse Aggregate – Crushed limestone coarse aggregate of size 3/8"
4. Fly Ash – Class F fly ash generated by the local power plant (from Mercer County, New Jersey) and fractionated using air classifier into six different size ranges (13F, 15F, 16F, 18F, 18C and MO). 13F to18C are classified as the finest to the coarsest by the mean particle size respectively. MO denotes the as-received fly ash (or raw fly ash). Table 4.1 shows chemical compositions of fractional fly ash and cement. Fly ashes used are classified as Class F fly ash according to ASTM 618 (as described in Chapter 2 Section 2.2.4). Most of the fractionated fly ashes have only some slight variation in their oxide composition when the particle sizes changed.
5. Silica Fume – particle size less than 1 μm. and consists of 96-98% reactive silicon dioxide.
6. Water – Tap water was used throughout the experiment program.

Table 4.1 Chemical Compositions of Coal Fly Ash and Cement

Sample	%SO_3	% SiO_2	%Al_2O_3	%Fe_2O_3	%CaO	%K_2O	%MgO	%Na_2O	%LOI	Specific Gravity
Cement	2.53	20.07	8.84	1.410	60.14	0.86	2.49	0.28	0.73	3.12
13F	3.81	38.93	24.91	12.89	6.85	2.10	1.55	1.31	2.67	2.75
15F	3.33	40.25	25.02	13.12	6.60	2.11	1.47	1.30	1.88	2.64
16F	3.05	40.65	24.92	13.26	6.55	2.09	1.41	1.26	2.06	2.61
18F	2.94	41.56	24.47	14.21	6.58	2.01	1.40	1.17	1.94	2.51
18C	2.40	43.25	23.31	17.19	7.38	2.00	1.30	0.88	2.55	2.42
MO	3.13	41.54	27.74	14.83	6.89	2.07	1.43	1.17	2.05	2.50

4.3 Particle Size Distribution Test of Fly Ash

The objective of this study is to obtain the mean size, particle size distribution and fineness of each different size range of fly ash used. All fly ash samples were subjected to particle size analysis by Leeds-Northrup Microtrac SR 150, a laser-based particle size analyzer. A small amount of sample (20 grams) is mixed with deionized water and made into an aqueous solution with the aid of a surfactant. The solution is then fed into a circulation reservoir, which supplies a stream of solution into the analyzer. Particles of different sizes ranging from 0.75 to 704.00 microns are counted based on percent volume basis. The computer then gives an average of a series of three measurements at the end of each run. The procedure is then repeated over the course of 20 minutes, or until the results are consistent with one another.

The particle size distribution clearly plays a significant role in the rate of chemical reactivity in concrete, and a satisfactory assessment of the fly ash size distribution could well clarify the variable behavior of fly ash in concrete. Two grading indices for the particle size distribution suggested are the grading modulus (G) and the mean equivalent diameter (D). Assuming that it is the surface area of the fly ash particles per unit volume concerned, and since the definition of the grading modulus is the surface area of spheres of the same size as the actual particles; the grading modulus will be even better suited for fly ash particles.

Considering a single grain size of diameter D as follows. The surface area of the equivalent size sphere is πD^2, and its corresponding volume is $\pi D^3 / 6$. Then the grading modulus (G) can be expressed as

$$G = \text{Surface area of sphere/ Volume of sphere} = \frac{6}{D} \tag{4.1}$$

The values of D for the particles are estimated or measured in terms of equivalent size spheres. Since the majority of the fly ash particles have spherical shapes, the parameter G can be used directly for fly ash fineness classification.

4.4 Compressive Strength of Mortar

In this study, the fly ashes were used as a replacement of cement of 0%, 15%, 25% and 50% by weight of cementitious materials (fly ash and cement). Silica Fume was used as a cement replacement of 10% by weight of cementitious materials (silica fume and cement). Details of the mix proportions of mortar used are presented in Table 4.2. The compression tests were performed in accordance with ASTM C-109. The 2 x 2 x 2 inch cube specimens were cast in steel molds and rested in the normal room environment. After 24 hours they were demolded, and cured in saturated lime water until the time of testing. The specimens were tested at the age of 7, 14, 28 and 56 days.

Table 4.2 Mix Proportions of Mortar by Weight

Materials	Fly Ash Mortar				Silica Fume Mortar
	Fly Ash Replacement				
	0%	15%	25%	50%	
Cement	1	0.85	0.75	0.5	0.9
Fly Ash	0	0.15	0.25	0.5	0
Sand	2.75	2.75	2.75	2.75	2.75
Water	0.5	0.5	0.5	0.5	0.5
Silica Fume	0	0	0	0	0.1

The objectives of these tests were as follows:

1. To study the compressive strength development of mortars incorporating fine particles such as silica fume and fly ash of various size ranges.

2. To evaluate the effect of particle size and percent replacement of fly ash on the compressive strength of mortar.
3. To evaluate the effect of fly ashes and silica fume on the change in bond strength between cement matrix and coarse aggregate.

4.5 Uniaxial Compression Test of Concrete

Details of the mix proportions of the concrete used for both Uniaxial Compression Tests and Three-Point Bend Tests on Notched Beams are presented in Table 4.3. In this study, the fly ashes were used as a replacement of cement of 25% by weight of cementitious materials (fly ash and cement). Silica Fume was used as a cement replacement of 10% by weight of cementitious materials (silica fume and cement). The control concrete without any additives were also cast and to be used as the reference. The 3 x 6 inch cylinder specimens were cast in plastic molds and rested in the normal room environment. After 24 hours they were demolded, and then transferred into a 100% humidity room for curing until one day before testing. All cylinders were tested at the ages of 28 and 56 days.

Table 4.3 Mix Proportions of Concrete by Weight

Materials	Fly Ash Concrete		Silica Fume Concrete
	Fly Ash Replacement		
	0%	25%	
Cement	1	0.75	0.9
Fly Ash	0	0.25	0
Sand	2	2	2
Coarse Aggregate	3	3	3
Water	0.5	0.5	0.5
Silica Fume	0	0	0.1

The uniaxial compression tests provide information of compressive stress versus strain response, which is of direct practical interest in the design of concrete structures. The primary objectives of conducting these tests on concrete are as follows:

1. To study the stress-strain behavior of concrete, primarily including the complete stress-strain curve.
2. To determine the concrete properties such as the uniaxial compressive strength (f_c'), the modulus of elasticity (E_c), the peak strain (ε_p) and the toughness of concrete. In this study the toughness of concrete is defined as the area under a stress-strain curve of concrete up to a strain of 0.003, which is assumed as the failure condition.
3. To evaluate the effect of fine-particle pozzolans such as silica fume and fly ash of various size ranges on stress-strain properties of concrete.
4. To evaluate the effect of fly ashes and silica fume on the change in bond strength between cement paste and coarse aggregate.

The compression test were performed according to the standard procedures, ASTM C-39 and ASTM C-469. Prior to testing, each 3 x 6 inch concrete cylinder was capped with sulfur compound at both ends to insure parallel, smooth surfaces of the test specimens and to maintain constant length for all cylinders. The test were performed in a 100-kip capacity material testing system (MTS 442), consisting of a servo-controlled, closed-loop machine. To obtain a complete stress-strain curve, the specimens were tested by applying uniaxial compression under deformation (axial strain) control, at the slow strain rate of 1.67×10^{-5} strain per second. The axial deformations were measured by two clip-on strain gages with four-inch gage length, which were mounted on the specimen. In order to maintain the average rate of axial deformation, the signals from the two strain

gages were averaged and fed back to the controller to constantly adjust the applied load in order to maintain a stable post-cracking response. An MTS digital data acquisition system was used to record the strain values and the corresponding loads. Figure 4.2 shows the picture of the test setup. It took approximately 15 to 20 minutes to complete the entire test.

Furthermore, for some of the selected specimens, the 4 x 8 inch cylinders were also cast to compare the results of concrete properties with that of the 3 x 6 inch cylinders. The results of these tests are presented in Chapter 5.

4.6 Three-Point-Bend Test on Notched Beams

Details of the mix proportions of the concrete used for the Three-Point Bend Tests on Notched Beams are the same as those for the Uniaxial Compression Tests (as shown in Table 4.3). In this study, the fly ashes were used as a replacement of cement of 0% and 25% by weight of cementitious materials (fly ash and cement). Silica Fume was used as cement replacement of 10% by weight of cementitious materials (silica fume and cement). The 3 x 3 x 16 inch beam specimens were cast in plexi-glass molds and rested in the normal room environment. After 24 hours they were demolded, and then transferred into a 100% humidity room for curing until one day before testing. All beams were tested at the age of 56 days.

The main purpose of the three-point-bend test on notched beams is to obtain the complete load versus crack-mouth-opening displacement (CMOD) curve and load versus load-line deflection (LLD) curve, and to study the fracture behavior of concrete. The details of the objectives of these tests are as follows:

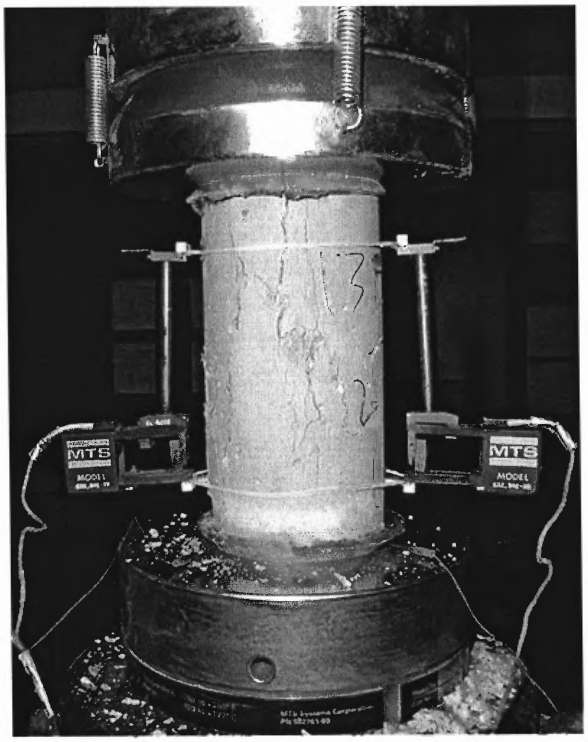

(a) Details of the Test Setup

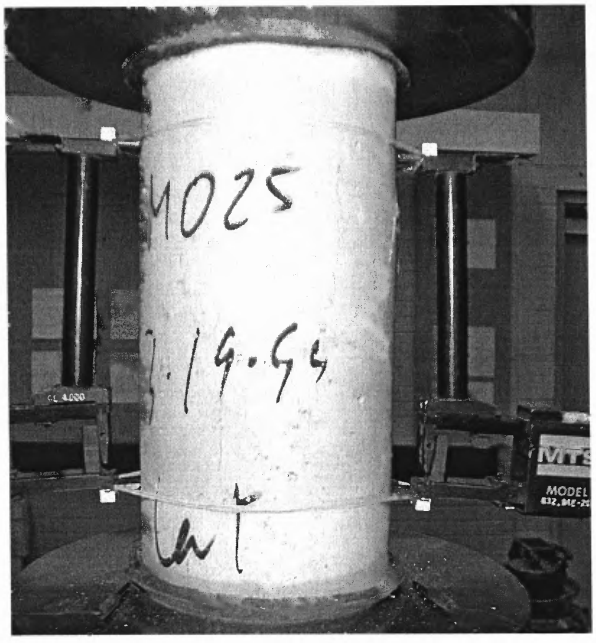

(b) Close-up View

Figure 4.2 Photographs of the Uniaxial Compression Test Setup

1. To determine the fracture energy (G_F) of concrete based on RILEM recommendation (RILEM 1985) that G_F is defined as the area under the load and load-line deflection (LLD) curve divided by the area of uncracked ligament (see Equation 2.12). Also, to determine G_F based on the bi-linear relationship between CMOD and LLD that G_F is determined from the load versus CMOD curve as previously described in Chapter 3 (see Equation 3.11).
2. To use the data consisting of load, LLD and CMOD obtained from the beam tests to implement the proposed fracture mechanics model as described in Chapter 3 for the study of fracture behavior of concrete such as the load-crack growth responses and the resistance curve. And, to determine the fracture mechanics parameters of concrete such as the critical crack growth, the critical energy release rate and the brittleness.
3. To use the load-CMOD responses obtained from the beam tests to implement the Two-Parameter Fracture Model (TPFM) as described in Chapter 2. And, to determine the fracture mechanics parameters in comparison to the related fracture mechanics parameters as determined by the proposed fracture mechanics model.
4. To evaluate the effect of fine-particle pozzolans such as silica fume and fly ash with various ranges of particle sizes on the fracture behavior and fracture mechanics parameters of concrete.

Figure 4.3 shows the photographs of the test setup of the three-point bending notched beam test where special arrangement was made to accurately measure the load-line deflection. Figure 4.4 shows the diagram of the three-point bending beam test setup and the dimension of the test specimens.

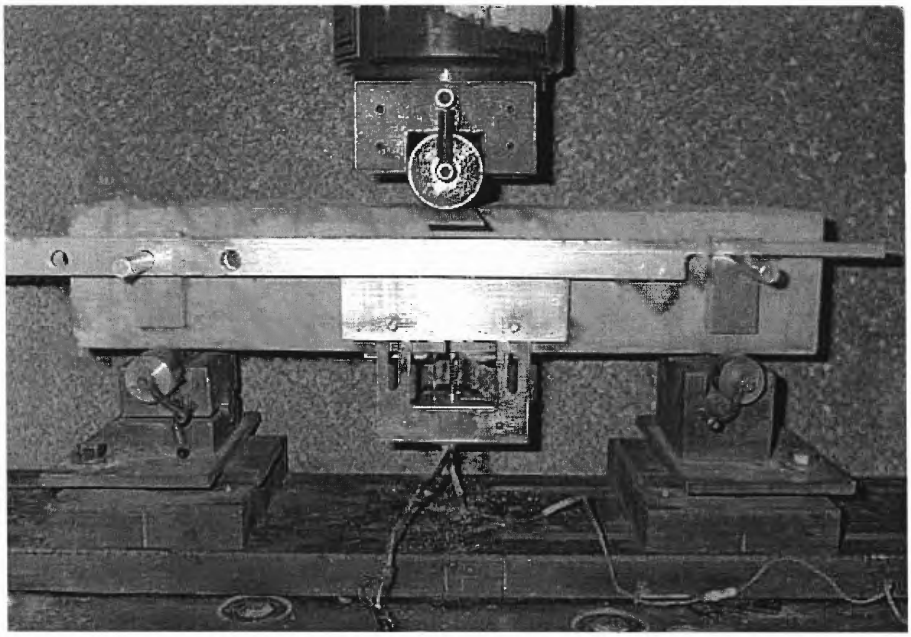

(a) Front View

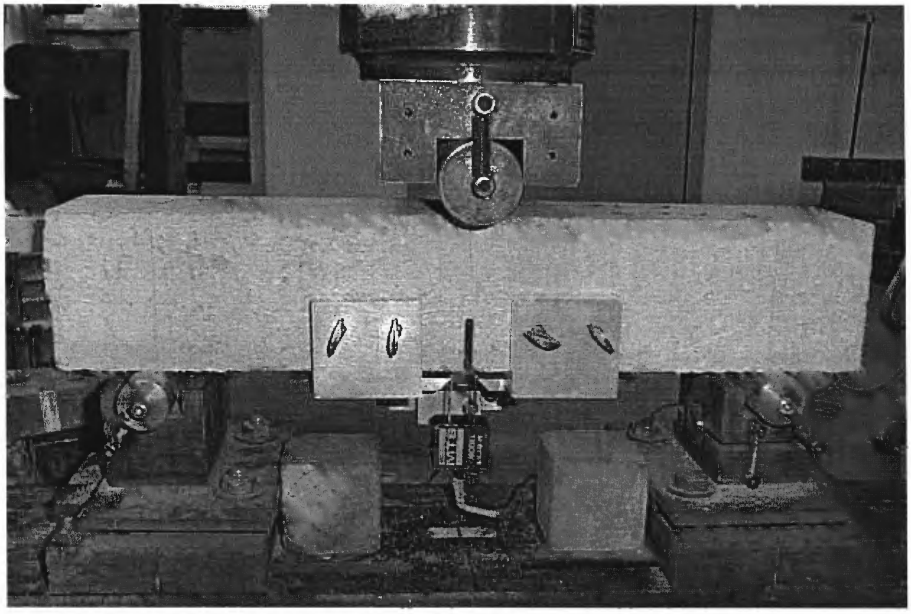

(b) Back View

Figure 4.3 Photographs of the Three-Point Bend Test Setup

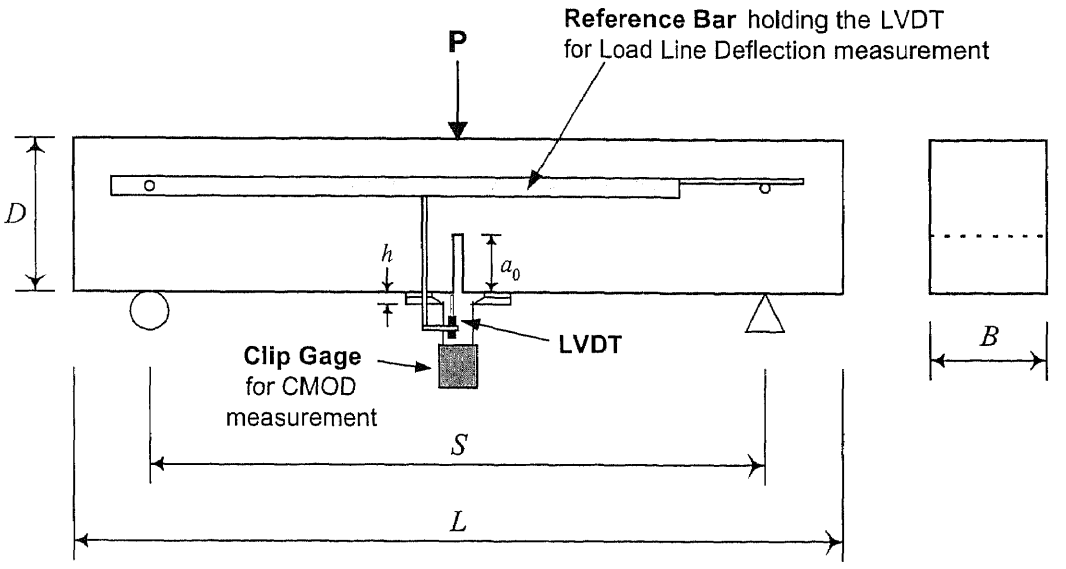

Figure 4.4 Test Setup Details for the Three-Point Bend Tests on Notched Beams
L is the specimen length of 16 inches; S is the span length of 12 inches; D is the beam depth of 3 inches; B is the width of 3 inches, and a_0 is the initial notch depth of 1 inch.

For the preparation of concrete specimens, about one day prior to testing, the specimens were removed from the 100% humidity curing room for notch preparation, attachment of the clip gage holders, and mounting of the reference frame holders. All beam tests were performed under the crack mouth opening displacement (CMOD) control in an MTS 442 closed-loop testing system at a displacement rate of 0.00002 inches/second to produce a controlled failure of the specimen, which allowed all parameters of interest to be measured. The applied loads were measured by a 5,000-pound load cell attached to the MTS piston. The load line deflections (LLD) were measured using a linear variable differential transformer (LVDT), measuring between the beam and a reference frame attached at the level of one half the unnotched depth. The measurements of CMOD were done by an MTS clip-on gage, and again the signals from

the clip-on gage were fed back to the controller to constantly adjust the applied load to ensure a stable crack growth. All test data were digitally recorded using a PC based data acquisition and control board (DACA) running the Unkelscope data acquisition program sampling. In these tests, the applied load is manually reduced (also termed unloading) when the load passed the maximum load and is at about 95% of the peak load. When the applied load is reduced near zero, reloading with the initial rate is applied. It took approximately 45 minutes to an hour to complete the entire test.

From Figures 4.3 and 4.4, the load line deflection was measured with reference to a frame mounted on the beam and floating with the beam, at the level of the initial neutral axis, on pivots attached over the supports. Based on past researches by Gopalaratnam et al. (1991), Kim (1996), and Navalurkar (1996), this method of measuring the load-line deflection provides a more reliable measurement of deflections without including the potential extraneous deflections caused by concrete crushing at the supports of the concrete beam specimens.

CHAPTER 5

RESULTS AND DISCUSSIONS

5.1 Introduction

In this chapter the results from this investigation are divided into two parts. The first contains the details of empirical results obtained from the experimental program as described in Chapter 4. Evaluation of the effects of size and fineness of fine-particle pozzolans (fly ash and silica fume) on the mechanical properties of concrete, e.g. compressive strength, modulus of elasticity and flexural strength are discussed. Also presented are the basic fracture mechanics properties such as the load-line deflection at peak load, the corresponding crack-mouth-opening displacement, the relationship between deflection and crack-mouth-opening displacement, and the fracture energy of different cementitious materials.

The latter part deals mainly with the analytical results obtained by applying the fracture mechanics models, namely, the proposed nonlinear fracture mechanics model and the Two-Parameter Fracture Model (Jenq and Shah 1985, RILEM 1990). The purpose of this part is to study the effect of high performance matrices, made by incorporating various size ranges of fine particles such as fly ash and silica fume, on the fracture behavior of concrete. In addition to typical standard fracture parameters (fracture toughness and stress intensity factor), several fracture mechanics parameters such as the critical crack growth, the critical energy release rate and the brittleness are also presented. Finally, the performance of the proposed fracture mechanics models is verified by means of comparison with results obtained from using the Two-Parameter Fracture Model.

Comparisons with test data of other researchers were also carried out to verify the validity of the proposed fracture mechanics model.

5.2 Empirical Results

5.2.1 Analysis of Particle Size Distribution of Fly Ash

The original feed class F fly ashes from the local power plant were fractionated by air classifier into five different size ranges (13F, 15F, 16F, 18F and 18C). MO denotes the original feed fly ash. Test results of the particle size analysis are presented in Table 5.1 (previously published by Bumrongjaroen 1999). The particle size ranges of fly ashes, 13F to 18C, are classified as the finest to the coarsest by the mean particle size respectively. The size ranges vary from 13F (1.5-15.6 microns) to MO (1.5-700 microns). In this study, the peak size is defined as the particle size that has the highest volume percentage. The mean diameter or the average particle size is defined as the size of which 50% of particles are smaller. The fineness of fly ashes is presented in terms of the grading modulus as described in Chapter 4. The larger grading modulus generally means the finer particle size. The 13F fly ash is the finest with the peak size of 2.52 microns and a mean diameter of 2.51 microns. The 18C fly ash on the other hand has the largest peak size (17 microns) and the largest mean diameter of 20.25 microns.

The plots of the differential particle size distributions of fly ashes are shown in Figure 5.1. The area under the curve represents the total volume of the fly ash as 100%. The 13F fly ash yields the highest percentage of the volume at peak size in the narrowest size ranges. It is the finest and most uniform fly ash of the batch. The other fly ashes, 15F, 16F, 18F and 18C, are not as well fractionated as the 13F. They tend to have wider

ranges of particle sizes, which also overlap with others. These mixes may pose difficulty when comparing the effect of particle size of fly ash on the behaviors of concrete.

The cumulative particle size distributions of fly ashes are presented in Figure 5.2. The 13F, 15F, 16F, 18F, MO and 18C fly ashes are classified as the finest to the coarsest by the average particle size respectively. The 13F, 15F and 16F fly ashes have more than 85% of the total volume smaller than 10 microns. Many researchers (Giergicany and Werynska 1989, Jaturapitakkul 1993, Bumrongjaroen 1999) found that concrete made of finer fly ashes exhibits higher strength than of the coarser one. Recent researches (Jaturapitakkul 1993, Bumrongjaroen 1999) also showed that fly ashes with particle size less than 10 microns yielded the highly active pozzolanic reaction, which is important to the strength development of concrete. From Figure 5.2, the curve of 13F fly ash shows the steepest slope and the narrowest range of particle sizes, indicating that it has the most uniform particles. The curve for the original feed fly ash (MO) is not as steep as the other fly ashes, and has the widest range of particle size distribution.

Table 5.1 Analysis of Particle Size Distribution of Fly Ashes

Type of Fly Ash	Differential Size Distribution Curve				Cumulative Size Distribution Curve	
	Size Range (microns)	90% Limit of Size Range (microns)	Peak Size (microns)	% of Volume at Peak Size	Mean Diameter (microns)	Grading Modulus ($micron^{-1}$)
MO	1.5 - 700	1.9 - 104.7	2.3 and 14.3	3.24 and 2.4	13.87	0.433
13F	1.5 - 15.6	1.6 - 7.1	2.52	13.09	2.51	2.390
15F	1.5 - 104.7	1.6 - 31.1	2.52	6.38	3.72	1.613
16F	1.5 - 124.5	1.9 - 37	7.7	5.23	6.49	0.924
18F	1.5 - 62.4	1.9 - 37	12	6.24	11.17	0.537
18C	1.5 - 296	3.5 - 114	17	5.05	20.25	0.296

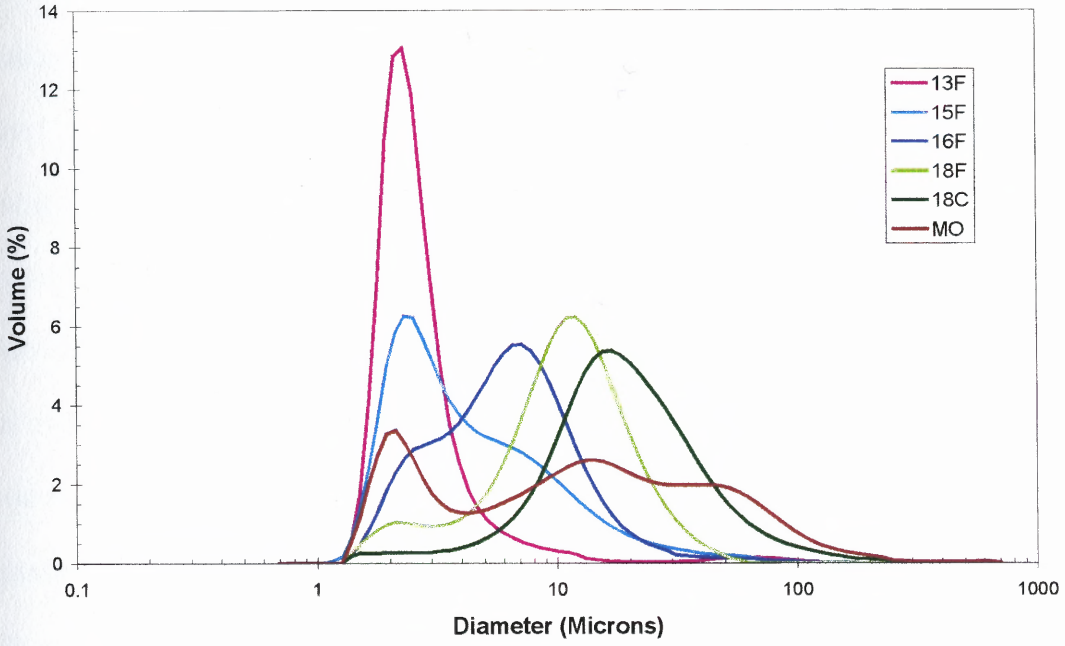

Figure 5.1 Differential Particle Size Distribution of Fractionated Fly Ashes

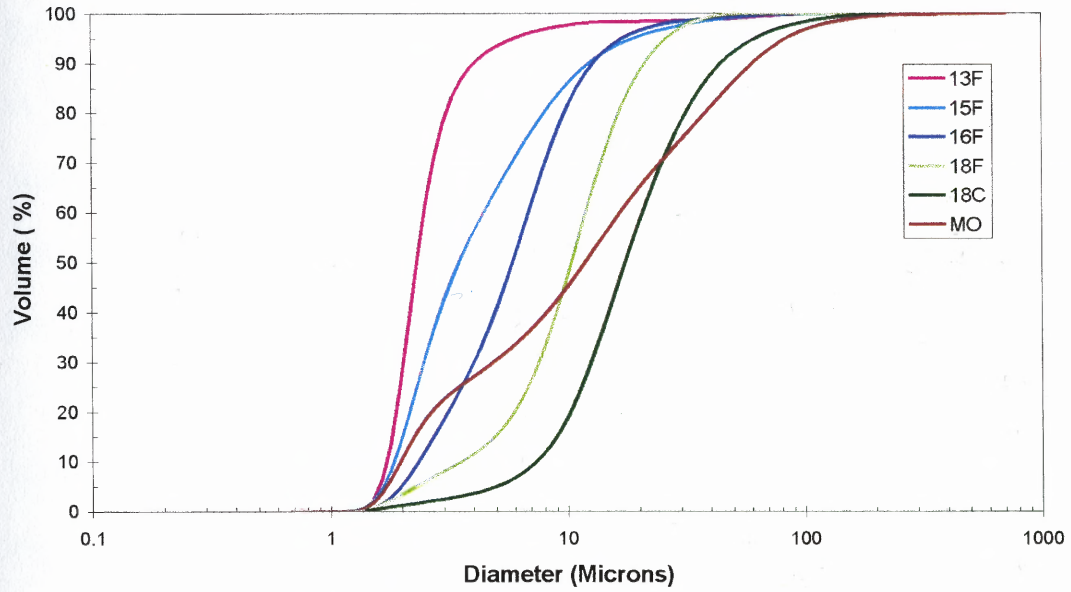

Figure 5.2 Cumulative Particle Size Distribution of Fractionated Fly Ashes

5.2.2 Effect of Fine Particles on the Compressive Strength of Mortar

In this section, the cement mortars were used to study the effect of fine particles (fly ashes and silica fume) on the compressive strength development of cement matrix. The fractionated fly ashes were used as a replacement for cement at 15%, 25% and 50% by weight of cementitious materials (cement and fly ash). Silica fume was used as a replacement for cement at 10% by weight of cementitious materials (cement and silica fume). Control mortars, which are conventional cement mortars without any fly ashes or silica fume, were also tested and used as references. The water to cementitious materials ratio of all specimens was kept constant at 0.5. The mortar mix proportions used in this study are shown in Table 4.2. The compressive strength of these specimens was tested at the age of 7, 14, 28 and 56 days.

CC represents the control mortar specimen where SF denotes silica fume mortar samples. The numbers 15, 25 and 50 following the abbreviation of fly ashes stand for the percentage of cement replaced by fly ash, e.g., 13F25 means fly ash mortars using 13F fly ash as a cement replacement of 25 percent by weight of cementitious materials. Some of results for the series of fly ash mortars presented here were obtained from Jaturapitakkul (1995). While tests on fly ash concrete were repeated, additional test series were conducted on silica fume mortars in this study. All test results are summarized and presented in Table 5.2.

The effects of fine particles to cementitious properties are evaluated in term of the compressive strength development of concrete. The strength of fly ash, silica fume, and normal concrete were compared and optimum percentage of fly ash as cement

replacement was selected as mixtures for studying the fracture behavior of high performance concrete.

Table 5.2 Results of Compressive Strength of Mortar

Mortar Type	Compressive Strength of Mortar (psi)			
	7 days	14 days	28 days	56 days
CC	7006	7883	9094	9872
SF	8058	8750	8849	8921
13F15	6807	7925	9402	11209
15F15	6707	7750	9111	10290
16F15	6613	7727	8867	10017
18F15	6293	7217	8242	9234
18C15	6007	6911	7724	8871
MO15	6683	7603	8671	9914
13F25	6501	7493	9112	10323
15F25	5834	6887	8398	9354
16F25	5820	6530	8086	9211
18F25	5674	6439	8001	8957
18C25	5239	5951	7356	8543
MO25	5833	6570	8031	8987
13F50	3851	4802	5692	6754
15F50	3631	4522	5384	6503
16F50	3543	4238	5405	6387
18F50	3078	3858	4732	5855
18C50	2836	3325	4068	4934
MO50	3407	4144	5313	6435

5.2.2.1 Compressive Strength of Fly Ash Mortar with 15% Cement Replacement: The development of the compressive strength of fly ash mortars with 15% cement replacement is presented along with that of the control mortar and silica fume mortar as shown in Figure 5.3. Numerical details of the strength development of all of the mortars tested are also listed in Table 5.2.

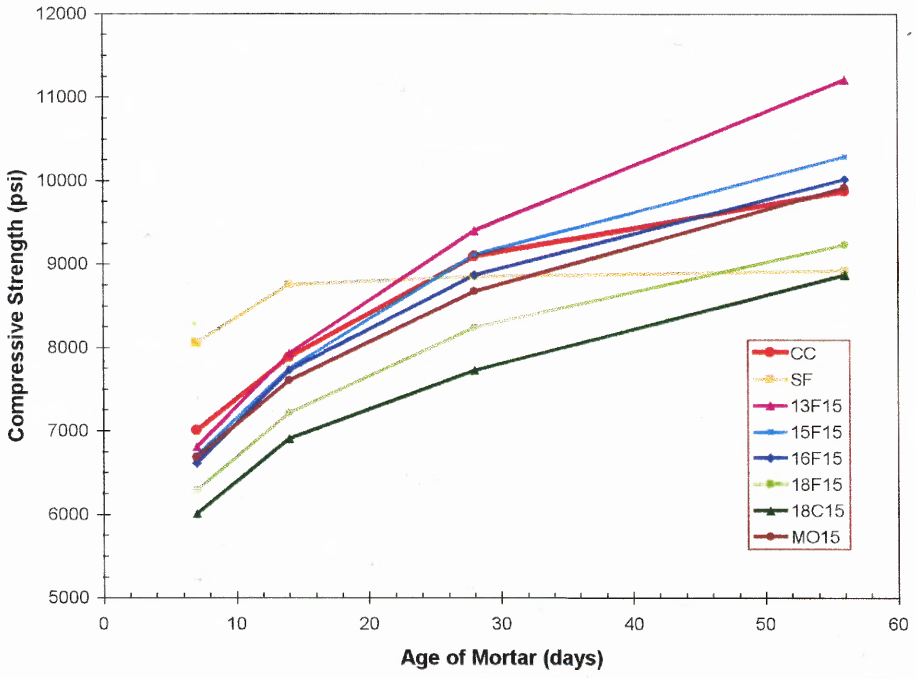

Figure 5.3 Compressive Strength of Fly Ash Mortars with 15% Cement Replacement

At the early age of 7 days, the compressive strength of the control mortar is higher than that of the fractionated fly ash mortars, but less than that of the silica fume mortar. This is due to the fact that less cement is present in fly ash mortar mixes, and also the silica components in fly ashes are not as chemically reactive at the early age as those in

silica fume. After 7 days of early strength gained, the strength development of silica fume mortar becomes steady, whereas the strengths of control mortar and fly ash mortars gradually increase with age surpassing those of silica fume mortars.

At the age of 14 days, the silica fume mortar still yields the highest compressive strength. The strengths of all fly ash mortars are lower than that of the control, except for mortar with the finest fly ash, 13F15. As the samples reached 28 days, the compressive strengths of mortar with finer fly ashes, 13F15 and 16F15 exceed the strength of the control mortar which also surpasses that of silica fume mortar. The strength of the 16F15 fly ash mortar is slightly higher than that of silica fume mortar, but remain lower than the control mortar.

At the age of 56 days, fly ash mortars with the mean particle size less than 10 microns (13F15, 15F15 and 16F15) yield the strength much higher than that of the control. The mortar made from the original feed fly ash, MO15, also surpasses the strength of the control mortar. It should be noted that the strength of MO15 mortar has higher strength than that of the 18F15 which has smaller mean particle size. This may be attributed to the fact that the MO fly ash contains more finer particles which are more chemically reactive than the 18F fly ash. For the coarser fly ashes of the 18F and 18C, it seems that the pozzolanic activity resulted from the fly ashes is less effective than the strength contributed by the amount of cement they replaced.

5.2.2.2 Compressive Strength of Fly Ash Mortar with 25% Cement Replacement: The relationship between the compressive strength and curing age of fly ash mortars with 25% replacement of cement is presented in Figure 5.4 along with that of the control and the silica fume mortar. Table 5.2 provides the values of compressive strength for all of the mortars tested.

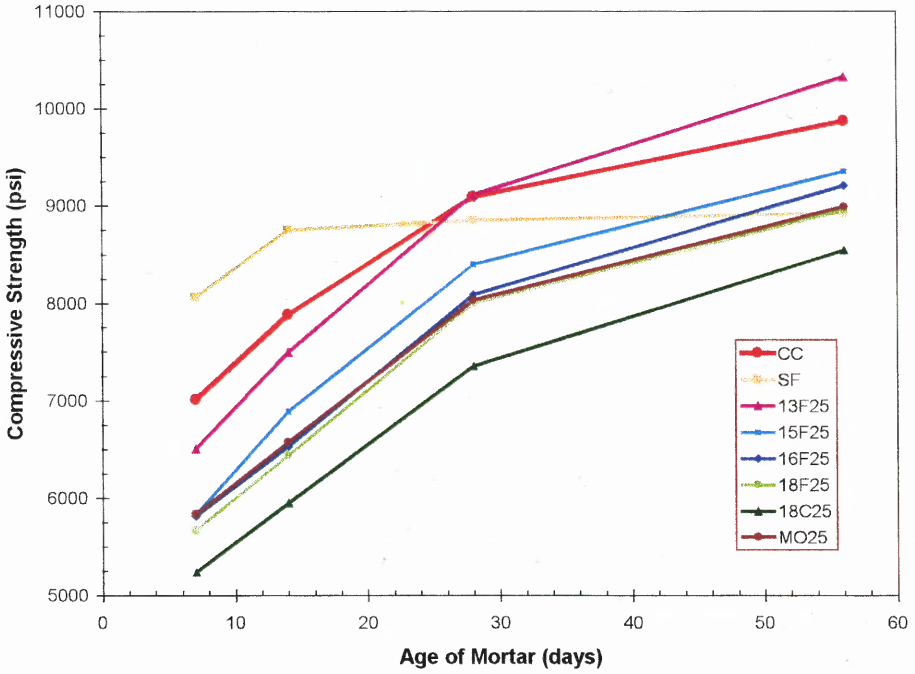

Figure 5.4 Compressive Strength of Fly Ash Mortars with 25% Cement Replacement

The compressive strengths of fractionated fly ash mortars with 25% replacement of cement are generally lower than that with 15% replacement. However, the effect of particle size of fly ash on the strength development of concrete shows a similar trend on those observed for the 15% replacement series. As more cement was replaced by fly ash (25% in this case), the strength of fly ash mortars at early ages (prior to 28 days) were

lower than that of the control. At the age of 28 days, only the samples made from the finest fly ash (13F25) showed a higher strength than the control, indicating that only the finer particles of fly ash were reactive at this stage.

As maturity of these samples progressed, most fly ash particles reacted with lime from the cement and resulted in the higher overall compressive strength of the matrices. It is clearly evident in Figure 5.4 that at the age of 56 days, all fly ash mortars except those with the coarsest particles, surpassed the strength of silica fume mortar, and the finer one (the 13F25) had a strength above the control. The results again indicate that the use of fine particles of fly ashes increases the rate of pozzolanic activity. The finer the particle size of fly ash, the greater is the rate of pozzolanic reaction resulting in a faster rate of the compressive strength development.

5.2.2.3 Compressive Strength of Fly Ash Mortar with 50% Cement Replacement: The relationship between the compressive strength of fly ash mortars with 50% replacement of cement and curing age are presented in Figure 5.5 along with that of the control mortar and silica fume mortar.

At 50% of the cement being replaced by fly ash, a rather inert material, the binding property of the cement matrices dropped drastically. As a result, it can be seen from Figure 5.5 that all fly ash mortars yield a much lower strength than the silica fume and the control mixes. The trend of increasing strength development as the specimens get older remains, but at a slower rate. At the age of 56 days, all fly ash mortars only exhibit strength of about 40%–60% of the control concrete.

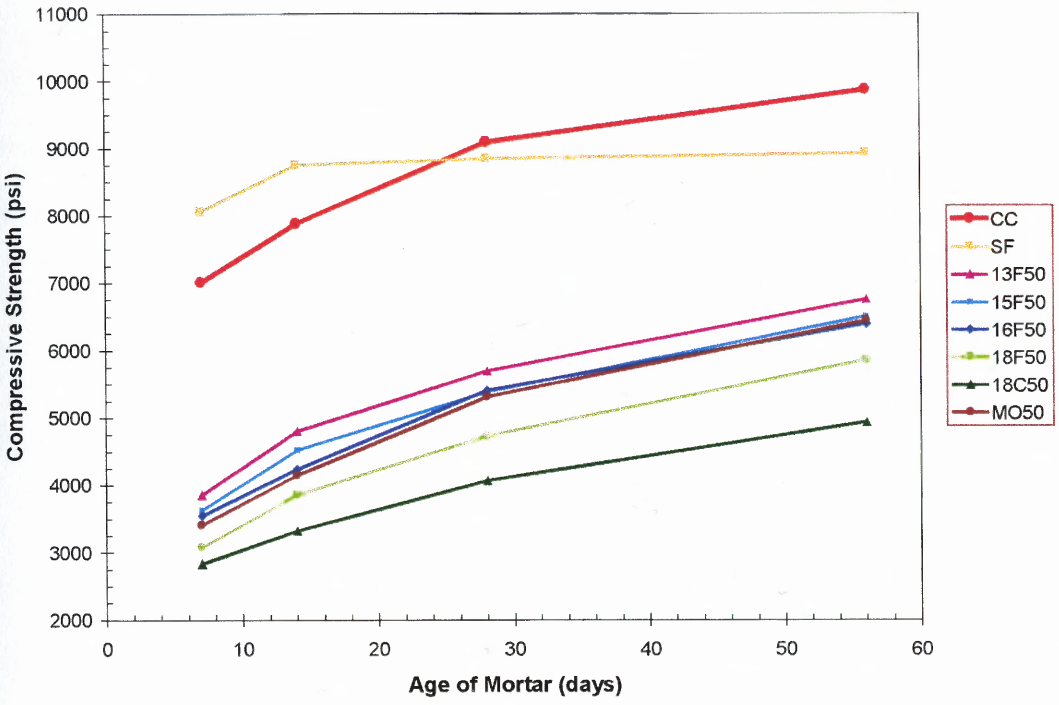

Figure 5.5 Compressive Strength of Fly Ash Mortars with 50% Cement Replacement

5.2.2.4 Optimal Percentage of Fractionated Fly Ash in Cement Matrix: In the previous sections, it was clear that the amount and sizes of fly ash in the mixes played a critical role on the strength development of the high performance fly ash concrete matrices. In this study, an optimum percentage replacement of fly ash in cement matrix will have to be selected so the mixes can be used to study the effect of high performance matrix on fracture behavior of concrete.

For the group of the 15% replacement shown in Figure 5.3, two types of fly ash mortars (13F15 and 15F15) exhibited a higher strength than the control at the age of 28 days. Whereas, at the age of 56 days, four fly ash mortars (13F15, 15F15, 16F15 and MO 15) broke the control strength barrier.

For the mixes using fly ashes of 25% as cement replacement shown in Figure 5.4, only the mortar made with the finest fly ash particles, 13F25, gains the strength more than that of the control mortar at the age of 28 and 56 days. Most other mortars (15F25, 16F25 and 18F25) showed a lower compressive strength at early ages but managed to achieve a comparable strength to that of control at 28 and 56 days of curing. From Figure 5.5, it is also clear that replacing 50% of cement by fly ash will not provide a usable mixture of cement matrices.

In this study the selected fly ash mortar mixes used fly ash as a cement replacement of 25% by weight of cementitious materials (cement and fly ash). For silica fume mortar, the percentage of cement replacement was 10% by weight of cementitious materials (cement and silica fume). Concrete specimens including cylinders and beams were cast and tested according to the experimental program as described in Chapter 4. These samples were used to study the effect of high performance matrix on the mechanical behavior and fracture behavior of concrete. Both the empirical data and analytical results are presented in the following sections.

5.2.3 Results of Uniaxial Compression Tests of Concrete

In this section, the effect of fine particles such as fly ashes and silica fume on the stress-strain behavior of high performance concrete under uniaxial compression is investigated. The primary objective of those tests was to determine the following properties of concrete:

1. The uniaxial compressive strength (f_c'),
2. The peak strain (ε_p), which is the strain at the peak load,

3. The Modulus of Elasticity (E_c), and
4. The toughness of concrete, defined in this study as the area under a stress-strain curve of concrete up to a strain of 0.003, which is specified by ACI Committee 318 (ACI 1994) as the ultimate strain for the failure condition.

Several fly ashes were used as a replacement for cement at 25% by weight of cementitious materials (cement and fly ash) to make high performance fly ash concrete. Silica fume was also used as cement replacement to produce silica fume concrete. Control concrete specimens, generally refer to normal concrete without any fly ashes or silica fume were also tested and used as reference. The water to cementitious materials ratio of all specimens was kept constant at 0.5 in accordance with ASTM recommendation. The concrete mix proportions used are given in Table 4.3. The uniaxial compression tests of cylindrical specimens were performed at the ages of 28 and 56 days.

CC represents the control concrete specimen whereas SF denotes silica fume concrete. The number 25 following the abbreviation of fly ashes stands for the percentage of cement replaced by fly ash, e.g., 13F25 means fly ash concrete using 13F fly ash as a cement replacement of 25 percent by weight of cementitious materials. The test results performed in this study with different specimen sizes are summarized and presented in Tables 5.3 through 5.10. The stress-strain curves of all the concrete specimens tested are shown in Appendix A. Analyses and discussions of the results are presented in the next sections.

Table 5.3 Compression Test Results of Control Concrete (**CC**)

Specimen Number	Specimen Size	Ages of Specimen (days)	Compressive Strength (ksi)	Peak Strain (in/in)	Modulus of Elasticity (ksi)	Toughness (ksi)
1	3" x 6"	28	5.434	0.001808	5195	0.01143
2	3" x 6"	28	5.437	0.001853	5219	0.01156
3	4" x 8"	28	5.644	0.001788	5329	0.01281
4	4" x 8"	28	5.407	0.001656	5351	0.01213
		Average	**5.480**	**0.001776**	**5273**	**0.01198**
1	3" x 6"	56	6.070	0.001753	5571	0.01294
2	3" x 6"	56	5.998	0.001827	5528	0.01262
3	3" x 6"	56	5.955	0.001658	5519	0.01254
		Average	**6.008**	**0.001746**	**5539**	**0.01270**

Table 5.4 Compression Test Results of Silica Fume Concrete (**SF**)
(Specimen size of 3"x 6")

Specimen Number	Ages of Specimen (days)	Compressive Strength (ksi)	Peak Strain (in/in)	Modulus of Elasticity (ksi)	Toughness (ksi)
1	28	7.326	0.001941	5065	0.01494
2	28	7.336	0.001856	5498	0.01391
3	28	7.304	0.001987	4990	0.01341
	Average	**7.322**	**0.001928**	**5185**	**0.01409**
1	56	7.514	0.001935	5473	0.01440
2	56	7.553	0.001939	5449	0.01485
3	56	7.241	0.001928	5431	0.01595
	Average	**7.436**	**0.001934**	**5451**	**0.01507**

Table 5.5 Compression Test Results of Fly Ash Concrete (**13F25**)
(Specimen size of 3"x 6")

Specimen Number	Ages of Specimen (days)	Compressive Strength (ksi)	Peak Strain (in/in)	Modulus of Elasticity (ksi)	Toughness (ksi)
1	28	6.440	0.001700	5581	0.01406
2	28	6.470	0.001830	5320	0.01371
3	28	6.335	0.001862	5144	0.01380
	Average	**6.415**	**0.001797**	**5349**	**0.01386**
1	56	6.758	0.001678	5493	0.01368
2	56	6.732	0.001701	5668	0.01393
3	56	6.868	0.001651	5857	0.01415
	Average	**6.786**	**0.001677**	**5673**	**0.01392**

Table 5.6 Compression Test Results of Fly Ash Concrete (**15F25**)
(Specimen size of 3"x 6")

Specimen Number	Ages of Specimen (days)	Compressive Strength (ksi)	Peak Strain (in/in)	Modulus of Elasticity (ksi)	Toughness (ksi)
1	28	6.086	0.00170	5321	0.01322
2	28	6.113	0.00164	5398	0.01282
3	28	6.061	0.00164	5273	0.01271
	Average	**6.087**	**0.001660**	**5330**	**0.01291**
1	56	6.591	0.00170	5785	0.01428
2	56	6.866	0.00156	6046	0.01455
3	56	6.781	0.00164	5871	0.01425
	Average	**6.746**	**0.001633**	**5901**	**0.01436**

Table 5.7 Compression Test Results of Fly Ash Concrete (**16F25**)
(Specimen size of 3"x 6")

Specimen Number	Ages of Specimen (days)	Compressive Strength (ksi)	Peak Strain (in/in)	Modulus of Elasticity (ksi)	Toughness (ksi)
1	28	6.097	0.00151	5335	0.01246
2	28	6.003	0.00158	5318	0.01251
3	28	5.933	0.00167	5269	0.01231
	Average	**6.011**	**0.001585**	**5307**	**0.01243**
1	56	6.854	0.001755	5773	0.01467
2	56	6.605	0.001488	6261	0.01372
3	56	6.844	0.001595	5932	0.01255
	Average	**6.768**	**0.001613**	**5989**	**0.01365**

Table 5.8 Compression Test Results of Fly Ash Concrete (**18F25**)

Specimen Number	Specimen Size	Ages of Specimen (days)	Compressive Strength (ksi)	Peak Strain (in/in)	Modulus of Elasticity (ksi)	Toughness (ksi)
1	3" x 6"	28	5.560	0.001653	5426	0.01243
2	3" x 6"	28	5.648	0.001619	5517	0.01184
3	3" x 6"	28	5.648	0.001672	5200	0.01302
		Average	**5.618**	**0.001648**	**5381**	**0.01243**
1	3" x 6"	56	5.935	0.001484	5881	0.01239
2	3" x 6"	56	6.342	0.001628	6091	0.01380
3	4" x 8"	56	6.200	0.001624	5638	0.01422
4	4" x 8"	56	6.159	0.001573	5866	0.01299
		Average	**6.234**	**0.001608**	**5865**	**0.01367**

Table 5.9 Compression Test Results of Fly Ash Concrete (**18C25**)
(Specimen size of 3"x 6")

Specimen Number	Ages of Specimen (days)	Compressive Strength (ksi)	Peak Strain (in/in)	Modulus of Elasticity (ksi)	Toughness (ksi)
1	28	5.203	0.001749	5460	0.01184
2	28	5.258	0.001627	5368	0.01213
3	28	5.233	0.001740	5248	0.01201
	Average	**5.232**	**0.001705**	**5359**	**0.01199**
1	56	5.465	0.001683	5569	0.01215
2	56	5.735	0.001652	5633	0.01201
3	56	5.660	0.001707	5493	0.01278
	Average	**5.620**	**0.001681**	**5565**	**0.01231**

Table 5.10 Compression Test Results of Fly Ash Concrete (**MO25**)
(Specimen size of 3"x 6")

Specimen Number	Ages of Specimen (days)	Compressive Strength (ksi)	Peak Strain (in/in)	Modulus of Elasticity (ksi)	Toughness (ksi)
1	28	5.818	0.001618	5261	0.01274
2	28	5.882	0.001512	5686	0.01273
3	28	6.001	0.001694	5445	0.01314
	Average	**5.900**	**0.001608**	**5464**	**0.01287**
1	56	6.483	0.001608	5845	0.01389
2	56	6.781	0.001711	5862	0.01471
3	56	6.727	0.001711	5911	0.01396
	Average	**6.664**	**0.001677**	**5873**	**0.01419**

5.2.3.1 Compressive Strength of Concrete: The compressive strength of all types of concrete tested is presented in Tables 5.3 through 5.10. Figure 5.6 shows the relationship between compressive strength of concrete and its corresponding age.

All cement particles in the paste of mortars or concrete do not essentially take part in cement hydration all at once to develop strength. The hydration process usually starts from the finest cement particles (Neville 1983). During the hydration, silicon dioxide (SiO_2) reacts with calcium oxide (CaO) in the presence of water to produce the hydrated product called calcium silicate hydrate (C-S-H) gel, which is the source of strength gain of cementitious materials. The hydrated cement then envelopes unhydrated cement particles and other fine-particle pozzolans such as silica fume and fly ash, and continues to grow from within.

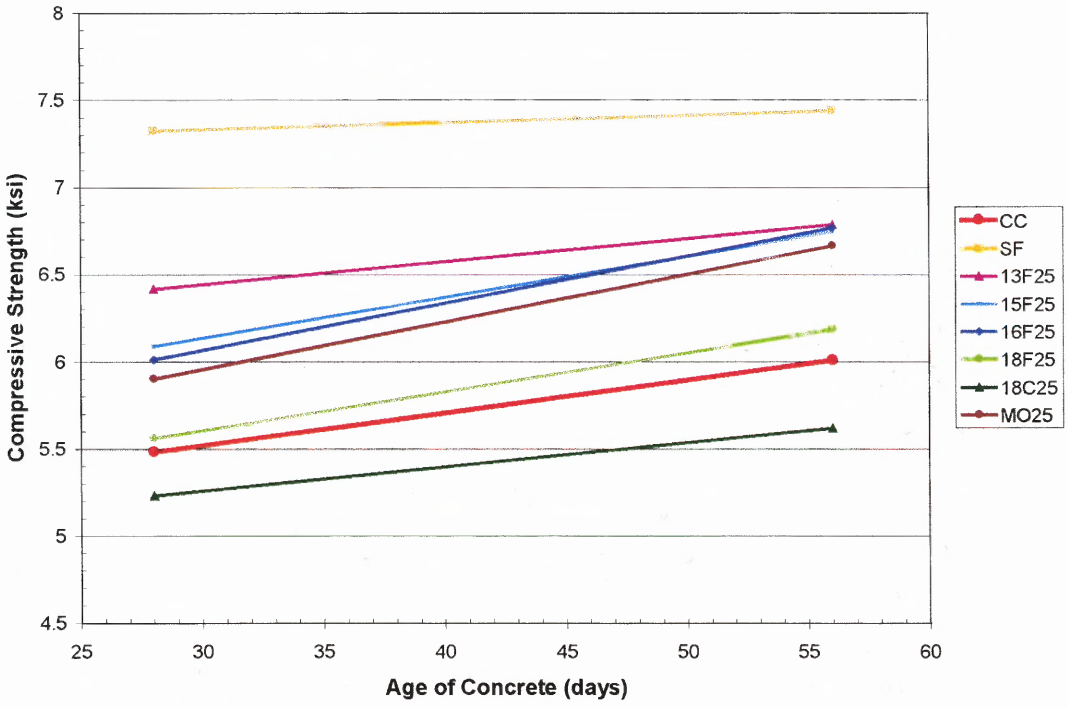

Figure 5.6 Relationship between the Compressive Strength of Concrete and Curing Age

As seen from Figure 5.6, the silica fume concrete yields the highest compressive strength at both 28 and 56 days of curing. This is due to the fact that silica fume has very fine particles (usually smaller than 1 micron), which consists of about 96 to 98 percent of reactive silicon dioxide in its compositions. Furthermore, silica compounds in silica fume also have a very high reactivity rate as compared to those in the fly ash. These reactive silica react rapidly with calcium hydroxide from cement particles at the beginning of the cement hydration process resulting in high strength of concrete at the very early age, commonly during the first 72 hours. After 28 days, silica fume barely generates any more hydrated products as clearly demonstrated in Figure 5.6, and the compressive strength of silica fume concrete is stable from the age of 28 days to 56 days.

As also shown in Figure 5.6, for fly ash concrete, the compressive strengths of all fly ash concrete specimens are higher than that of the control concrete except for the fly ash concrete 18C25 (using the coarsest fly ash), which yields the strength of about 94 percent of the control. At the age of 28 days, the results clearly show that the strength of fly ash concrete is strongly influenced by the particle size of the fly ash. Table 5.1, and Figures 5.1 and 5.2 show the results of the particle size distribution analysis of these fly ashes. A smaller particle size of fly ash in concrete tends to yield the higher compressive strength. As shown in Figure 5.6, specimen 13F25 using fly ash with the smallest mean particle diameter (2.51 microns) exhibits a strength higher than those of the control and all other fly ash concretes.

Although the mean particle sizes between the 13F and 15F fly ashes area about the same, Figure 5.1 shows that the 13F fly ash has the highest volume of the finer particle sizes that are smaller than 10 microns. Fly ash with more volume of the finer

particles generally provides a better packing effect, which fills up voids between cement particles in the cement matrix resulting in a stronger concrete. Noticeably, specimen MO25 made from the raw-feed fly ash gives a higher strength than the 18F25 series even though its mean particle size is slightly larger. A closer look at the particle size distribution of these two fly ashes reveals that the MO fly ash has a higher volume of finer particle than the 18F fly ash (see Figure 5.1). This confirms that the volume of finer fly ash particles has a strong influence on the strength development of the cement matrix. In case of the 18C25 concrete, made from the coarsest 18C fly ash with particles larger than 10 microns, as expected the mix yields the lowest compressive strength. It seems that for coarser particle size fly ash the pozzolanic activity was so slow that the presence of fly ash provides no beneficial impact to the cement matrix.

After 56 days of curing, the specimens 13F25, 15F25 and 16F25 yielded the same compressive strength, which is about 15% higher than the strength of the control concrete. This seems to indicate that the pozzolanic reaction of fly ash continues to consume calcium hydroxide to produce additional calcium silicate hydrate (C-S-H) gel as long as calcium hydroxide is present in the pore spaces of the cement matrix. This reaction continues far beyond the standard 28-day test commonly used in the concrete industry. The samples that were made from the raw feed fly ash (MO25) exhibits lower strength than those with the very fine particles (13F, 15F, 16F). These results follow the same trend as those tested at 28 days in that the larger the volume of the very fine particles, the higher is the strength of the fly ash concrete.

Due to the fact that the chemical compositions of all fly ashes used in the present study are almost the same (as shown in Table 4.1), the aforementioned results show that

particle size of fly ash is the major factor affecting the compressive strength of fly ash concrete. In general, the compressive strength of fly ash concrete made of the finer particle is higher than that of the coarser ones. The finer particles tend to react with cement faster as a result of larger surface area. The results of this study indicate that the compressive strength of concrete can be improved by incorporating fly ash of finer particle sizes.

5.2.3.2 Interfacial Bond Strength between Cement Matrix and Coarse Aggregate: The use of fine particle pozzolans such as silica fume and fly ash as a cement replacement has been shown to result in significant increase in the strength of concrete. It is believed that the main influence of silica fume and fly ash is on the improvement of interfacial bond strength between cement paste and aggregate. Due to the very fine particle size of these materials, their presence tends to densify the matrix and improve the strength of the interfacial transition zone (ITZ). Some studies reported that these enhancements only took place in concrete but not in mortar (Bentur et al. 1988, Rosenberg and Gaidis 1989, Goldman and Bentur 1989).

It is widely recognized that there are significant differences in the matrix structure of bulk cement paste and cement paste located in proximity to coarse aggregates (Bentur et al. 1988, Bentur and M. D. Cohen 1987, Regourd 1985). Pastes near an aggregate surface exhibit a smaller fraction of unhydrated cement pastes (out to about 40 microns) and greater porosity (especially out to about 10 microns) than cement pastes in regions located farther from the aggregate (Scrivener et al. 1988). This region is referred to as the interfacial transition zone (ITZ) and has an estimated thickness of 15 to 50 microns,

depending on the method of estimation (Scrivener et al. 1988, Windslow et al. 1994). More detailed studies using flat polished surfaces indicated that the material in the interfacial zone is principally calcium silica hydrate (C-S-H) (Scrivener and Gartner 1988), with an average calcium hydroxide ($CaOH_2$) content slightly higher than surrounding paste. It is quite common among researchers to assume that the interfacial transition zone plays a dominant role in the compressive strength as well as tensile strength of concrete (Bentur et al. 1988, Bentur and M. D. Cohen 1987, Popovics 1987, Rosenberg and Gaidis 1989, Cong et al. 1992).

In this study, the interfacial transition zone is determined by comparing the strengths of mortars and concrete of the same matrix's mix proportions. This strength ratio is termed the bond strength index (Cong et al. 1992). The bond strength index used here is defined as the ratio of concrete strength to mortar strength ($f_c^{'} / f_m^{'}$) as a function of the normalized mortar strength. With the same matrix composition, the presence of coarse aggregate in concrete will create a somewhat weaker aggregate-matrix interface. This is typically known as aggregate-matrix interfacial transition zone. The addition of pozzolanic particles of silica fume and fly ash will undoubtedly alter the bonding characteristics of this region. The bond strength index as described above can be one of the indicators used to measure the influence of these pozzolanic materials in the cementitious composites.

Since the strength of various fly ash mortars tends to vary, comparison of these mixes will require some form of normalization. The approach used here normalizes the strength of each fly ash mortar by the strongest mix, the 13F25 in this case. The

normalized factor is then used to adjust the bond strength ratio, leading to the final bond strength index as shown in Table 5.11b.

Table 5.11a Compressive Strength of Mortar and Concrete

Specimen Type	Concrete Strength, f_c' (ksi)		Mortar Strength, f_m' (ksi)	
	28 days	56 days	28 days	56 days
Control	5.480	6.008	9.094	9.872
SF	7.322	7.436	8.849	8.921
13F25	6.415	6.786	9.112	10.323
15F25	6.087	6.746	8.398	9.354
16F25	6.011	6.768	8.086	9.211
18F25	5.618	6.234	8.001	8.957
18C25	5.232	5.620	7.356	8.543
MO25	5.900	6.664	8.031	8.987

Table 5.11b Bond Strength Indexes of Concrete

Specimen Type	f_c' / f_m'		Normalized Mortar Strength		Bond Strength Index	
	28 days	56 days	28 days	56 days	28 days	56 days
Control	0.603	0.609	0.998	0.956	0.601	0.582
SF	0.827	0.834	0.971	0.864	0.804	0.720
13F25	0.704	0.657	1.000	1.000	0.704	0.657
15F25	0.725	0.721	0.922	0.906	0.668	0.653
16F25	0.743	0.735	0.887	0.892	0.660	0.656
18F25	0.702	0.696	0.878	0.868	0.617	0.604
18C25	0.711	0.658	0.807	0.828	0.574	0.544
MO25	0.735	0.741	0.881	0.871	0.648	0.646

Table 5.11a compares compressive strength of mortar and concrete at the ages of 28 and 56 days, whereas the bond strength indices for each concrete series are listed in Table 5.11b. It can be seen that the bond strength index decreases as the particle size of fly ash in the mixture becomes larger. Silica fume concrete has the highest bond strength indices both at the age of 28 days and 56 days while the coarsest fly ash mixes of 18C25 have the lowest. The indices for the control concrete and the raw-feed fly ash concrete are somewhere in between.

The size of the interfacial zone was reported to be about 10 microns from the aggregate. In general, for cementitious matrix this zone tends to have greater porosity than the regions farther away from the aggregate. The results from this study show that the fine particle pozzolans with particle size smaller than 10 microns can increase the density and reduce the thickness of the interfacial transition zone between cement matrix and aggregate, resulting in the increase in the bond strength.

5.2.3.3 Stress–Strain Behavior of Concrete: Experimental results of the uniaxial compression tests of all mixes are presented in Tables 5.3 through 5.10. A typical stress-strain curve of concrete is shown in Figure 5.7. The curves for all other concretes are presented in Appendix A. Among all the properties obtained from the compression test, the compressive strength is by far the most important parameter used both for design purpose and during construction. Other important parameters include the Modulus of Elasticity, peak strain (strain at peak load), and toughness (or total energy absorption).

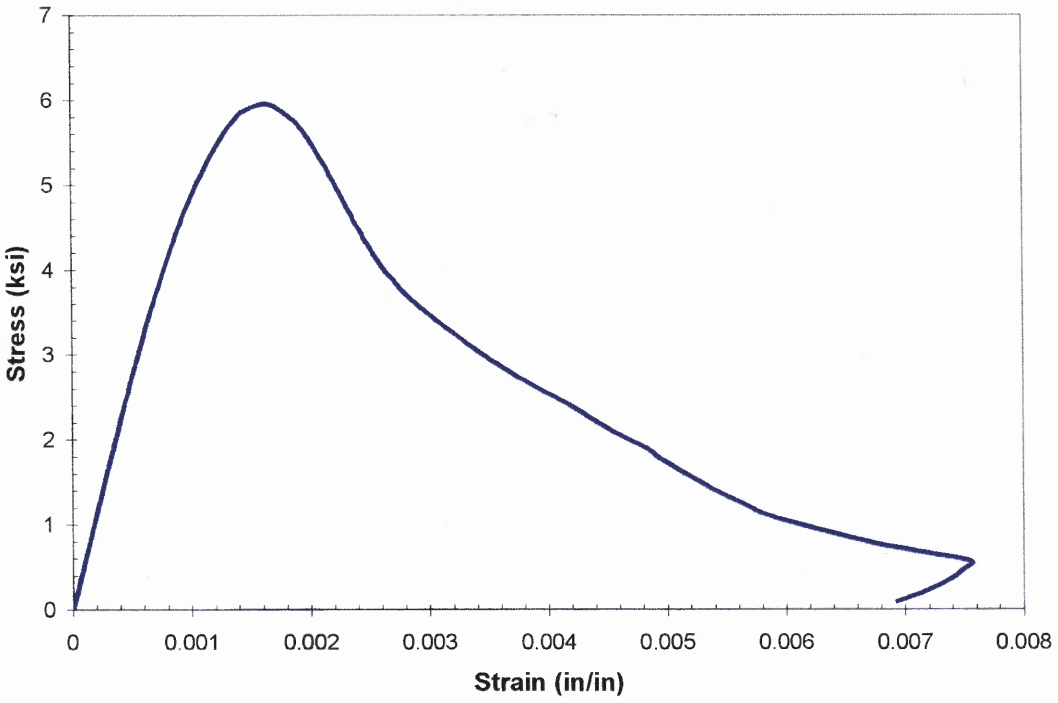

Figure 5.7 Typical Compressive Stress-Strain Curve for Concrete

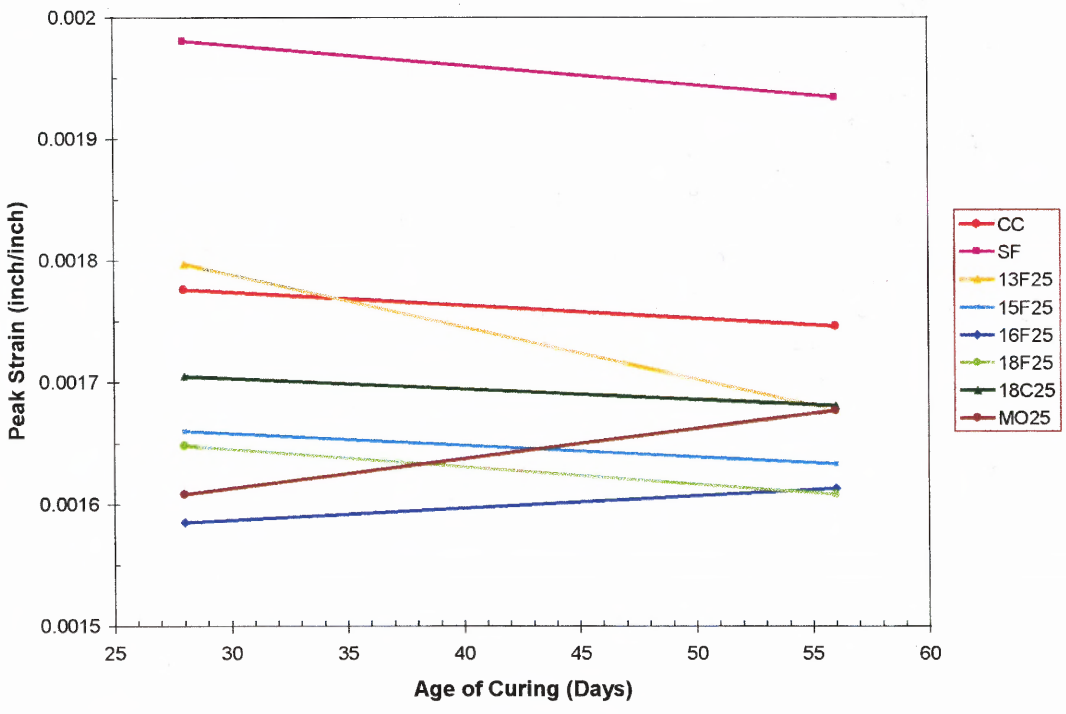

Figure 5.8 Relationship between Peak Strain of Concrete and Curing Age

Peak strain or strain at peak load serves as an indicator to reflect the failure mechanism within the concrete test cylinder. As cracks develop under lateral tensile stresses, the axial strain increases. When the matrix compositions vary as in different fly ash concretes tested in this study, the peak strain provides an overall response of the aggregate-matrix interfacial bonding within the concrete specimen.

In this study, the results of peak strain for each mix series were tabulated in Tables 5.3 to 5.10. It was found that there is no significant variation of the peak strain with different curing ages (28 and 56 days) except for the 13F series. Peak strains of all fly ash concretes and the control are in the range of 0.0016 to 0.0018. Only the silica fume concrete has a much higher value of 0.002 (see Figure 5.8).

It should be noted that the peak strain values reported in Figure 5.8 show no correlation with the compressive strength of the matrices. This is in contradiction to results reported by other researchers (Carrasquillo 1981, Hsu and Hsu 1994) that in general the peak strain of the higher strength concrete is greater than that of the lower strength one. As the grain size and distribution of both fine and coarse aggregate used in theses studies are varied, it is inconclusive to draw any conclusion at this stage. More research will be needed to understand this relationship.

5.2.3.4 Modulus of Elasticity of Concrete: In this study the modulus of elasticity was calculated in accordance with ASTM C-469 standard (ASTM 1994) as the slope of the best-fitted line of the stress-strain curve drawn from a longitudinal strain of 0.00005 to a stress level of 40 percent of the ultimate load. This procedure is also similar to the

definition of modulus of elasticity given by ACI (ACI 318 1994). Figure 5.7 shows a typical stress-strain curve obtained from the uniaxial compression tests in this study.

Table 5.12 Modulus of Elasticity and Compressive Strength of Concrete

Specimen Type	Age of Specimen (days)	Compressive Strength (ksi)	Modulus of Elasticity E_c^{test} (ksi)	Modulus of Elasticity * E_c^{ACI} (ksi)	$\frac{E_c^{test}}{E_c^{ACI}}$
CC	28	5.480	5273	4714	1.119
SF	28	7.322	5185	5449	0.951
13F25	28	6.415	5349	5100	1.049
15F25	28	6.087	5330	4968	1.073
16F25	28	6.011	5307	4937	1.075
18F25	28	5.618	5381	4773	1.127
18C25	28	5.232	5359	4606	1.163
MO25	28	5.900	5464	4892	1.117
CC	56	6.008	5539	4936	1.122
SF	56	7.436	5451	5491	0.993
13F25	56	6.786	5673	5246	1.081
15F25	56	6.746	5901	5230	1.128
16F25	56	6.768	5989	5239	1.143
18F25	56	6.234	5865	5028	1.166
18C25	56	5.620	5565	4774	1.166
MO25	56	6.664	5873	5198	1.130

* ACI 318-83: Modulus of Elasticity, $E_c = W_c^{1.5} 33\sqrt{f_c'}$ (in psi)

where W_c is the unit weight of concrete (155 lb per cu ft.),

f_c' is the compressive strength of concrete.

Table 5.12 shows the results of the compressive strength of the concrete specimens tested and the corresponding modulus of elasticity (E_C). Also presented for comparison is the predicted Modulus of Elasticity as recommended by ACI Committee 318 (ACI 318 1994). The ratio between the two Moduli (from the tests and by ACI) is also given.

A closer study of Table 5.12 reveals that ACI 318 expression overestimated the modulus of elasticity for the silica fume concrete (SF) at the age of 28 days. This result confirms what was presented in the ACI Manual of Concrete Practice (ACI 318 1994) that the ACI 318 expression overestimates the modulus of elasticity of concrete with compressive strengths over 6000 psi. At the age of 56 days, the same ACI expression closely predicts the modulus of elasticity of the silica fume concrete. For all other fly ash concretes, the expression tends to underestimate the modulus of elasticity even though almost all of the fly ash concretes have the compressive strengths over 6000 psi. Many other researchers (ACI 363R 1994) have reported the values of modulus of elasticity to be between 4500 to 6500 ksi, with which the results reported in this study are in good agreement.

Figure 5.9 shows the change of modulus of elasticity with the age of curing. Silica fume concrete (SF), which has the highest compressive strength, yields the lowest modulus of elasticity as compared to other types of concrete at the same age. Silica fume and the control concrete seem to have the same rate of development on the elasticity of the matrices. All fly ash concretes exhibited a stiffer matrix at 56 days. The rate of stiffness development is also faster for all fly ash concretes than those of the control and the silica fume concrete.

The results for the fly ash concrete having the higher modulus of elasticity may be explained by the presence of fly ashes in the concrete mixture which increases the density of cement matrix and thus improves the transfer of stresses from the cement paste to the stronger aggregate, leading to the increase of modulus of elasticity. In general, strong interfacial zone or bond strength between cement matrix and aggregate enhances the strength, stiffness and durability of concrete.

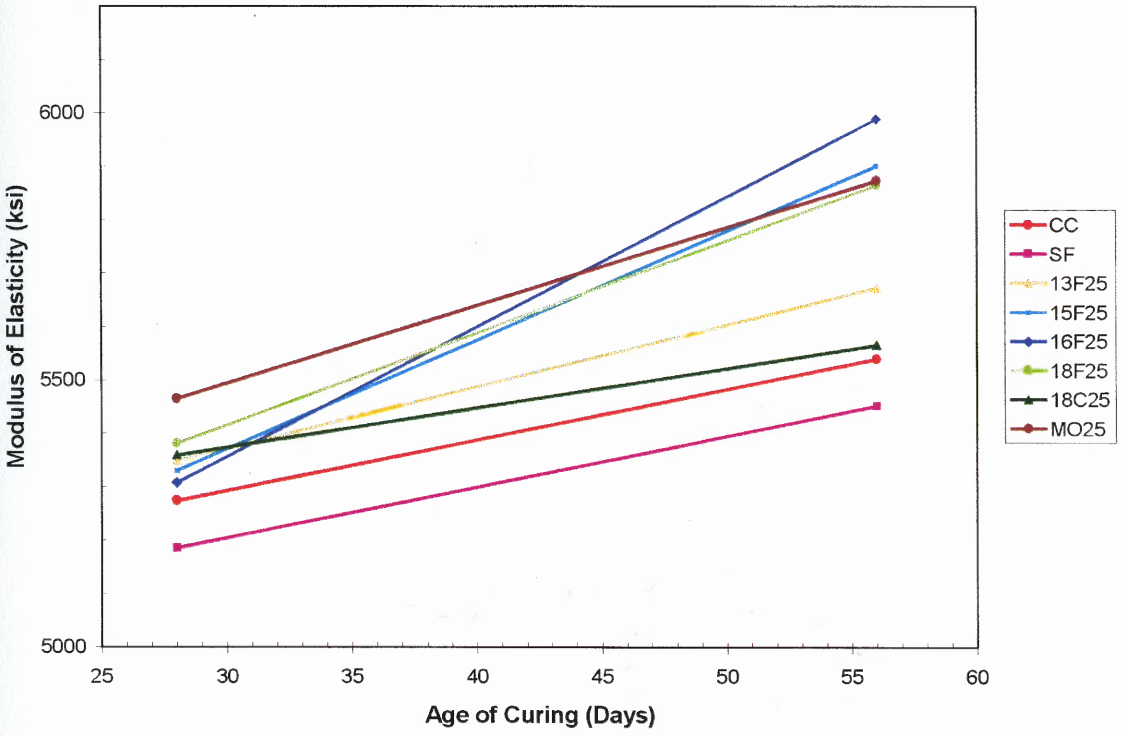

Figure 5.9 Relationship between Modulus of Elasticity of Concrete and Curing Age

5.2.3.5 Toughness of Concrete: The toughness of concrete under applied compressive load is related to its ability to absorb energy. In this study the toughness of concrete is defined as the area under the stress-strain curve of the uniaxial compression test up to a strain of 0.003, which is specified by ACI Committee 318 (ACI 318R 1994) as the ultimate strain for the failure condition of concrete. Tables 5.3 through 5.10 provide all the test results of the uniaxial compression tests conducted in this study. The relationship between the toughness of concrete and curing age is shown in Figure 5.10.

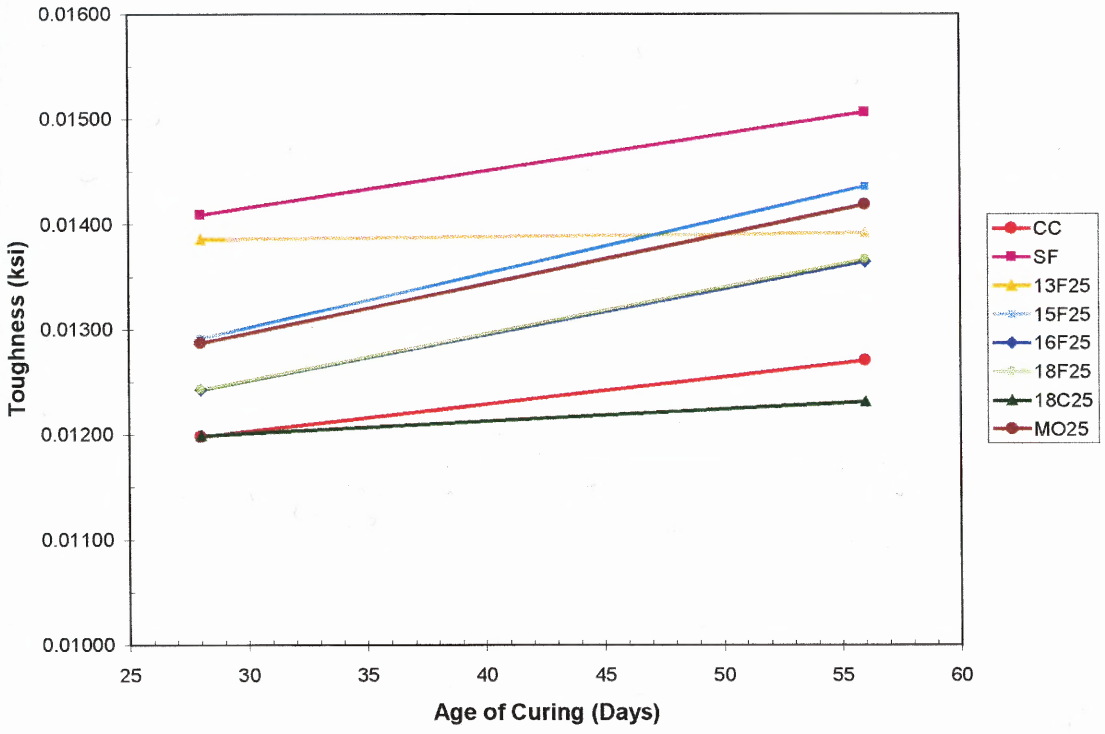

Figure 5.10 Relationship between Toughness of Concrete and Curing Age

The toughness of all concretes increase with the curing time from the age of 28 days to 56 days. The 13F is the only series that did not show the same improvement as the others. The overall results seem to be in good agreement with the maturity of these cementitious products. As these high performance concretes get older, more C-S-H gels were formed as a result of the pozzolanic reaction between $Ca(OH)_2$ and the Si in the silica fume and fly ash. The silica compound in silica fume is generally more reactive than those in the fly ash. As a result, silica fume concrete tends to gain strength early and be much stiffer during the early age. As shown in Figure 5.10, silica fume concrete has the highest toughness among all the concrete tested. Also observed from these tests is that the replacement of cement by fly ash in these concretes enhances the toughness of the cement composites by as much as 20% depending on the size and amount of fly ash used.

5.2.3.6 Size Effect of Test Specimen on the Compressive Strength of Concrete: The addition of silica fume and fly ash to concrete mixture provide means to produce high strength concrete (ACI defined high strength concrete with compressive strength higher than 6000 psi). Since these pozzolanic materials tend to improve the strength of the cement matrices either by reducing the voids or by providing addition C-S-H gels or both, failure characteristics of these high performance concretes are different from normal concrete. In some cases, silica fume and fly ash improve the interfacial bond strength between aggregate and matrix by pozzolanic effect, while in other instances these fine particles fill up the voids and thus densify the matrix. Both phenomena make the high performance matrix tougher, resulting in a different fracture mode of cracks breaking through the aggregates rather going around it.

With this fracture behavior, the size of test specimen tends to influence the result of the compression test. If the test specimen is small, crack growth can reach free surface faster resulting in a weaker compressive strength. However, for a larger test specimen the greater load often causes local failure. Any uneven capping or local defect tends to prematurely cause end failure and lead to a lower compressive strength. With these in mind, researchers will have to select a test specimen configuration that provides reliable results. Often, for high strength concrete, the 4 x 8 inch cylinder is used instead of the 6 x 12 inch or the 3 x 6 inch cylinders.

In this study, two different sizes of test specimens, namely, the 3 x 6 inch and the 4 x 8 inch cylinders were used. Two types of high performance concretes were tested to study the effect of specimen size on the compressive strength of these cement matrices, the control concrete (CC) at the age of 28 days and the 18F25 fly ash concrete at the age of 56 days. The results of the control concrete (CC) are presented in Table 5.3, where as the results for the 18F25 fly ash concrete are shown in Table 5.8.

From the results presented, there is no significant difference found in any properties of the concretes, including the compressive strength, peak strain, modulus of elasticity and toughness, between the two specimen sizes used. It is therefore concluded for simplicity and practical reasons that the 3 x 6 inch cylinders be used in this study for the evaluation of the compressive strength of concretes and the other properties under the uniaxial compression test.

5.2.4 Three-Point-Bend Beam Tests of Concrete

All crackings in concrete are primarily the results of tensile failure whether the applied loads are tension or compression. There are three modes of fracture failure as described in Chapter two. In studying fracture behavior of brittle materials like concrete, traditionally, the direct tension test should be the primary means of testing. Unfortunately, due to the brittle nature of cement composites, the direct tensile response is rather unstable and difficult to obtain. Furthermore, since the tensile load carrying capacity of brittle cement composites is rather low, it is a common practice in engineering design to ignore the tensile capacity of concrete. In case that this behavior is absolutely needed, indirect tension tests such as the split cylinder or the Modulus of Rupture will be used as substitutes. However as the analytical tools get more sophisticated, the effect of tensile resistance of concrete becomes critical to the ultimate solutions, especially for the fracture behavior of concrete structures.

With the brittle nature of cement-based materials, the most commonly used standard tests for fracture study is the three-point bend notched beam as recommended by ASTM E-399. Although the test does not directly represent the true fracture of the composites under the pure Mode-I failure due to the presence of compression zone under bending, it provides a simple and stable testing configuration as compared to the direct tension test. Many fracture models have been proposed by means of the notched beam bending tests. These models include the fictitious crack model (Hillerborg et al. 1976), crack-band model (Bazant and Oh 1983), and the two-parameter fracture model (Jenq and Shah 1985).

For the past twenty years, most researches have studied fracture behavior of concrete and high strength concrete by means of the notched beam models. While some conclusions have been drawn, many questions remain due to the fact that the input material models were inaccurate as well as the erroneous measurement of the load-line deflection (Kim 1996, Navalurkar 1996). Moreover, none has ever investigated the effect of fine pozzolanic additives on the fracture behavior of these high performance concretes.

In this study, attempts were made to study the effect of fine particle pozzolans such as silica fume and fly ash on the fracture behavior of concrete. The selected fly ash concrete was the 25% series in which fly ashes were used as a replacement of cement at 25% by weight of total cementitious materials (cement plus fly ash). As for silica fume concrete, 10% of the total cementitious materials (cement plus silica fume) was replaced by silica fume.

The main purpose of the three-point-bend test on notched beams is to obtain the complete load versus crack-mouth-opening displacement (CMOD) curve and load versus load-line deflection (LLD) curve. These results were then used to study the fracture behavior of concrete. Details of these tests are described in Chapter 4.

5.2.4.1 Results of Beam Tests: Typical load vs. load-line deflection and load vs. crack-mouth-opening displacement curves are shown in Figure 5.11 and 5.12. All other graphs for all concrete mixes are presented in Appendix B. As described in the theoretical background section presented in Chapter 3, the fracture energy (G_F) for all types of concrete studied were calculated from the data of the load vs. crack-mouth-opening displacement curves and the bi-linear relationships between crack-mouth-opening

displacement and load-line deflection (S_1 and S_2). The fracture energy calculated from the load vs. load-line deflection curves as recommended by RILEM (1985) are also determined and presented for comparison.

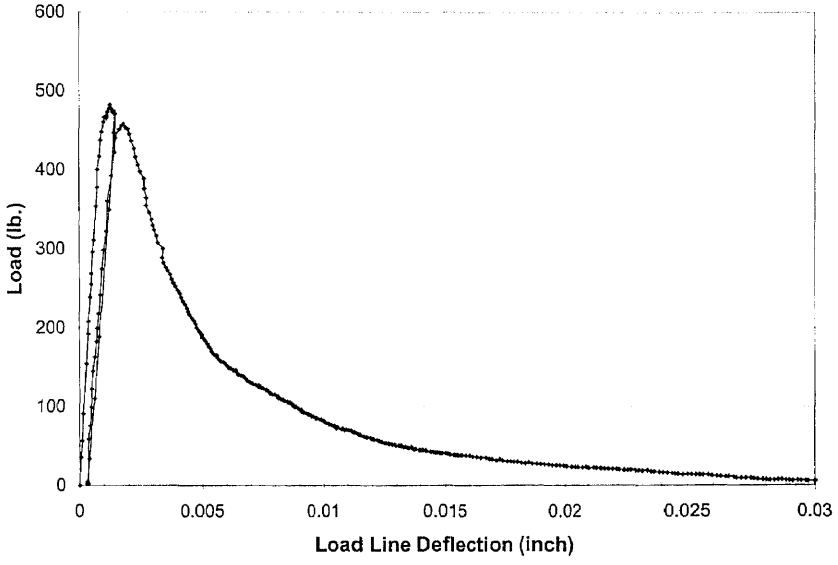

Figure 5.11 Typical Load vs. Load-Line Deflection Response of Concrete

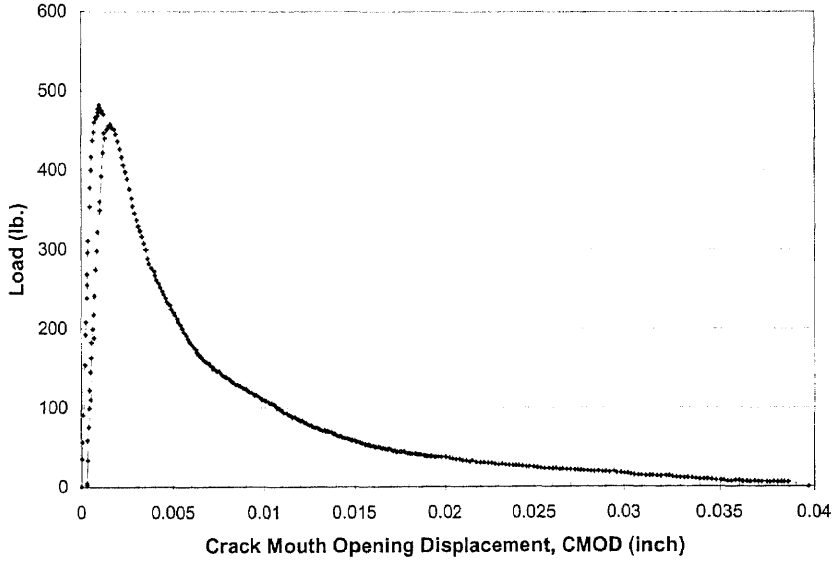

Figure 5.12 Typical Load vs. Crack-Mouth-Opening Displacement Response of Concrete

Tables 5.13 through 5.20 summarize the test data which include peak load, flexural strength, peak CMOD (CMOD at the peak load), peak deflection (deflection at peak load), S_1, S_2 and fracture energy. CC represents the control concrete, without any additives, SF denotes silica fume concrete, and XXX25 refers to fly ash concrete using XXX (13F, 15F, 16F, 18F, 18C and MO) fly ash.

Table 5.13 Beam Test Results of Control Concrete (CC) at the Age of 56 Days

Specimen Number	Peak Load	Flexural Strength	Peak CMOD	Peak Deflection	Relationship between CMOD and Deflection		Fracture Energy	
					S_1	S_2	CMOD Method	Deflection Method
	(pounds)	(psi)	(inch)	(inch)	(in/in)	(in/in)	(lbs./in)	(lbs./in)
1	485	727	0.000996	0.001272	1.279	0.780	0.4733	0.4741
2	445	667	0.000935	0.001203	1.284	0.829	0.4048	0.4041
3	487	730	0.001120	0.001438	1.247	0.731	0.4389	0.4379
Average	**472**	**708**	**0.001017**	**0.001304**	**1.270**	**0.780**	**0.4390**	**0.4387**

Table 5.14 Beam Test Results of Silica Fume Concrete (SF) at the Age of 56 Days

Specimen Number	Peak Load	Flexural Strength	Peak CMOD	Peak Deflection	Relationship between CMOD and Deflection		Fracture Energy	
					S_1	S_2	CMOD Method	Deflection Method
	(pounds)	(psi)	(inch)	(inch)	(in/in)	(in/in)	(lbs./in)	(lbs./in)
1	469	703	0.001243	0.001774	1.445	0.903	0.5109	0.4987
2	515	772	0.001191	0.001594	1.446	0.883	0.4942	0.4903
3	540	810	0.001292	0.002011	1.565	0.906	0.5498	0.5398
Average	**508**	**762**	**0.001242**	**0.001793**	**1.486**	**0.897**	**0.5183**	**0.5096**

Table 5.15 Beam Test Results of Fly Ash Concrete (13F25) at the Age of 56 Days

Specimen Number	Peak Load	Flexural Strength	Peak CMOD	Peak Deflection	Relationship between CMOD and Deflection		Fracture Energy	
					S_1	S_2	CMOD Method	Deflection Method
	(pounds)	(psi)	(inch)	(inch)	(in/in)	(in/in)	(lbs./in)	(lbs./in)
1	495	743	0.001346	0.001679	1.277	0.857	0.5468	0.5498
2	459	688	0.001118	0.001571	1.371	0.937	0.5495	0.5611
3	526	789	0.001365	0.001596	1.207	0.830	0.5254	0.5186
Average	**493**	**740**	**0.001276**	**0.001616**	**1.285**	**0.875**	**0.5406**	**0.5431**

Table 5.16 Beam Test Results of Fly Ash Concrete (15F25) at the Age of 56 Days

Specimen Number	Peak Load	Flexural Strength	Peak CMOD	Peak Deflection	Relationship between CMOD and Deflection		Fracture Energy	
					S_1	S_2	CMOD Method	Deflection Method
	(pounds)	(psi)	(inch)	(inch)	(in/in)	(in/in)	(lbs./in)	(lbs./in)
1	457	685	0.001191	0.001363	1.208	0.812	0.4427	0.4343
2	526	789	0.001125	0.001460	1.296	0.778	0.4829	0.4837
3	519	779	0.001119	0.001387	1.243	0.790	0.4914	0.4960
Average	**501**	**751**	**0.001145**	**0.001404**	**1.249**	**0.794**	**0.4723**	**0.4713**

Table 5.17 Beam Test Results of Fly Ash Concrete (16F25) at the Age of 56 Days

Specimen Number	Peak Load	Flexural Strength	Peak CMOD	Peak Deflection	Relationship between CMOD and Deflection		Fracture Energy	
					S_1	S_2	CMOD Method	Deflection Method
	(pounds)	(psi)	(inch)	(inch)	(in/in)	(in/in)	(lbs./in)	(lbs./in)
1	473	709	0.001011	0.001270	1.254	0.808	0.4149	0.4122
2	526	790	0.001384	0.001439	1.152	0.762	0.4726	0.4645
3	528	792	0.001199	0.001350	1.180	0.758	0.4752	0.4652
Average	**509**	**763**	**0.001198**	**0.001353**	**1.195**	**0.776**	**0.4542**	**0.4473**

Table 5.18 Beam Test Results of Fly Ash Concrete (18F25) at the Age of 56 Days

Specimen Number	Peak Load (pounds)	Flexural Strength (psi)	Peak CMOD (inch)	Peak Deflection (inch)	Relationship between CMOD and Deflection		Fracture Energy	
					S_1 (in/in)	S_2 (in/in)	CMOD Method (lbs./in)	Deflection Method (lbs./in)
1	480	719	0.001094	0.001279	1.227	0.795	0.3877	0.3789
2	499	749	0.001195	0.001370	1.249	0.791	0.5034	0.4946
3	496	744	0.001186	0.001286	1.190	0.773	0.4636	0.4652
Average	**492**	**737**	**0.001158**	**0.001312**	**1.222**	**0.786**	**0.4516**	**0.4462**

Table 5.19 Beam Test Results of Fly Ash Concrete (18C25) at the Age of 56 Days

Specimen Number	Peak Load (pounds)	Flexural Strength (psi)	Peak CMOD (inch)	Peak Deflection (inch)	Relationship between CMOD and Deflection		Fracture Energy	
					S_1 (in/in)	S_2 (in/in)	CMOD Method (lbs./in)	Deflection Method (lbs./in)
1	391	586	0.001284	0.001385	1.101	0.779	0.4191	0.4098
2	442	663	0.001183	0.001116	1.046	0.753	0.3499	0.3372
3	453	679	0.001257	0.001355	1.169	0.804	0.3592	0.3592
Average	**429**	**643**	**0.001241**	**0.001285**	**1.105**	**0.779**	**0.3761**	**0.3688**

Table 5.20 Beam Test Results of Fly Ash Concrete (MO25) at the Age of 56 Days

Specimen Number	Peak Load (pounds)	Flexural Strength (psi)	Peak CMOD (inch)	Peak Deflection (inch)	Relationship between CMOD and Deflection		Fracture Energy	
					S_1 (in/in)	S_2 (in/in)	CMOD Method (lbs./in)	Deflection Method (lbs./in)
1	493	739	0.001190	0.001236	1.133	0.710	0.4144	0.3987
2	508	761	0.001039	0.001290	1.316	0.783	0.5115	0.5077
3	445	668	0.001257	0.001468	1.208	0.789	0.4547	0.4510
Average	**482**	**723**	**0.001162**	**0.001331**	**1.219**	**0.761**	**0.4602**	**0.4525**

It should be noted that fracture energy reported in these tables was computed by two different means, one by the load vs. CMOD curves and the other by the load vs. load-line deflection curves. If the test setup was designed properly to account for extraneous deformation due to support crushing, these two values should be the same. Also, since the two-parameter fracture model (TPFM) requires unloading at the peak load to determine the unloading compliance (C_u) as described in Chapter two, all tests conducted here were performed with the unloading at peak load as shown in Figure 5.12.

5.2.4.2 Flexural Strength of Concrete: As discussed earlier, Modulus of Rupture (or Flexural Strength) is sometimes used to represent the tensile behavior of concrete. Table 5.21 presents the average flexural strength and compressive strength of concrete along with values from the ACI recommended flexural strength equation, $f_r = 7.5\ (f'_c)^{0.5}$. In order to correlate the f_r value with the compressive strength (f'_c) of each cement composite, the ratio of f_r / f'_c and f_r^{test} / f_r^{ACI} were also calculated and listed in Table 5.21. The flexural strength or modulus of rupture of all concretes tested in this study is calculated by the following equation.

$$f_r = \frac{3PS}{2B(D-a_0)^2} \tag{5.1}$$

where P = maximum applied load (pounds), S = span length (12 inches in this study), B = width of beam (3 inches in this study), D = depth of beam (3 inches in this study), and a_0 = initial notch length (1 inch in this study). Figure 4.2 shows the diagram of the three-point bending beam test setup and the testing configuration.

Table 5.21 Relationship between Flexural Strength and Compressive Strength of Concrete

Specimen Type	Age of Specimen (days)	Compressive Strength f_c' (psi)	Flexural Strength f_r^{test} (psi)	Flexural Strength* f_r^{ACI} (psi)	$\frac{f_r^{test}}{f_c'}$	$\frac{f_r^{test}}{f_r^{ACI}}$
CC	56	6008	708	581	0.118	1.218
SF	56	7436	762	647	0.102	1.178
13F25	56	6786	740	618	0.109	1.198
15F25	56	6746	751	616	0.111	1.219
16F25	56	6768	763	617	0.113	1.237
18F25	56	6234	737	592	0.118	1.245
18C25	56	5620	643	562	0.114	1.144
MO25	56	6664	723	612	0.108	1.181

From the results shown in Table 5.21, the flexural strength of all high performance concretes is approximately 10 to 12 percent of the compressive strength. The silica fume concrete and fly ash concrete (13F25, 15F25, 18F25 and MO25) provide noticeably higher flexural strength than the control concrete. The flexural strengths of the silica fume concrete and fly ash concrete, 13F25, 15F25, 16F25 and 18F25, are about the same, even though the compressive strength of silica fume concrete is somewhat higher. As expected, the 18C25 fly ash concrete, made with the coarsest fly ash and having the lowest compressive strength, yields the lowest flexural strength.

In comparison with the ACI flexural strength equation, the flexural strengths from the test are generally higher by about 20 percent, except for the 18C25 fly ash concrete, which is slightly lower at about 14 percent.

In summary, it may be concluded that the flexural strength of concrete tested in this study is related to the compressive strength. The concrete with higher compressive strength tends to have higher flexural strength as well. Partial replacement of cement by

silica fume and fly ash in the concrete mixture can improve both the compressive strength and the flexural strength of concrete.

5.2.4.3 Load versus Load-Line Deflection and Crack-Mouth-Opening Displacement (CMOD) Responses: Typical load vs. load-line deflection and load vs. CMOD curves are previously presented in Figures 5.11 and 5.12. All graphs for other mix series are presented in Appendix B. From Figures 5.11 and 5.12, the unloading after the peak load was performed to obtain the compliance (C_u) at the peak load. This is needed in order to calculate the critical crack length (a_c) as specified by the Two-Parameter Fracture Model (TPFM), described in Chapter 2.

Table 5.22 Results of the Uniaxial Compression Tests and Three-Point-Bend Notched Beam Tests of Concrete

Specimen Type	Compressive Strength	Flexural Strength	Peak CMOD	Peak Deflection	Relationship between CMOD and Deflection		Fracture Energy	
							CMOD Method	Deflection Method
	f_c' (psi)	f_r^{test} (psi)	(inch)	(inch)	S_1 (in/in)	S_2 (in/in)	(lbs./in)	(lbs./in)
CC	6008	708	0.001017	0.001304	1.270	0.780	0.4390	0.4387
SF	7436	762	0.001242	0.001793	1.486	0.897	0.5183	0.5096
13F25	6786	740	0.001276	0.001616	1.285	0.875	0.5406	0.5431
15F25	6746	751	0.001145	0.001404	1.249	0.794	0.4723	0.4713
16F25	6768	763	0.001198	0.001353	1.195	0.776	0.4542	0.4473
18F25	6234	737	0.001158	0.001312	1.222	0.786	0.4516	0.4462
18C25	5620	643	0.001241	0.001285	1.105	0.779	0.3761	0.3688
MO25	6664	723	0.001162	0.001331	1.219	0.761	0.4602	0.4525

Table 5.22 presents the average values of the compressive strength, flexural strength, peak CMOD (CMOD at peak load), peak deflection (deflection at peak load), the relationships between CMOD and load-line deflection (S_1 and S_2), and the fracture energy of concrete. The flexural strength was determined from the measured peak load. The fracture energy was calculated from area under the load vs. deflection curve and the load-CMOD curve.

The results in Table 5.22 also indicated that there was a relationship between the peak deflection and the strength of concrete, both compression and tension. The stronger the concrete is, the larger the peak deflection observed. Silica fume concrete, having the highest compressive strength, has the largest peak deflection (0.001793 inches), while the 18C25 fly ash concrete yields the lowest peak deflection of 0.001285 inches. The peak deflections of all the fly ash concretes, except the 18C25 specimen, are higher than that of the control. Overall it seems that concrete made with finer fly ash particles tends to have larger peak deflection than the one with coarser particles.

As for the crack-mouth-opening displacement (CMOD) at peak load, the results from Table 5.22 show no strong evidence to relate the peak CMOD to neither the compressive strength nor flexural strength of concrete. Evidently, the values of the peak CMOD of all concrete series are almost the same, except for the control concrete, which is somewhat lower.

Fracture energy, calculated either from the load-deflection curve or the load-CMOD curve, was found to be in good agreement. This is different from the results reported by a few other researchers who found large discrepancy between two concepts. It has long been articulated that the difference was due to extraneous deflection as a result

of support crushing. With the designed notched beam test setup developed in this study to overcome this support condition and thus provide a more accurate load-line deflection, the two curves (load vs. CMOD and load vs. deflection) provide the same value of fracture energy.

By introducing the relationship between CMOD and deflection, testing procedure to determine the fracture energy of concrete can be simplified. With consistent agreement observed for the fracture energy as described above, one only needs to measure either the load vs. CMOD or the load vs. load-line deflection curve during testing. Based on the energy principle, the load vs. deflection is more commonly accepted. However, due to potential error that might exist in the measured load-line deflection, a more reliable test result will be from the load-CMOD response.

S_1 and S_2 represent the relationships (physically, the slopes of the CMOD-Deflection curve) between the deflection and the CMOD. S_1 corresponds to the relationship of the region in which the process zone is developing. S_2 provides the same relationship in the region for which the fully developed fracture process zone shifts forward during crack growth. The value of S_1 is more sensitive to the strength of concrete whereas S_2 is rather consistent. This seems to show that the size of the fracture process zone is somewhat related to the strength and grain size of the added pozzolanic materials. Once the process zone has fully developed, the shifting of this zone forward during crack propagation that corresponds to the post-peak softening regime seems to be more geometry dependent, i.e. beam-size dependent. Hence, the S_2 results for different high performance concretes were consistent and less material dependent.

5.2.4.4 Bi-linear Relationship between Deflection and CMOD: As seen in Figure 5.13, a typical relationship between the accurately measured load-line deflection and CMOD is bi-linear in shape. The initial part of S_1 shows the deflection-CMOD relationship in the linear elastic region. The slope S_1 gradually changes to S_2 during the formation of the fracture process zone in the vicinity of the crack tip. Around the peak load the process zone is fully developed and reaches a certain size, which is governed by material characteristics and specimen configuration. Thereafter, the specimen exhibits a linear relationship between deflection and CMOD with a constant slope of S_2. The second part of S_2, is maintained as the crack propagates until complete failure. Since the size of the process zone in front of the crack tip after the peak load remains fully developed, the process zone shifts upward toward the compression zone of the beam as crack continues to grow. Recent work by Kim (1996) reported that when the load-line deflection was measured inaccurately, which included the extraneous deformations due to beam-support crushing, the bi-linear relationship between deflection and CMOD is not at all apparent.

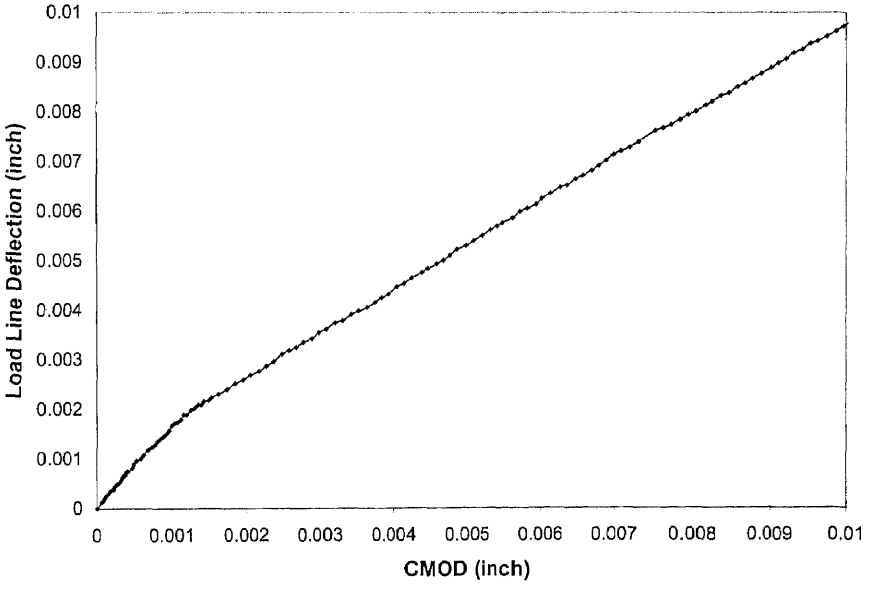

Figure 5.13 Typical Load-Line Deflection and CMOD Response

From the results in Table 5.22 and by sorting the values of S_1 from the highest to the lowest, the following can be observed. The highest S_1 found is from the silica fume concrete (1.486 inch/inch), while the lowest is by the 18C25 fly ash concrete, which is 1.105 inch/inch. Noticeably, S_1 of all fly ash concrete specimens, except 13F25, are lower than that of the control concrete. These differences may be attributed to the effect of the fracture process zone size of these cementitious materials.

Since the constant value of S_1 was observed within the linear-elastic range of the load-deflection curve, it may be concluded that S_1 is related to the elastic energy absorption of the three-point bend notched beam. Theoretically, both the CMOD and the load-line deflection are the direct results of a combined material and structural response of the beam under the applied load. The relationship between these two indicators is a result of the fracture process zone developed within the test specimen configuration. A larger and softer process zone usually means a lower value of S_1. This conclusion can be reinforced by the results of S_1 of the silica fume concrete (1.486 inch/inch) as compared to that of the 18C25 fly ash concrete (1.105 inch/inch).

As explained earlier, S_2 is the slope of the deflection and CMOD response as the crack propagates through the specimen. Table 5.22 tabulates the average values of S_2 of the specimens tested for each concrete series. The silica fume concrete has the largest S_2 of 0.897 inch/inch, followed by the 13F25 fly ash concrete with an S_2 of 0.875 inch/inch. The rest of the specimens produce approximately the same level of S_2 at about 0.780 inch/inch. Kim (1996) reported the average value of S_2 for concrete with the compressive strength of about 7000 to 8000 psi to be 0.872 inch/inch, which is closed to the value for the silica fume concrete observed in this study. Navalurkar (1996) found that the average

value of S_2 for concrete with the compressive strength of about 6000 psi to be 0.790 inch/inch, which agrees well with the results of the fly ash concrete and the control concrete shown in Table 5.22. Furthermore, Kim (1996) had also concluded that S_2 is a material property in the same way as the fracture energy, G_F.

Due to the fact that the zone of microcracking is under development prior to reaching the peak load, the overall response of the test specimen generally exhibits a linear behavior, which can be quantified by the linear relationship of S_1. At the peak load region, the fracture process zone has fully developed under the constraint of the test specimen configuration and the slope of a deflection-CMOD curve changes from S_1 to S_2. After the peak load, the size of the fracture process zone remains unchanged, and the slope S_2 is maintained until reaching the ultimate failure. This shows that the difference between S_1 and S_2 (or S_1-S_2) is closely related to the size of the fracture process zone ahead of the crack tip. The larger variation of the values of S_1-S_2 indicates a smaller size of the fracture process zone. This is because the material with a smaller process zone will exhibit non-linear behavior which is less than that with a larger process zone, resulting in the higher values of S_1 and the difference of S_1-S_2. From Table 5.22, silica fume concrete has the highest S_1-S_2 of 0.589 indicating that the fracture process zone of the silica fume concrete is smaller than that of the other types of concrete, which yields the average values of S_1-S_2 about 0.440.

5.2.4.5 Fracture Energy: Fracture energy is a very important parameter used in studying the fracture behavior of concrete. It is the amount of energy required to extend a unit area of crack growth through the material, or in other words, the energy required for unit area of crack propagation of the material. If the value of fracture energy for a given material is known, the fracture behavior of a structure made of that material can be predicted more accurately.

As a common practice, fracture energy is usually taken as the area under the load-deflection curve of a three-point-bend notched beam test as recommended by RILEM (1985) (see Equation 2.12 and 3.2). However, due to the difficulties encountered measuring the exact load-line deflection (LLD), many discrepancies have been reported for the value of fracture energy of cementitious composites. Kim (1996) showed that the deflections measured with reference to the crosshead of the beam test setup were usually greater than those measured with reference to the neutral axis. The difference in measurement was a result of the extraneous deformation due to support crushing. Calculation of fracture energy based upon this overstated deflection has led to most of the discrepancies as discussed above. It is therefore critical to eliminate all the extraneous deformations from the test setup and choose the appropriate relationship in determining the fracture energy and toughness of concrete. These problems can be eliminated by determining the fracture energy and toughness of concrete as described in detail in Chapter 3 by using the bilinear relationship between the CMOD and the load-line deflection. The fracture energy (G_F) can then be calculated using the following expression (also see Equation 3.11):

$$G_F B(D-a_0) = \int_{\delta=0}^{\delta=\infty} P d\delta = S_1 \int_{0}^{CMOD_P} P dCMOD + S_2 \int_{CMOD_P}^{\infty} P dCMOD \qquad (5.2)$$

where B = width of beam, D = depth of beam, a_0 = initial notch length,

$S_1 = (d\delta / dCMOD)$, the slope of the LLD-CMOD curve in the linear elastic region,

$S_2 = (d\delta / dCMOD)$, the slope of the LLD-CMOD curve in the post- peak region.

Table 5.22 lists the average fracture energy for each of the concretes tested. The fracture energy calculated from area under the load-CMOD curves using the bilinear concept was designated as the *CMOD Method*, and those calculated from the load-deflection curves are shown as the Deflection Method. The results of fracture energy (G_F), for each concrete series calculated from both methods show very good agreement as it should be theoretically. Since the CMOD measurement is independent of any support conditions, unlike the load-line deflection, the values of fracture energy for every concrete series were determined from the load-CMOD response (*CMOD Method*) and found to be as shown in Table 5.22.

From Table 5.22, the 13F25 fly ash concrete had the highest fracture energy of 0.5406 lbs./inch, followed by the silica fume concrete (0.5183 lbs./inch) with the rest of the fly ash concrete ranging from 0.3761 to 0.4723 lbs./inch. Fracture energy of most fly ash concretes, except the 18C25 series, is higher than that of the control.

In general, fracture energy is commonly used to characterize fracture behavior of concrete, which includes pre- and post-peak behaviors of the material. Prior to reaching the peak load, microcracking within the fracture process zone and the bond strength between matrix and aggregate play the dominant roles affecting the fracture energy of concrete. However, after the peak load, as the process zone size remains constant it is the specimen configuration that affects the fracture energy since crack propagation simply involves shifting forward of the fracture process zone. The results from Table 5.22

indicated that even though silica fume concrete had the highest bond strength index, its fracture energy was lower than the 13F fly ash concrete. This implies that among all the cement matrices in this study the 13F fly ash concrete is toughest, citing the largest fracture energy (G_F).

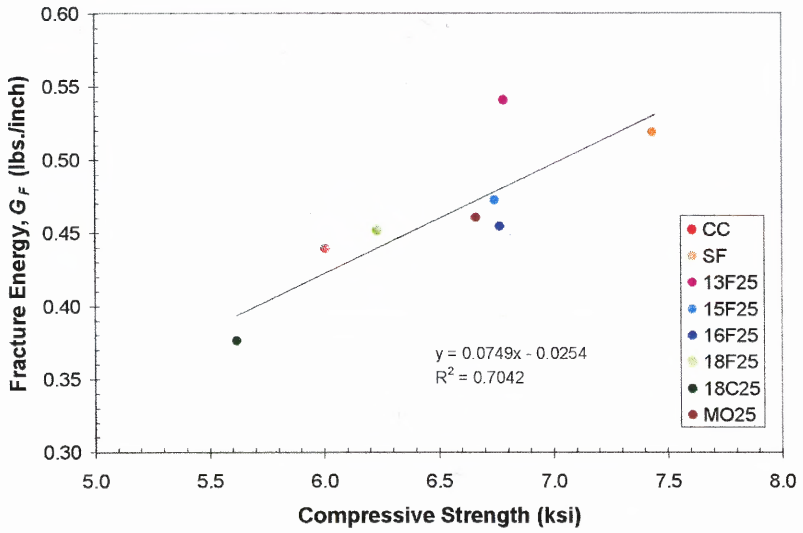

Figure 5.14 Relationship between Fracture Energy and Compressive Strength

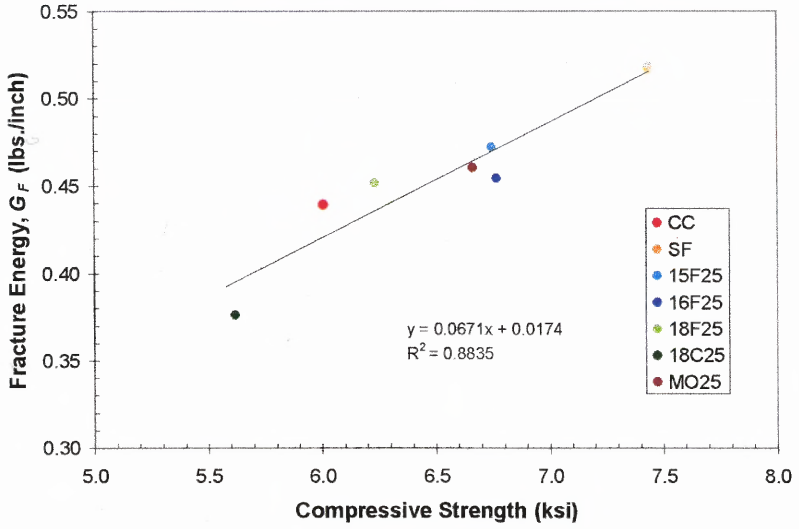

Figure 5.15 Relationship between Fracture Energy and Compressive Strength (without the data for the fly ash concrete 13F25)

Figure 5.14 plots the relationship between fracture energy (G_F) and compressive strength (f'_c) of concrete. The results lead to the conclusion that fracture energy is somewhat related to the compressive strength of the cement composites. The largest variation was found in the 13F series, which was slightly higher. Interestingly, when the data for the 13F25 fly ash concrete were excluded, as shown in Figure 5.15, the results clearly show that the fracture energy is dependent on the compressive strength.

In general, one may say that the fracture energy increases with increasing compressive strength of the cement composites. In addition, one may also conclude that the presence of fine pozzolans such as silica fume and fly ash in the cement matrix tends to improve the fracture energy of concrete.

In case of the fly ash concrete, finer particle size clearly show its influence on the fracture energy of concrete. With about 80% of the 13F fly ash particles smaller than 3 microns, compared to 45% for the 15F fly ash, fracture energy of the 13F series was about 15% higher than that of the 15F series. It should be noted that for fly ash concretes with the same level of compressive strength and flexural strength, such as the 13F, 15F, and 16F series, the values of their fracture energy are rather different (0.5186, 0.4723, and 0.4542 respectively). This seems to indicate that the very fine particles of fly ash play an important role, contributing to a higher fracture energy of concrete.

Finally, no clear correlation was found between fracture energy and other properties of concrete, e.g. the bond strength index, the modulus of elasticity, flexural strength, and the peak deflection since these parameters do not represent the overall material and structural performance.

5.3 Results Based on the Proposed Fracture Mechanics Model

In this section, the proposed fracture mechanics model as described in Chapter 3 was applied to the test data obtained from the notched beam tests. The predicted fracture mechanics parameters of all high performance concretes are presented.

Tables 5.23 through 5.30 summarize the test data from the notched beam tests including peak load, peak CMOD, peak deflection, S_1 , S_2 and fracture energy, and the corresponding analytical results from the proposed model such as the critical crack length (a_c), the critical energy release rate (G_C) and the brittleness of concrete. All test specimens were evaluated at the age of 56 days.

In the next sections, the investigation and evaluation of the effect of high performance matrices incorporating fine-particle pozzolans on fracture behavior of concrete are presented. Each of the analytical parameters predicted by the proposed fracture mechanics model are evaluated and compared with the related empirical data obtained from the uniaxial compression tests and the three-point-bend notched beam tests. The proposed model was compared to the Two Parameter Fracture Model (RILEM 1990), and also re-evaluated in Section 5.4 by applying it to the test data reported by several other researchers (Jenq and Shah 1985, Ratanalert and Wecharatana 1989, Gopalaratnam and Ye 1991).

Table 5.23 Analytical Results of Fracture Parameters of Control Concrete (CC)

Specimen Number	Peak Load	Peak CMOD	Peak Deflection	Relationship between CMOD and Deflection		Fracture Energy		Critical Crack Length		Critial Energy Release Rate		Brittleness Index	
				S_1	S_2	CMOD Method	Deflection Method	CMOD Method	Deflection Method	CMOD Method	Deflection Method	CMOD Method	Deflection Method
	(pounds)	(inch)	(inch)	(in/in)	(in/in)	(lbs./in)	(lbs./in)	(inch)	(inch)	(lbs./in)	(lbs./in)		
1	485	0.000996	0.001272	1.279	0.780	0.4733	0.4741	1.2788	1.2708	0.2580	0.2425	0.7539	0.7339
2	445	0.000935	0.001203	1.284	0.829	0.4048	0.4041	1.2967	1.2803	0.2492	0.2435	0.7542	0.7226
3	487	0.001120	0.001438	1.247	0.731	0.4389	0.4379	1.3333	1.3397	0.2568	0.2593	0.7246	0.7274
Average	**472**	**0.001017**	**0.001304**	**1.270**	**0.780**	**0.4390**	**0.4387**	**1.3030**	**1.2969**	**0.2547**	**0.2484**	**0.7442**	**0.7280**

Table 5.24 Analytical Results of Fracture Parameters of Silica Fume Concrete (SF)

Specimen Number	Peak Load	Peak CMOD	Peak Deflection	Relationship between CMOD and Deflection		Fracture Energy		Critical Crack Length		Critial Energy Release Rate		Brittleness Index	
				S_1	S_2	CMOD Method	Deflection Method	CMOD Method	Deflection Method	CMOD Method	Deflection Method	CMOD Method	Deflection Method
	(pounds)	(inch)	(inch)	(in/in)	(in/in)	(lbs./in)	(lbs./in)	(inch)	(inch)	(lbs./in)	(lbs./in)		
1	469	0.001243	0.001774	1.445	0.903	0.5109	0.4987	1.3785	1.3593	0.3365	0.3149	0.4575	0.4679
2	515	0.001191	0.001594	1.446	0.883	0.4942	0.4903	1.3706	1.3482	0.2906	0.2866	0.4645	0.4696
3	540	0.001292	0.002011	1.565	0.906	0.5498	0.5398	1.4238	1.4119	0.3239	0.3075	0.4782	0.4736
Average	**508**	**0.001242**	**0.001793**	**1.486**	**0.897**	**0.5183**	**0.5096**	**1.3910**	**1.3732**	**0.3170**	**0.3030**	**0.4667**	**0.4704**

Table 5.25 Analytical Results of Fracture Parameters of Fly Ash Concrete (13F25)

Specimen Number	Peak Load	Peak CMOD	Peak Deflection	Relationship between CMOD and Deflection		Fracture Energy		Critical Crack Length		Critial Energy Release Rate		Brittleness Index	
				S_1	S_2	CMOD Method	Deflection Method	CMOD Method	Deflection Method	CMOD Method	Deflection Method	CMOD Method	Deflection Method
	(pounds)	(inch)	(inch)	(in/in)	(in/in)	(lbs./in)	(lbs./in)	(inch)	(inch)	(lbs./in)	(lbs./in)		
1	495	0.001346	0.001679	1.277	0.857	0.5468	0.5498	1.3357	1.3230	0.3040	0.2828	0.8022	0.8010
2	459	0.001118	0.001571	1.371	0.937	0.5495	0.5611	1.2521	1.2406	0.3006	0.3002	0.8197	0.8182
3	526	0.001365	0.001596	1.207	0.830	0.5254	0.5186	1.3475	1.3436	0.2924	0.2829	0.8481	0.8227
Average	**493**	**0.001276**	**0.001616**	**1.285**	**0.875**	**0.5406**	**0.5431**	**1.3118**	**1.3024**	**0.2990**	**0.2887**	**0.8233**	**0.8140**

Table 5.26 Analytical Results of Fracture Parameters of Fly Ash Concrete (15F25)

Specimen Number	Peak Load	Peak CMOD	Peak Deflection	Relationship between CMOD and Deflection		Fracture Energy		Critical Crack Length		Critial Energy Release Rate		Brittleness Index	
				S_1	S_2	CMOD Method	Deflection Method	CMOD Method	Deflection Method	CMOD Method	Deflection Method	CMOD Method	Deflection Method
	(pounds)	(inch)	(inch)	(in/in)	(in/in)	(lbs./in)	(lbs./in)	(inch)	(inch)	(lbs./in)	(lbs./in)		
1	457	0.001191	0.001363	1.208	0.812	0.4427	0.4343	1.3362	1.3097	0.2714	0.2484	0.7327	0.7513
2	526	0.001125	0.001460	1.296	0.778	0.4829	0.4837	1.3327	1.3158	0.2714	0.2609	0.7540	0.7898
3	519	0.001119	0.001387	1.243	0.790	0.4914	0.4960	1.3090	1.3137	0.2709	0.2788	0.7789	0.7824
Average	**501**	**0.001145**	**0.001404**	**1.249**	**0.794**	**0.4723**	**0.4713**	**1.3260**	**1.3131**	**0.2712**	**0.2627**	**0.7552**	**0.7745**

Table 5.27 Analytical Results of Fracture Parameters of Fly Ash Concrete (16F25)

Specimen Number	Peak Load	Peak CMOD	Peak Deflection	Relationship between CMOD and Deflection		Fracture Energy		Critical Crack Length		Critial Energy Release Rate		Brittleness Index	
				S_1	S_2	CMOD Method	Deflection Method	CMOD Method	Deflection Method	CMOD Method	Deflection Method	CMOD Method	Deflection Method
	(pounds)	(inch)	(inch)	(in/in)	(in/in)	(lbs./in)	(lbs./in)	(inch)	(inch)	(lbs./in)	(lbs./in)		
1	473	0.001011	0.001270	1.254	0.808	0.4149	0.4122	1.3113	1.3129	0.2605	0.2530	0.6218	0.6233
2	526	0.001384	0.001439	1.152	0.762	0.4726	0.4645	1.3660	1.3584	0.2777	0.2535	0.6233	0.6249
3	528	0.001199	0.001350	1.180	0.758	0.4752	0.4652	1.3290	1.3193	0.2648	0.2489	0.6152	0.6529
Average	**509**	**0.001198**	**0.001353**	**1.195**	**0.776**	**0.4542**	**0.4473**	**1.3354**	**1.3302**	**0.2677**	**0.2518**	**0.6201**	**0.6337**

Table 5.28 Analytical Results of Fracture Parameters of Fly Ash Concrete (18F25)

Specimen Number	Peak Load	Peak CMOD	Peak Deflection	Relationship between CMOD and Deflection		Fracture Energy		Critical Crack Length		Critial Energy Release Rate		Brittleness Index	
				S_1	S_2	CMOD Method	Deflection Method	CMOD Method	Deflection Method	CMOD Method	Deflection Method	CMOD Method	Deflection Method
	(pounds)	(inch)	(inch)	(in/in)	(in/in)	(lbs./in)	(lbs./in)	(inch)	(inch)	(lbs./in)	(lbs./in)		
1	480	0.001094	0.001279	1.227	0.795	0.3877	0.3789	1.3734	1.3550	0.2515	0.2431	0.6537	0.6419
2	499	0.001195	0.001370	1.249	0.791	0.5034	0.4946	1.3254	1.2863	0.2764	0.2618	0.6305	0.6485
3	496	0.001186	0.001286	1.190	0.773	0.4636	0.4652	1.3311	1.2949	0.2774	0.2676	0.6042	0.6022
Average	**492**	**0.001158**	**0.001312**	**1.222**	**0.786**	**0.4516**	**0.4462**	**1.3433**	**1.3120**	**0.2685**	**0.2575**	**0.6295**	**0.6309**

Table 5.29 Analytical Results of Fracture Parameters of Fly Ash Concrete (18C25)

Specimen Number	Peak Load	Peak CMOD	Peak Deflection	Relationship between CMOD and Deflection		Fracture Energy		Critical Crack Length		Critial Energy Release Rate		Brittleness Index	
				S_1	S_2	CMOD Method	Deflection Method	CMOD Method	Deflection Method	CMOD Method	Deflection Method	CMOD Method	Deflection Method
	(pounds)	(inch)	(inch)	(in/in)	(in/in)	(lbs./in)	(lbs./in)	(inch)	(inch)	(lbs./in)	(lbs./in)		
1	391	0.001284	0.001385	1.101	0.779	0.4191	0.4098	1.3030	1.2828	0.2368	0.2214	0.5324	0.5579
2	442	0.001183	0.001116	1.046	0.753	0.3499	0.3372	1.3483	1.3087	0.2278	0.1967	0.5080	0.5533
3	453	0.001257	0.001355	1.169	0.804	0.3592	0.3592	1.3614	1.3592	0.2177	0.2037	0.5105	0.5036
Average	**429**	**0.001241**	**0.001285**	**1.105**	**0.779**	**0.3761**	**0.3688**	**1.3376**	**1.3169**	**0.2274**	**0.2073**	**0.5170**	**0.5383**

Table 5.30 Analytical Results of Fracture Parameters of Fly Ash Concrete (MO25)

Specimen Number	Peak Load	Peak CMOD	Peak Deflection	Relationship between CMOD and Deflection		Fracture Energy		Critical Crack Length		Critial Energy Release Rate		Brittleness Index	
				S_1	S_2	CMOD Method	Deflection Method	CMOD Method	Deflection Method	CMOD Method	Deflection Method	CMOD Method	Deflection Method
	(pounds)	(inch)	(inch)	(in/in)	(in/in)	(lbs./in)	(lbs./in)	(inch)	(inch)	(lbs./in)	(lbs./in)		
1	493	0.001190	0.001236	1.133	0.710	0.4144	0.3987	1.3533	1.3427	0.2574	0.2439	0.6170	0.6244
2	508	0.001039	0.001290	1.316	0.783	0.5115	0.5077	1.2784	1.2580	0.2545	0.2369	0.6767	0.6916
3	445	0.001257	0.001468	1.208	0.789	0.4547	0.4510	1.3400	1.3189	0.2673	0.2456	0.6226	0.6127
Average	**482**	**0.001162**	**0.001331**	**1.219**	**0.761**	**0.4602**	**0.4525**	**1.3239**	**1.3065**	**0.2597**	**0.2421**	**0.6388**	**0.6429**

5.3.1 Critical Crack Growth

Based on the proposed fracture mechanics model, the fracture behavior of concrete can be derived in terms of the applied load, P, and a function of crack growth, Δa (see Equation 3.12b and Figure 3.3). The details of theoretical development are presented in Chapter 3. Figure 5.16 shows a typical load-crack growth response predicted by the proposed model. All other load-crack growth curves are presented in Appendix C.

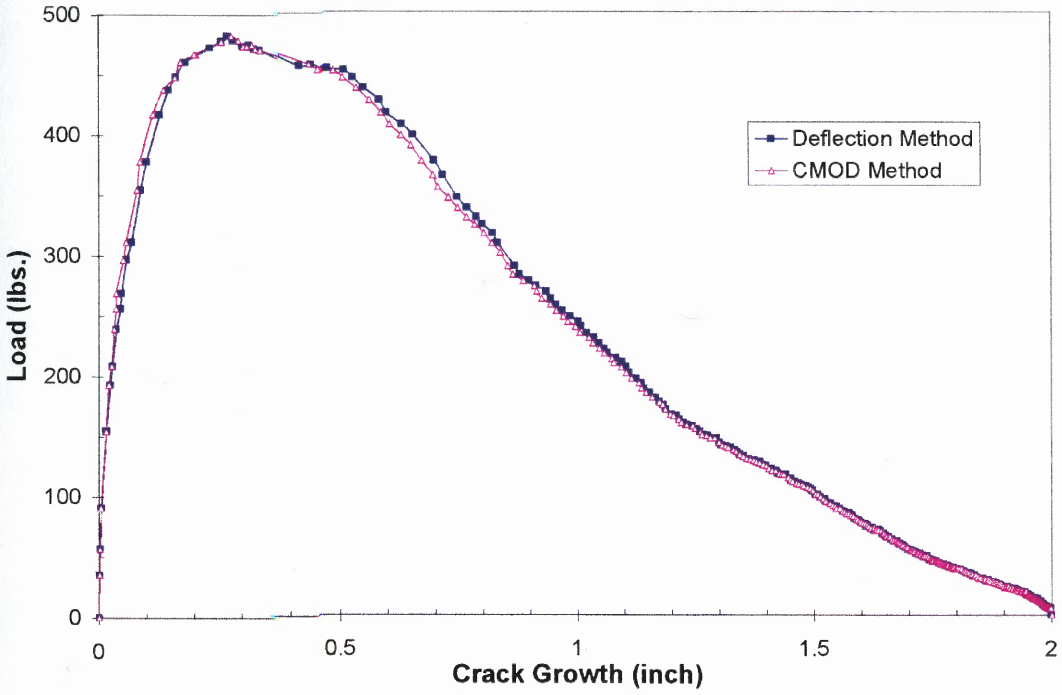

Figure 5.16 Typical Load-Crack Growth Response from the Proposed Model

In Figure 5.16, the applied load versus the corresponding crack growth based on both the load-deflection response and the load-CMOD response are plotted in the same figure. The plots based on the load-deflection response were called *Deflection Method*, while the ones based on the load-CMOD response were named *CMOD Method*. In this study, the load-line deflection was measured with reference to a simple support-like

frame mounted on two pivots, which are attached on the beam over the supports at the level of the initial neutral axis (see Figure 4.2 and 4.3). This test setup was designed to prevent the erroneous deflection from being unintentionally included in the measurement.

The predicted load-crack growth response based on the *Deflection Method* agreed well with those based on the *CMOD Method*. This is largely due to the accurate measurement of load-line deflection, making it compatible to the load-CMOD response. However, Figure 5.16 also shows that at the same load, the corresponding crack growth calculated from the load-deflection response is slightly larger than the one calculated from the load-CMOD curve. Even though the deflections were accurately measured with respect to the reference frame, the deflections did not completely extricate the effect of support crushing that took place under the load application points or at the supports. On the contrary, it is noticed from Tables 5.23 to 5.30 that for almost all of the specimens tested the critical crack growth derived from the *CMOD Method* is a little higher than the critical crack growth from the *Deflection Method*. This is possibly because at peak load (or the moment of fracture), the deflection response is not as sensitive to crack growth and beam bending as the CMOD which is directly a result of crack opening.

It is widely recognized that fracture behavior of nonlinear elastic brittle materials like cement-based composites is rather complex and thus multiple parameters are often fused to predict the fracture characteristics. In this study, in addition to the load-crack growth response, the critical crack length (a_c) was used as another key fracture parameter. The critical crack length (a_c) is defined as the summation of the initial notch depth (a_0) and the crack growth at peak load (Δa_c), or $a_c = a_0 + \Delta a_c$. In this study, the beam depth was 3 inches with 1-inch initial notch depth (a_0). The maximum critical crack growth

(Δa_c) was therefore equal to 2 inches, and the maximum total critical crack length was 3 inches, which equals the beam depth.

Table 5.31 Critical Crack Length (a_c) of Concrete and Other Related Parameters

Specimen Type	Compressive Strength f'_c (ksi)	Bending Beam Test		Fracture Energy		Critical Crack Length	
		Peak Load (pounds)	Peak Deflection (inch)	CMOD Method (lbs./in)	Deflection Method (lbs./in)	CMOD Method (inch)	Deflection Method (inch)
CC	6.008	472	0.001304	0.4390	0.4387	1.3030	1.2969
SF	7.436	508	0.001793	0.5183	0.5096	1.3910	1.3732
13F25	6.786	493	0.001616	0.5406	0.5431	1.3118	1.3024
15F25	6.746	501	0.001404	0.4723	0.4713	1.3260	1.3131
16F25	6.768	509	0.001353	0.4542	0.4473	1.3354	1.3302
18F25	6.234	492	0.001312	0.4516	0.4462	1.3433	1.3120
18C25	5.620	429	0.001285	0.3761	0.3688	1.3376	1.3169
MO25	6.664	482	0.001331	0.4602	0.4525	1.3239	1.3065

Table 5.31 shows the average values of the critical crack lengths of the specimens tested and the other corresponding fracture parameters. The critical crack lengths (a_c) determined by the *Deflection Method* for all the specimens tested were very consistent, except for the silica fume concrete, which is noticeably higher than that of the control concrete and the fly ash concrete. The a_c of the control concrete is slightly smaller than the fly ash concrete. When *CMOD Method* was used, the difference was a bit more obvious. Silica fume concrete yields the highest critical crack length (a_c), while the control concrete gives the smallest a_c. Overall, the control concrete and the fly ash concrete yield very similar values of a_c.

In the present study, referring to the proposed fracture mechanics model developed in Chapter 3, the crack growth was derived with consideration of the fracture process zone in front of the visible crack tip. Based on the proposed model, the crack growth (Δa) represents only the growth of the visible crack in which the fracture process zone length is not included. The fracture process zone, also considered as a fictitious crack (Hillerborg et al 1976, Petersson 1981), consisted of microcracks and the cement matrix-aggregate bridging zone, on which the closure forces act to resist crack growth. In fact, a larger fracture process zone often indicates the non-linear behavior of material and the more elastic energy being dissipated across the bridging zone and microcracks prior to the peak load. In contrast, material with a smaller process zone usually means less elastic energy being dissipated before the peak load. Then, at peak load, large amount of energy that was absorbed within the process zone was suddenly released, causing a rapid crack growth and brittle failure of the structure. Hence, material with a smaller fracture process zone tends to exhibit unstable crack growth.

5.3.2 Critical Energy Release Rate

It is generally accepted that high strength concretes are more brittle than, normal strength concretes. In most linear elastic fracture mechanics (LEFM) models (e.g. the Two-Parameter Fracture Model), the critical stress intensity factor, K_{IC}, a measure of fracture toughness, is expressed by the same principle and test methods as those developed for metals. The Two-Parameter Fracture Model showed that K_{IC} of concrete increased with increasing compressive strength (Shah 1988). This is contrary to the generally accepted observation that high strength concretes are more brittle, or have less toughness. Thus,

there is a need to define fracture toughness that is more appropriate for high performance cementitious materials.

Fracture toughness for metals is designed to prevent brittle fracture as well as to predict fatigue crack growth. In general, K_{IC} is designed to express the strain-toughening or yielding behavior when unstable fracture occurs. For metals, a zone where material has yielded ahead of a crack tip is defined as the plastic zone. On the contrary, for concrete, at the moment of unstable fracture in concrete, the strain-softening behavior occurs because a fracture process zone (or slow crack growth) ahead of the crack tip has developed soon after concrete is subjected to the applied load. This causes a substantial crack (microcracks) growth that precedes the critical load. The fracture process zone in concrete was often compared with the plastic zone in metals. The fracture process zone in concrete was represented by a region of strain-softening behavior by Hillerborg et al. 1976 and Petersson 1981. In order to use fracture toughness in design, K_{IC} for concrete should represent the ability of the fracture process zone to resist crack growth, or absorb the energy applied by the external load before unstable fracture occurs.

Referring to the theoretical development of the proposed fracture mechanics model described in Chapter 3, crack propagation at the crack tip consumes certain amount of energy (W), which is the plastic energy. The rate of change of W with respect to the crack growth (Δa), denoted by G_R, is termed the *fracture resistance* or the *strain energy release rate*. From Equation 3.22, G_R at any instant can be determined from either the load-deflection curve or the load-CMOD curve.

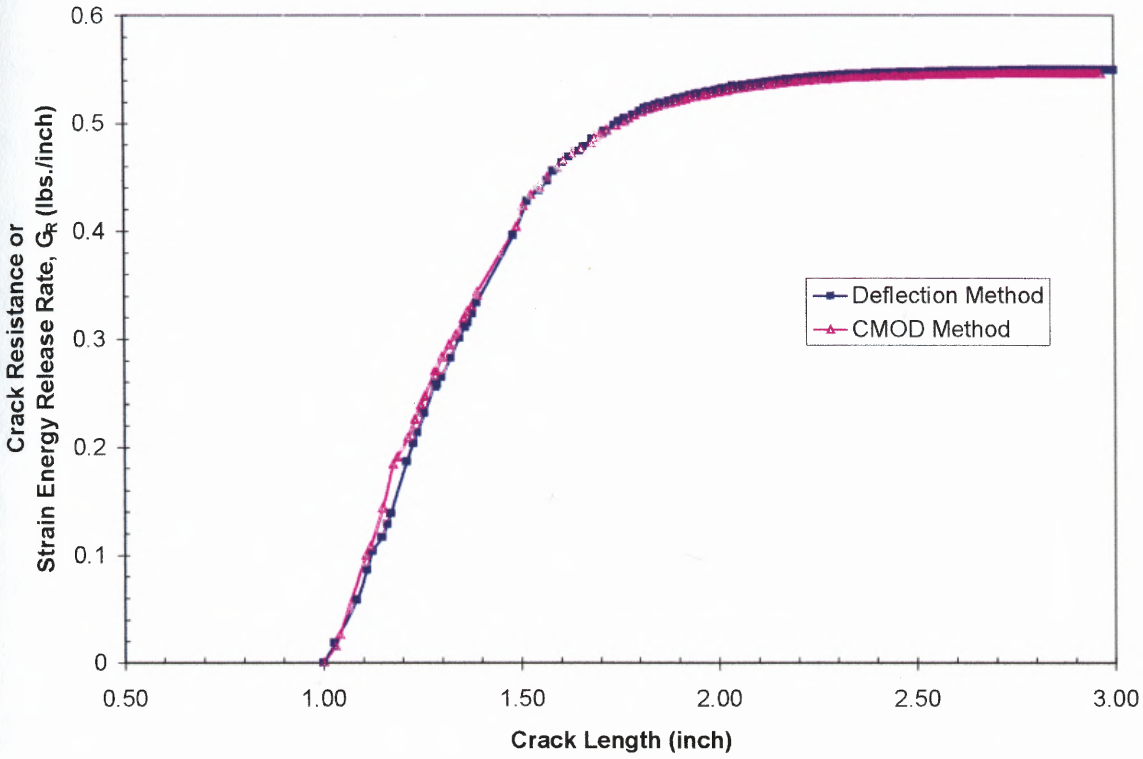

Figure 5.17 Typical Resistance Curve (*R* curve) in the Present Study

A plot between G_R and crack growth (or crack length) response is called the *resistance curve* or *R curve*. Figure 5.17 shows typical *R* curves obtained from both the load-CMOD response (*CMOD Method*) and the load-deflection response (*Deflection Method*) of this study. It can be seen that *R* curves from both concepts agree well with each other due to the improved procedure for measuring the load-line deflection. All other *R* curves of concrete specimens tested are presented in Appendix C. In this section, the fracture parameter, which is of interest from the *R* curve, is the critical energy release rate. The critical energy release rate, G_C, is defined as the value of the energy release rate, G_R, at the peak load or at the on-set of critical crack propagation. The value of G_C can be graphically determined from the *R* curve at the instant when G_C is equal to G_R at the critical crack length, a_c.

In this study, since G_C is closely related to K_{IC}, G_C can therefore be used as a measure of fracture toughness in the same way that the critical stress intensity factor (K_{IC}) is for the linear fracture mechanics. Unlike K_{IC} and G_C from the LEFM which are derived solely on the elastic part of material response (see Section 2.4.3), the value of G_C obtained by the proposed model was computed on the basis of crack growth (Δa) by taking account the effect of the fracture process zone in front of the crack tip. During fracture, the inelastic part of the material response occurs at the crack tip by forming the fracture process zone (plastic zone in metallic materials). Theoretical development to account for this zone in the fracture of cement composites were presented in Chapter 3.

Table 5.32 Critical Energy Release Rate (G_C) of Concrete and Other Related Parameters

Specimen Type	Compressive Strength f'_c (ksi)	Bond Strength Index	Bending Beam Test		Crititcal Crack Length (CMOD Method) (inch)	Critial Energy Release Rate	
			Peak Load (pounds)	Peak Deflection (inch)		CMOD Method (lbs./in)	Deflection Method (lbs./in)
CC	6.008	0.582	472	0.001304	1.3030	0.2547	0.2484
SF	7.436	0.720	508	0.001793	1.3910	0.3170	0.3030
13F25	6.786	0.657	493	0.001616	1.3118	0.2990	0.2887
15F25	6.746	0.653	501	0.001404	1.3260	0.2712	0.2627
16F25	6.768	0.656	509	0.001353	1.3354	0.2677	0.2518
18F25	6.234	0.604	492	0.001312	1.3433	0.2685	0.2575
18C25	5.620	0.544	429	0.001285	1.3376	0.2274	0.2073
MO25	6.664	0.646	482	0.001331	1.3239	0.2597	0.2421

Table 5.32 presents the average value of G_C for each type of specimens tested along with the related fracture parameters. There is no significant difference observed on the values of G_C for each concrete mix series when the G_C values were calculated by both the *Deflection Method* and the *CMOD Method* provided that the load-line deflection was

accurately measured without extraneous deformations. The values of G_C from both methods give the same trend for the behavior of concrete tested. Due to the fact that the CMOD measurement is not affected by support crushing as in the case of deflection, in this study the results of all concrete specimens tested were evaluated by using the value of fracture energy obtained from the load-CMOD response (*CMOD Method*).

From Table 5.32, the results show that silica fume concrete (SF) with the highest compressive strength gives the highest critical energy release rate (G_C) of 0.3170 lbs./inch. The 18C25 fly ash concrete, which has the lowest compressive strength, has the lowest G_C of 0.2274 lbs./inch. The G_C of all fly ash concrete specimens, except the 18C25, are higher than that of the control (CC). It is also noted that as the fly ash particle size gets coarser, the critical energy release rate becomes smaller. From the results in Table 5.32, attempts were made to correlate the critical energy release rate with the other fracture parameters. These are discussed in the following sections.

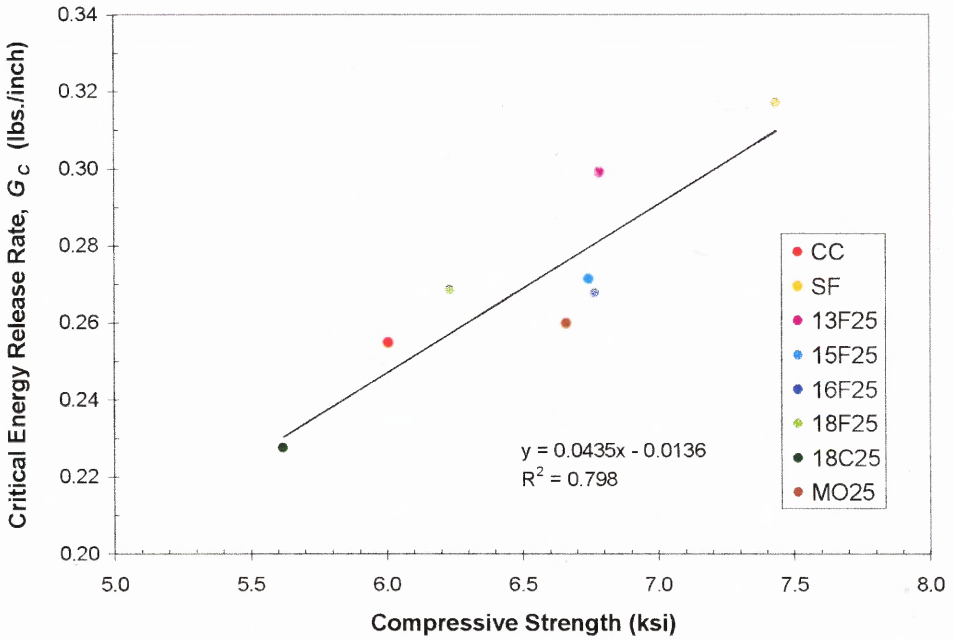

Figure 5.18 Relationship between G_C and Compressive Strength of Concrete

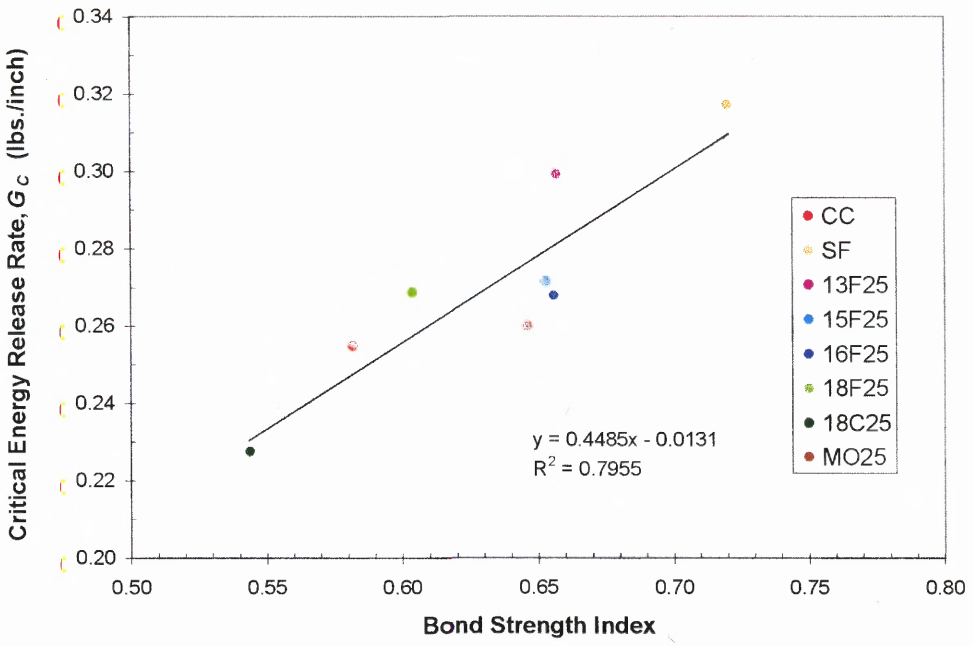

Figure 5.19 Relationship between G_C and Bond Strength Index

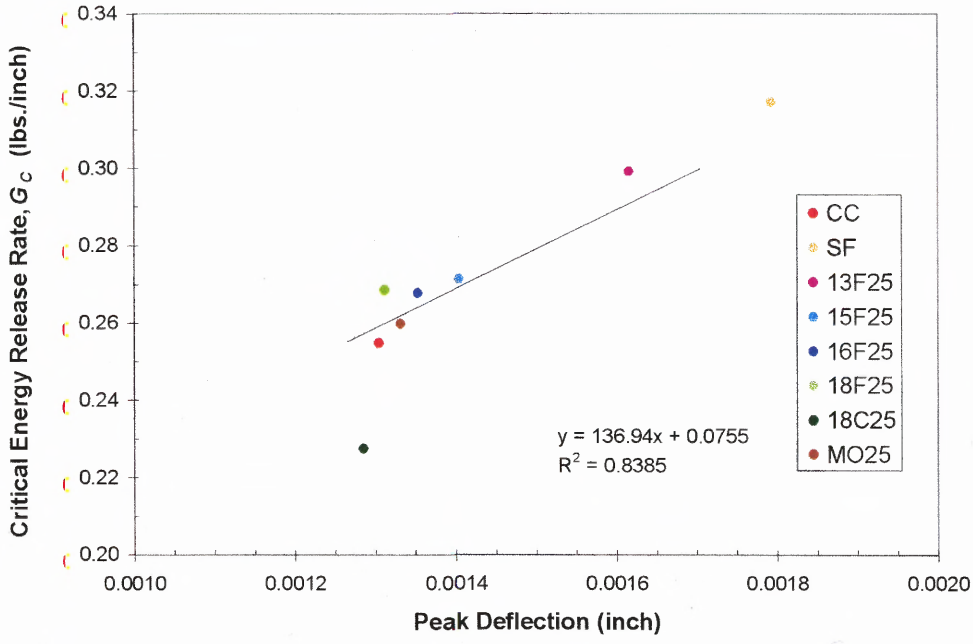

Figure 5.20 Relationship between G_C and Peak Deflection

Figure 5.18 presents the relationship between critical energy release rate (G_C) and the compressive strength for each concrete series tested. The relationship between G_C and bond strength index were plotted in Figure 5.19, while Figure 5.20 shows the relationship between G_C and the peak deflection from the notched beam tests.

Overall, the results from Figures 5.18, 5.19 and 5.20 show that the critical energy release rate (G_C), which is also a measure of fracture toughness can be expressed in terms of the compressive strength of concrete, the bond strength index and the peak deflection. The value of G_C tends to increase as the compressive strength and the bond strength index of concrete increases (see Figures 5.18 and 5.19). For the peak deflection from the notched beam tests (see Figure 5.20), G_C also increases with increasing peak deflection.

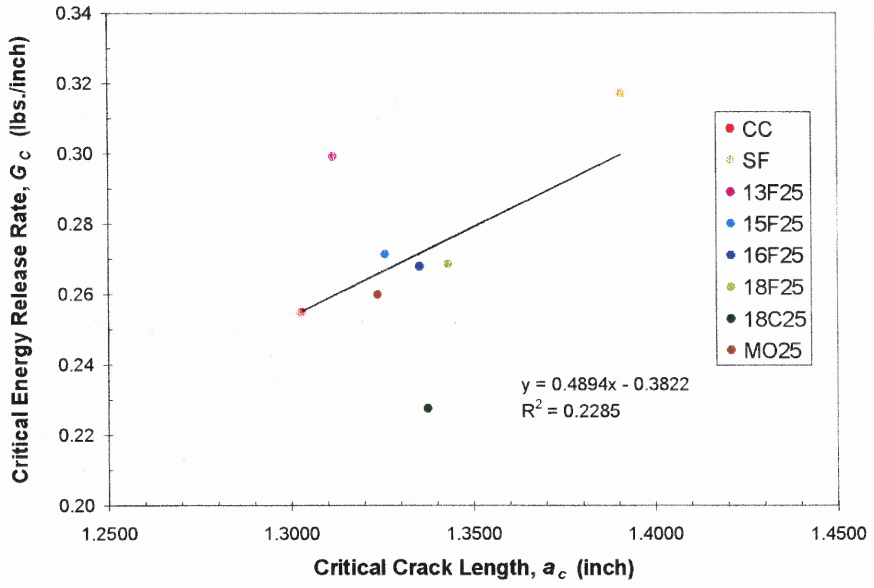

Figure 5.21 Relationship between G_C and Critical Crack Length

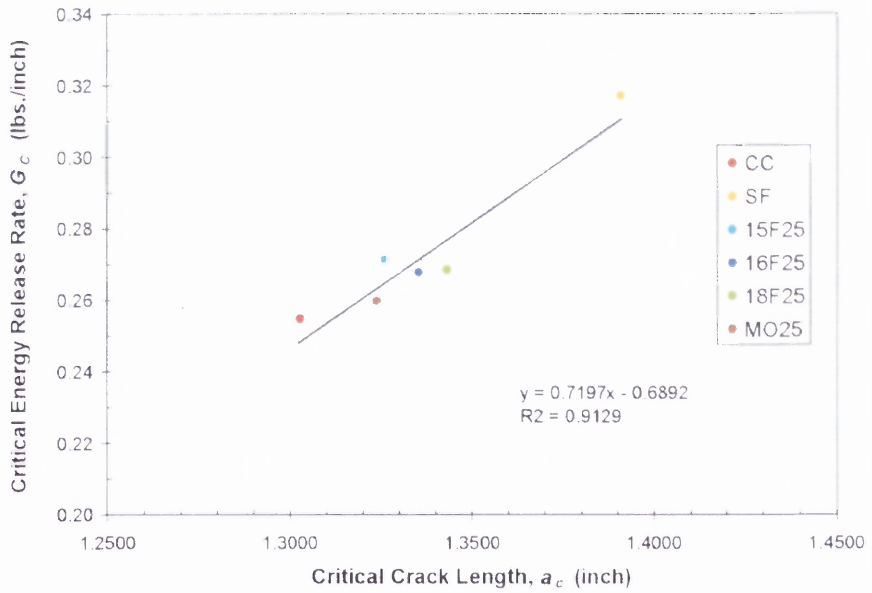

Figure 5.22 Relationship between G_C and Critical Crack Length (without the data for the specimens 13F25 and 18C25)

Figure 5.21 shows the relationship between critical energy release rate (G_C) and critical crack length (a_c). As can be seen, no relationship between G_C and a_c was observed. Interestingly, when the data for the 13F25 and 18C25 fly ash concretes were not included, the G_C seems to have a linear relationship with a_c (as shown in Figure 5.22). In general, G_C increases with increasing a_c (see Figure 5.22). Noticeably, the 13F25 fly ash concrete yields the second highest G_C (0.2990 lbs./inch) among the specimens tested even though it has the relatively small a_c as compared to the other specimens (see Figure 5.21). On the other hand, the 18C25 fly ash concrete yields the lowest G_C, regardless of its relatively large a_c. With these findings, it is worthwhile to revisit the basic material composition here in order to better understand its effects in the cement matrix. For the 13F fly ash, which has the finest particle size (see Figure 5.1), it tends to produce a more reactive pozzolanic compound and a better packing effect in the cement matrix that enhance the density and toughness of the cement composite. For the coarsest 18C fly ash,

which is large, porous and weak, it produces a lesser pozzolanic reaction and a lower density cement matrix as compared to other types of concrete, resulting in the lowest fracture toughness (G_C).

In case of fly ash concrete, the particle size of fly ash clearly shows its influence on the critical energy release rate of concrete (G_C), regardless of compressive strength. From Table 5.1 and Figures 5.1 and 5.2, and by sorting from the finest to the coarsest mean particle size of fly ash, the order of fly ashes are as follows: 13F, 15F, 16F, 18F, 18C and MO. By comparing this order of fly ash with that sorted by the value of the critical energy release rate, it can be seen that the critical energy release rate increases with the reduction of the particle size of fly ash. This indicates that the particle size of fly ash plays an important role on the critical energy release rate of concrete. The critical energy release rate of concrete can be improved by reducing the particle size of fly ash, when used as cement replacement.

In general, replacing cement by fine pozzolans such as silica fume and fly ash in the cement matrix can increase the stress intensity factor (K_{IC}) and the critical energy release rate (G_C) of concrete. Incorporating silica fume and fly ash in concrete can increase the density and reduce the thickness of the interfacial zone between cement matrix and aggregate, which results in a stronger interfacial bond strength. However, the modifications of the interfacial zone and the cement matrix affect the cracking characteristics and the deformation of concrete under loading, which consequently influence the brittleness behavior of concrete. Therefore, the quantification of brittleness is of interest to evaluate the effect of fine particle pozzolans on fracture behavior of concrete.

5.3.3 Brittleness

The increase in brittleness along with the compressive strength of concrete has prompted a series of discussion on how ductility of high performance concrete can be improved. It is essential to first establish a definition and measure of the brittleness. As mentioned in the previous section, the K_{IC} or G_C of concrete should, in fact, express the ability of the fracture process zone to resist crack growth, or to absorb the energy applied by the external load before unstable fracture occurs. Through this process, one may attempt to relate brittleness with the fracture behavior of composite. In this section, a fracture parameter called *the brittleness index* is proposed for evaluating the fracture toughness of concrete.

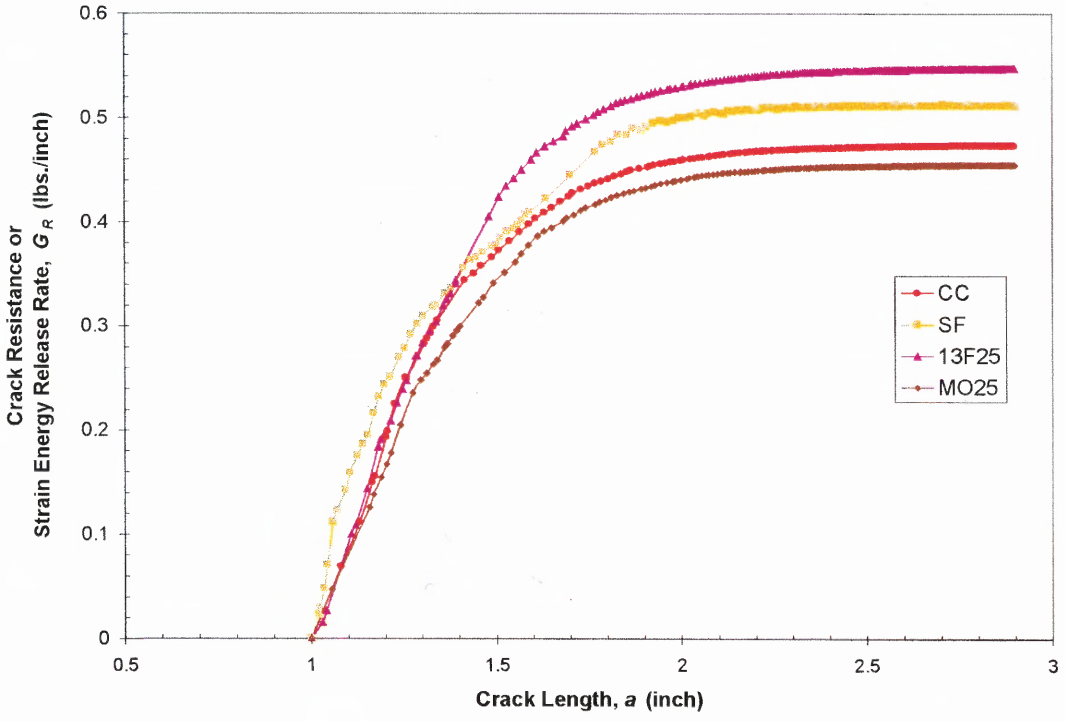

Figure 5.23a Effect of Fine Particle Pozzolans on *Resistance Curve* of Concrete

As described early in the theoretical development in Chapter 3, the *brittleness index*, developed in this study, is defined as slope of the *Resistance curve* (*R* curve) at peak load. Generally, the lower the brittleness index, the more brittle the material. The higher brittleness index means a tougher material. Considering that *R* curve is related to fracture behavior of the composite, it can easily be seen that its shape is related to the brittleness of the material.

Figure 5.23a shows the effect of fine particle pozzolans such as silica fume and fly ash on the *R* curves obtained from the proposed fracture model using the load-CMOD response. All other *R* curves for the concrete specimens studied are presented in Appendix C. For the *R* curves in Figure 5.23a, the vertical axis represents the crack resistance or so-called the energy release rate (G_R) whereas the horizontal axis represents the crack length during the fracture process. Referring to Section 2.3.4 and 3.5, G_R is the energy absorbed in the fracture process zone for crack propagation and equals the energy released per unit area of crack growth ($\Delta U / \Delta a$).

From Figure 5.23a, at the initial stage, *R* curve of silica fume concrete (SF) rose quickly with a steeper slope compared to other types of concrete. This means that SF absorbs more strain energy for crack extension than other types of concrete, and which results in a slower crack growth. Then, at the crack length (a) of 1.35 inches, approximately the same critical crack length (a_c) for all concrete tested, the slope of *R* curve for SF became less than other concretes. This means that the SF has lesser energy absorption capacity for crack extension than other concretes, resulting in a faster crack growth. After that, the *R* curve of SF rapidly became flat. On the other hand, *R* curves for other types of concrete are gradually reaching its steady state. This indicates that the

silica fume concrete is more brittle than other types of concrete and could mean a higher risk of catastrophic failures of material and structure. Overall, it seems to indicate that R curve can be a clear indication of fracture behavior of cementitious materials.

Table 5.33 Brittleness Index of Concrete and Other Related Parameters

Specimen Type	Compressive Strength f'_c (ksi)	Peak Load (Beam Tests) (pounds)	Fracture Energy (CMOD Method) (lbs./in)	Crititcal Crack Length (CMOD Method) (inch)	Critical Energy Release Rate (CMOD Method) (lbs./in)	Brittleness Index	
						CMOD Method	Deflection Method
CC	6.008	472	0.4390	1.3030	0.2547	0.7442	0.7280
SF	7.436	508	0.5183	1.3910	0.3170	0.4667	0.4704
13F25	6.786	493	0.5406	1.3118	0.2990	0.8233	0.8140
15F25	6.746	501	0.4723	1.3260	0.2712	0.7552	0.7745
16F25	6.768	509	0.4542	1.3354	0.2677	0.6201	0.6337
18F25	6.234	492	0.4516	1.3433	0.2685	0.6295	0.6309
18C25	5.620	429	0.3761	1.3376	0.2274	0.5170	0.5383
MO25	6.664	482	0.4602	1.3239	0.2597	0.6388	0.6429

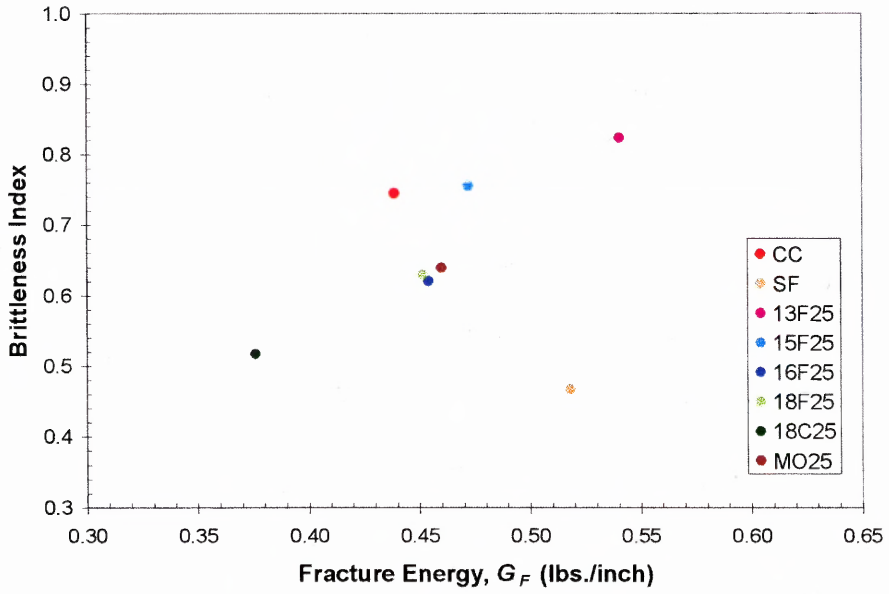

Figure 5.23b Relationship between Brittleness Index and Fracture Energy of Concrete

Details of empirical results from the notched beam tests and analytical results based on the proposed model for all concrete specimens tested have previously been presented in Tables 5.23 through 5.30. Table 5.33 presents the average value of the brittleness index for each type of concrete along with the related fracture parameters. The brittleness indices calculated by both the *Deflection Method* and the *CMOD Method* show no significant difference. Both methods showed similar trend in which the brittleness index is related to the fracture behavior of concretes. In this study, the value of brittleness indices were determined by means of the load-CMOD response for reasons of potential erroneous load-line deflection as described earlier. These values were correlated with other fracture parameters of the concretes.

Figure 5.23b shows the plots between the brittleness index and the fracture energy of concrete. From Table 5.33 and Figure 5.23b, the 13F fly ash concrete has the highest brittleness index of 0.8233, and in contrary the silica fume concrete has the lowest index of 0.4667. This means that the 13F fly ash concrete is the toughest material among all the concrete specimens tested. As expected, silica fume concrete, which has the highest compressive strength, is the most brittle material. Only the 13F25 fly ash concrete, which used the finest fly ash (the average particle diameter of 2.51 microns), has noticeably higher brittleness index than the control concrete (CC). It can be seen from Figure 5.23a that R curve of the 13F25 concrete continues to rise while R curves of the others become flat. The 15F25 fly ash concrete, made with the very fine fly ash (the average particle size of 3.72 microns), produces the brittleness index of 0.7552 similar to that of the control concrete (0.7442). The results shown seem to lead to the conclusion that very fine fly ash can improve the brittleness (or toughness) of concrete.

The results in Table 5.33 and Figure 5.23b also showed that fracture parameters such as fracture energy (G_F), critical energy release rate (G_C) and brittleness index, varied differently to different material characteristics. In many cases, while some of these parameters increase, the others decrease under the same loading environment. From the results, the silica fume concrete has the highest bond strength index and also the highest critical energy release rate (G_C) as compared to other materials (see Table 5.32). But silica fume concrete produces less toughness (or lower brittleness index) and lower G_F than the finest 13F fly ash. Due to the fact that brittleness is the fracture parameter expressing the post-peak behavior of concrete, this also implies that the 13F fly ash produces the toughest cement matrix. The above observations were mainly related to the cement matrix-aggregate interfacial bond and the microstructural heterogeneity in the concrete. It is generally believed that the enhanced interfacial bond is responsible for the brittleness of the silica fume concrete, and renders a more homogeneous microstructure, leading to rapid crack propagation after the peak load, and hence a lower G_F value.

For fly ash concrete, the above results reveal that replacing cement by the very fine fly ashes in the cement matrix has beneficial effects on the fracture behavior of concrete. According to the Zhang's model (Zhang 1995), fly ash cement paste can be considered as a multiphase composite material. The unreacted fly ash particles in the paste may act as micro-aggregates with higher modulus of elasticity than normal matrix of cement hydrates, which increase the resistance to crack propagation. Also, cracking around the fly ash particles results in more energy to be dissipated before failure (peak load). With these phenomena, the fracture process of fly ash concrete become less linear and the materials become tougher.

Typical high strength concrete has a matrix that is very strong and stiff, and possesses well-bonded mortar-aggregate interfaces. Due to its composition, several of the toughening mechanisms found in normal concrete are absent during the fracture process. Microcracking at interfaces, flaws and voids is infrequent, and cracks propagate through the coarse aggregates instead of being deflected by them. As its compressive strength increases concrete behaves more like a homogeneous material. This decrease in toughening leads to an increase in brittleness, an aspect that has largely been neglected in research. Designers have been forced to confine high strength concrete with steel in order to prevent catastrophical failure, especially under seismic loading. The brittleness could be further decreased by the addition of fibers, which provide considerable bridging and frictional energy dissipation during fiber pullout. Other remedies could include the modification of the aggregate-mortar interface properties as investigated in the present study. Obviously, a less brittle material would make design more economical and safer.

Overall, replacing cement by the very fine fly ashes (such as the fly ashes 13F and 15F that the average particle size is smaller than 3.72 microns) in the cement matrix can improve both the pre-peak and post-peak fracture behavior of concrete. For the pre-peak behavior, the critical energy release rate can be increased, and as for the post-peak behavior, the brittleness on the contrary can be reduced. In general, incorporating fly ashes in concrete increases the density and reduces the thickness of interfacial zone between cement matrix and aggregate, which results in the enhanced interfacial bond. Furthermore, the results also show that fly ashes can increase the density and improve the toughness of cement matrices.

5.4 Performance of the Proposed Model

5.4.1 Comparison with the Two-Parameter Fracture Model

Several investigators have applied linear elastic fracture mechanics (LEFM) principles to concrete, and concluded that fracture toughness and fracture energy of concrete increase with the compressive strength. This might have led some to assume that concrete becomes tougher as the strength increases. Using the two-parameter fracture model (TPFM), Jenq and Shah (1985) and Shah (1990) showed that along with the increase in critical stress intensity factor (K_{IC}) with compressive strength (f'_c) there was a considerable decrease in the pre-peak nonlinearity or the critical effective crack length (a_c). The results from the TPFM generally implies that the brittleness increases with f'_c.

In the present study, the fracture mechanics model based on the non-linear fracture mechanics was used to study the fracture behavior of high performance concrete. Table 5.34 shows the analytical results of the present study obtained from the proposed fracture mechanics model and the two-parameter fracture model (TPFM). Among the parameters listed are the compressive strength, the fracture energy, the critical crack length (a_c), the critical energy release rate (G_C) and the brittleness index.

In this section, comparisons of the fracture parameters obtained from the proposed fracture model and the two-parameter fracture model (TPFM) are presented. In evaluating the performance of the proposed fracture mechanics model, two fracture parameters, the critical crack length (a_c) and the critical energy release rate (G_C), obtained from the proposed model and the TPFM model are compared and discussed.

Table 5.34 Analytical Results from the Proposed Fracture Model and the TPFM Model

Specimen Type	Compressive Strength f'_c (ksi)	Fracture Energy G_F (CMOD Method) (lbs./in)	Critical Crack Length (a_c)		Critial Energy Release Rate (G_C)		Brittleness Index (Proposed CMOD Method)
			Proposed CMOD Method (inch)	TPFM Method (inch)	Proposed CMOD Method (lbs./in)	TPFM Method (lbs./in)	
CC -1	6.008	0.4733	1.2788	1.4075	0.2580	0.2806	0.7539
CC -2	6.008	0.4048	1.2967	1.3920	0.2492	0.2502	0.7542
CC -3	6.008	0.4389	1.3333	1.4651	0.2568	0.2947	0.7246
CC - avg.	**6.008**	**0.4390**	**1.3030**	**1.4215**	**0.2547**	**0.2752**	**0.7442**
SF -1	7.436	0.5109	1.3785	1.4080	0.3365	0.3106	0.4575
SF -2	7.436	0.4942	1.3706	1.3945	0.2906	0.3181	0.4645
SF -3	7.436	0.5498	1.4238	1.4015	0.3239	0.3518	0.4782
SF - avg.	**7.436**	**0.5183**	**1.3910**	**1.4013**	**0.3170**	**0.3268**	**0.4667**
13F25 -1	6.786	0.5468	1.3357	1.3776	0.3040	0.2797	0.8022
13F25 -2	6.786	0.5495	1.2521	1.3910	0.3006	0.2468	0.8197
13F25 -3	6.786	0.5254	1.3475	1.4053	0.2924	0.3354	0.8481
13F25 - avg.	**6.786**	**0.5406**	**1.3118**	**1.3913**	**0.2990**	**0.2873**	**0.8233**
15F25 -1	6.746	0.4427	1.3362	1.4307	0.2714	0.2676	0.7327
15F25 -2	6.746	0.4829	1.3327	1.3886	0.2714	0.3095	0.7540
15F25 -3	6.746	0.4914	1.3090	1.3710	0.2709	0.2678	0.7789
15F25 - avg.	**6.746**	**0.4723**	**1.3260**	**1.3968**	**0.2712**	**0.2816**	**0.7552**
16F25 -1	6.768	0.4149	1.3113	1.4618	0.2605	0.2604	0.6218
16F25 -2	6.768	0.4726	1.3660	1.3729	0.2777	0.2982	0.6233
16F25 -3	6.768	0.4752	1.3290	1.3715	0.2648	0.2995	0.6152
16F25 - avg.	**6.768**	**0.4542**	**1.3354**	**1.4021**	**0.2677**	**0.2861**	**0.6201**
18F25 -1	6.234	0.3877	1.3734	1.4202	0.2515	0.2730	0.6537
18F25 -2	6.234	0.5034	1.3254	1.4487	0.2764	0.2627	0.6305
18F25 -3	6.234	0.4636	1.3311	1.4153	0.2774	0.2788	0.6042
18F25 - avg.	**6.234**	**0.4516**	**1.3433**	**1.4281**	**0.2685**	**0.2715**	**0.6295**
18C25-1	5.620	0.4191	1.3030	1.4225	0.2368	0.1843	0.5324
18C25-2	5.620	0.3499	1.3483	1.5065	0.2278	0.2277	0.5080
18C25 -3	5.620	0.3592	1.3614	1.4504	0.2177	0.2515	0.5105
18C25 - avg.	**5.620**	**0.3761**	**1.3376**	**1.4598**	**0.2274**	**0.2211**	**0.5170**
MO25 -1	6.664	0.4144	1.3533	1.4527	0.2574	0.2792	0.6170
MO25 -2	6.664	0.5115	1.2784	1.3812	0.2545	0.2845	0.6767
MO25 -3	6.664	0.4547	1.3400	1.4156	0.2673	0.2644	0.6226
MO25 - avg.	**6.664**	**0.4602**	**1.3239**	**1.4165**	**0.2597**	**0.2760**	**0.6388**

5.4.1.1 Critical Crack Length: Based on the TPFM (Jenq and Shah 1985), the critical crack length (a_c) and the stress intensity factor (K_{IC}) are two material properties defined according to the elastic behavior of the material response (initial compliance and unloading compliance) without any consideration of the fracture process zone. Due to the fact that higher strength concrete generally behaves more like a homogeneous material, this phenomenon can be confirmed from the values of S_1, which is the slope in the elastic range of the deflection vs. crack-mouth-opening displacement curve. From Table 5.22, S_1 of silica fume concrete (SF) is higher than that of the other concretes. This means that in the elastic range and at the same amount of beam deflection, the crack growth in the silica fume concrete is less than that in other types of concrete.

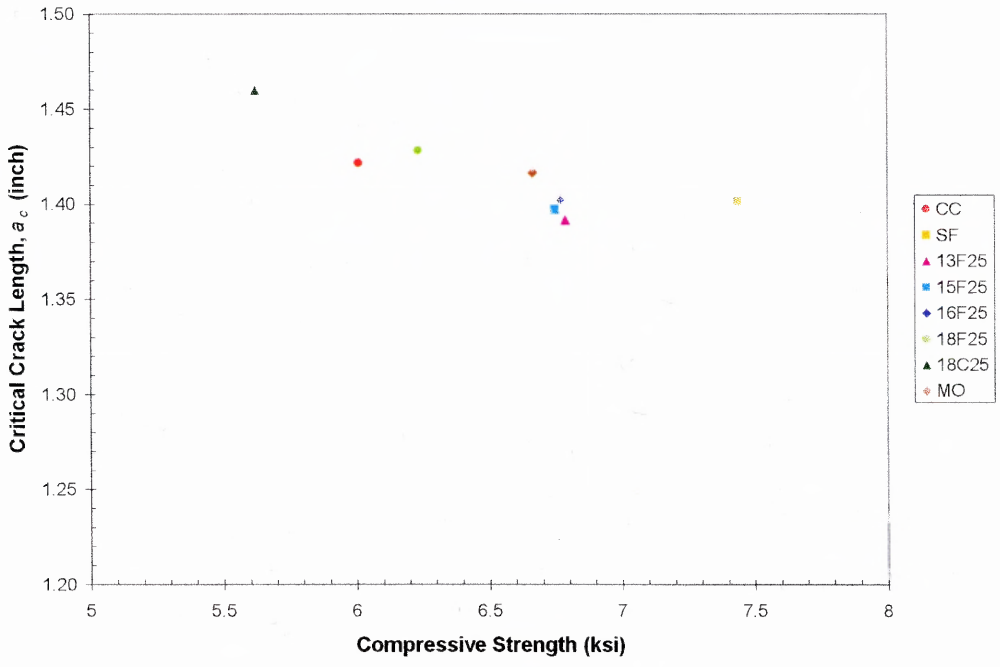

Figure 5.24 Relationship between Critical Crack Length and Compressive Strength of Concrete (from TPFM Model)

Figure 5.24 shows the plots between the critical crack length (a_c), computed based on the TPFM model, and the compressive strength (f'_c) for all concretes tested in this study. From Figure 5.24, the results from the TPFM model show the same trend as suggested by Shah (1990) that there was a decrease in the pre-peak nonlinearity or the critical crack length (a_c) when f'_c increases, and the smaller of a_c means a more brittle material. The results from the TPFM model for the concretes tested in this study indicated that the brittleness of concrete increased with increasing compressive strength. With modern materials science technology, the modification of the cement matrix-aggregate interfaces can possibly produce high strength concretes, which are also less brittle. Obviously, without considering the non-linear behavior of the fracture process zone, which is quite sensitive to the changes of cement matrix-aggregate interfaces, the TPFM model may not be suitable for studying the fracture behavior of high performance concrete.

Based on the proposed fracture mechanics model (presented in Chapter 3), the critical crack length (a_c) is calculated based on both the elastic and the inelastic parts of the material response taking into account the effect of the fracture process zone. With modification on the test setup in order to accurately measure deflection and CMOD, the model proposed has the proper rationale to deal with the fracture process zone and is more appropriate for fracture study of concrete. The proposed model predicts the fracture behavior of concrete in terms of the applied load and a function of crack growth. The energy release rate (G_R) as a function of crack length is also evaluated and used to quantify the brittleness of cementitious materials.

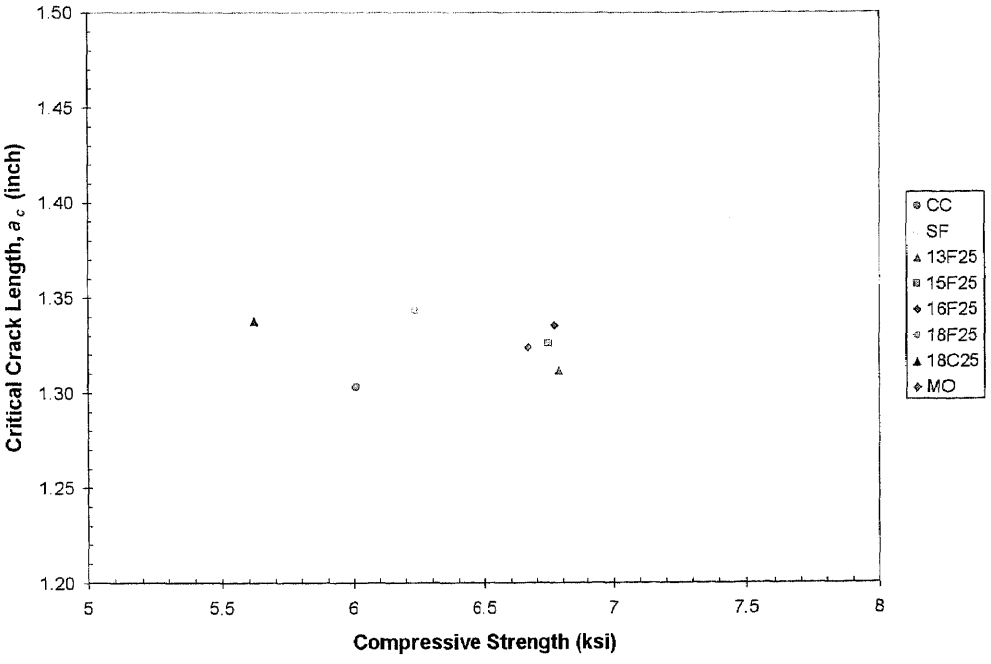

Figure 5.25 Relationship between Critical Crack Length and Compressive Strength of Concrete (from the Proposed Model)

Figure 5.25 shows the relationship between the critical crack length (a_c), computed based on the proposed model, and the compressive strength (f'_c). From Figure 5.25, the results contradicts the suggestion by Shah (1990) that there was a decrease in the critical effective crack length (a_c) when the f'_c increases. Instead, a constant crack length was observed as the compressive strength increases. The results from the proposed model show that the control concrete (CC) and the fly ash concrete yield the comparable values of a_c, while the silica fume concrete (SF) has a noticeably higher a_c than other types of concrete. It should be noted that, from Table 5.11b, the silica fume has the highest bond strength index (0.720) as compared to other types of concrete tested (ranging from 0.544 to 0.657). This means the silica fume concrete has the most well-

bonded cement matrix-aggregate interface. Furthermore, from Table 5.34, the silica fume concrete also has the lowest brittleness index (0.4667) among all the concretes tested (ranging from 0.5170 to 0.8233). The lowest brittleness index implies that it is the most brittle material.

Taking into consideration that the average size of coarse aggregate used in the present study is 3/8 inches (0.375 inches), only the silica fume concrete (SF) yields the average critical crack growth of 0.3910 inches, which is more than the average size of the coarse aggregate. Note that the initial notch length is 1.0 inch, and the critical crack length of silica fume concrete (SF) is 1.3910 inches, therefore its critical crack growth is 0.3910 inches. The control concrete (CC) and the fly ash concrete yield the critical crack growth ranging from 0.3030 to 0.3433 inches, which are less than the average size of the coarse aggregate (0.375 inches). During the fracture process, the critical state of stresses develops within the fracture process zone causing microcracking in front of the crack tip. This consumes energy that decreases the energy release rate (G_R) available for crack propagation. The effect is commonly known as toughening or crack shielding.

From our test results, for silica fume concrete, due to the strong bond between cement matrix and coarse aggregate, the cracks tend to penetrate straight through the coarse aggregates rather than deflect around them. The straight crack through coarse aggregate, which is a tougher homogenous material consumes higher energy (G_R) to propagate than the crack that goes through the cement matrix-aggregate interface. At the moment of fracture (at the peak load), the coarse aggregate releases the energy (G_R), absorbed while resisting the crack from propagating at a shorter time period resulting in a larger critical crack length (a_c) and an abrupt brittle fracture of the structure.

On the other hand, for the control and the fly ash concrete, due to the weaker cement matrix-coarse aggregate interface compared to those the silica fume concrete, the cracks tend to deflect to the path of least resistance, which is along the interface or around the coarse aggregate particles. Since the cement matrix-coarse aggregate interface, considered to be non-homogeneous, is weaker than the coarse aggregate, the non-planar crack along the interface gradually consumes G_R, and slowly propagates during fracture, resulting in a more stable crack propagation.

However, it is not recommended to determine the brittleness of material based only on the value of the critical crack length (a_c) because a_c alone does not reflect the overall brittleness and energy absorptive capacity of the material. The R curve, which expresses the relationship between the energy release rate (G_R) and the crack extension, is a better indicator for the toughening behavior of concrete. The results of the brittleness of concrete determined based on the R-curve were previously discussed in Section 5.3.4.

5.4.1.2 Critical Energy Release Rate: In this study, the critical energy release rate (G_C) is used instead of the critical stress intensity factor (K_{IC}) to determine the fracture toughness of concrete. This is due to the fact that that G_C is closely related to K_{IC}, and furthermore, the proposed model presented a fracture toughness parameter in term of G_C. As described in Chapter 2, G_C is equal to $(K_{IC})^2/E$, where E is the modulus of elasticity of concrete, presented in Table 5.12. Table 5.34 shows the analytical results of the present study obtained from the proposed fracture mechanics model and the TPFM model.

Based on the TPFM model (Jenq and Shah 1985), G_C is a material property defined according to the elastic part of the material response without consideration of

fracture process zone. It was derived on the assumption of an equivalent crack length and based on the initial compliance, unloading compliance, initial notch depth and the peak load. Figure 5.26 shows the relationship between the critical energy release rate (G_C) obtained from the TPFM model and the compressive strength of concrete (f'_c), while Figure 5.27 shows the relationship between the average value of G_C obtained from the TPFM model and the compressive strength of concrete (f'_c).

Based on the proposed fracture mechanics model, the critical energy release rate (G_C) was calculated based on both the elastic and inelastic parts of the material response taking into account the effect of the fracture process zone. The proposed model presents the fracture behavior in the terms of the energy release rate (G_R) and a function of crack length (a) or so-called R curve. The value of G_R at the peak load or at the on-set of critical crack growth is defined as the critical energy release rate, G_C.

Figure 5.28 shows the relationship between the critical energy release rate (G_C) obtained from the proposed model and the compressive strength of concrete (f'_c), and Figure 5.29 shows the relationship between the average value of G_C obtained from the proposed model and the compressive strength of concrete (f'_c).

From Table 5.34 and Figures 5.26, 5.27, 5.28 and 5.29, the results from both the TPFM and the proposed model show the similar trend that G_C increases with increasing f'_c. The values of G_C obtained from the TPFM show more scatter than that of the proposed model. This may be because of the way G_C was obtained in the TPFM as a function of the peak load, initial compliance (C_i) and unloading compliance (C_u), and a testing procedure by which a stable unloading at the peak load was required (see Section 2.4.3). The stable unloading at the peak load is rather difficult to perform and that may be

the source of potential erroneous unloading compliance (C_i) causing error and scattering of the G_C calculated by the TPFM (see Figure 5.26). Overall, the results of G_C obtained from the proposed fracture model compare favorably and in agreement with those calculated from the TPFM model.

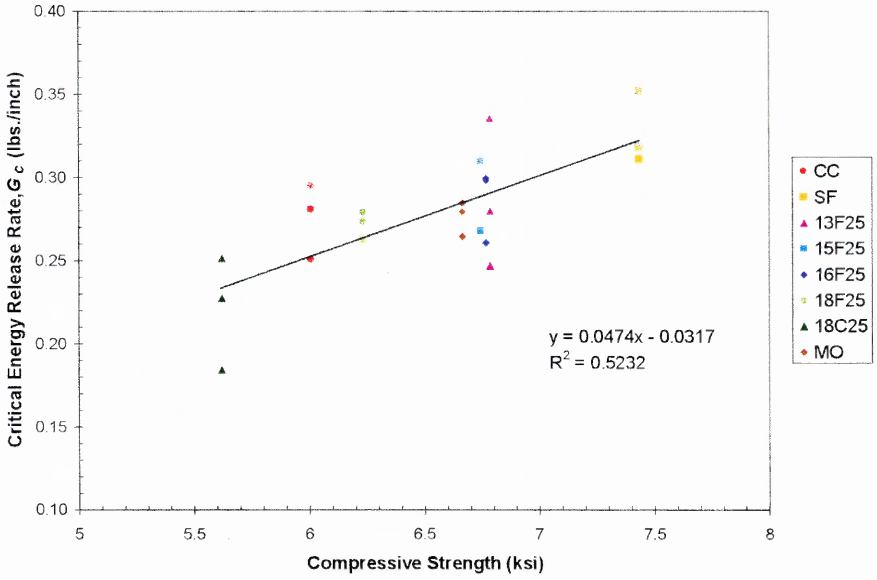

Figure 5.26 Relationship between Critical Energy Release Rate and Compressive Strength of Concrete (from TPFM Model)

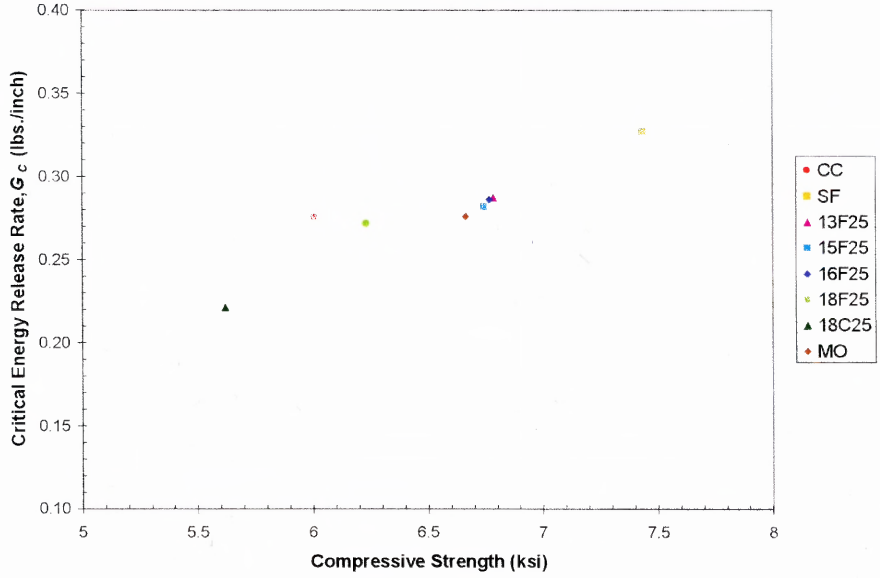

Figure 5.27 Relationship between Average Critical Energy Release Rate and Compressive Strength of Concrete (from TPFM Model)

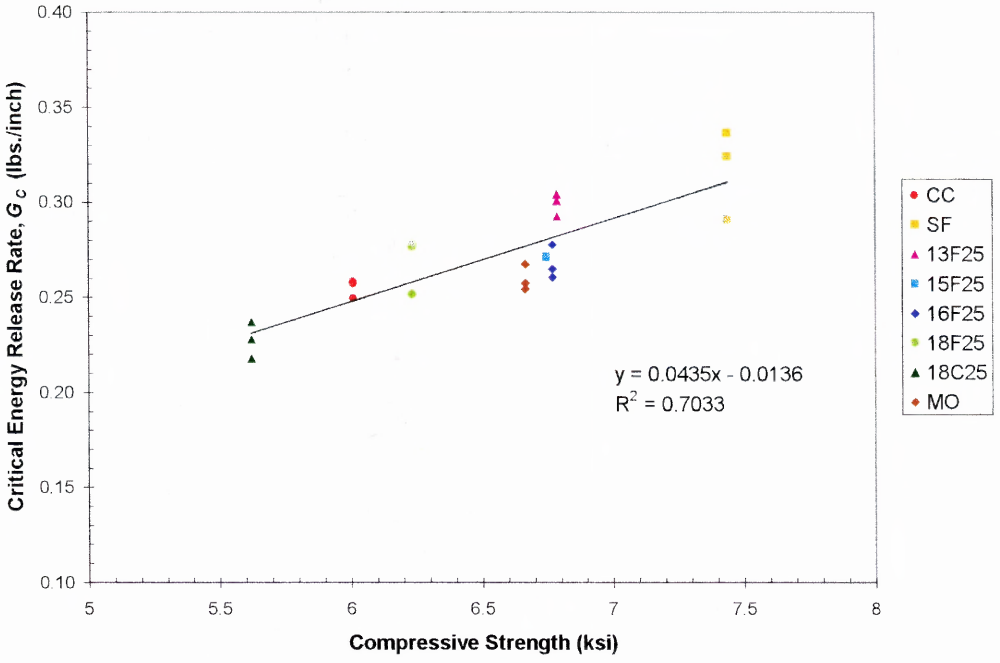

Figure 5.28 Relationship between Critical Energy Release Rate and Compressive Strength of Concrete (from the Proposed Model)

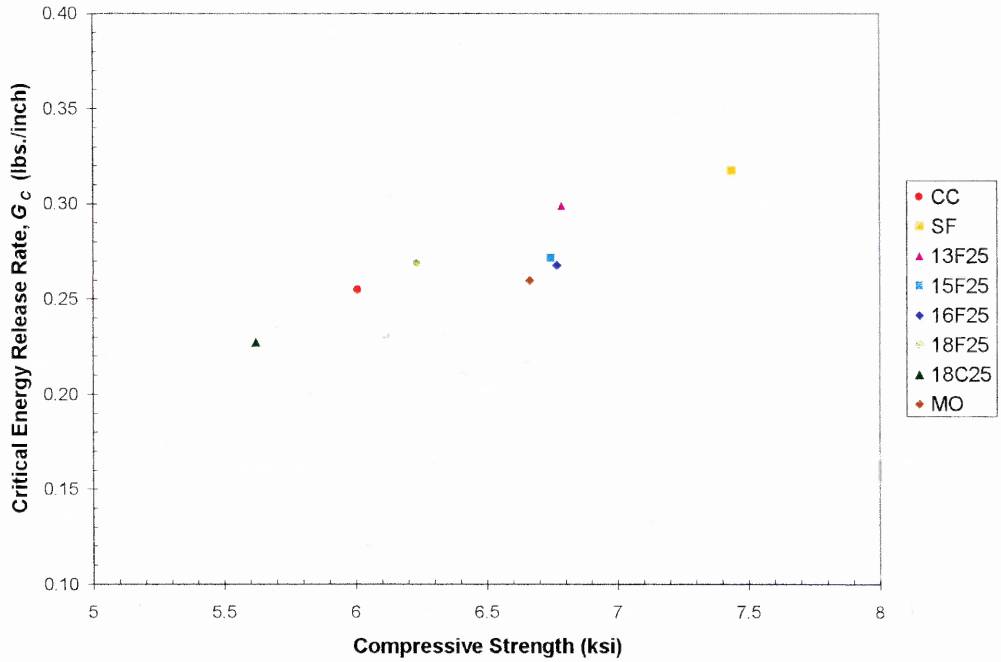

Figure 5.29 Relationship between Average Critical Energy Release Rate and Compressive Strength of Concrete (from the Proposed Model)

5.4.2 Comparison with Test Results of Other Researchers

In this section, test data and analytical results of other researchers were used to compare with those predicted by the proposed fracture mechanics model. Although a large number of the fracture tests of concrete have been reported in the literature, the corresponding load vs. deflection responses and load vs. crack-mouth-opening displacement (CMOD) responses of the notched beams were rarely published in details. As mentioned previously, error in load-line deflection measurement greatly affects the fracture energy (G_F) and the fracture parameters such as the critical crack length (a_c), the critical stress intensity factor (K_{IC}) and the critical energy release rate (G_C). Test data referred to in this section were selected to highlight the importance of the accurate measurement of the load-line deflections and also to verify the validity of the proposed fracture mechanics model. The selected test series were from:

1. Jenq and Shah (1985) for normal strength concrete

   Two concrete beams, JS1 and JS2, were made with a mix-proportion by weight of 1: 2.6: 2.6: 0.65 of cement, sand, coarse aggregate and water. The maximum aggregate size was 3/4 inches. The dimensions of the beams are shown in Table 5.35.

2. Ratanalert and Wecharatana (1989) for medium strength mortar

   Two mortar beams, RW1 and RW2 were made with a mix proportion by weight of 1: 2.6: 0.45 of cement, sand and water. The maximum aggregate size was 3/8 inches. The dimensions of the beams are listed in Table 5.35.

3. Gopalaratnam and Ye (1991) for plain concrete model

   A plain concrete beam, GY1, was modeled by a numerical model and the finite element method. The dimensions of the beam are shown in Table 5.35.

Common test data from these literatures needed to implement the proposed model are the load vs. deflection curves and load vs. CMOD curves of the notched beam specimens. The procedure to apply the proposed model for studying the behavior of material during fracture process can be briefly described as follows:

1. *Determination of crack growth due to applied load*

The crack growth (Δa) at any instant of time Δt, under the applied load P, can be determined by using the following expression:

$$\Delta a = \frac{1}{G_F B}\left(S_1 \int_0^{CMOD_P} PdCMOD + S_2 \int_{CMOD_P}^{CMOD} PdCMOD \right) \tag{5.3}$$

where $S_1 = (d\delta / dCMOD)$, the slope of the deflection-CMOD curve in the linear elastic region; $S_2 = (d\delta / dCMOD)$, the slope of the deflection-CMOD curve in the post-peak region. The region between the linear elastic range and post-peak response is approximated by extrapolating both the slopes S_1 and S_2 till they intersect, which is represented by $CMOD_P$, as shown in Figure 3.2(b). B = the width of the beam, and G_F = the fracture energy (a material property), which can be calculated from:

$$G_F B(D - a_0) = S_1 \int_0^{CMOD_P} PdCMOD + S_2 \int_{CMOD_P}^{\infty} PdCMOD \tag{5.4}$$

where D is the depth of the beam and a_0 is the pre-notched or initial crack length.

2. *Determination of energy release rate or R curve*

The energy release rate (G_R) at any instant of time during the fracture process can be determined by the following expression:

$$G_R = \frac{1}{B\Delta a}\left[S_1 \int_0^{CMOD_P} PdCMOD + S_2 \int_{CMOD_P}^{CMOD} PdCMOD \right] - \frac{S_1}{B\Delta a}\left[\frac{P^2}{2K_i^{CMOD}} \right] \tag{5.5}$$

where K_i^{CMOD} is the initial stiffness of the beam determined from the slope of the load-CMOD curve. By knowing Δa, P, S_1, S_2 and the area under *P-CMOD* curve at any instant of time, G_R at that instant can be determined. Note that details of the theoretical development were described in Chapter 3.

Table 5.35 Results for Three-Point-Bend Notched Beam Tests of Other Researchers along with the Analytical Results by the Proposed Model

Specimen Type	Beam Dimensions S x B x D x a_0 (inch)
JS1	24 x 2.25 x 6 x 1.94
JS2	12 x 1.125 x 3 x 0.88
RW1	22.5 x 2 x 6 x 1.88
RW2	8 x 2 x 2 x 0.94
GY1	48 x 4 x 12 x 2.00

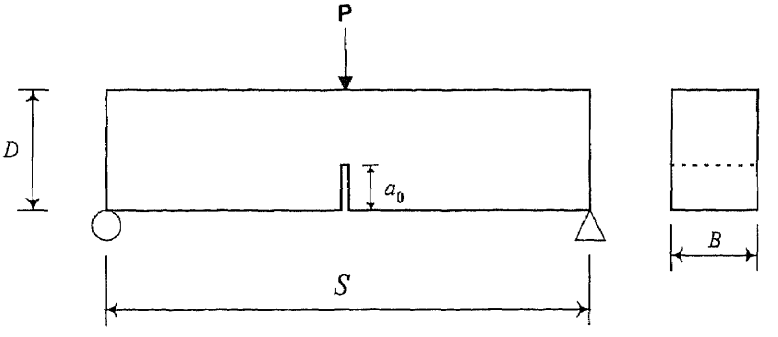

Specimen Type	S_1 or Initial Slope of Deflection - CMOD curve		G_F		a_c		G_C	
	Refer to Literature	Proposed Model	Refer to Literature (lbs./in)	Proposed Model (lbs./in)	Refer to Literature (inch)	Proposed Model (inch)	Refer to Literature (lbs./in)	Proposed Model (lbs./in)
JS1	1.087	1.087	0.506	0.506*	3.055	3.002	0.362	0.381
JS2	1.324	1.324	0.378	0.378*	1.600	1.625	0.313	0.307
RW1	2.678	1.270	0.290	0.206	N.A.	3.737	0.112	0.127
RW2	3.184	1.270	0.370	0.282	N.A.	1.109	0.104	0.105
GY1	2.441	1.270	0.300	0.300+	4.290	4.184	N.A.	0.144

* The load-deflection curves were not modified by the proposed model, and therefore G_F were not re-calculated.

+ The load-deflection curve was modified by the proposed model, but G_F, which is a given material property for the model in the literature, was not altered.

Table 5.35 shows the results for the three-point-bend notched beam tests of the other researchers along with the analytical results predicted by the proposed model. For the compatibility of specimen geometry, all of the beams referred here have the ratio between span length to beam depth ratio (S/D) of approximately or equal to 4, which is the same as S/D of the beam tested in the present study (see Table 5.35).

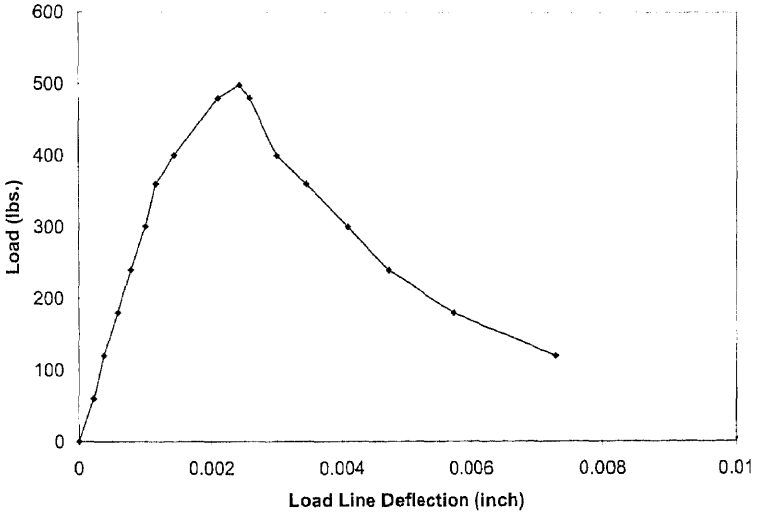

Figure 5.30a Load-Deflection Relationship of Beam JS1 (Jenq and Shah 1985)

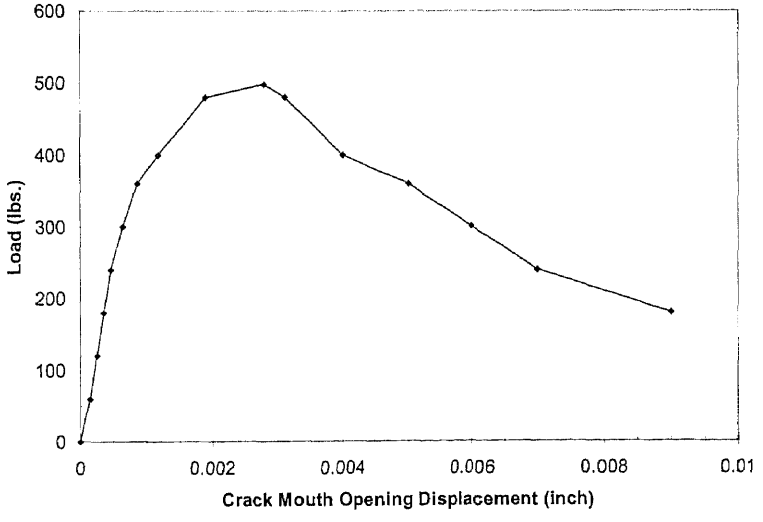

Figure 5.30b Load-CMOD Relationship of Beam JS1 (Jenq and Shah 1985)

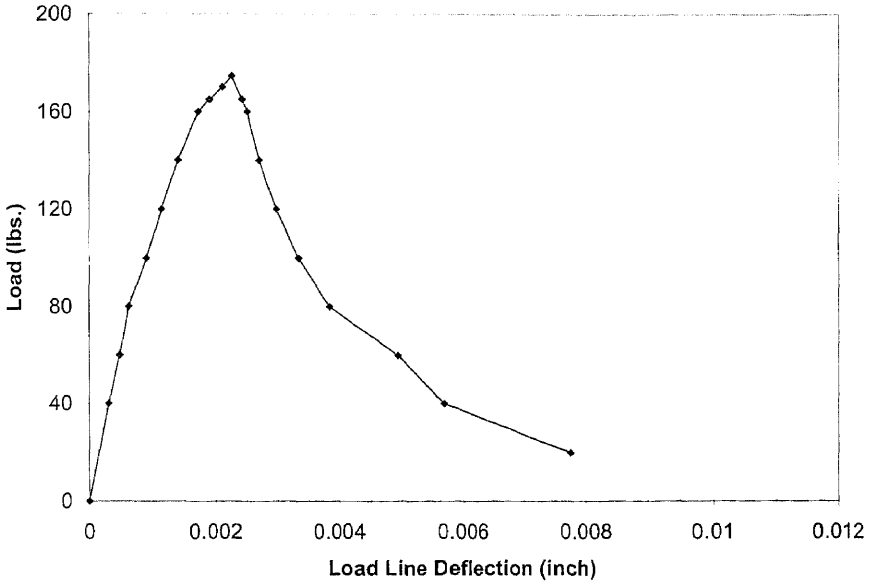

Figure 5.31a Load-Deflection Relationship of Beam JS2 (Jenq and Shah 1985)

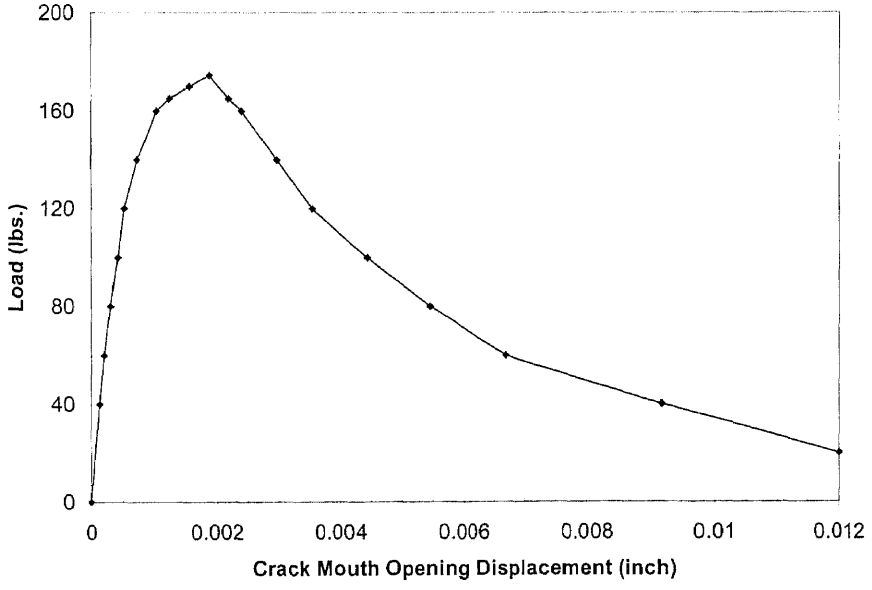

Figure 5.31b Load-CMOD Relationship of Beam JS2 (Jenq and Shah 1985)

Figures 5.30 and 5.31 present the test data adapted from Jenq and Shah's study (1985) for the concrete beam JS1 and JS2 respectively. The fracture parameters, the critical crack length (a_c) and the critical energy release rate (G_C), in the literature were calculated based on the Two Parameter Fracture Model (TPFM) using the relationships from the load vs. crack mouth opening displacement (CMOD) curves. For comparisons, the proposed fracture mechanics model was implemented using the referred data to determine the above mentioned fracture parameters.

Figures 5.32 and 5.33 show the deflection-CMOD relationships of the beams JS1 and JS2 respectively. From Table 5.35, the results of S_1 or the initial slope of deflection-CMOD curve for JS1 and JS2 beam tests are 1.087 and 1.324 respectively, which are similar to the S_1 of 1.270 for the control concrete (CC) beam tested in the present study. With a bilinear behavior shown, this tends to indicate that the load-line deflection measurements from these tests seem to be accurate.

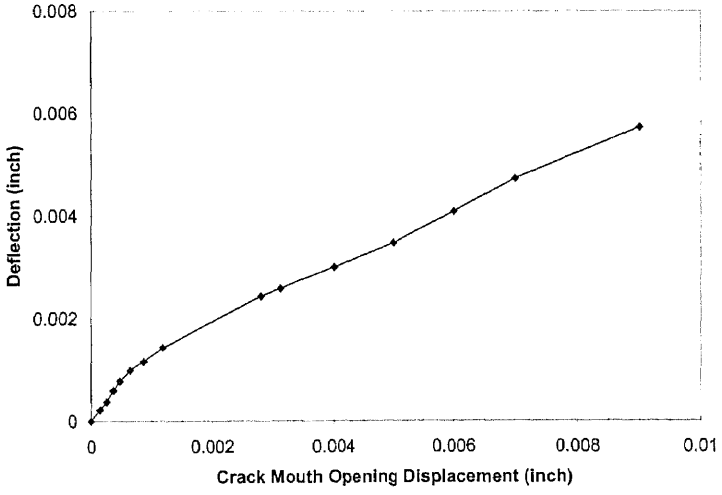

Figure 5.32 Deflection-CMOD Relationship of Beam JS1

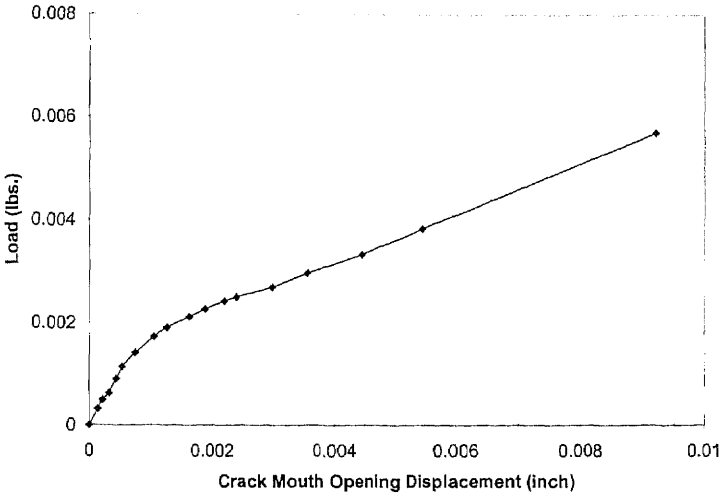

Figure 5.33 Deflection-CMOD Relationship of Beam JS2

For the beam JS1, the analytical results of the load vs. crack length relationship of beam JS1 obtained by the proposed model is shown in Figure 5.34. From Table 5.35, the critical crack length (a_c) of 3.002 inches predicted by the proposed model compares favorably with 3.055 inches reported by Jenq and Shah (1985), whereas the critical energy release rate (G_C) of 0.381 lbs./inch also agrees well with the 0.362 lbs./inch reported in the literature.

For the beam JS2, the fracture parameters predicted by the proposed model have the critical crack length (a_c) of 1.625 inches which is closed to the 1.600 reported, and the critical energy release rate (G_C) of 0.307 lbs./inch is in good agreement with the 0.303 lbs./inch from the reference. Figure 5.35 shows the analytical results of load vs. crack length relationship of beam JS2 obtained by the proposed model. From the results discussed above, the material behavior and the fracture parameters obtained by the proposed model are found to be in good agreement with those from the literature (see Table 5.35).

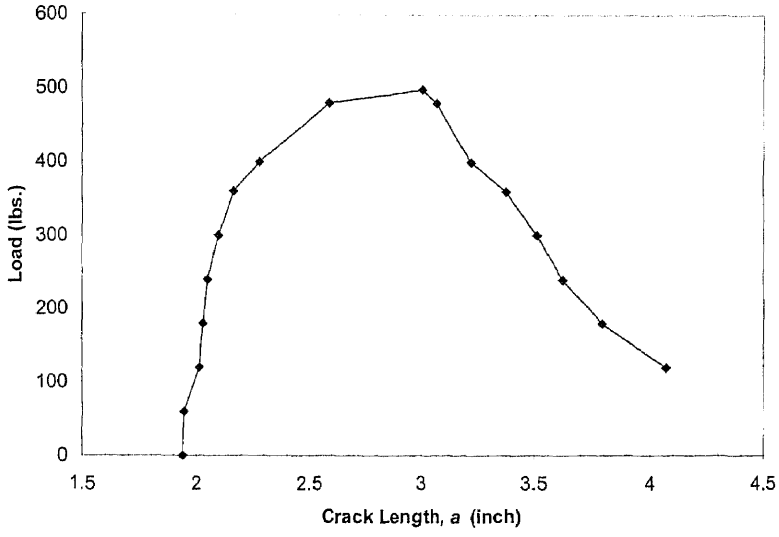

Figure 5.34 Load-Crack Length Relationship of Beam JS1

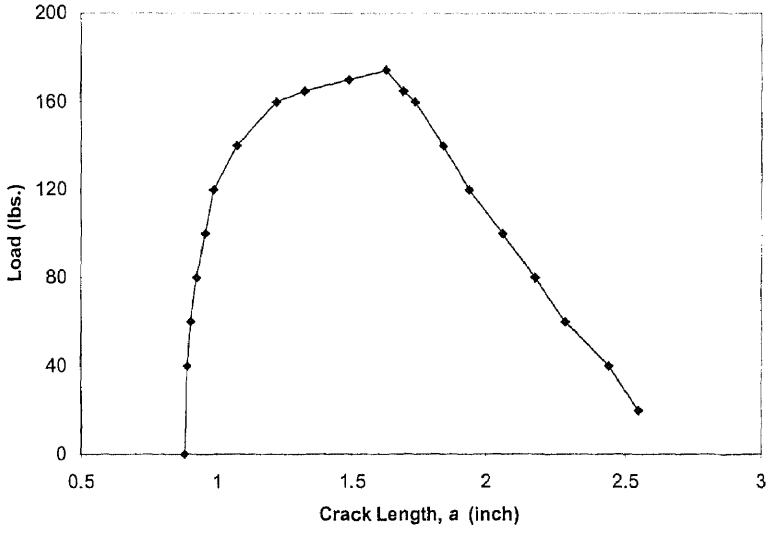

Figure 5.35 Load-Crack Length Relationship of Beam JS2

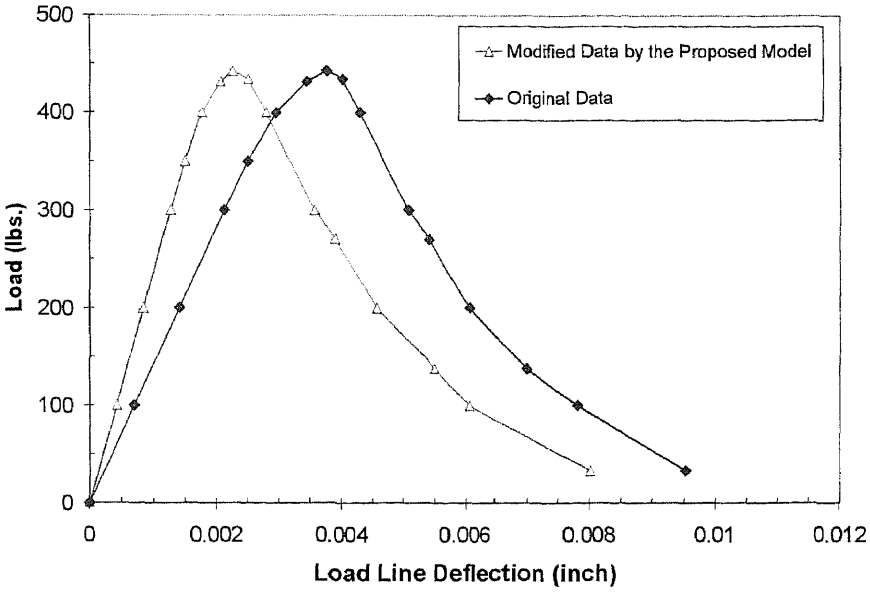

Figure 5.36a Load-Deflection Relationship of Beam RW1
(Ratanalert and Wecharatana 1989)

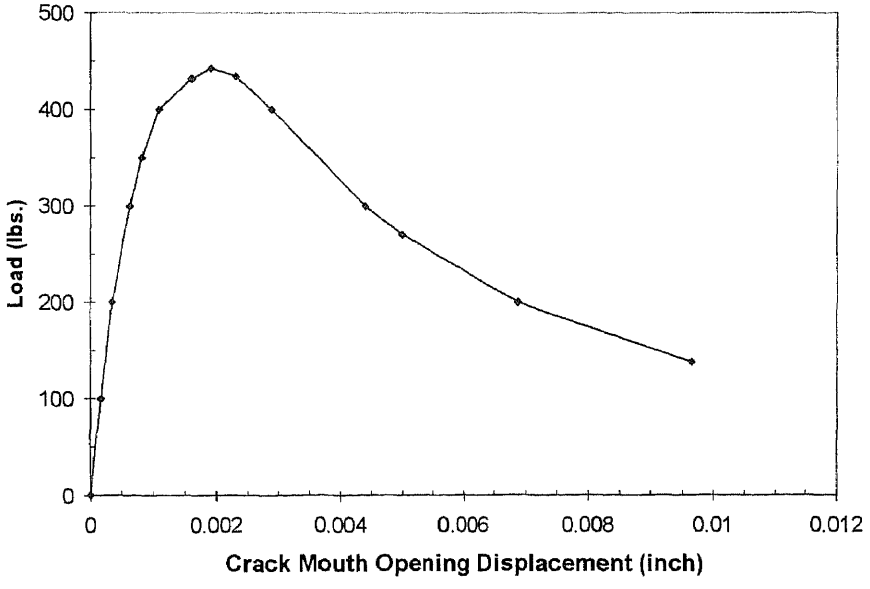

Figure 5.36b Load-CMOD Relationship of Beam RW1
(Ratanalert and Wecharatana 1989)

In Figures 5.36 and 5.39, test data adapted from the study of Ratanalert and Wecharatana (Ratanalert and Wecharatana 1989) are presented. In their study, the critical energy release rate (G_C) was also calculated by applying the TPFM model. For the mortar beam RW1, by using the original load-deflection curve and the load-CMOD curve from the literature as shown in Figure 5.36, the G_C calculated by the proposed model is 0.278 lbs./inch, which is noticeably higher than the G_C of 0.112 lbs./inch found in the literature. With reference to the proposed model, the G_C can be calculated from the load vs. CMOD curve when the value of S_1 is known (see Chapter 3). From Table 5.35, the value of S_1 for the beam RW1 calculated from the original data is 2.678, which is higher than S_1 of 1.270 for the normal strength concrete (CC) obtained in the present study (see Table 5.22). This indicates that the deflection could be inaccurately measured. Therefore, in the present study, the original load vs. deflection curve was modified to have S_1 equal to 1.270 in order to investigate the effect of the deflection measurement on determination of the fracture behavior. Figure 5.37 shows the deflection-CMOD relationships (S_1 and S_2) of the beam RW1 for the original data and the data modified by the proposed model.

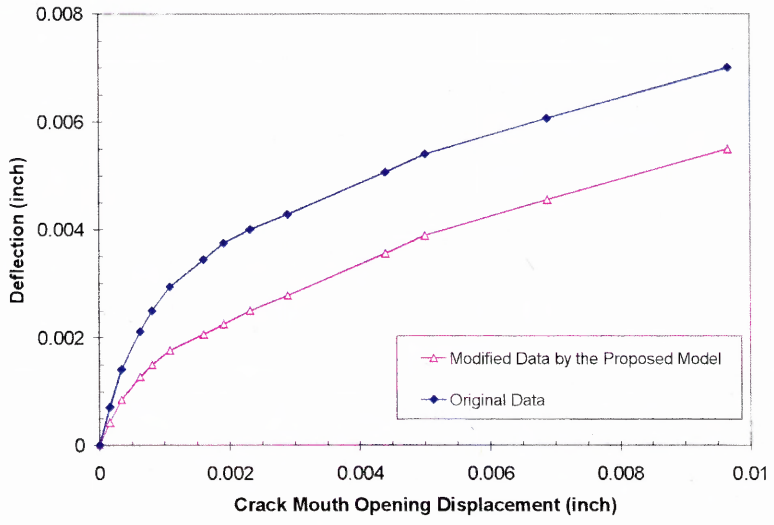

Figure 5.37 Deflection-CMOD Relationship of Beam RW1

By using the data from the modified load-deflection curve and the original load-CMOD curve for the beam RW1 as shown in Figure 5.36, the value of G_C obtained by the proposed model was 0.127 lbs./inch, which compares favorably with the G_C of 0.112 lbs./inch in the literature. Furthermore, from table 5.35, the fracture energy (G_F) reported in their study was 0.290 lbs./inch, which is about 30% higher than the G_F calculated by the modified load-deflection curve. Figure 5.38 shows the analytical results of the load vs. crack length relationship of beam RW1 obtained by the proposed model. It is interesting to note that, from Figure 5.36a, the difference between the measured peak deflection in the literature (0.00375 inches) and that of the modified curve (0.00224 inches) is more than 65%. The above results indicate that the deflection measurements reported in the literature possibly included the erroneous deflections caused by concrete crushing at the supports and/or the method of measurement.

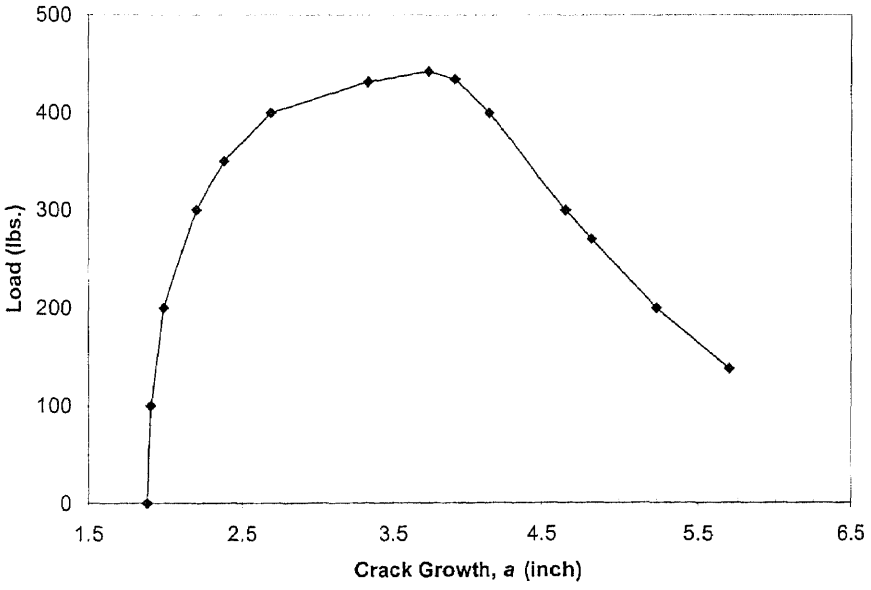

Figure 5.38 Load-Crack Length Relationship of Beam RW1

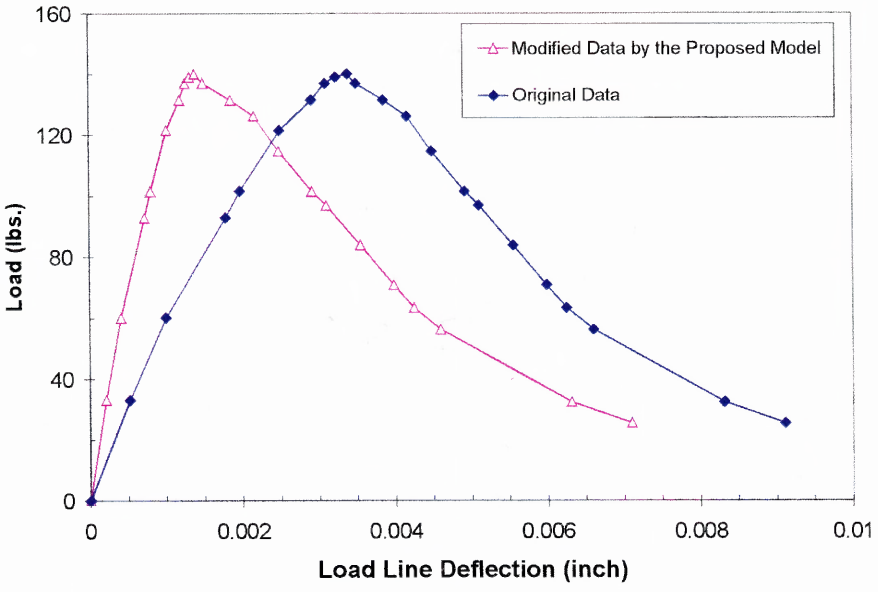

Figure 5.39a Load-Deflection Relationship of Beam RW2 (Ratanalert and Wecharatana 1989)

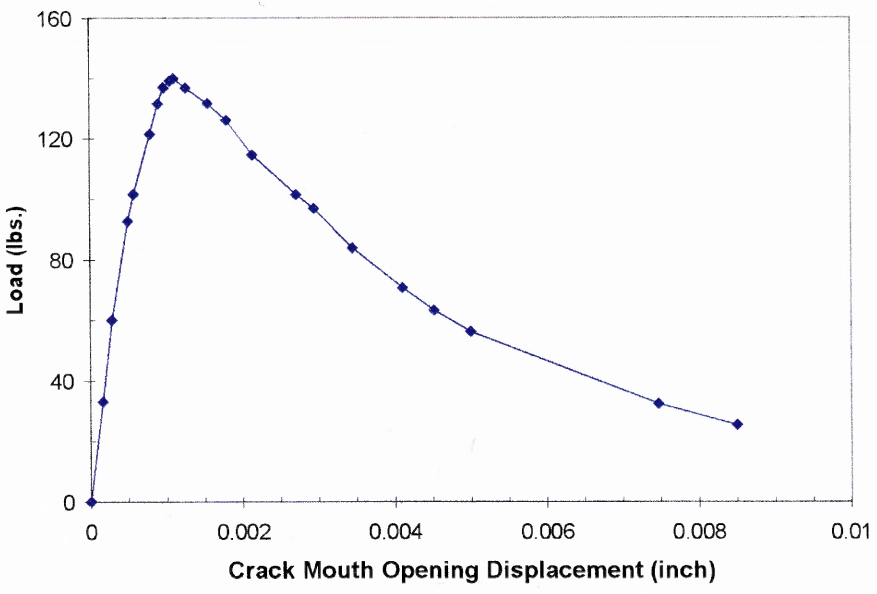

Figure 5.39b Load-CMOD Relationship of Beam RW2 (Ratanalert and Wecharatana 1989)

For the other mortar beam, RW2, by using the original load-deflection curve and load-CMOD curve from the literature as shown in Figure 5.39, the G_C calculated by the proposed model is 0.173 lbs./inch, which is noticeably higher than the G_C of 0.104 lbs./inch found in the literature. However, it is noted that from Table 5.35, the value of S_1 for the mortar beam RW2 calculated from the original is 3.184, which is noticeably higher than S_1 of 1.270 for normal strength concrete (CC) obtained in the present study (see Table 5.22). This again indicates that the deflection of the beam RW2 could be inaccurately measured as well. Therefore in the present study, the original load-deflection curve was modified so S_1 equal to 1.270. The modified responses were then used to study the effect of the deflection measurement on fracture behavior of material as well as to evaluate the performance of the proposed model. Figure 5.40 shows the deflection-CMOD relationship of beam RW2 from the original data and that from the data modified by the proposed model.

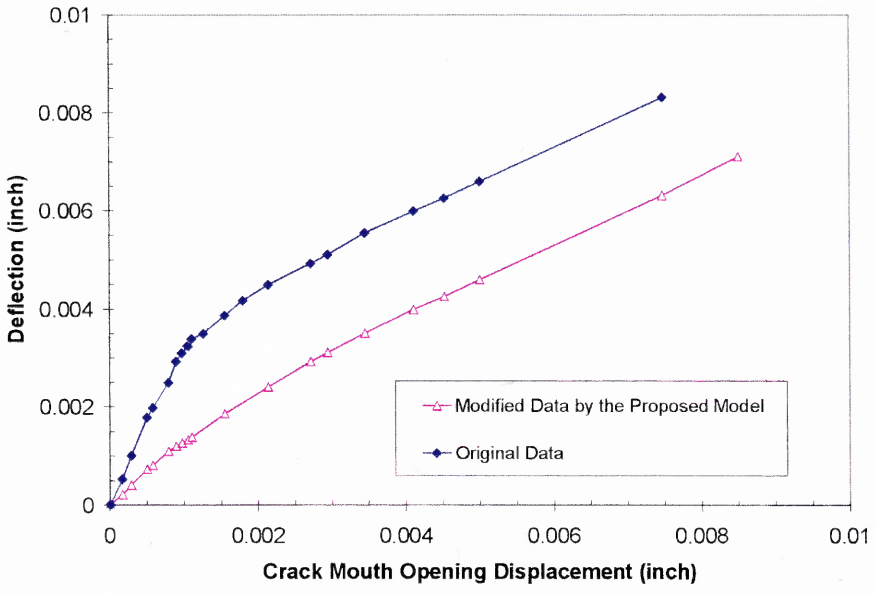

Figure 5.40 Deflection-CMOD Relationship of Beam RW2

By using the modified load-deflection curve and the original load-CMOD curve of beam RW2 as shown in Figure 5.39, the G_C obtained by the proposed model is found to be 0.105 lbs./inch, which agrees well with the G_C of 0.104 lbs./inch reported in the literature. Furthermore, from Table 5.35, the fracture energy (G_F) reported in their study was 0.370 lbs./inch, which is about 30% higher than that calculated by the modified load-deflection curve. Figure 5.41 shows the analytical results of the load vs. crack length relationship of beam RW2 obtained by the proposed model. It is interesting to note that, from Figure 5.39a, the measured peak deflection in the literature (0.00338 inches) are much higher than that of the modified curve (0.00138 inches). The above results again reflect the possible erroneous deflection measurements reported in the literature. When the load-deflection curve was modified to correct the erroneous deflection response, the fracture parameters obtained by the proposed model are found to be in good agreement with the referred literature.

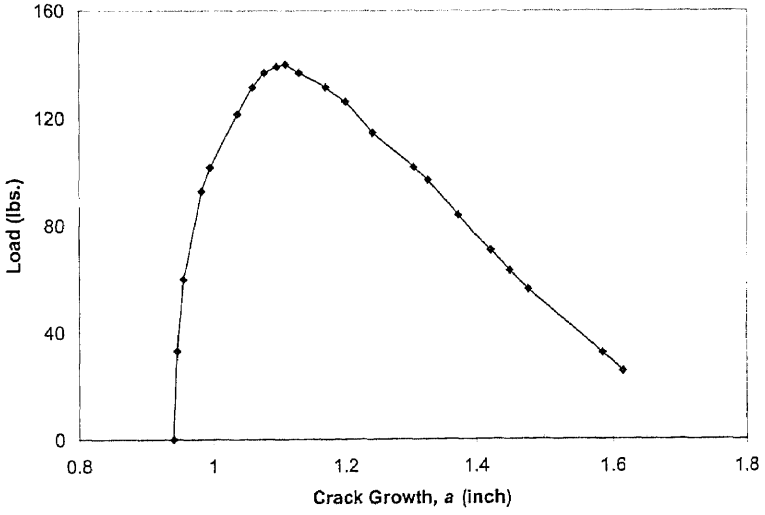

Figure 5.41 Load-Crack Length Relationship of Beam RW2

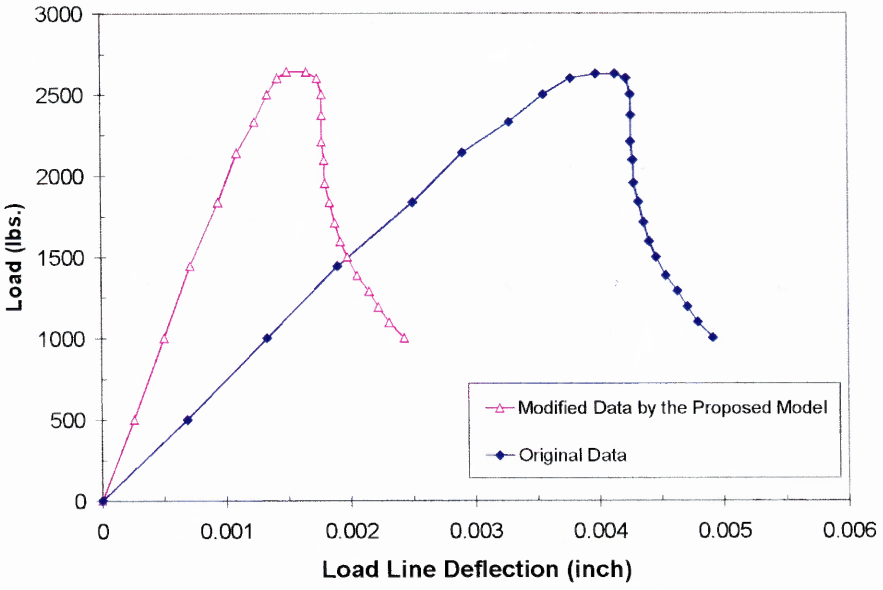

Figure 5.42a Load-Deflection Relationship of Beam GY1 (Gopalaratnam and Ye 1991)

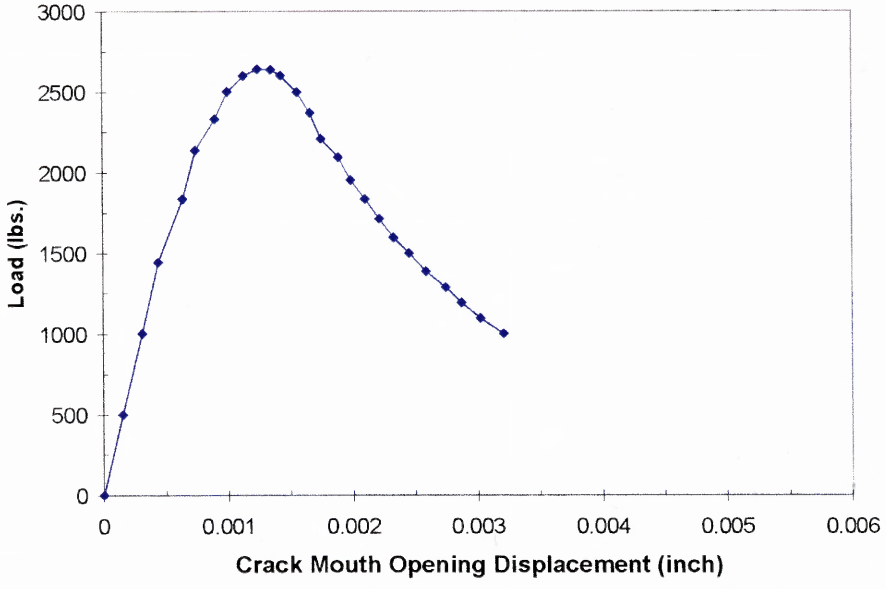

Figure 5.42b Load-CMOD Relationship of Beam GY1 (Gopalaratnam and Ye 1991)

Figure 5.42 presents the test data adapted from Gopalaratnam and Ye's study (1991) for the modeled concrete beam GY1. In their study, the critical crack length (a_c) was calculated by applying a numerical model and the finite element method. The fracture behavior of the beam was modeled as functions of the crack-tip-opening displacement and the tensile strength based on the fictitious crack model (Hillerborg 1976). Referring to the proposed model, the fracture parameters a_c and G_C can be calculated from the load vs. CMOD curve when the value of S_1, which is consider a material property, is known. For beam GY1, by using the original load-deflection curve and load-CMOD curve from the literature as shown in Figure 5.44, the a_c calculated by the proposed model is 6.198 inches, which is noticeably higher than the value 4.290 inches found in the literature.

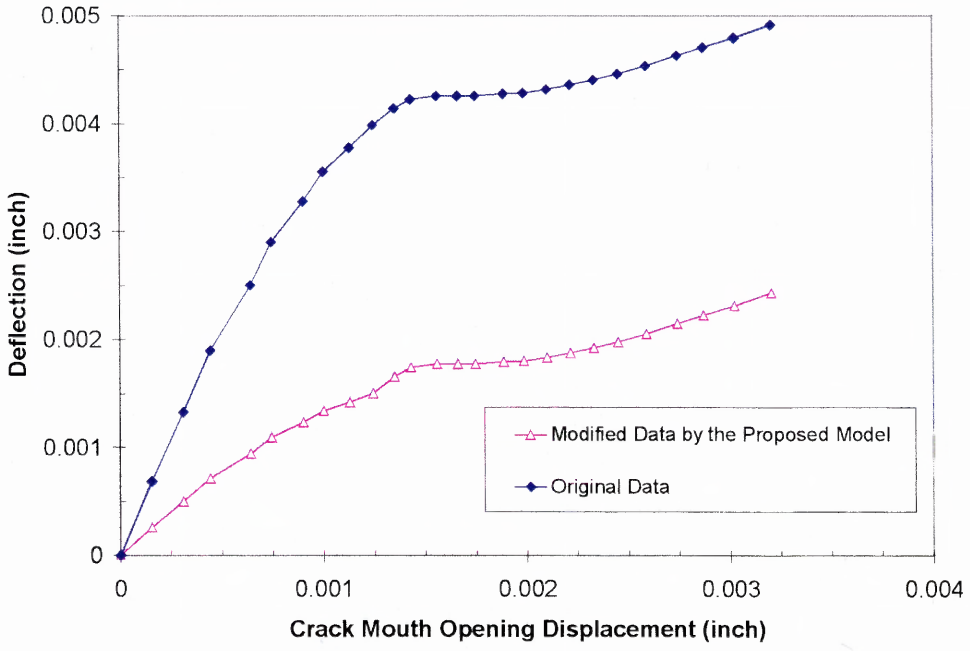

Figure 5.43 Deflection-CMOD Relationship of Beam GY1

From the discrepancy observed between the analytical result from the literature and the proposed model, it is interesting to investigate the relationship between the deflection and CMOD generated by the finite element model. Figure 5.43 shows the deflection-CMOD relationship of the modeled beam GY1. The deflection-CMOD curve from the original data does not show the bi-linear relationship (S_1 and S_2) as occurred in the real concrete or mortar structures. On the other hand, the curve begins rising with the constant slope, and becomes flat after the peak load. Then, it starts to rise again with the slope less than that at the initial stage. From Table 5.35, the value of S_1 for the beam GY1 calculated from the original data is 2.441, which is higher than S_1 of 1.270 for the control concrete (CC) obtained in the present study (see Table 5.22). This indicates that the deflection responding to the applied load could be modeled in such a way that it does not represent the true deflection behavior of the material.

Referring to the proposed model, the true or reasonably assumed values of fracture energy (G_F) and S_1 of the material are required for evaluating the fracture behavior and determining the fracture parameters. Therefore, in the present study for evaluating the performance of the proposed model, the original load-deflection curve was modified to obtain the S_1 equal to 1.270 as assumed for normal strength concrete. Figure 5.43 shows the deflection-CMOD relationship (S_1 and S_2) of the beam GY1 for the original data and the data modified by the proposed model. It is noted that the fracture energy (G_F) of 0.300 lbs./inch from the original data was also used for the modified load-deflection curve to calculate the a_c by the proposed model. This is because the value of G_F of 0.300 lbs./inch was given as a concrete property for the model in their study and not calculated from the area under the load vs. deflection curve.

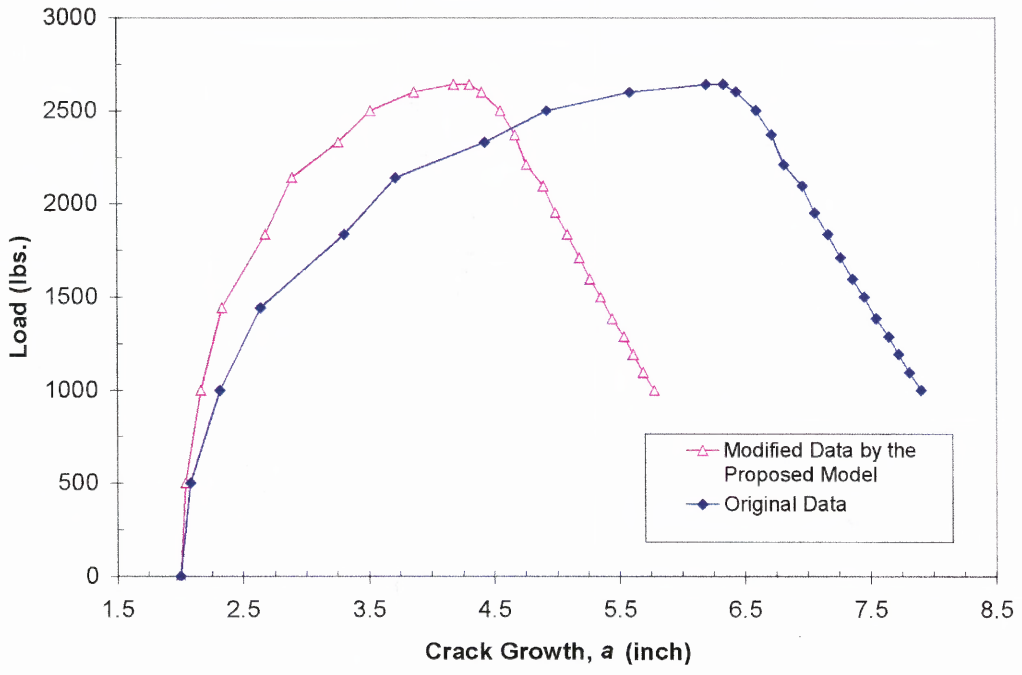

Figure 5.44 Load-Crack Length Relationship of Beam GY1

By using the data from the modified load-deflection curve and the original load-CMOD curve for the beam GY1 as shown in Figure 5.42, the critical crack length (a_c) obtained by the proposed model becomes 4.187 inches, which compares favorably with that of 4.290 inches found in the literature. The results show that S_1 is a material property and important for the proposed model in utilizing the load-CMOD curve to evaluate the fracture behavior of cement-based material. Furthermore, it should be noted that S_1 from the finite element model used by Gopalaratnam and Ye is also sensitive to the modeling of the response of beam deflection. Figure 5.44 shows the analytical results of load vs. crack length relationship of the beam GY1 obtained by the proposed model for both the original data in the literature and the modified one. Based on the results discussed above,

the proposed fracture mechanics model for studying the fracture behavior of cementitious material is found to be in good agreement with the finite element model from the literature.

Referring to the present investigation for the performance of the proposed model using test results from other researchers (Ratanalert and Wecharatana 1989, and Gopalaratnam and Ye 1991), in order to reduce the effect of erroneous deflection during fracture process, only the S_1 value was modified, while S_2 remained unchanged. This is due to the fact that the fracture parameters discussed here were determined based on the critical values at the peak load, therefore the S_1, which represents the pre-peak behavior of material, is properly related to the interested fracture parameters rather than the S_2, which covers the post-peak behavior. Eventually, regardless of the S_2, the analytical results for the fracture parameters obtained by the fracture models were found to be in good agreement with those reported experimentally by other researchers. These results confirm that erroneous deflection measurement due to support crushing strongly affects the pre-peak behavior rather than the post-peak behavior of the material during the fracture process.

In the finite element model reported by Gopalaratnam and Ye (1991), the fictitious crack concept (Hillerborg 1976) was used in the numerical scheme to simulate the fracture process zone or the inelastic zone ahead of the traction-free crack into a discrete fictitious crack capable of supporting some traction. Crack growth along crack path was controlled by incrementally releasing one node at a time when the tensile stress at that node reaches the tensile strength of the material. This ensured post-peak stability similar to a crack mouth opening controlled experiment performed in the present study.

In their model, the deflection response was not involved in the numerical formulations of the finite element model for the fracture behavior of concrete.

In the proposed fracture model, the crack growth during fracture can be determined from the inelastic energy absorbed in the fracture process, which is calculated by applying the area under the load-CMOD curve, S_1, S_2 and the fracture energy (G_F) as described in Chapter 3. By means of three-point bend tests on notched beams, traditional methods of measuring load-line deflection in the notched beams, which was commonly measured with respect to the base of the testing machine, contain extraneous measurements that affect the values of S_1, S_2 and the fracture energy (G_F). To eliminate these extraneous deformations, the deflections must be measured with reference to its neutral axis using a reference frame attached to the beam as performed in the present study.

Based on the results of the fracture parameters previously discussed, S_1 and G_F, which are considered material properties, are sensitive to the method of measuring load-line deflection, while S_2 is not. However, from the results throughout the present study, S_1 of cementitious materials can be reasonably predicted if there is sufficient database to relate S_1 with the type of material or the mechanical property of material such as compressive strength. Regardless of the recommended method for measuring accurate deflection, when the S_1 is properly assumed and the S_2 is empirically determined, the fracture behavior of the material during fracture process and other fracture parameters can be reliably obtained by applying the load-CMOD curve using the proposed fracture mechanics model.

Finally, whether the complicated beam test setup required for properly measuring load-line deflection is available or not, the load-CMOD response, which is not affected by the support conditions, is a more reliable measurement than the load-deflection response. Use of the load-CMOD relationship along with the proposed fracture model could lead to a new testing standard for studying fracture behavior and measuring fracture parameters (e.g. fracture toughness and fracture energy) of cementitious materials.

5.5 Practical Application of the Proposed Fracture Model

The proposed fracture model can be applied for practical use with existing concrete structures. For a cracked concrete structure with an initial crack length of a_0 and initial applied load P, the conceptual procedure for determining the critical load (P_C) causing the unstable condition can be described as the following. First, by rearranging Equation 3.2b it gives

$$\Delta a = \frac{1}{G_F B}\left(S_1 \int_0^{CMOD_P} PdCMOD + S_2 \int_{CMOD_P}^{CMOD} PdCMOD \right) \tag{5.6}$$

$$\Delta a = \frac{1}{G_F B}\left((S_1 - S_2) \int_0^{CMOD_P} PdCMOD + S_2 \int_0^{CMOD} PdCMOD \right) \tag{5.7}$$

where descriptions of the parameters used in the equations here are previously presented in Chapter 3. The first term on the right side of Equation 5.7 represents the elastic strain energy, which can be expressed by the following equation

$$(S_1 - S_2) \int^{CMOD_P} PdCMOD = G_F - G_C \tag{5.8}$$

For cementitious material, the values of S_1, S_2, G_F and G_C are known, therefore, the integration term on the left side of Equation 5.8 can be obtained. Hence, for any existing concrete structure, the critical crack growth can be obtained by the following equation

$$\Delta a_c = \frac{1}{G_F B}\left(S_1 \int_0^{CMOD_P} P dCMOD \right) \tag{5.9}$$

and then the critical crack length (a_c) can be expressed as

$$a_c = \Delta a_c + a_0 \tag{5.10}$$

From this point, the concept of Linear Elastic Fracture Mechanics (LEFM) as described in Section 2.4.3 can be applied to determine the critical load (P_C) for cracked concrete structure with E as the Modulus of Elasticity. By equating Equations 2.14 and 2.15, the following equation is obtained,

$$E = \frac{6Sa_0 V(\alpha)}{C_i D^2 B} = \frac{6Sa_c V(\alpha)}{C_u D^2 B} \tag{5.11}$$

Rearranging the above equation leads to

$$\frac{a_0}{a_c} = \frac{C_i}{C_u} = \frac{CMOD_0}{CMOD_P}\frac{P_C}{P} \tag{5.12}$$

where $CMOD_0$ can be calculated using the LEFM formulae (Equation 2.14) when the initial applied load P is known (see Section 2.4.3), and $CMOD_P$ for cementitious material can also be determined by the procedure described in Section 3.3.

Therefore, the critical load (P_C) of a cracked concrete structure can be predicted by using the following expression

$$P_C = \frac{a_0}{a_c}\frac{CMOD_P}{CMOD_0} P \tag{5.13}$$

So, in practice, if cracks were reported in any existing structure, one would immediately determine the extent of the damage, i.e., the existing load, the appeared crack length and the crack-opening displacement (CMOD). With these data and the proposed concept as described above, one can determine the maximum load (P_C) and the critical crack growth (a_c) of the structure. And, thus the safety and load carrying capacity of the damaged structure can be predicted.

CHAPTER 6

CONCLUSIONS AND SUGGESTIONS

6.1 Conclusions

The experimental program and a fracture mechanics model proposed herein were carried out to study the influence of high performance matrices on fracture behavior of concrete. Fine particle pozzolans such as silica fume and coal fly ash were used as cement replacement to produce high performance concrete matrices. The average particle size of silica fume is less than 1 micron. The coal fly ashes were fractionated by the air classifier into six different average particle sizes (13F, 15F, 16F, 18F, 18C and MO) ranging from 2.5 to 20 microns. With 10% of silica fume and 25% of fly ashes used as cement replacement in the mixture, the compressive strengths of concrete ranged from 5600 to 7400 psi. Based on the results obtained, the following conclusions can be drawn:

1. Incorporating the fine particle pozzolans in cement matrix increased the density and toughness of the cement matrix-coarse aggregate interface, but did not necessarily improve the density and toughness of the cement matrix. The modifications of the cement matrix-coarse aggregate interfacial bond and the cement matrix affect the cracking characteristics and the deformation capability of concrete before and during fracture failure.
2. Replacing cement by silica fume or fly ashes (16F, 18F, 18C and MO) enhanced the interfacial bond, but did not improve the toughness of the cement matrix. Only the very fine fly ashes (the fly ashes 13F and 15F with the average particle size smaller than 3.71 microns) enhanced both the interfacial bond and the toughness of cement matrix.

3. The silica fume replacement in the concrete mixture had the most positive effect on the interfacial bond, which results in the highest compressive strength and the highest critical energy release rate (G_C) among all types of concrete tested. The fracture energy (G_F) of the silica fume concrete is less than that of the concrete mixed with the finest fly ash, 13F, but higher than the other fly ash concretes and the control concrete. Furthermore, the silica fume produced the most brittle concrete. The enhanced interfacial bond by the presence of silica fume is responsible for the brittleness, and renders a more homogeneous microstructure of the concrete.
4. The replacement of cement by the moderately fine fly ashes (16F, 18F, 18C and MO) improved the interfacial bond between cement matrix and aggregate, but did not enhance the toughness of cement matrix. Consequently, the compressive strengths, G_C and G_F of the fly ash concretes are higher than those of the control concrete, but the fly ash concrete tend to be more brittle.
5. Replacing cement by the finest fly ash 13F (with the average particle size of 2.5 microns) enhanced both the interfacial bond and the toughness of cement matrix. Consequently, the 13F fly ash yielded the highest G_F, and the second highest of G_C. Furthermore, it produced the least brittle concrete, which is tougher than the control concrete.
6. Improving interfacial bond between cement matrix and aggregate by fine particle pozzolans has beneficial effect on the compressive strength, tensile strength and the G_C of concrete, but does not necessarily enhance G_F and brittleness of concrete. High performance cement matrices are essential to improving fracture behavior of concrete.

7. Fineness of fly ash is a very important factor effecting the fracture behavior of concrete, regardless of the comparable compressive strength and tensile strength of the concretes produced by the fly ashes with different particle size range. By incorporating fly ash in concrete, the fracture behavior of concrete can be improved by reducing the particle size of fly ash.
8. For the notched beam fracture test in the present study, by measuring the beam deflections with reference to its neutral axis using a reference frame attached to the beam, the extraneous deflection measurements as a result of support crushing can be eliminated. With a more accurate beam test setup to measure the load-line deflection, the proposed fracture mechanics model is developed as an alternative means to study the fracture behavior and to determine the fracture parameters of concrete based on the load vs. crack-mouth-opening displacement (CMOD) response.
9. When proper measurements of beam deflection are performed along with CMOD measurements, the bilinear relationships between the deflection and the CMOD defined as the values of S_1 and S_2 are found to exist. For the proposed model, S_1 and S_2 served as the important factors to relate the CMOD to the fracture behavior and the fracture parameters of concrete.
10. In implementing the proposed model, the fracture behavior of concrete such as the load-crack growth response and the energy release rate-crack growth response (R curve) can be determined without applying the finite element method. The conventional fracture parameters (e.g. a_c, G_C and K_{IC}) can be obtained as well by the proposed model without performing the complicated stable unloading-reloading during testing as required by the TPFM model.

11. The analytical results of the fracture behavior and the fracture parameters of concrete obtained by the proposed model are found to be in good agreement with the test data and the fracture models of other researchers. It is found that better and less scattering estimates of the fracture parameters are obtained by using the proposed model accompanying with the load-CMOD response as compared to the TPFM beam test results (RILEM 1990).
12. The deflection-CMOD relationships in the pre-peak and post-peak regions of the concrete beams, S_1 and S_2 respectively, are material properties. The S_1 is more likely than S_2 to be affected by the erroneous measurements of the beam deflection.
13. Survey of literature on concrete fracture tests found that a large number of tests were carried out by using the erroneous measurements of beam deflections which often included the crushing of concrete at supports. By applying the reasonably assumed values of S_1 for the true deflections and the empirically determined values of S_2 from the literature, the proper evaluation of the fracture behavior and the fracture properties of concrete can be obtained by using the load-CMOD response based on the proposed model.
14. For the three-point bend tests on notched beams, the use of the proposed fracture mechanics model along with the load-CMOD relationship, which is unaffected by conditions of beam supports or other erroneous deflection measurement, could lead to a new testing standard for determining the fracture properties of cementitious materials.

6.2 Suggestions for Future Studies

For future investigation on fracture behavior of cementitious materials, the author would like to suggest as follows:

1. For enhancement of both strength and fracture behavior of concrete, combinations of fine particle pozzolans such as silica fume and fly ash or other materials in concrete mixture should be investigated.
2. Fiber reinforced concretes have been known to increase the ability of structure to resist crack growth. It is of interest to apply the proposed fracture model to study the fracture behavior of fiber reinforced concrete.
3. For the fracture test setup, performance of the proposed fracture model with other types of the test method such as four-point-bend test and direct tension test should be studied as well as different sizes and shapes of test specimens.
4. Further development of applying the proposed fracture model to predict fracture behavior of the existing full-scale structures would be of great benefit.

APPENDIX A

EXPERIMENTAL DATA OF COMPRESSION TESTS

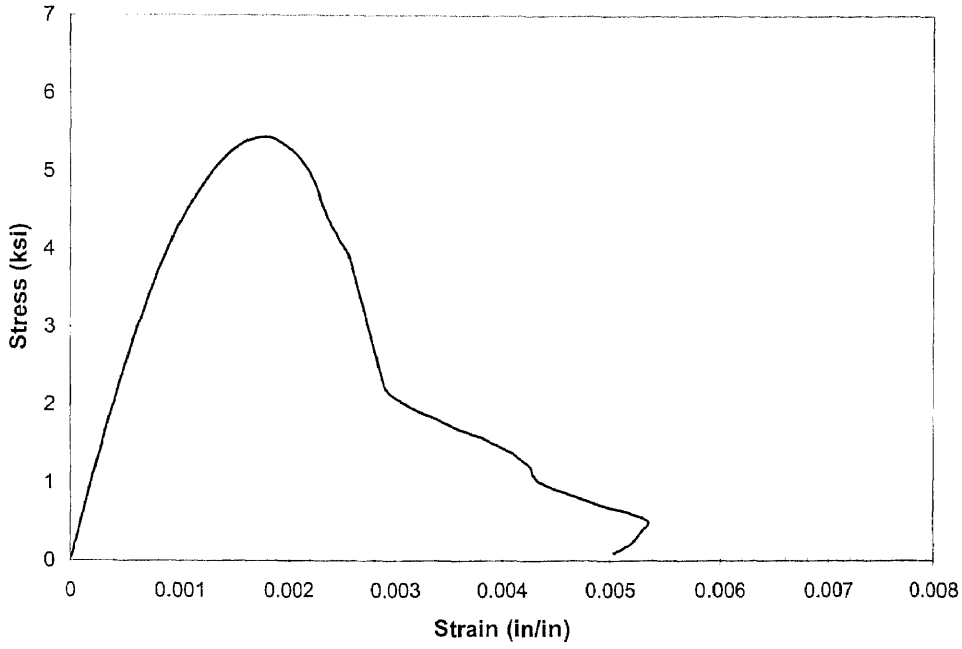

Figure A 1a Stress-Strain Curve for Control Concrete (CC) at 28 days Specimen No.1 (3 x 6 inch cylinder)

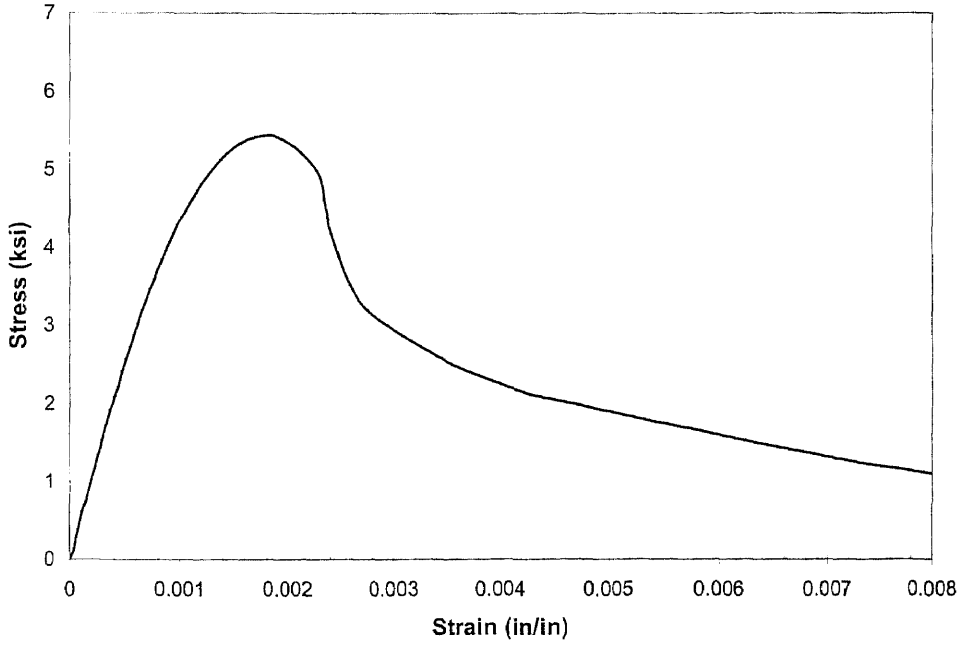

Figure A 1b Stress-Strain Curve for Control Concrete (CC) at 28 days Specimen No.2 (3 x 6 inch cylinder)

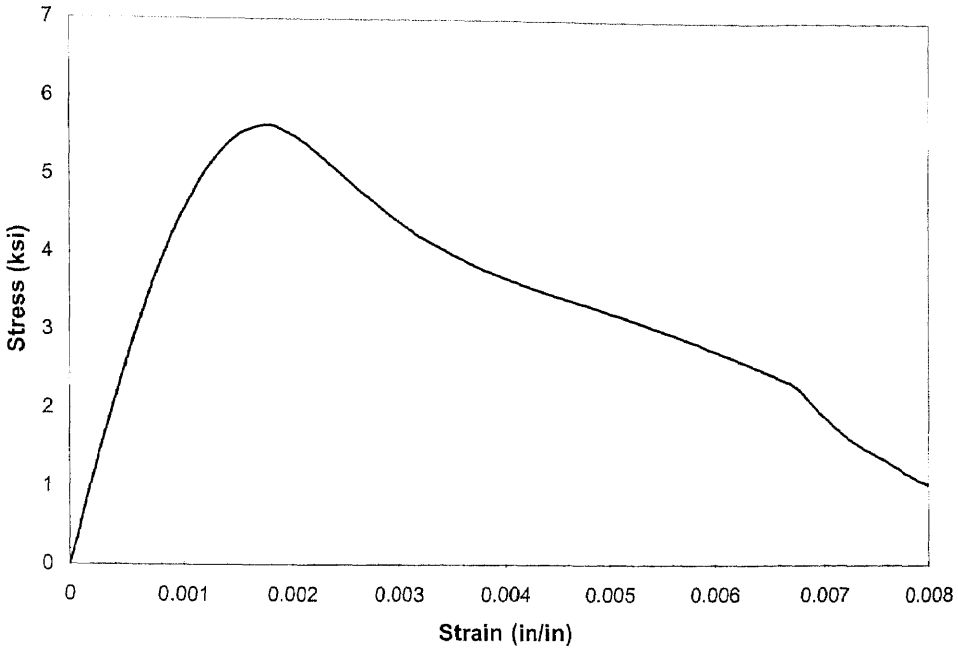

Figure A 1c Stress-Strain Curve for Control Concrete (CC) at 28 days Specimen No.3 (4 x 8 inch cylinder)

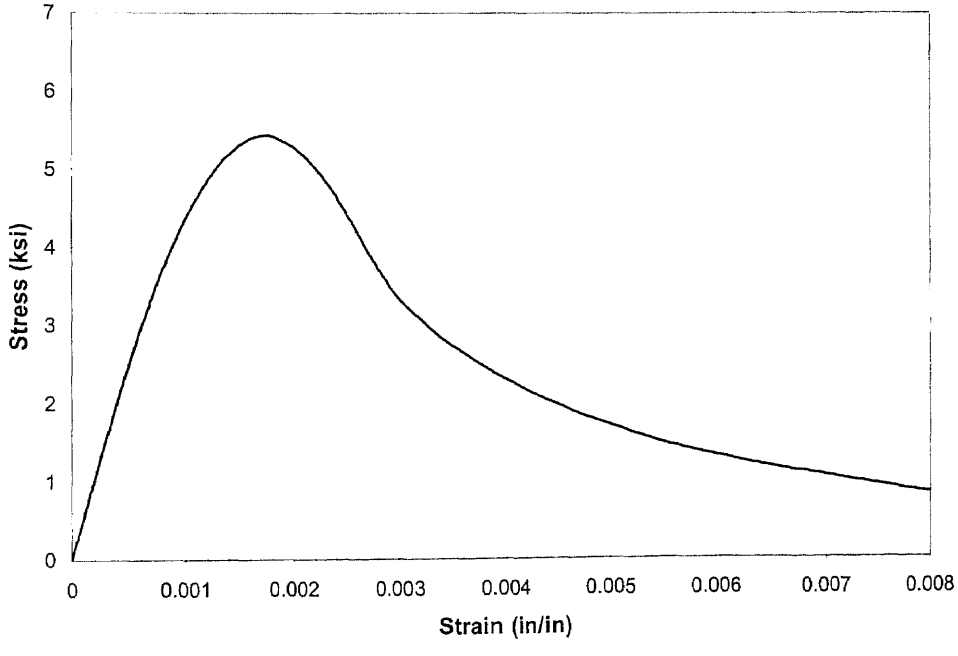

Figure A 1d Stress-Strain Curve for Control Concrete (CC) at 28 days Specimen No.4 (4 x 8 inch cylinder)

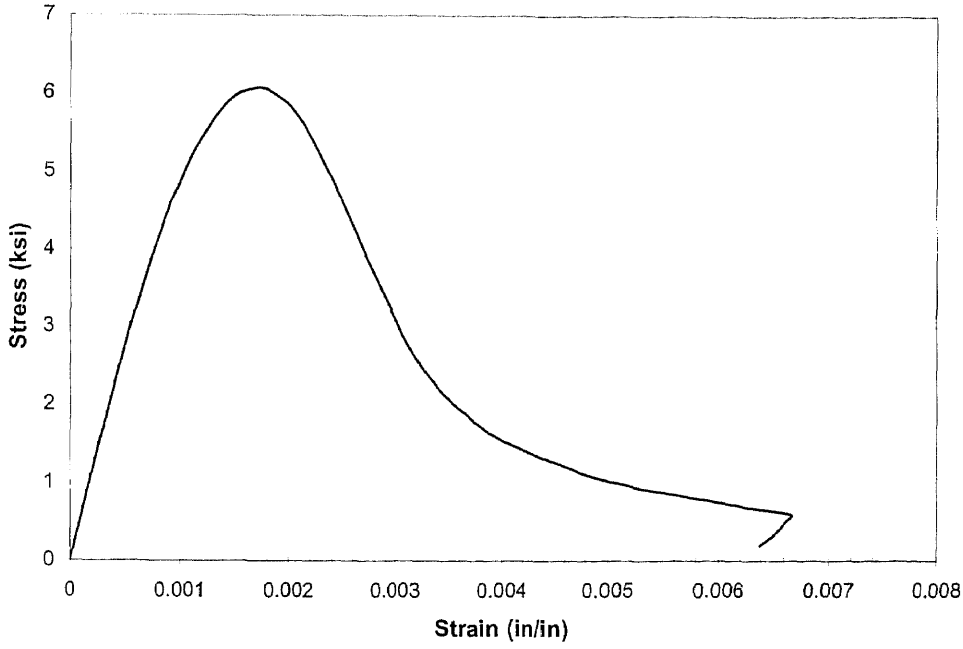

Figure A 1e Stress-Strain Curve for Control Concrete (CC) at 56 days Specimen No.1 (3 x 6 inch cylinder)

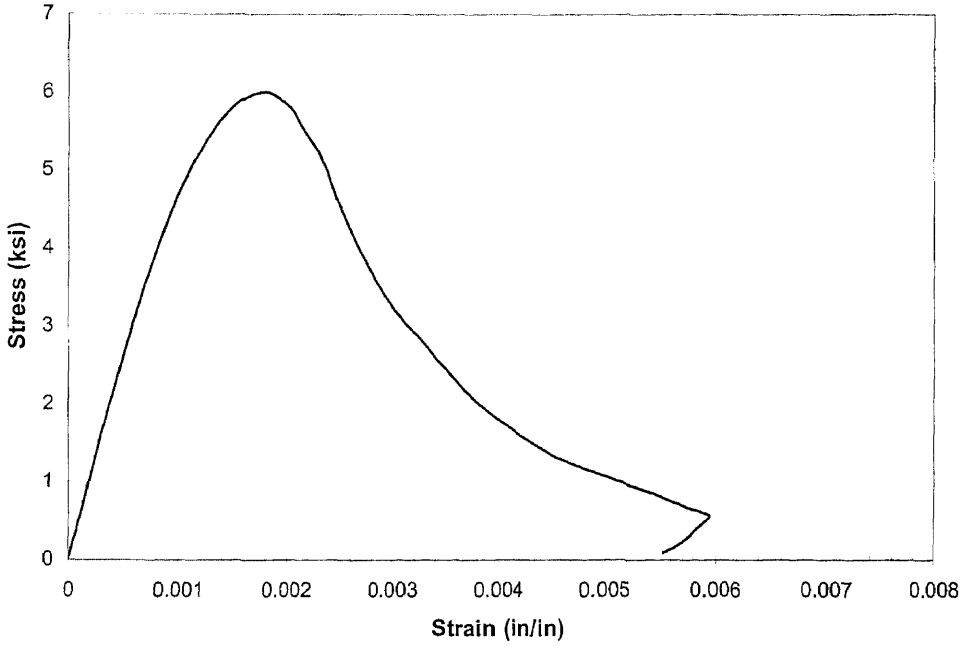

Figure A 1f Stress-Strain Curve for Control Concrete (CC) at 56 days Specimen No.2 (3 x 6 inch cylinder)

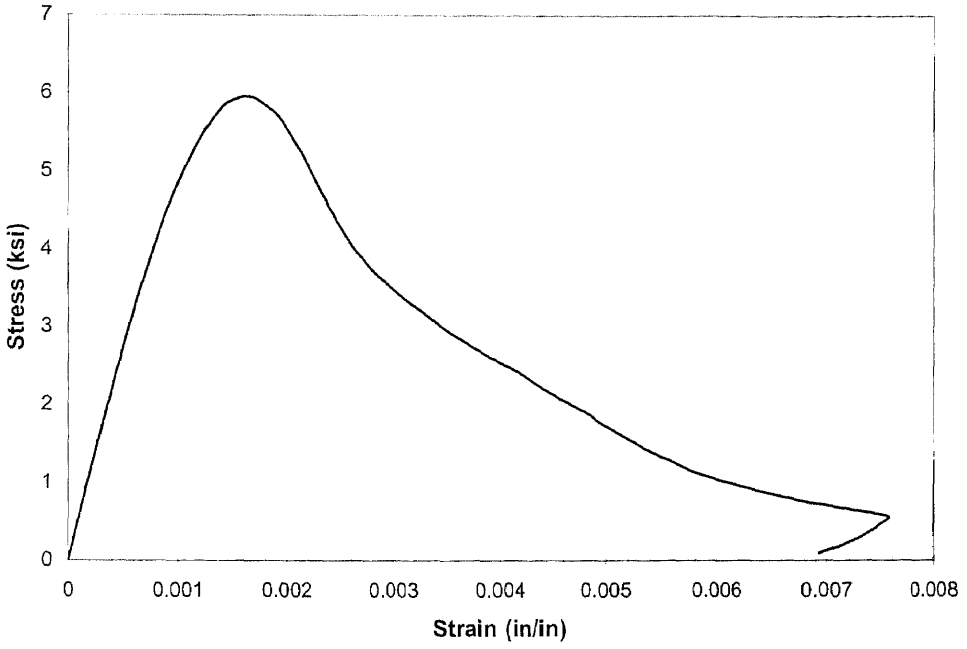

Figure A 1g Stress-Strain Curve for Control Concrete (CC) at 56 days Specimen No.3 (3 x 6 inch cylinder)

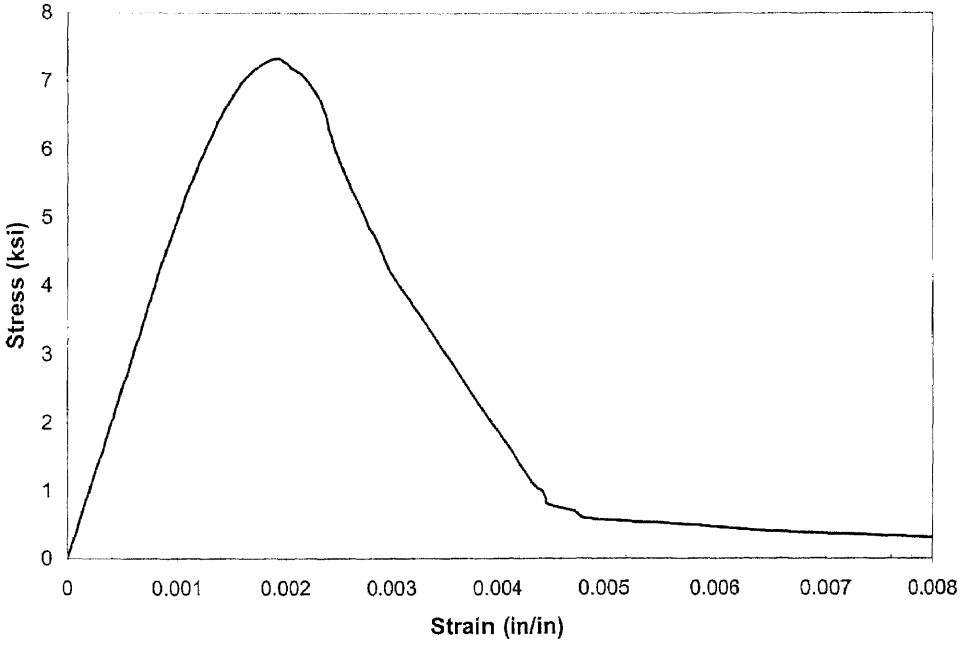

Figure A 2a Stress-Strain Curve for Silica Fume Concrete (SF) at 28 days Specimen No.1 (3 x 6 inch cylinder)

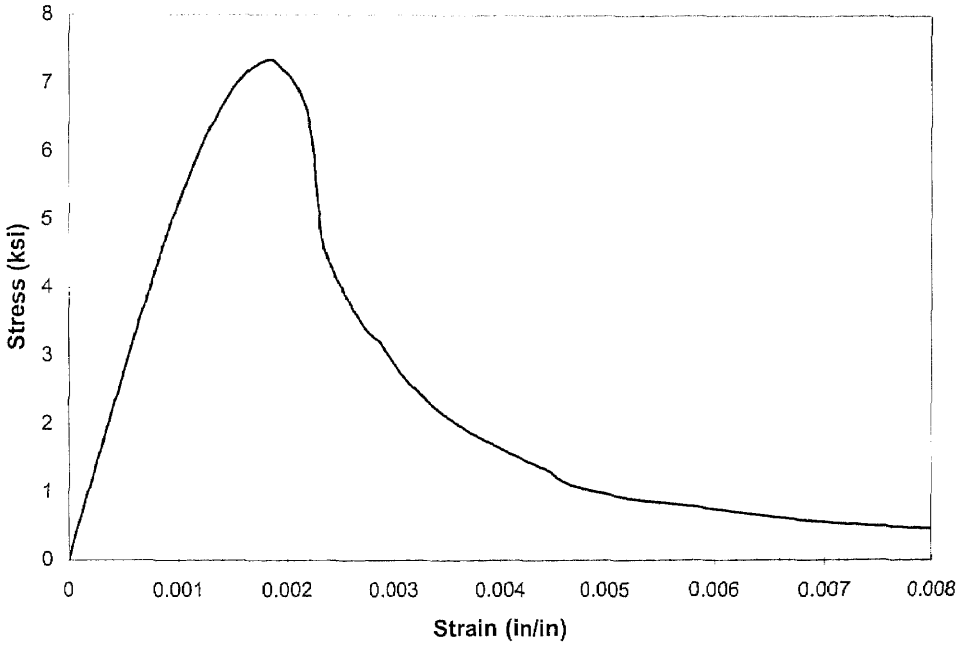

Figure A 2b Stress-Strain Curve for Silica Fume Concrete (SF) at 28 days Specimen No.2 (3 x 6 inch cylinder)

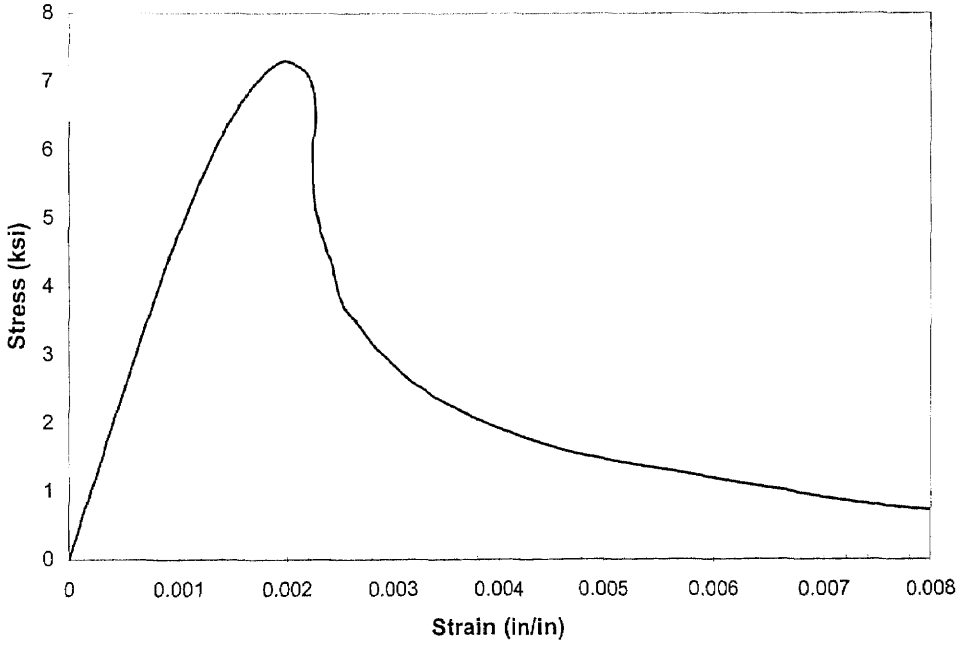

Figure A 2c Stress-Strain Curve for Silica Fume Concrete (SF) at 28 days Specimen No.3 (3 x 6 inch cylinder)

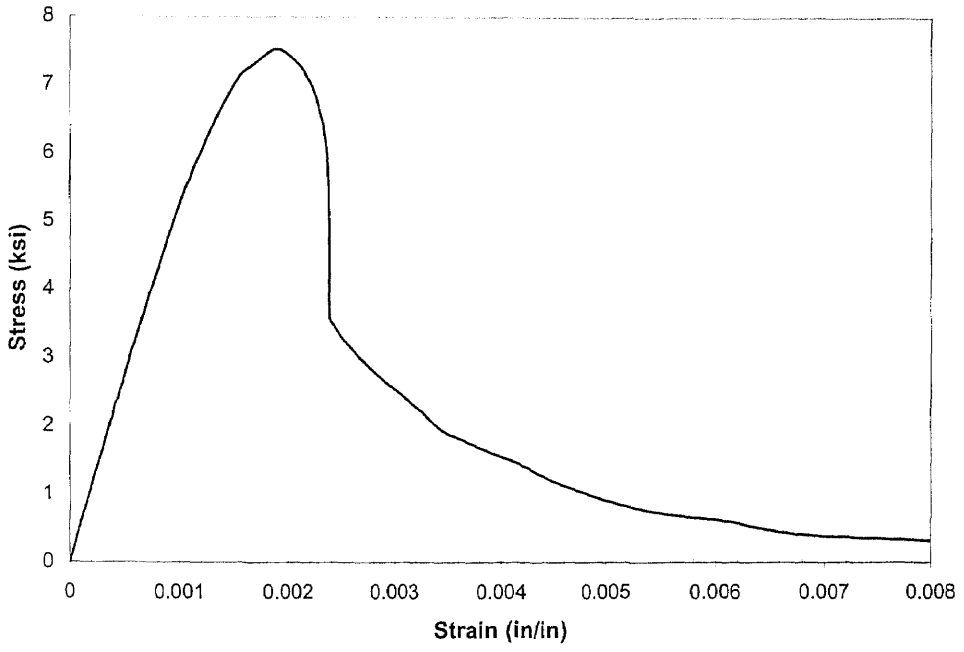

Figure A 2d Stress-Strain Curve for Silica Fume Concrete (SF) at 56 days Specimen No.1 (3 x 6 inch cylinder)

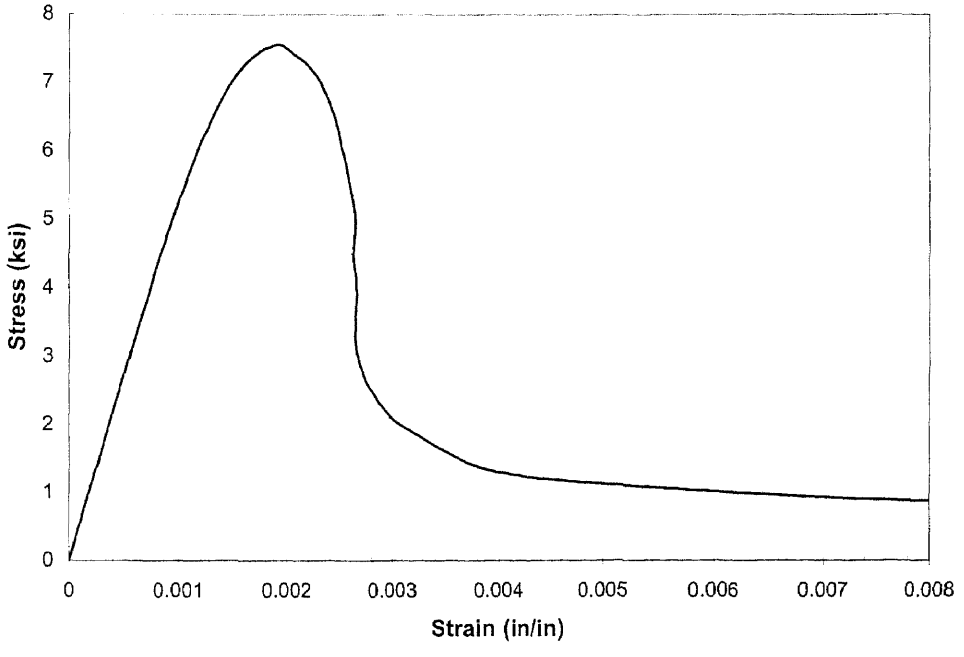

Figure A 2e Stress-Strain Curve for Silica Fume Concrete (SF) at 56 days Specimen No.2 (3 x 6 inch cylinder)

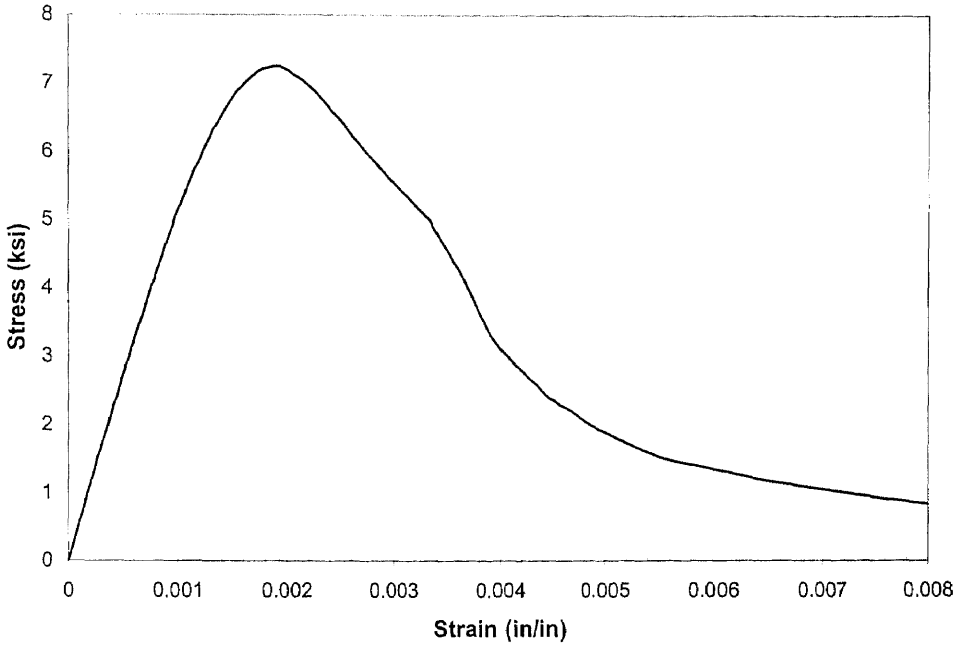

Figure A 2f Stress-Strain Curve for Silica Fume Concrete (SF) at 56 days Specimen No.3 (3 x 6 inch cylinder)

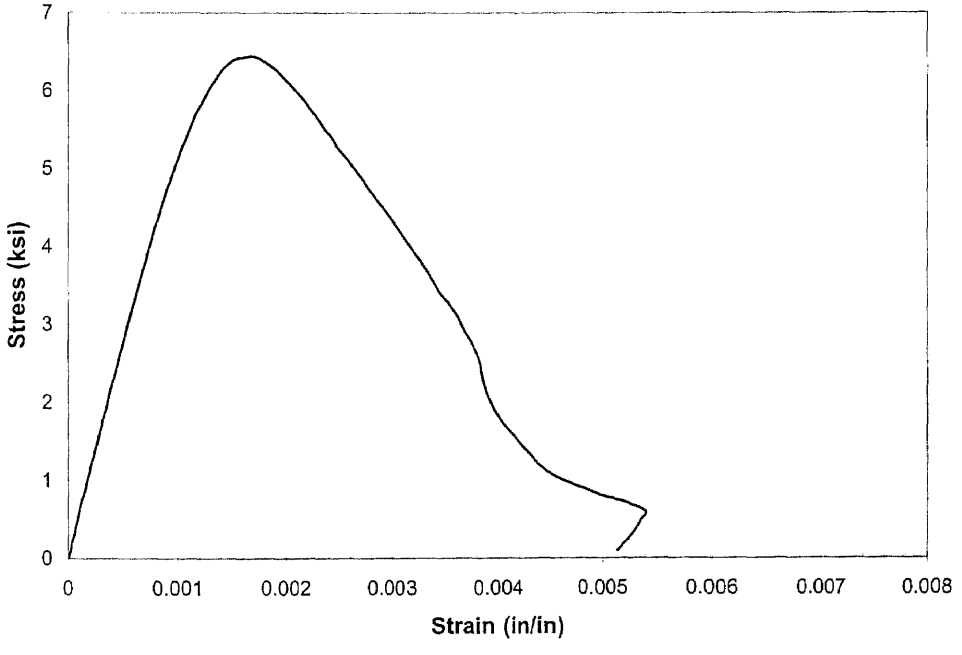

Figure A 3a Stress-Strain Curve for Fly Ash Concrete (13F25) at 28 days Specimen No.1 (3 x 6 inch cylinder)

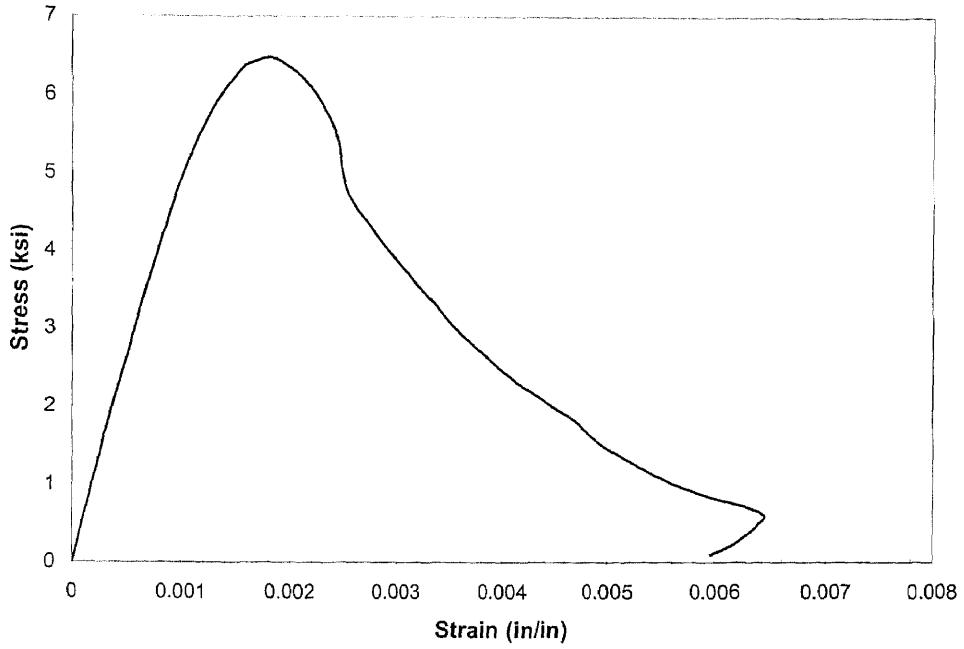

Figure A 3b Stress-Strain Curve for Fly Ash Concrete (13F25) at 28 days Specimen No.2 (3 x 6 inch cylinder)

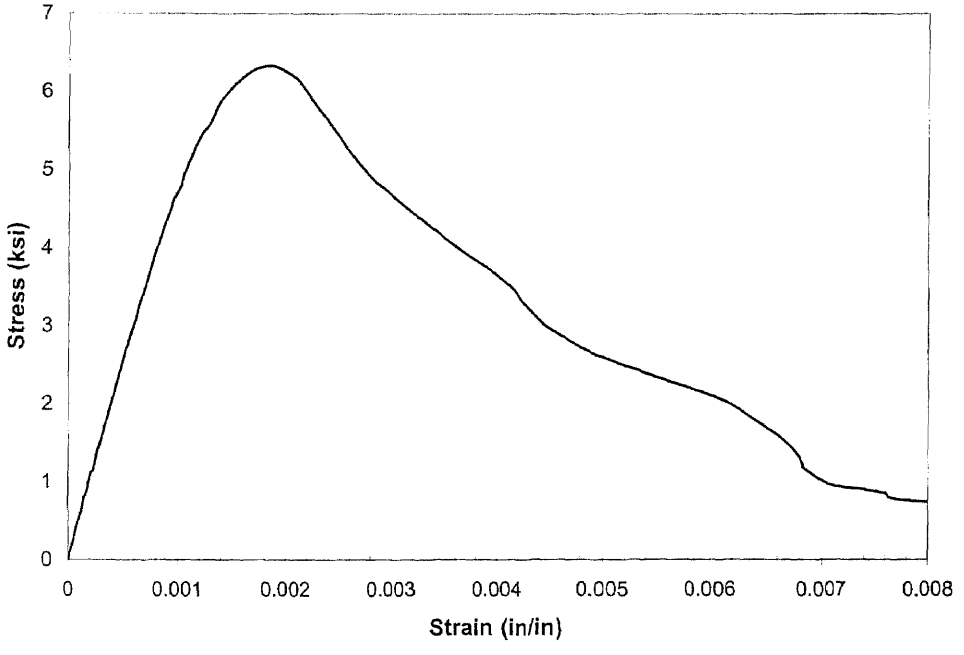

Figure A 3c Stress-Strain Curve for Fly Ash Concrete (13F25) at 28 days Specimen No.3 (3 x 6 inch cylinder)

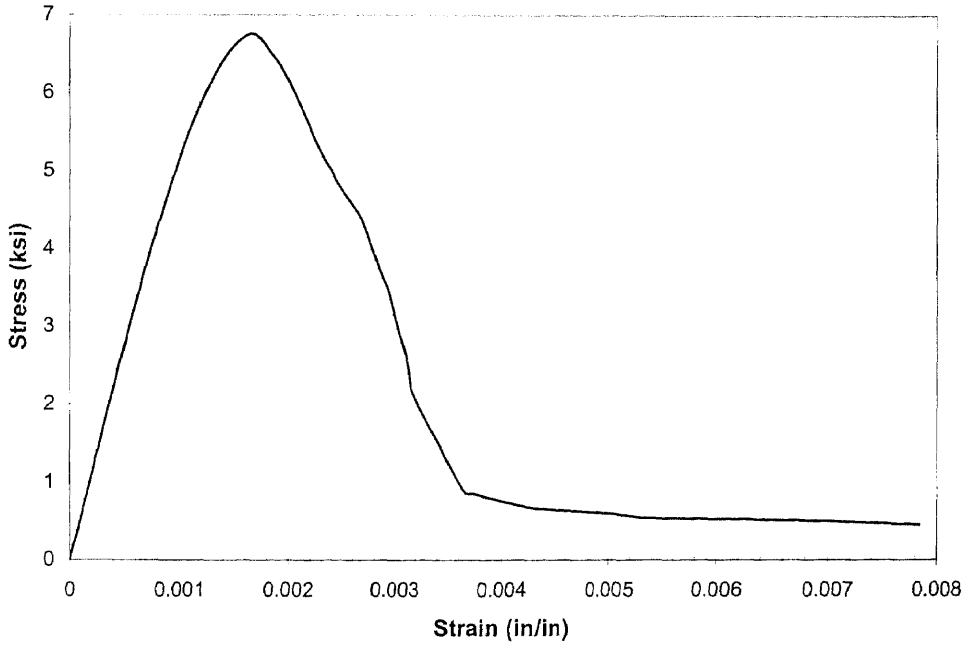

Figure A 3d Stress-Strain Curve for Fly Ash Concrete (13F25) at 56 days Specimen No.1 (3 x 6 inch cylinder)

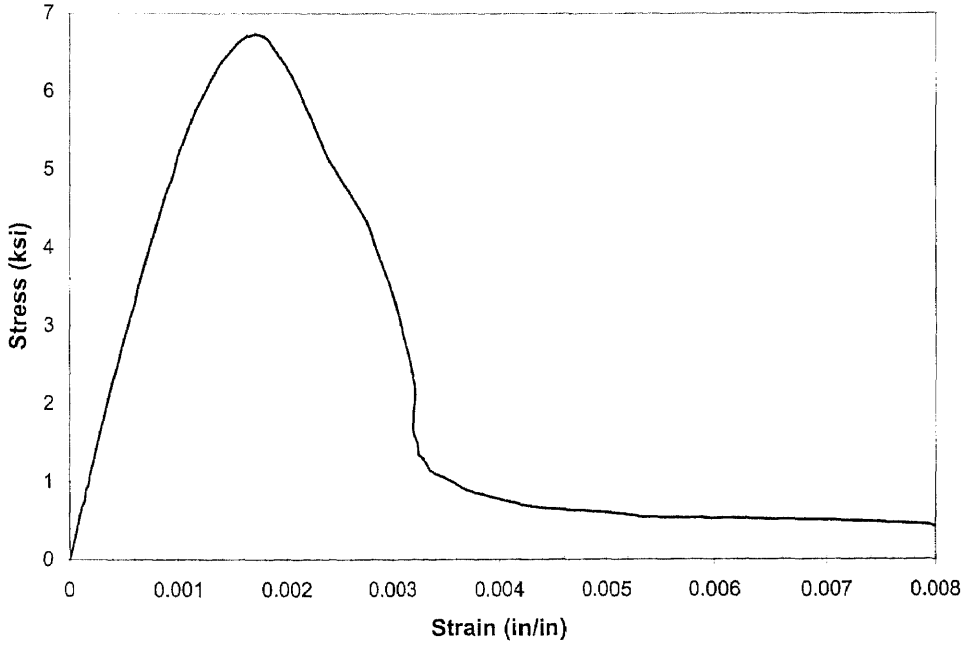

Figure A 3e Stress-Strain Curve for Fly Ash Concrete (13F25) at 56 days Specimen No.2 (3 x 6 inch cylinder)

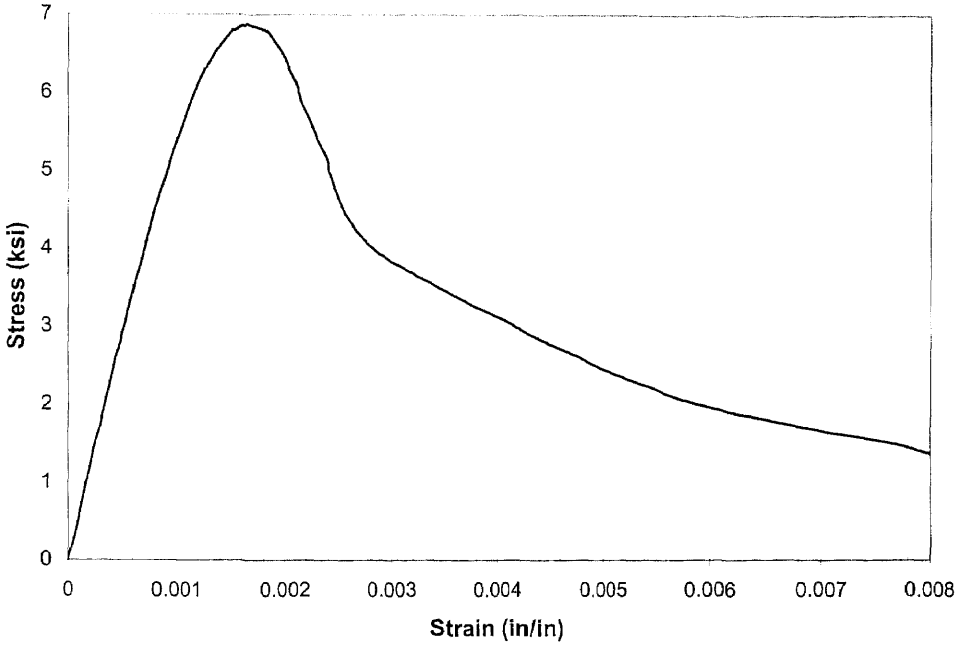

Figure A 3f Stress-Strain Curve for Fly Ash Concrete (13F25) at 56 days Specimen No.2 (3 x 6 inch cylinder)

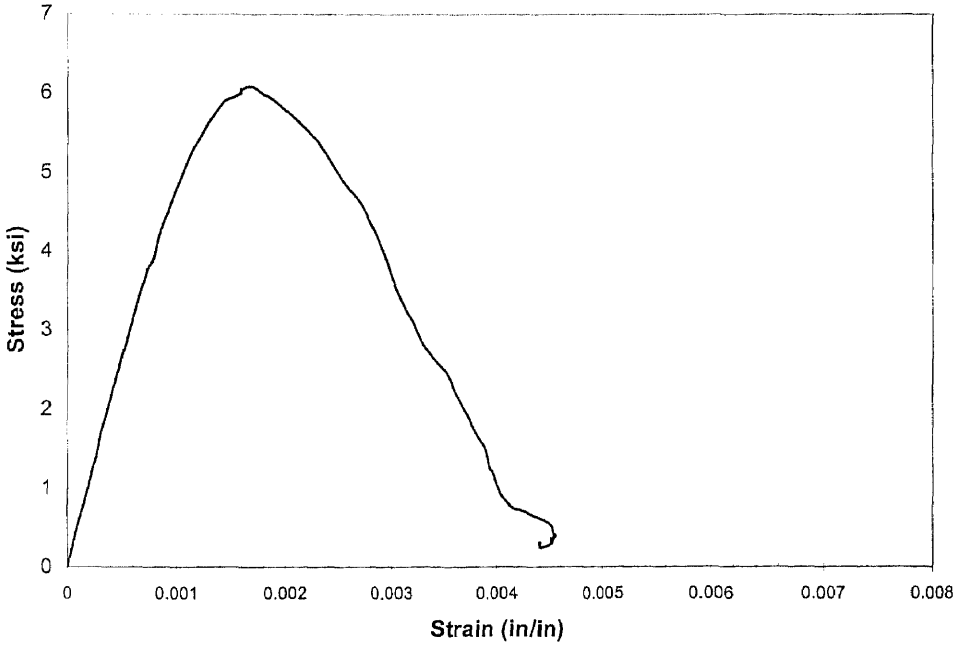

Figure A 4a Stress-Strain Curve for Fly Ash Concrete (15F25) at 28 days Specimen No.1 (3 x 6 inch cylinder

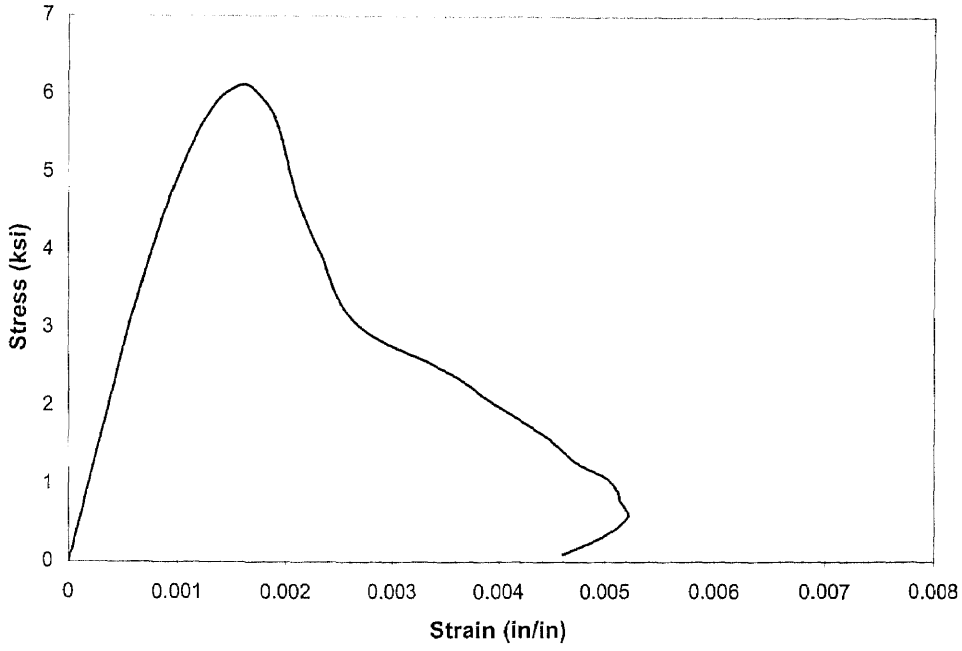

Figure A 4b Stress-Strain Curve for Fly Ash Concrete (15F25) at 28 days Specimen No.2 (3 x 6 inch cylinder)

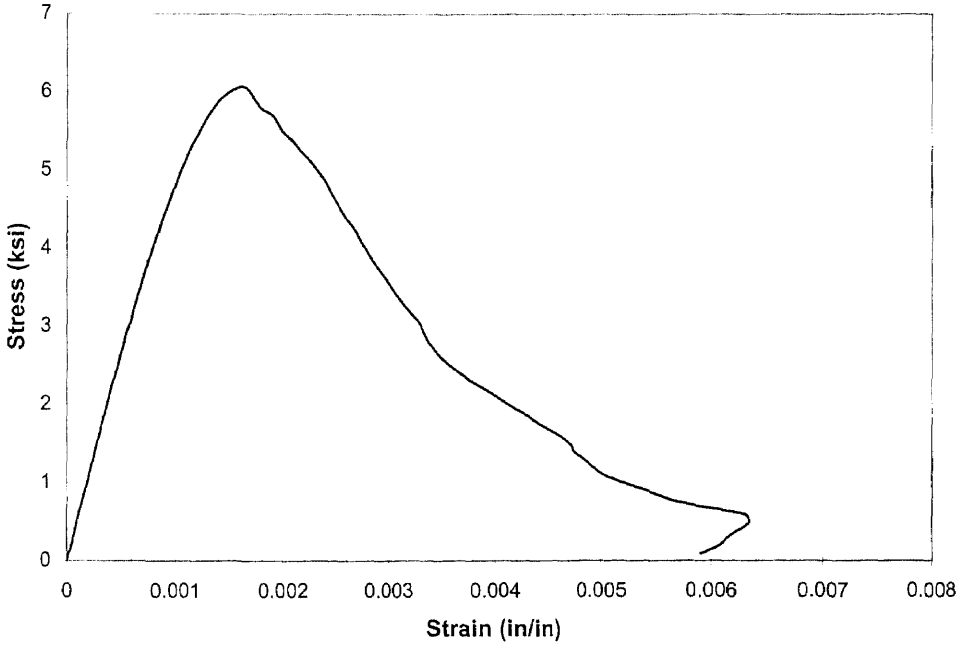

Figure A 4c Stress-Strain Curve for Fly Ash Concrete (15F25) at 28 days Specimen No.3 (3 x 6 inch cylinder)

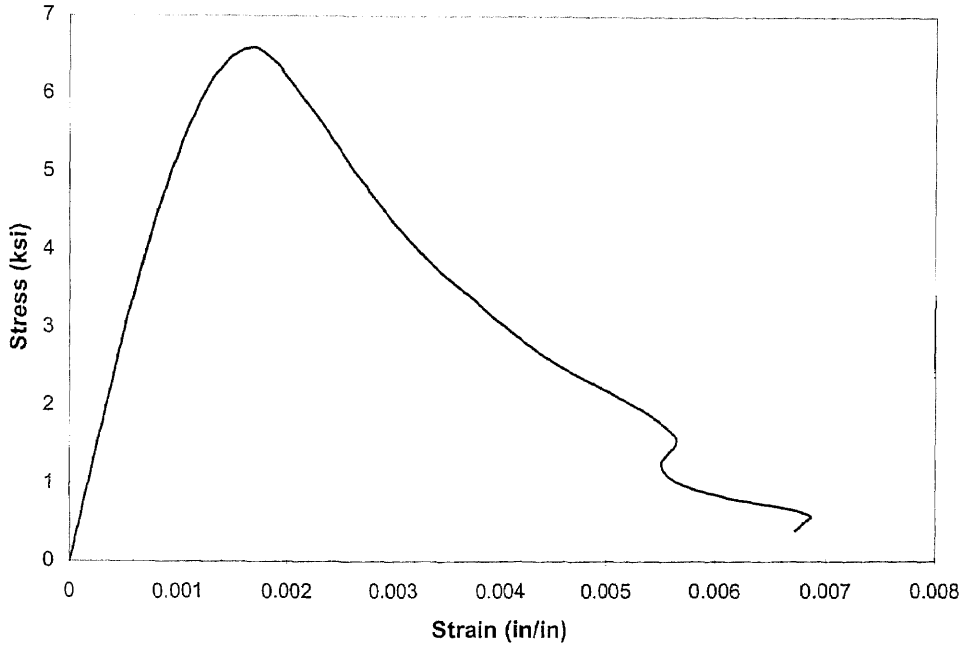

Figure A 4d Stress-Strain Curve for Fly Ash Concrete (15F25) at 56 days Specimen No.1 (3 x 6 inch cylinder)

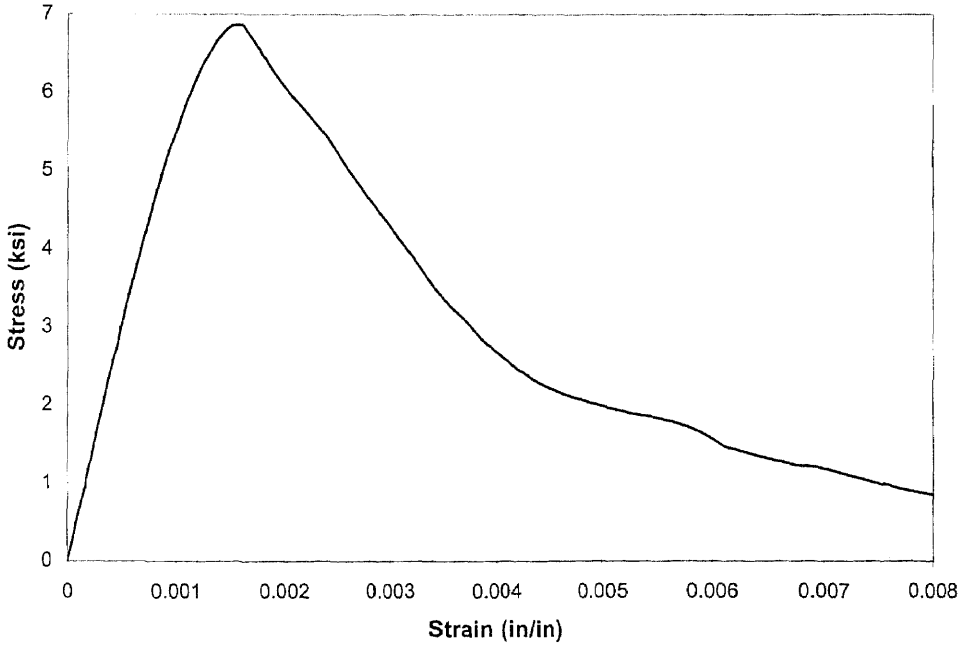

Figure A 4e Stress-Strain Curve for Fly Ash Concrete (15F25) at 56 days Specimen No.2 (3 x 6 inch cylinder)

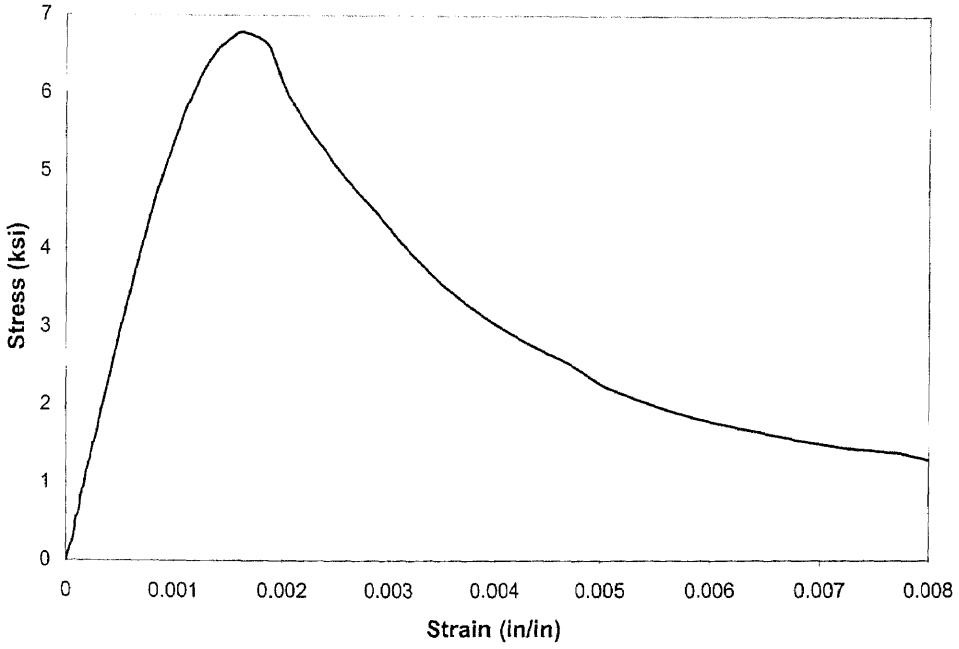

Figure A 4f Stress-Strain Curve for Fly Ash Concrete (15F25) at 56 days Specimen No.3 (3 x 6 inch cylinder)

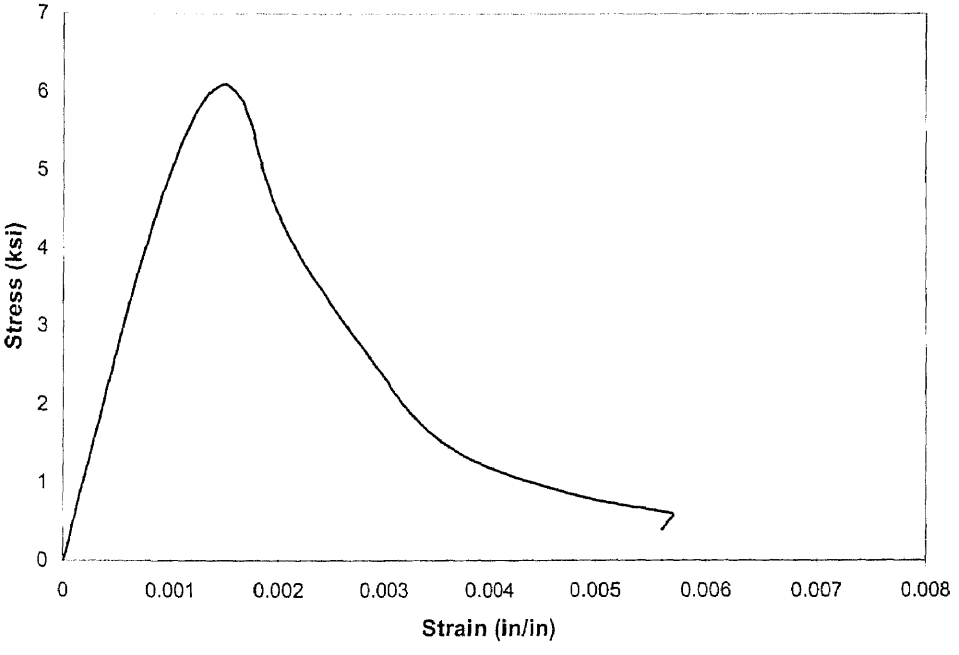

Figure A 5a Stress-Strain Curve for Fly Ash Concrete (16F25) at 28 days Specimen No.1 (3 x 6 inch cylinder)

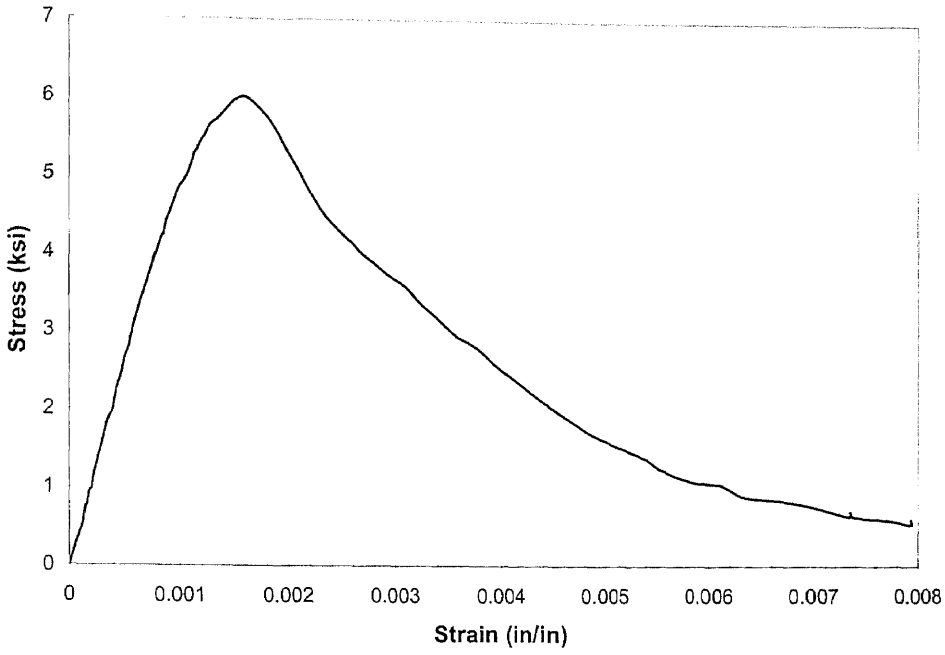

Figure A 5b Stress-Strain Curve for Fly Ash Concrete (16F25) at 28 days Specimen No.2 (3 x 6 inch cylinder)

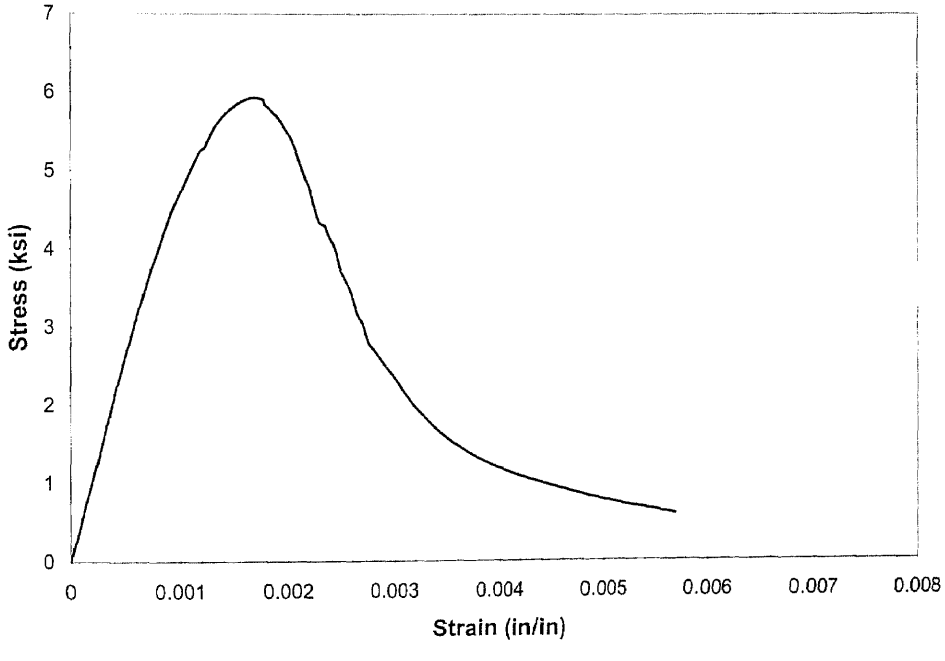

Figure A 5c Stress-Strain Curve for Fly Ash Concrete (16F25) at 28 days Specimen No.3 (3 x 6 inch cylinder)

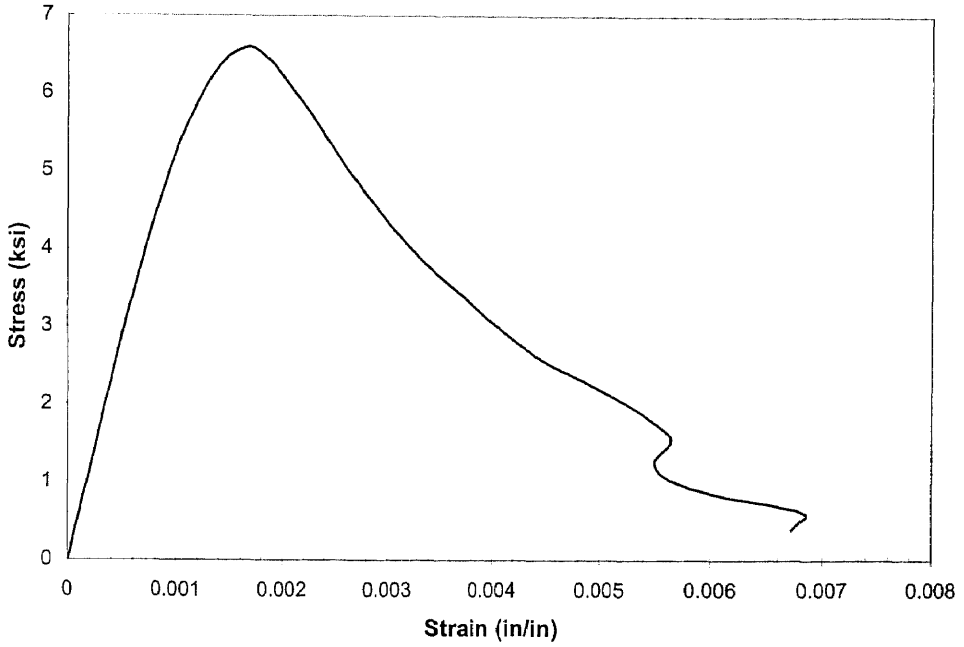

Figure A 5d Stress-Strain Curve for Fly Ash Concrete (16F25) at 56 days Specimen No.1 (3 x 6 inch cylinder)

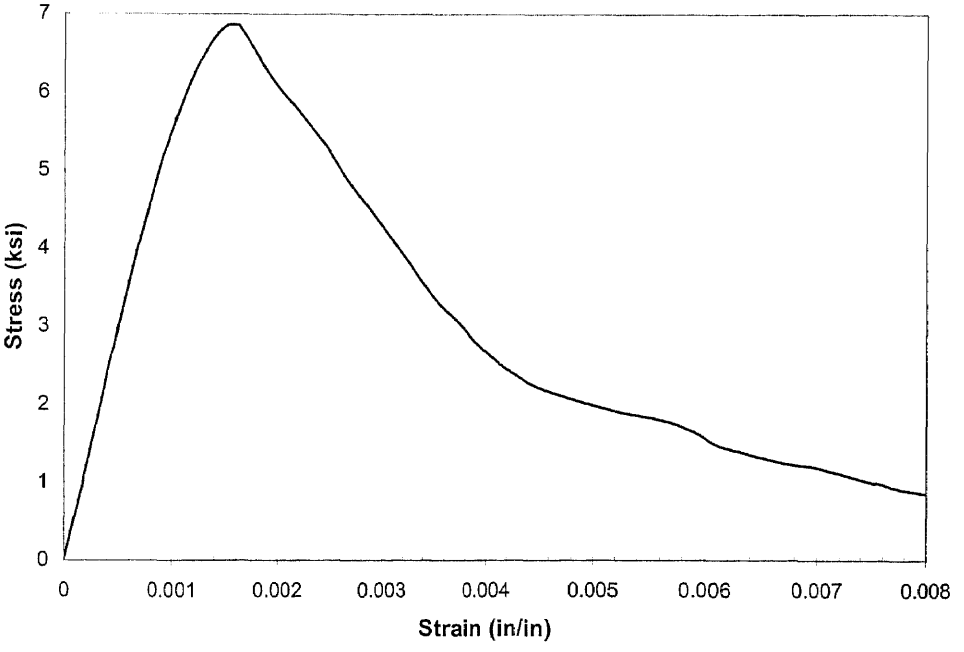

Figure A 5e Stress-Strain Curve for Fly Ash Concrete (16F25) at 56 days Specimen No.2 (3 x 6 inch cylinder)

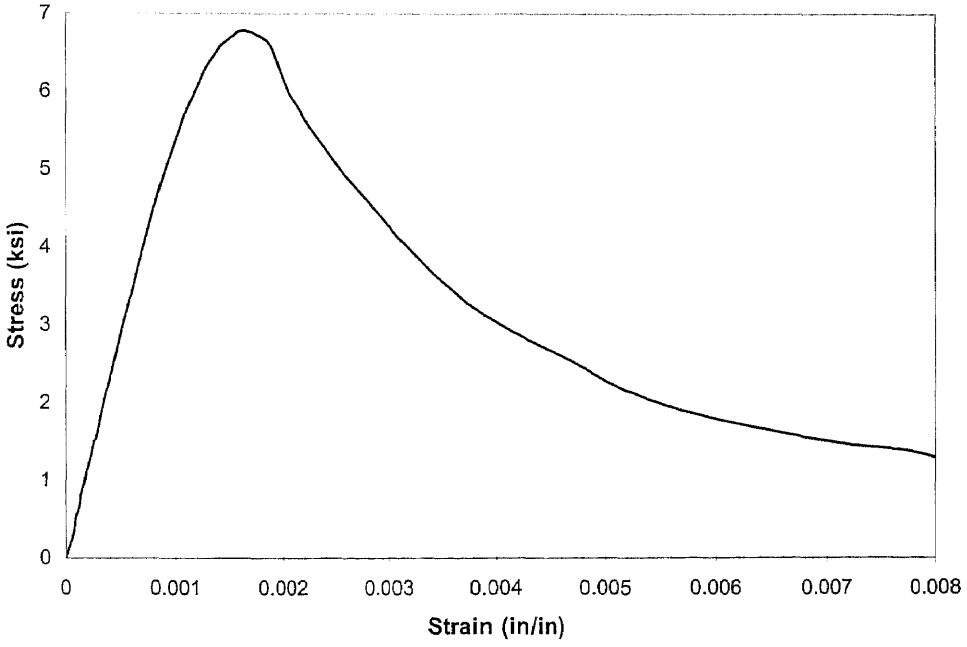

Figure A 5f Stress-Strain Curve for Fly Ash Concrete (16F25) at 56 days Specimen No.3 (3 x 6 inch cylinder)

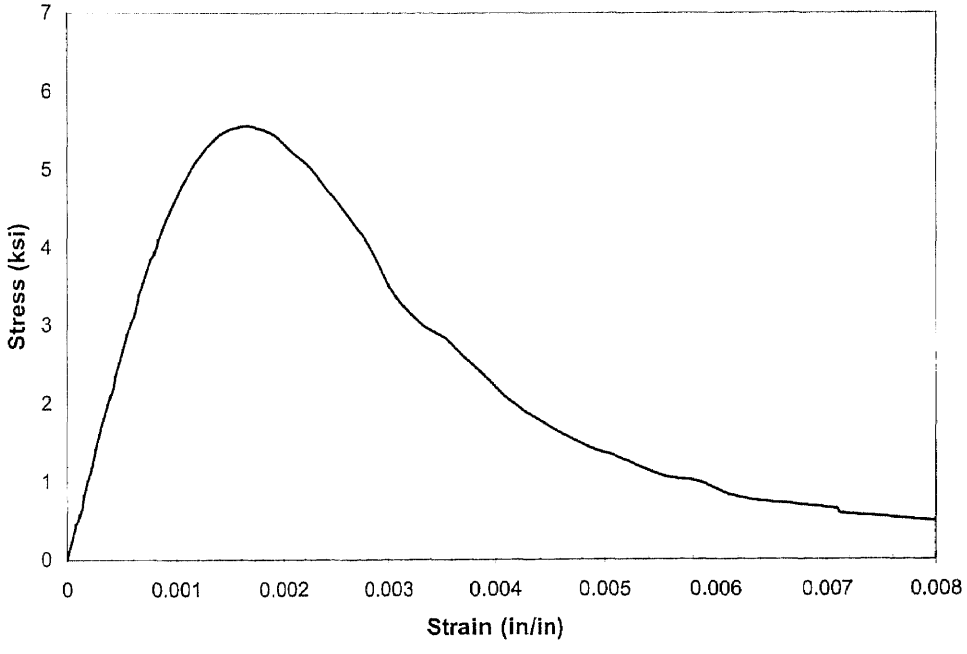

Figure A 6a Stress-Strain Curve for Fly Ash Concrete (18F25) at 28 days Specimen No.1 (3 x 6 inch cylinder)

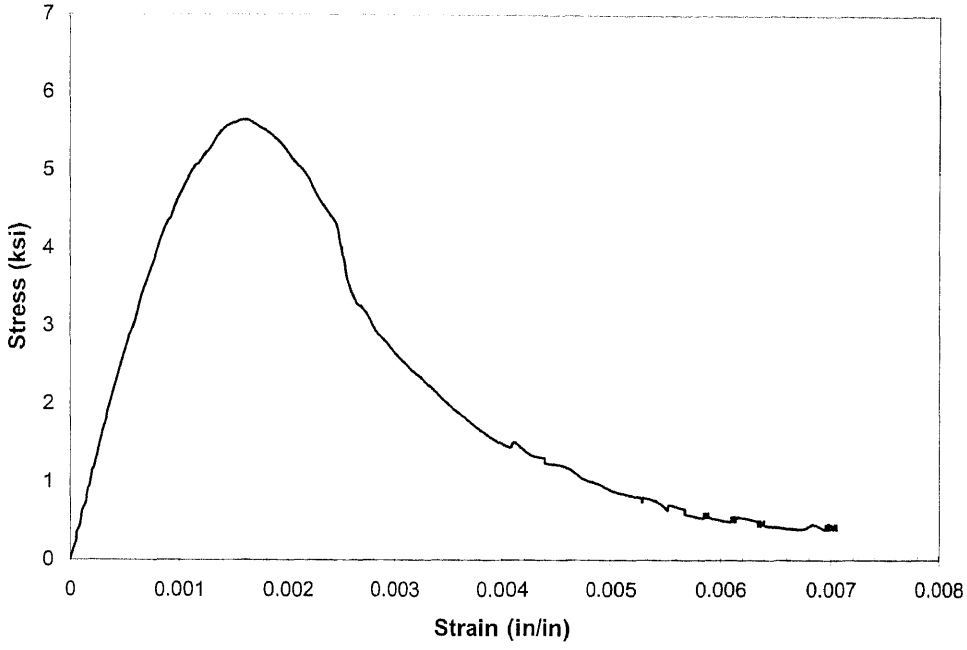

Figure A 6b Stress-Strain Curve for Fly Ash Concrete (18F25) at 28 days Specimen No.2 (3 x 6 inch cylinder)

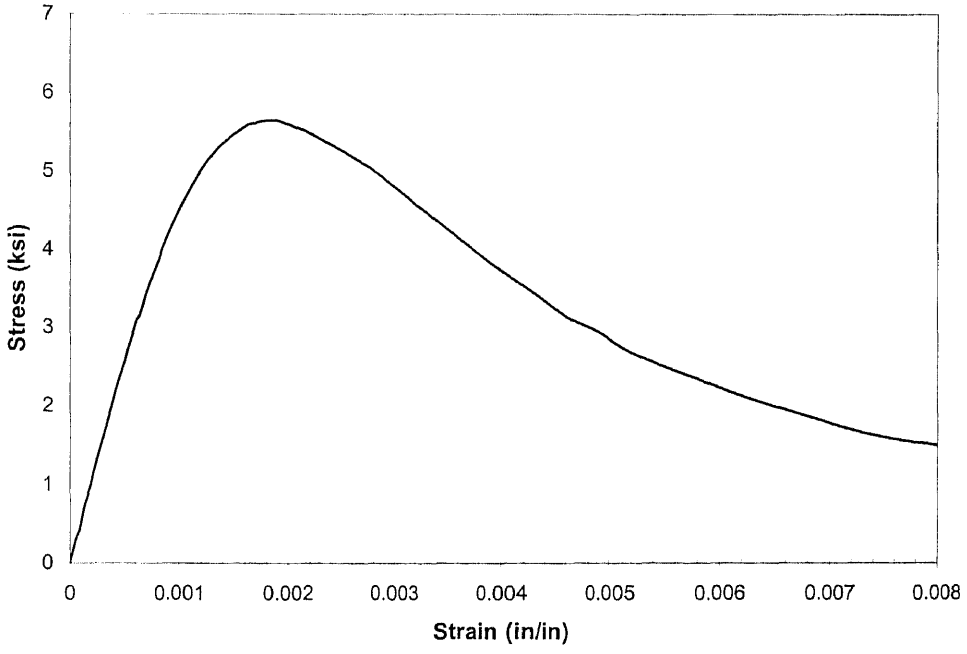

Figure A 6c Stress-Strain Curve for Fly Ash Concrete (18F25) at 28 days Specimen No.3 (3 x 6 inch cylinder)

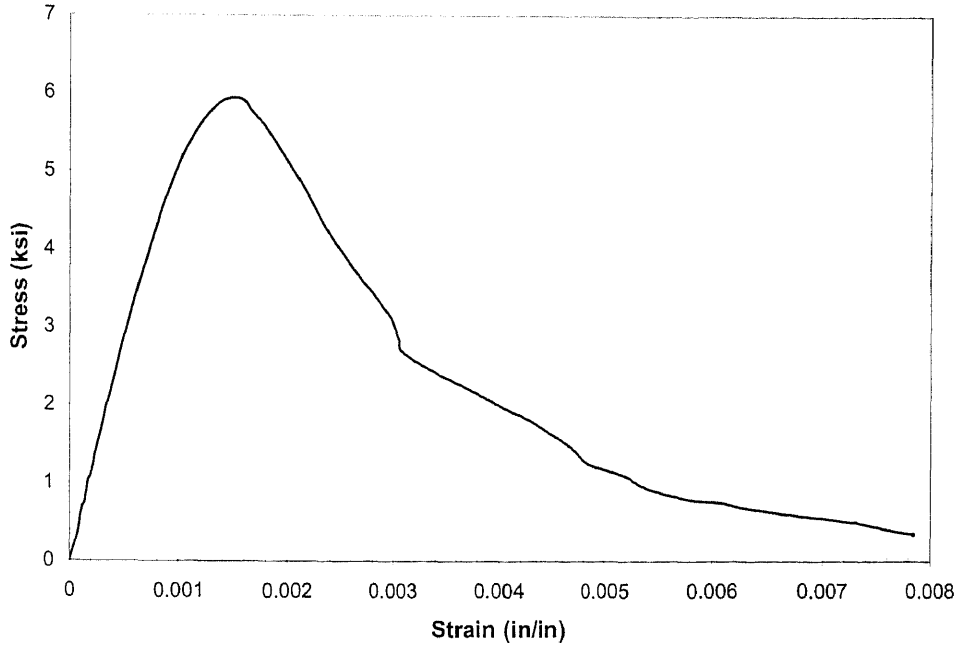

Figure A 6d Stress-Strain Curve for Fly Ash Concrete (18F25) at 56 days Specimen No.1 (3 x 6 inch cylinder)

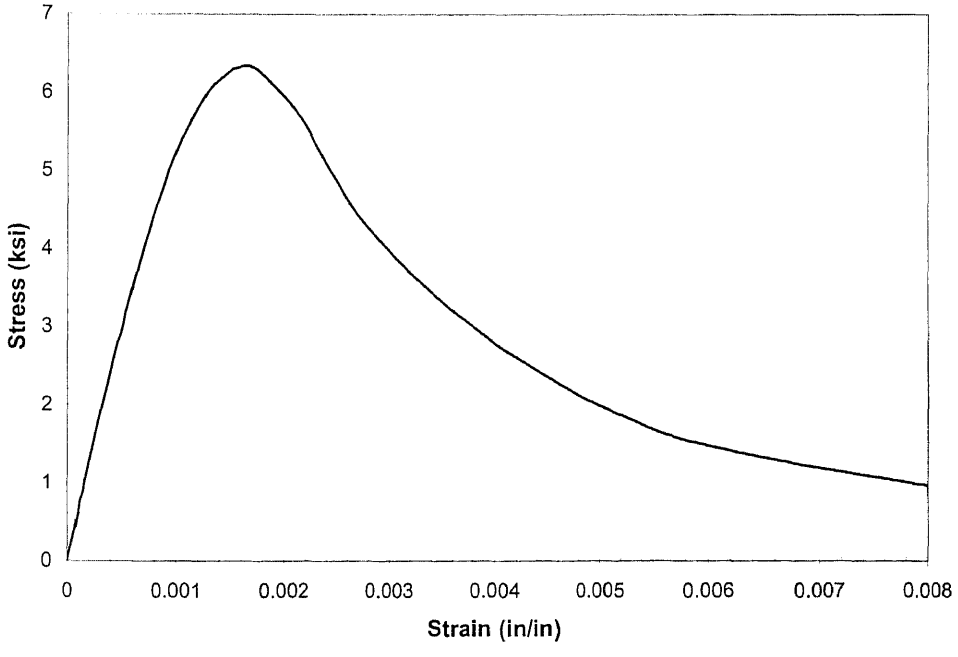

Figure A 6e Stress-Strain Curve for Fly Ash Concrete (18F25) at 56 days Specimen No.2 (3 x 6 inch cylinder)

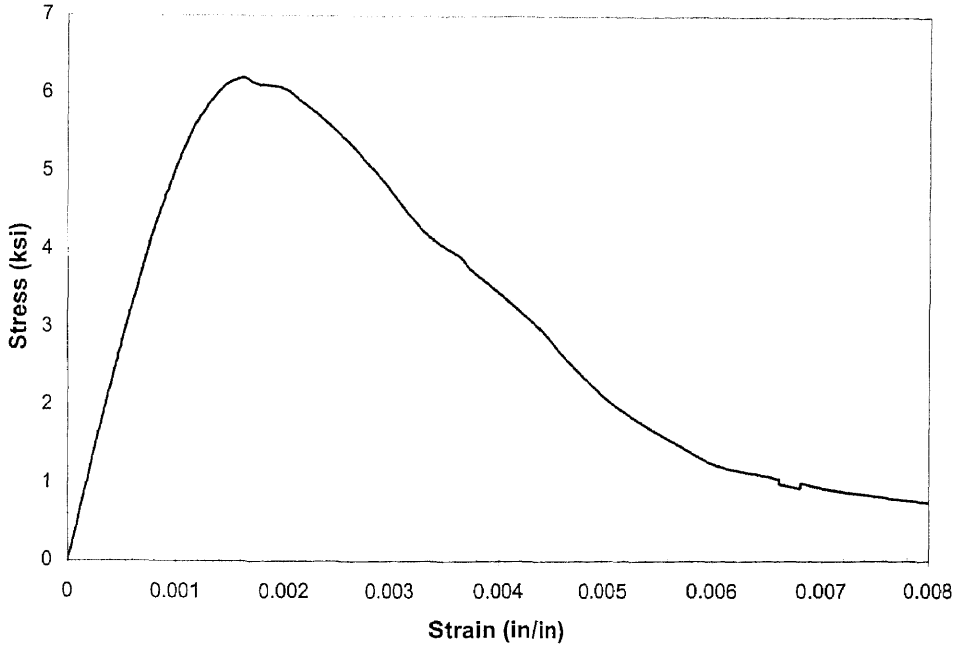

Figure A 6f Stress-Strain Curve for Fly Ash Concrete (18F25) at 56 days Specimen No.3 (4 x 8 inch cylinder)

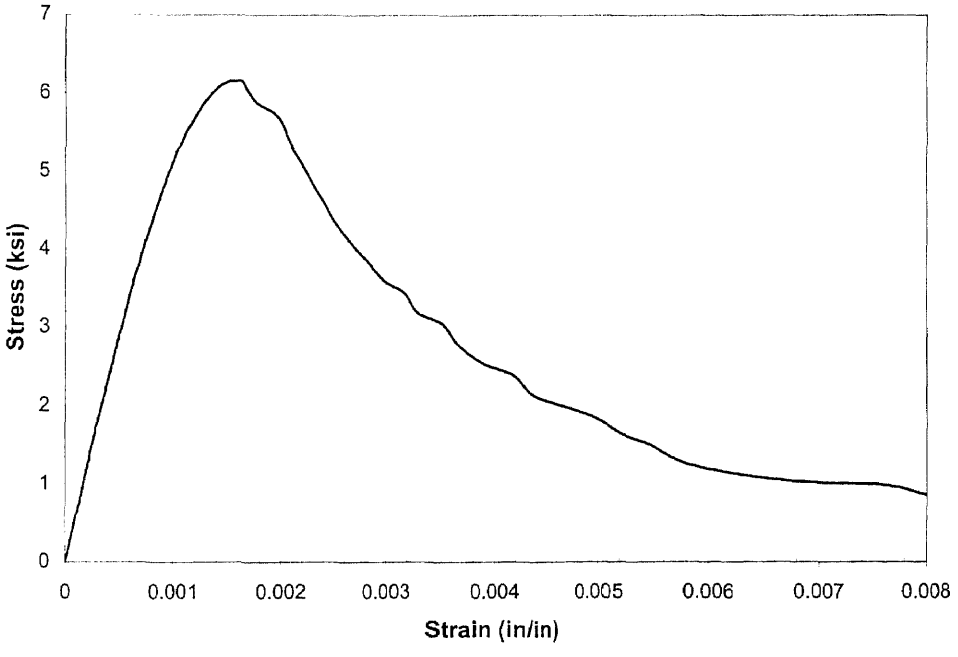

Figure A 6g Stress-Strain Curve for Fly Ash Concrete (18F25) at 56 days Specimen No.4 (4 x 8 inch cylinder)

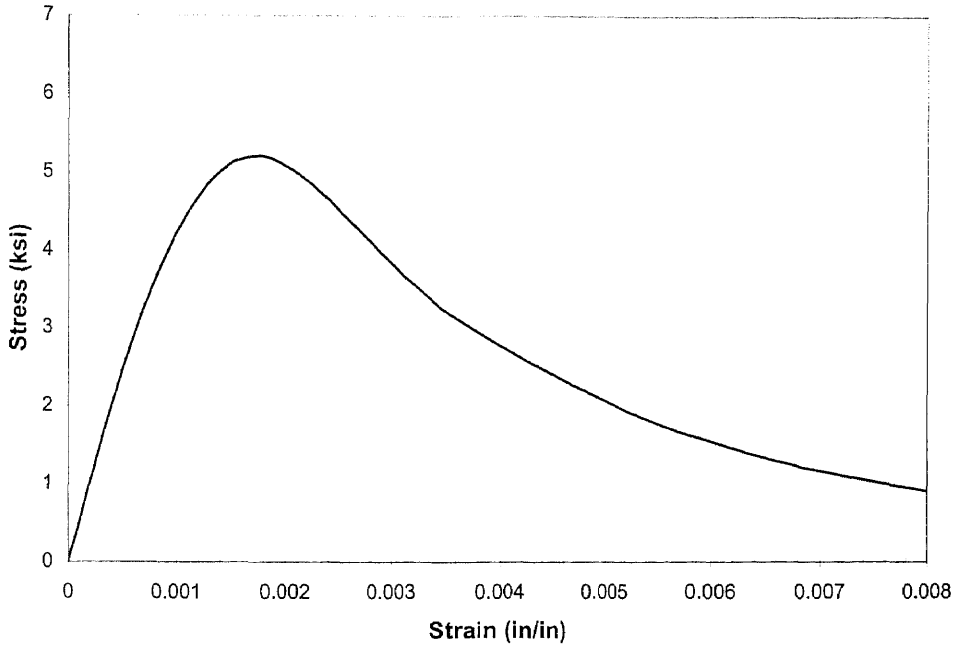

Figure A 7a Stress-Strain Curve for Fly Ash Concrete (18C25) at 28 days Specimen No.1 (3 x 6 inch cylinder)

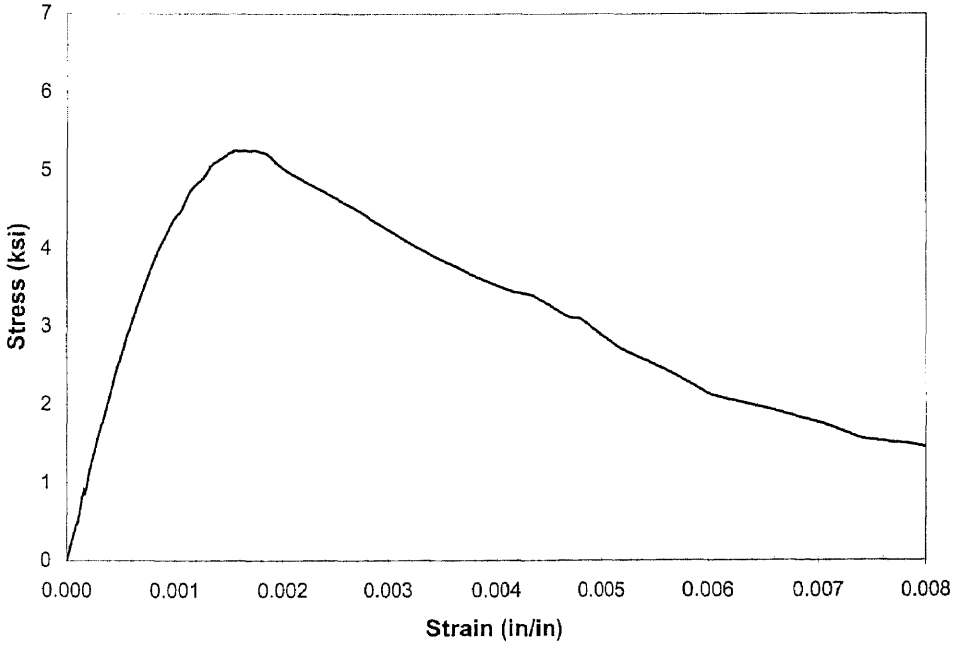

Figure A 7b Stress-Strain Curve for Fly Ash Concrete (18C25) at 28 days Specimen No.2 (3 x 6 inch cylinder)

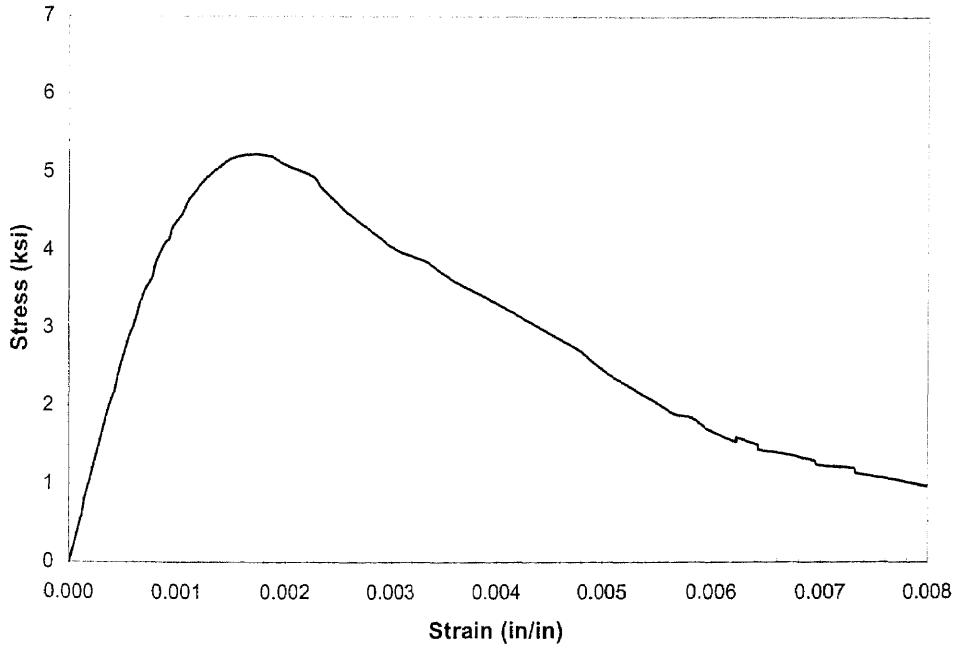

Figure A 7c Stress-Strain Curve for Fly Ash Concrete (18C25) at 28 days Specimen No.3 (3 x 6 inch cylinder)

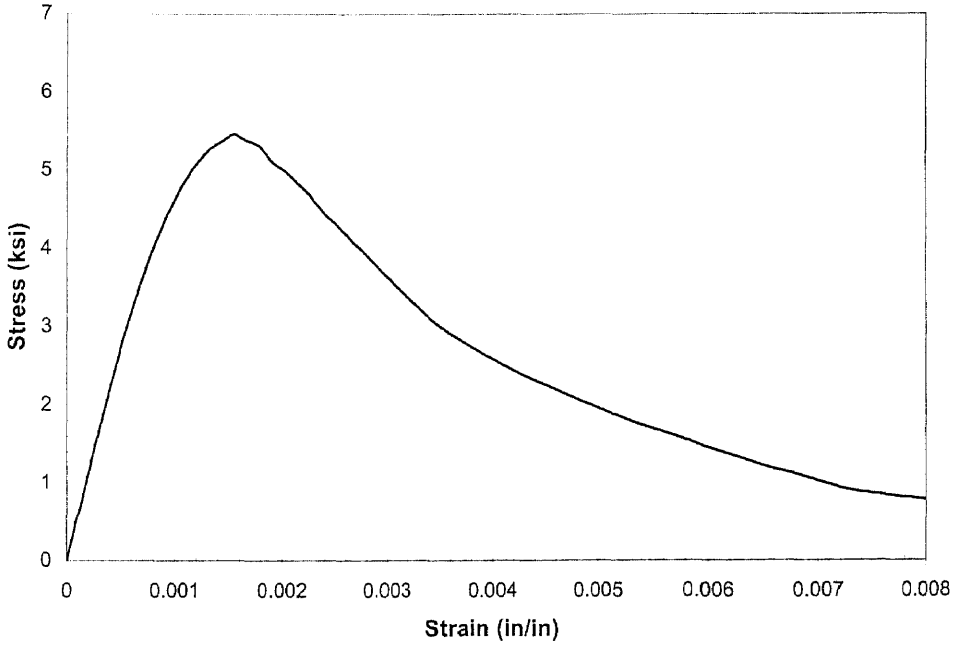

Figure A 7d Stress-Strain Curve for Fly Ash Concrete (18C25) at 56 days Specimen No.1 (3 x 6 inch cylinder)

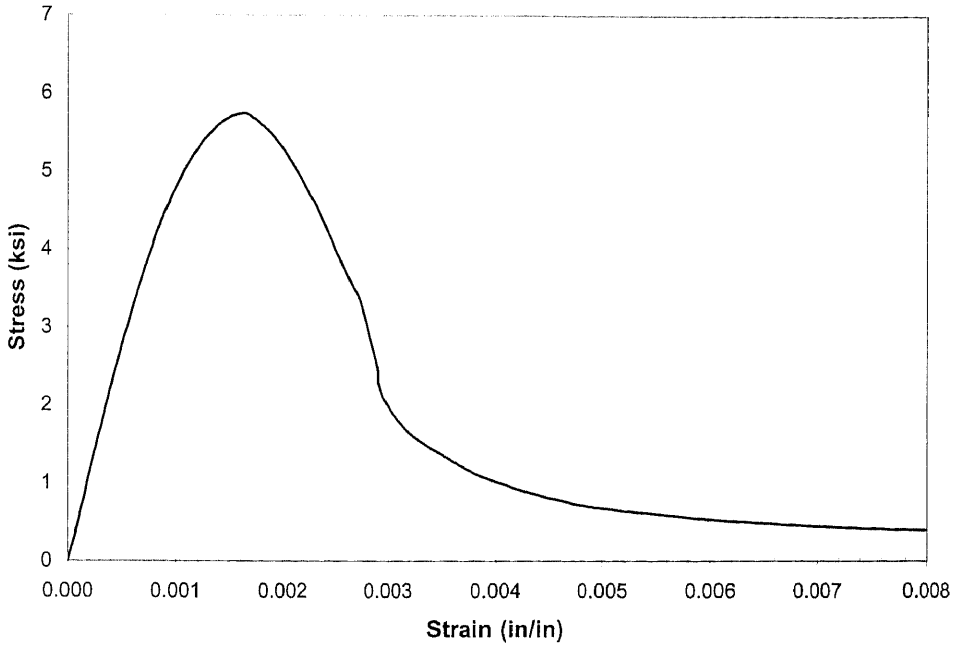

Figure A 7e Stress-Strain Curve for Fly Ash Concrete (18C25) at 56 days Specimen No.2 (3 x 6 inch cylinder)

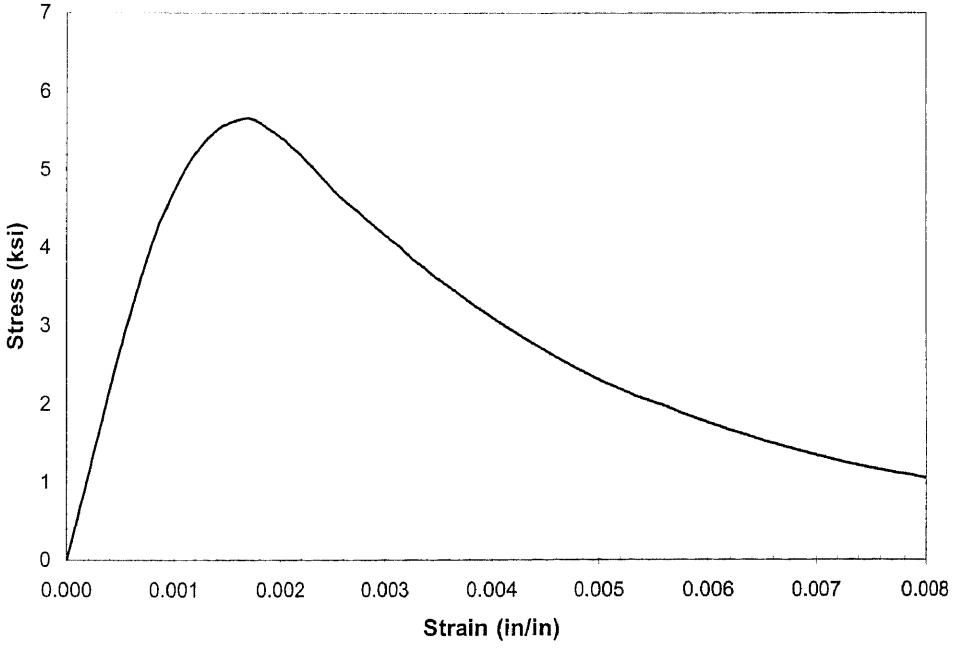

Figure A 7f Stress-Strain Curve for Fly Ash Concrete (18C25) at 56 days Specimen No.3 (3 x 6 inch cylinder)

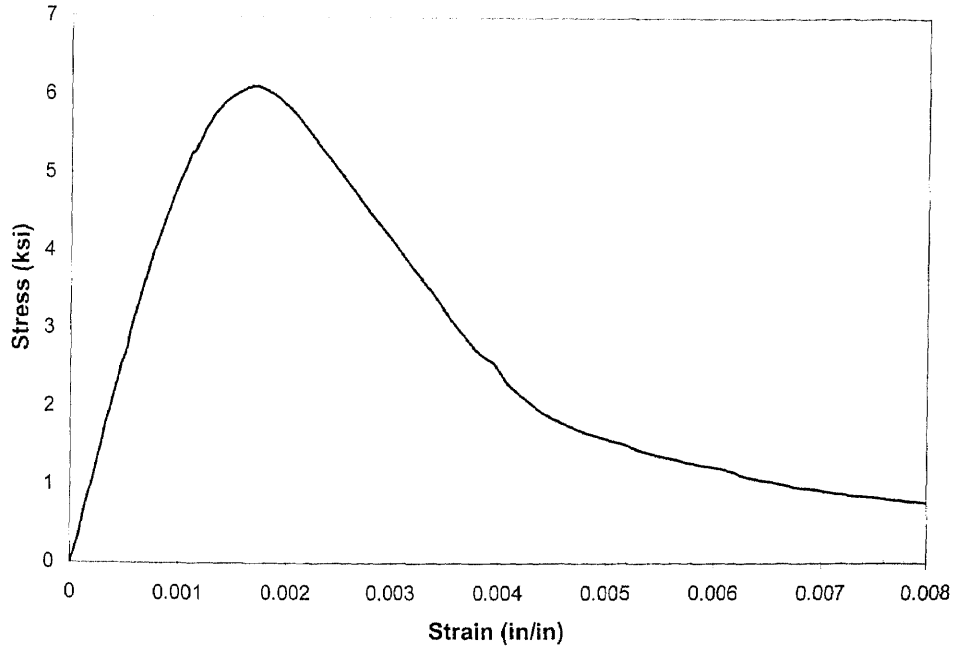

Figure A 8a Stress-Strain Curve for Fly Ash Concrete (MO25) at 28 days Specimen No.1 (3 x 6 inch cylinder)

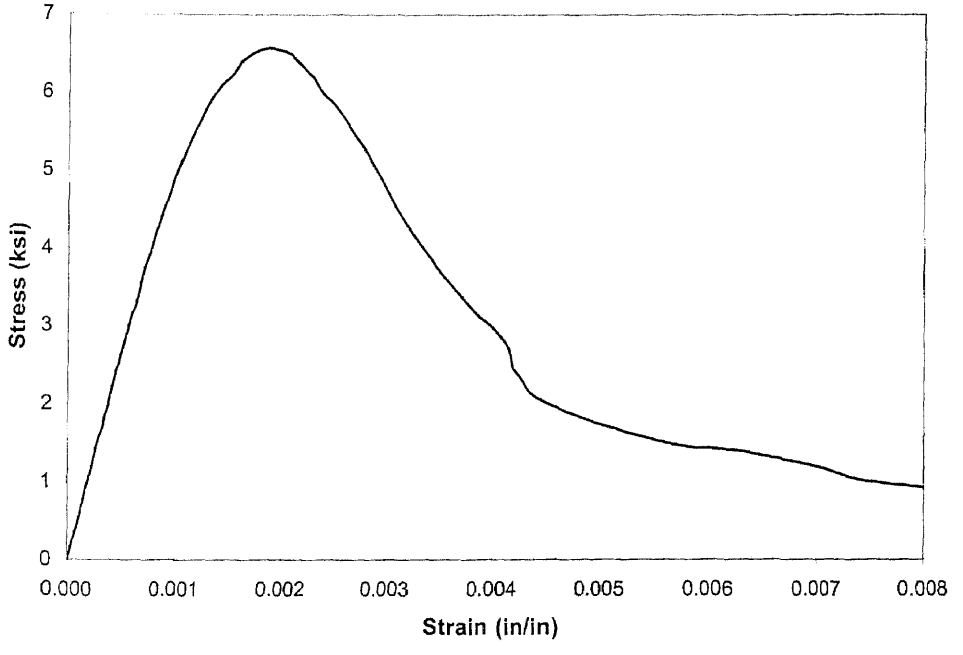

Figure A 8b Stress-Strain Curve for Fly Ash Concrete (MO25) at 28 days Specimen No.2 (3 x 6 inch cylinder)

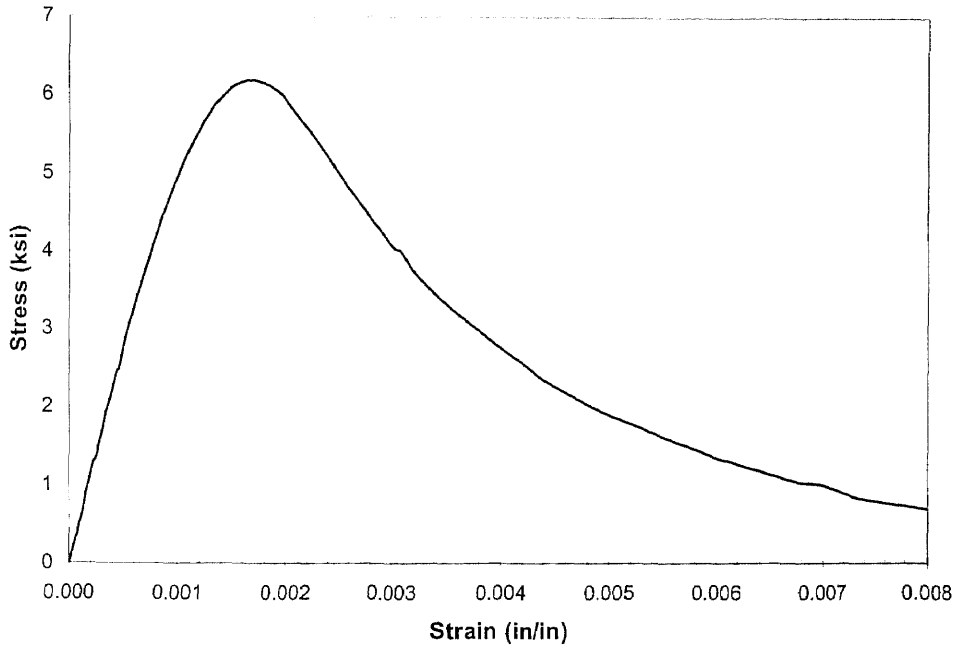

Figure A 8c Stress-Strain Curve for Fly Ash Concrete (MO25) at 28 days Specimen No.3 (3 x 6 inch cylinder)

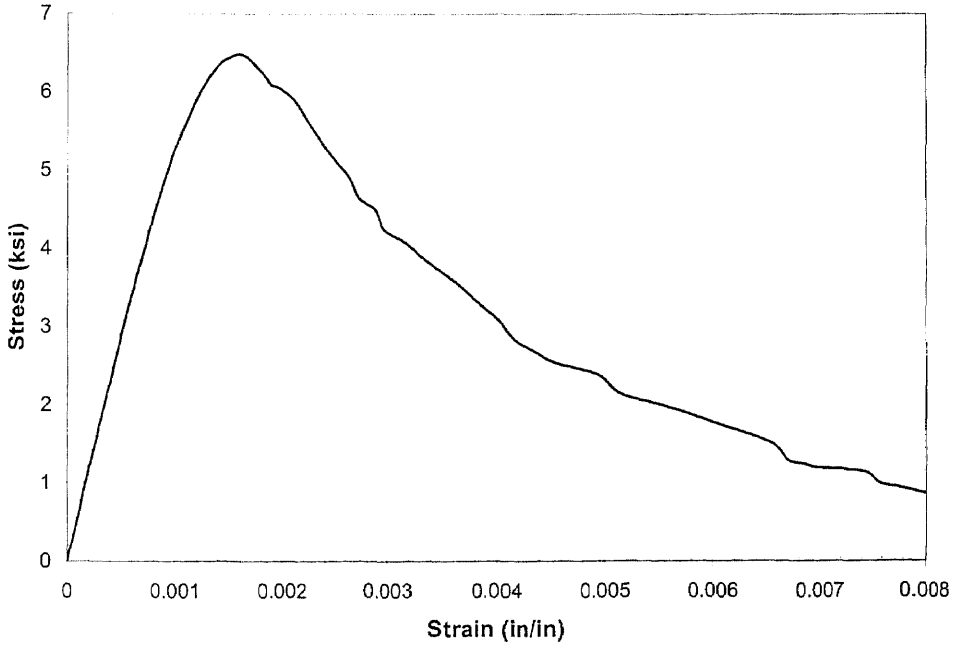

Figure A 8d Stress-Strain Curve for Fly Ash Concrete (MO25) at 56 days Specimen No.1 (3 x 6 inch cylinder)

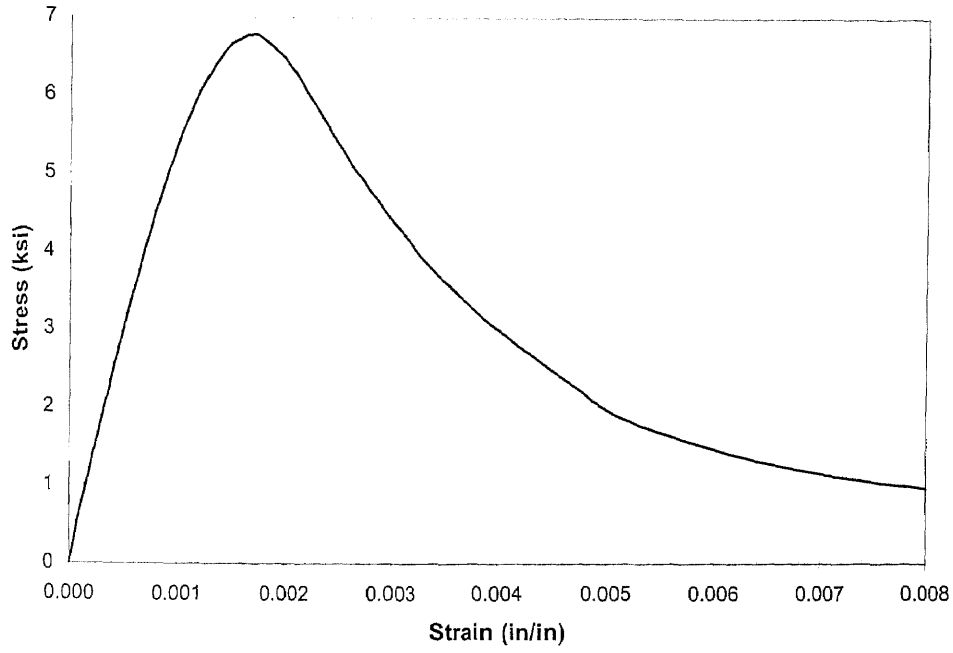

Figure A 8e Stress-Strain Curve for Fly Ash Concrete (MO25) at 56 days Specimen No.2 (3 x 6 inch cylinder)

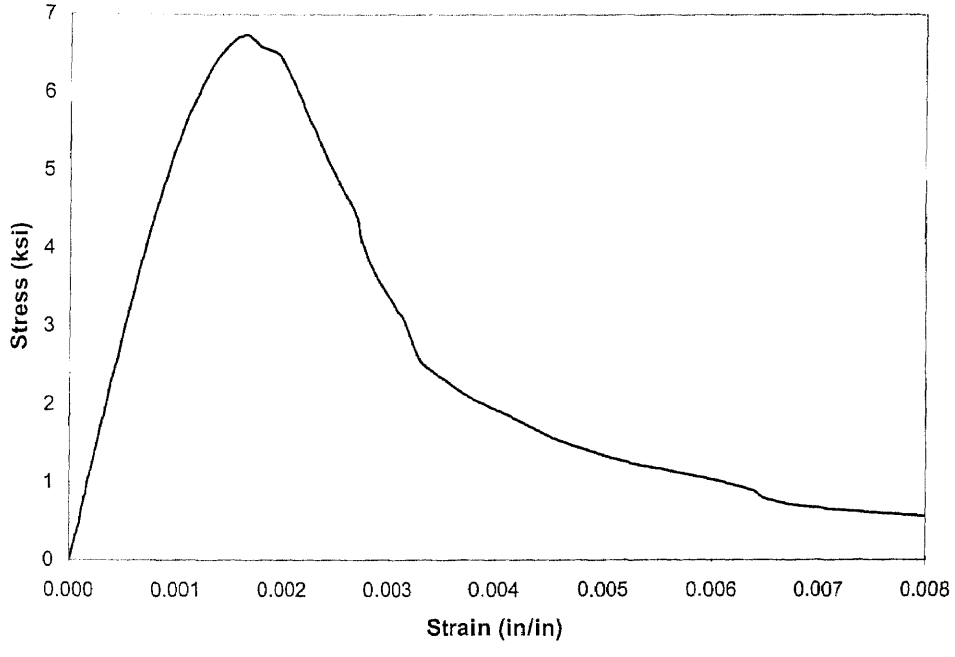

Figure A 8f Stress-Strain Curve for Fly Ash Concrete (MO25) at 56 days Specimen No.3 (3 x 6 inch cylinder)

APPENDIX B

EXPERIMENTAL DATA OF BEAM TESTS

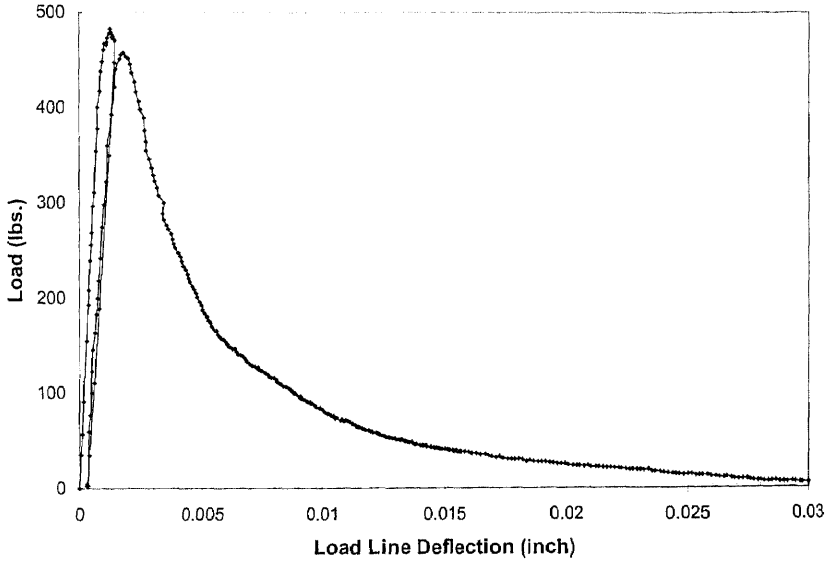

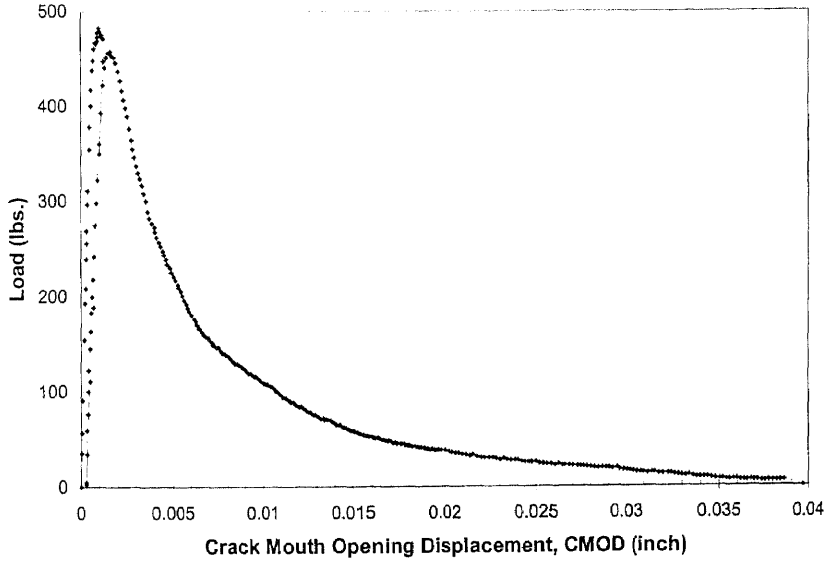

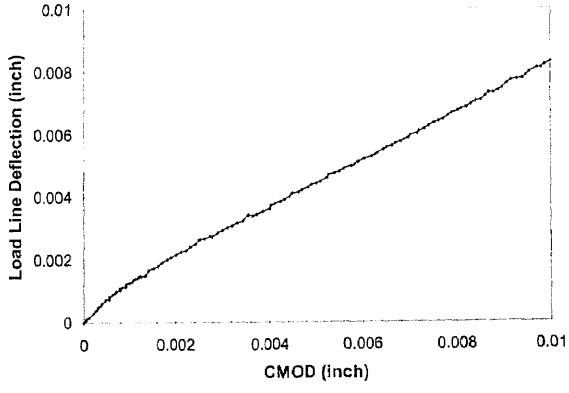

Figure B 1a Load-Deflection-CMOD Relationship of Control Concrete (CC) (Specimen No.1)

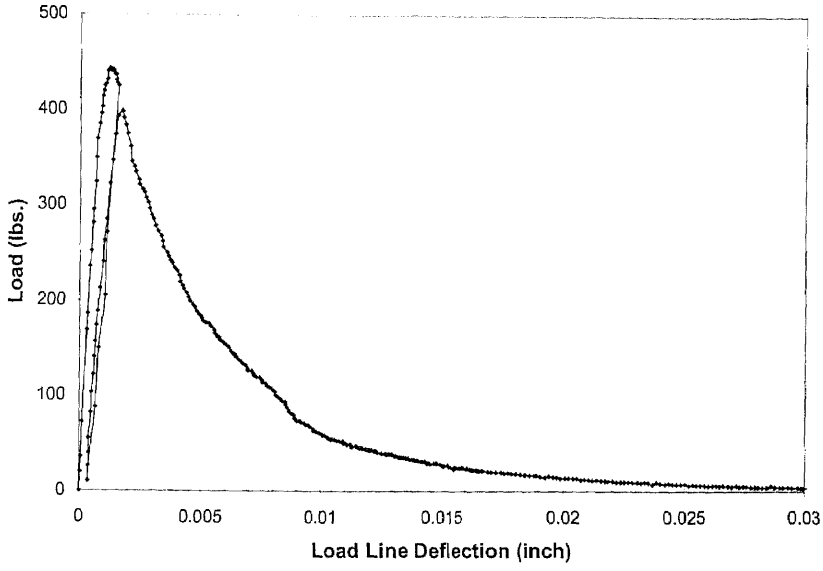

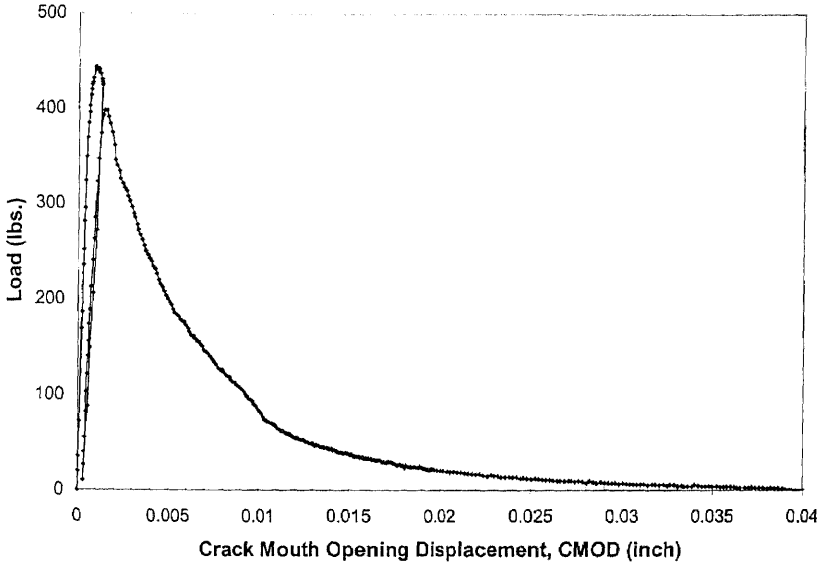

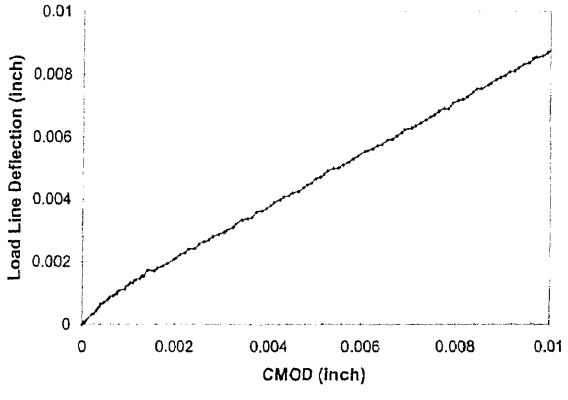

Figure B 1b Load-Deflection-CMOD Relationship of Control Concrete (CC) (Specimen No.2)

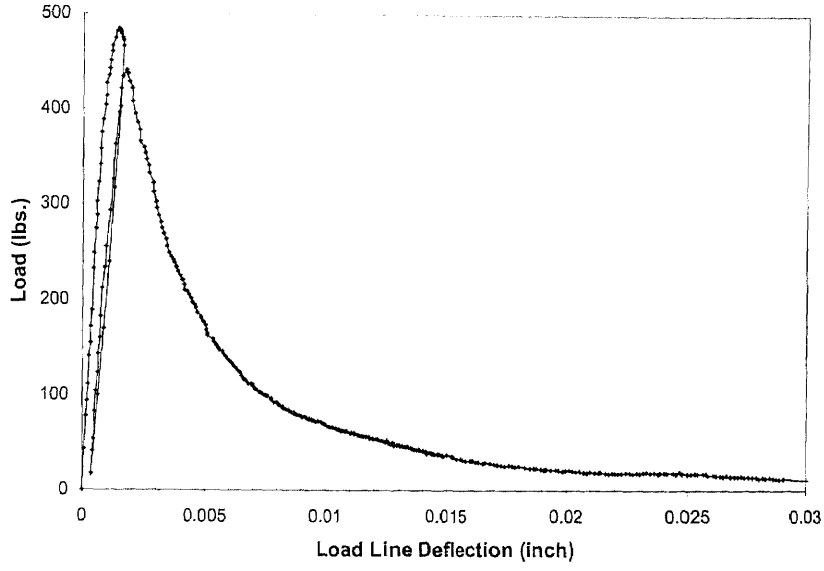

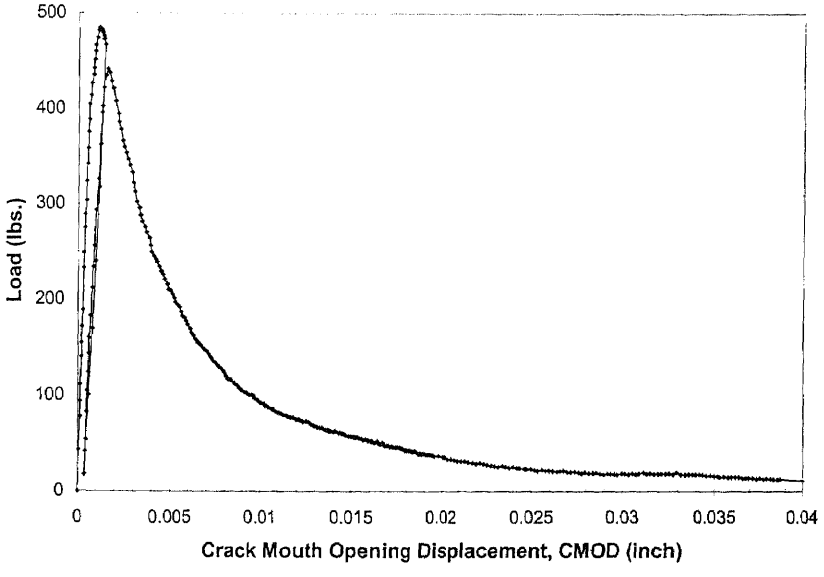

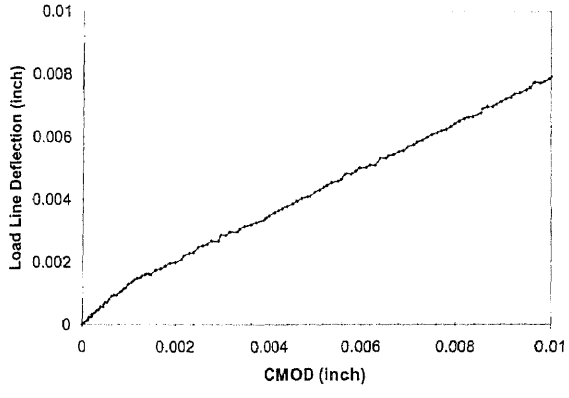

Figure B 1c Load-Deflection-CMOD Relationship of Control Concrete (CC) (Specimen No.3)

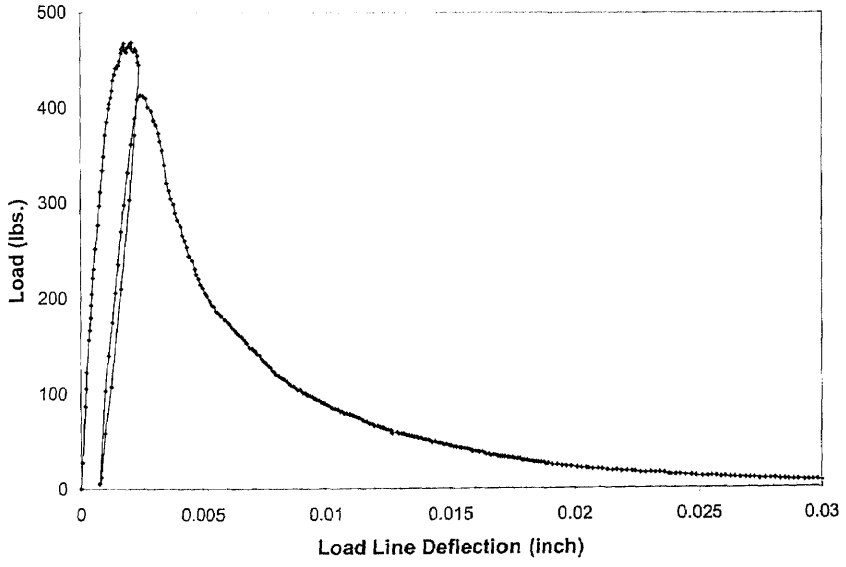

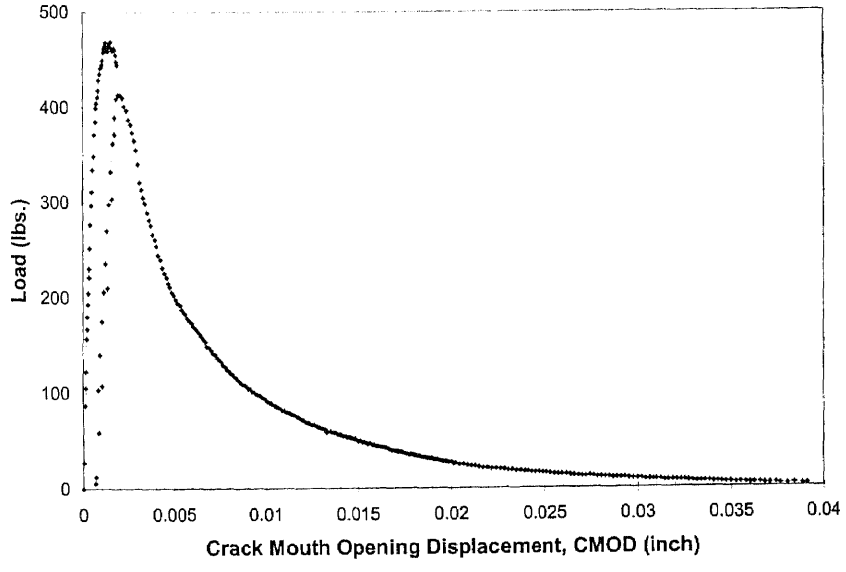

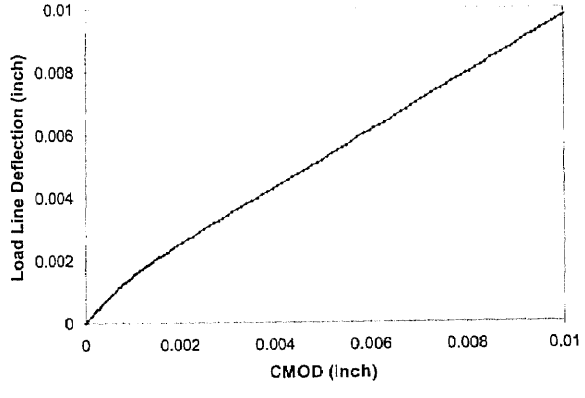

Figure B 2a Load-Deflection-CMOD Relationship of Silica Fume Concrete (SF) (Specimen No.1)

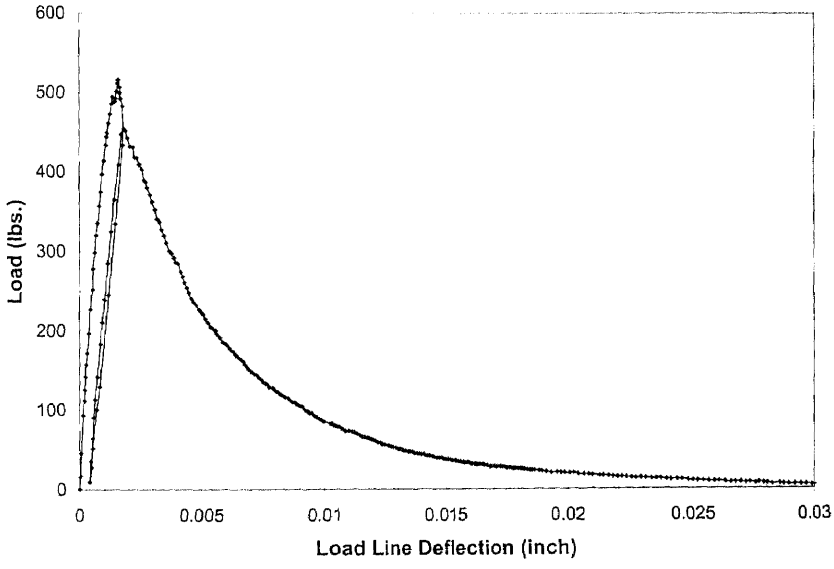

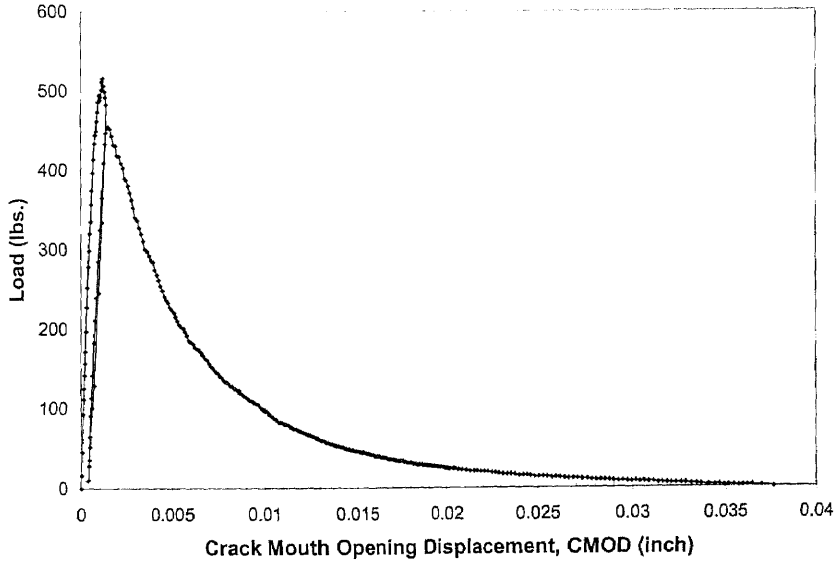

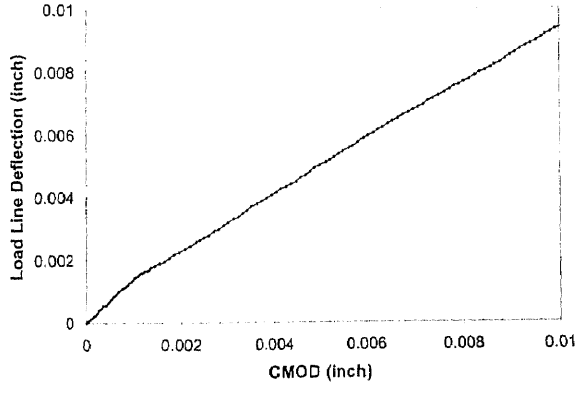

Figure B 2b Load-Deflection-CMOD Relationship of Silica Fume Concrete (SF) (Specimen No.2)

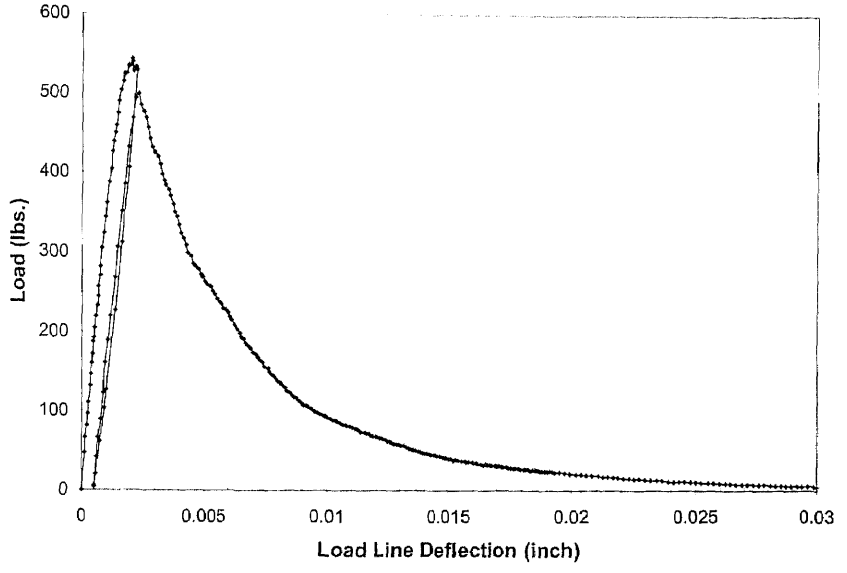

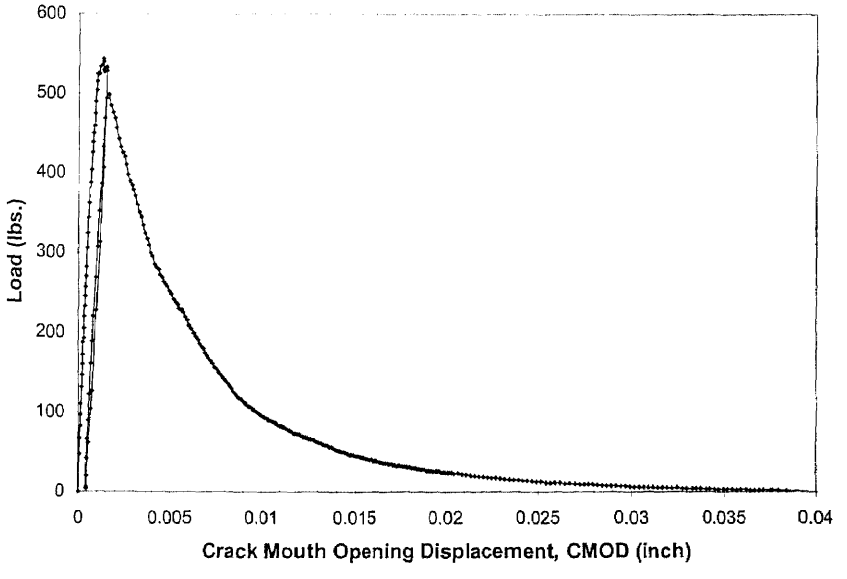

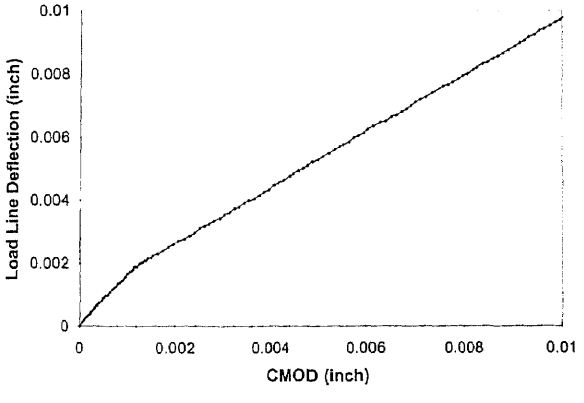

Figure B 2c Load-Deflection-CMOD Relationship of Silica Fume Concrete (SF) (Specimen No.3)

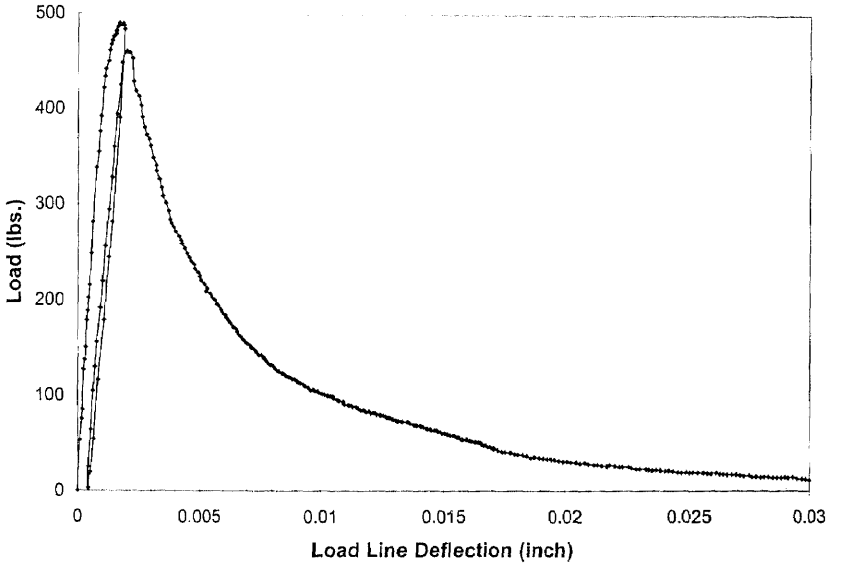

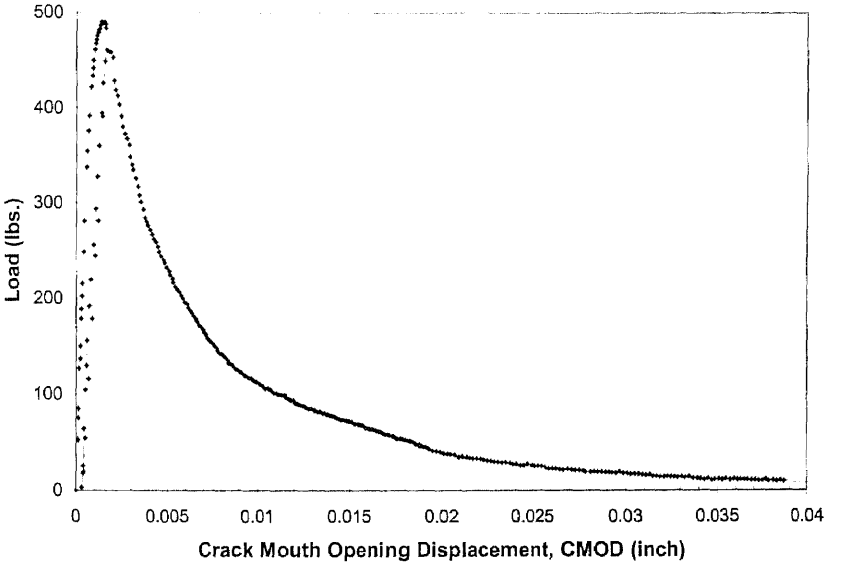

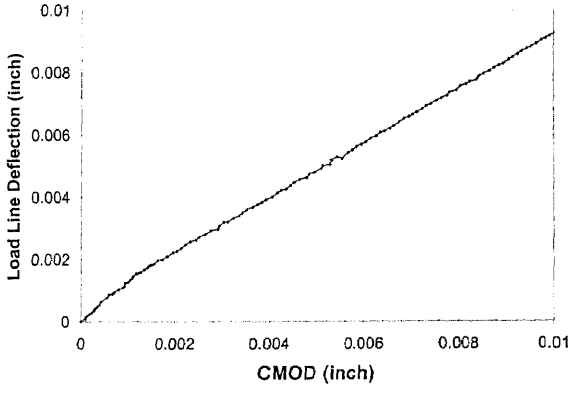

Figure B 3a Load-Deflection-CMOD Relationship of Fly Ash Concrete (13F25) (Specimen No.1)

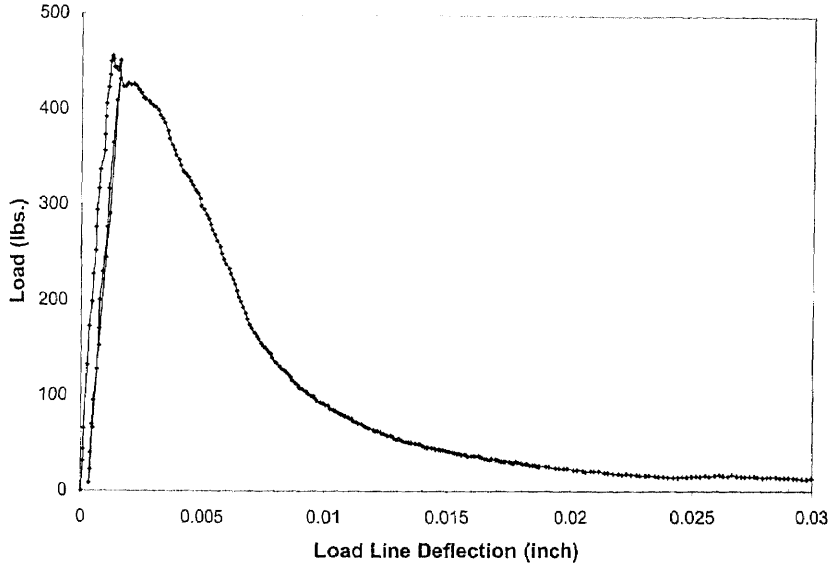

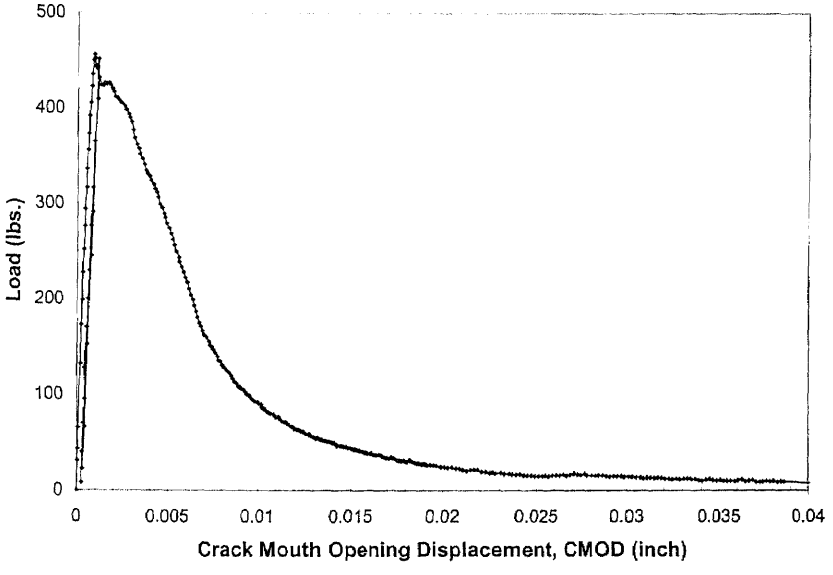

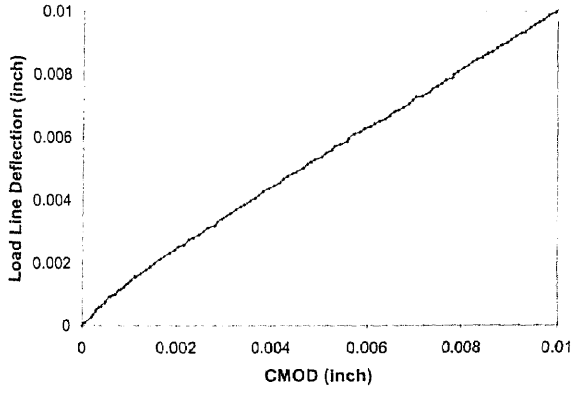

Figure B 3b Load-Deflection-CMOD Relationship of Fly Ash Concrete (13F25) (Specimen No.2)

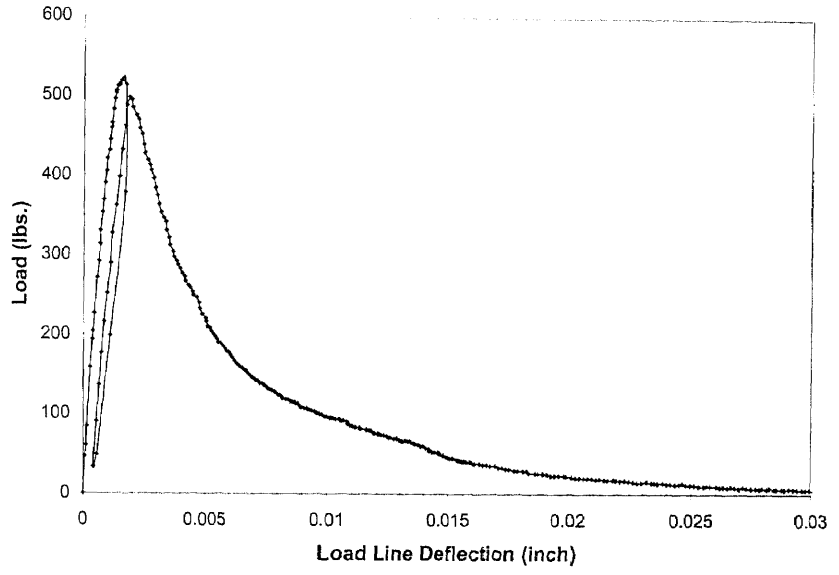

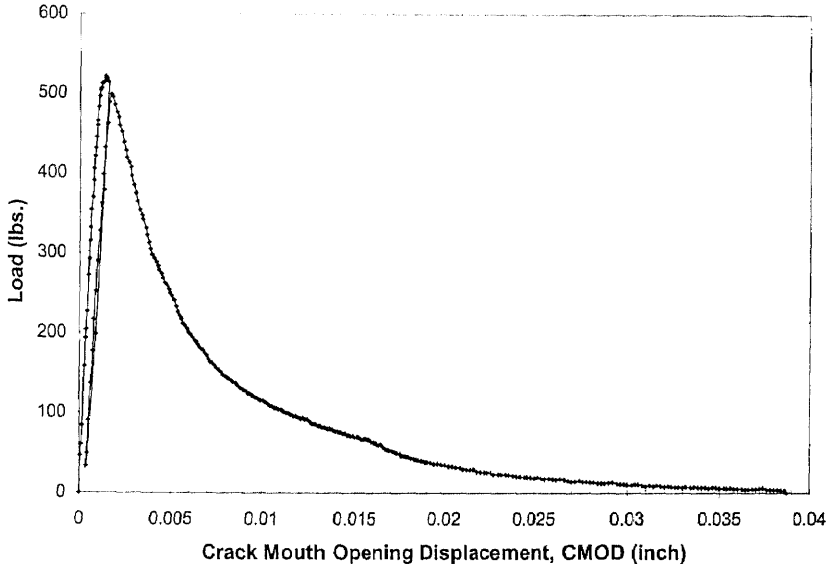

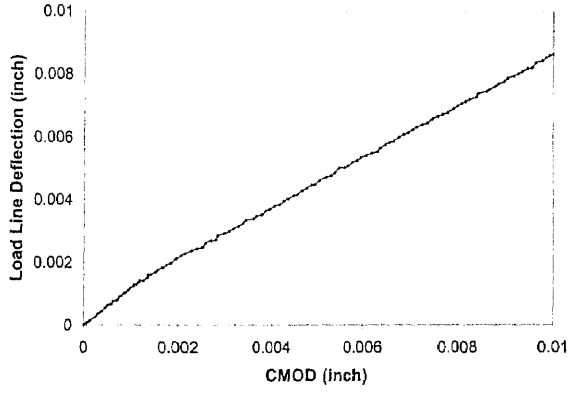

Figure B 3c Load-Deflection-CMOD Relationship of Fly Ash Concrete (13F25) (Specimen No.3)

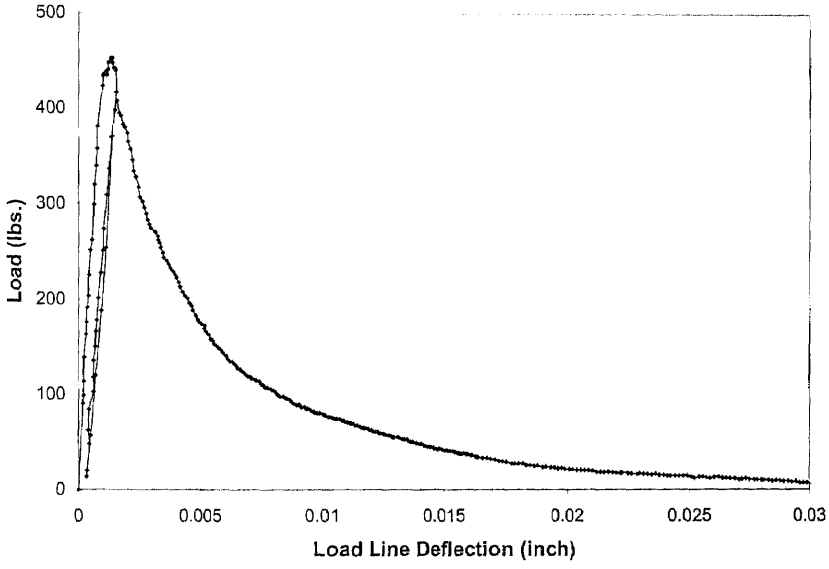

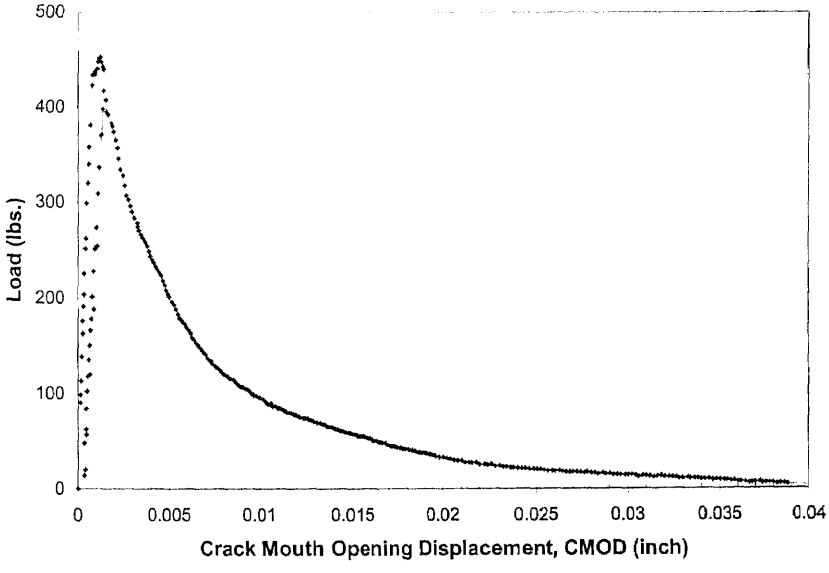

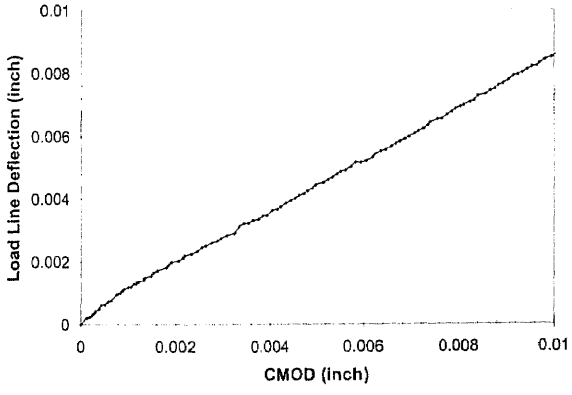

Figure B 4a Load-Deflection-CMOD Relationship of Fly Ash Concrete (15F25) (Specimen No.1)

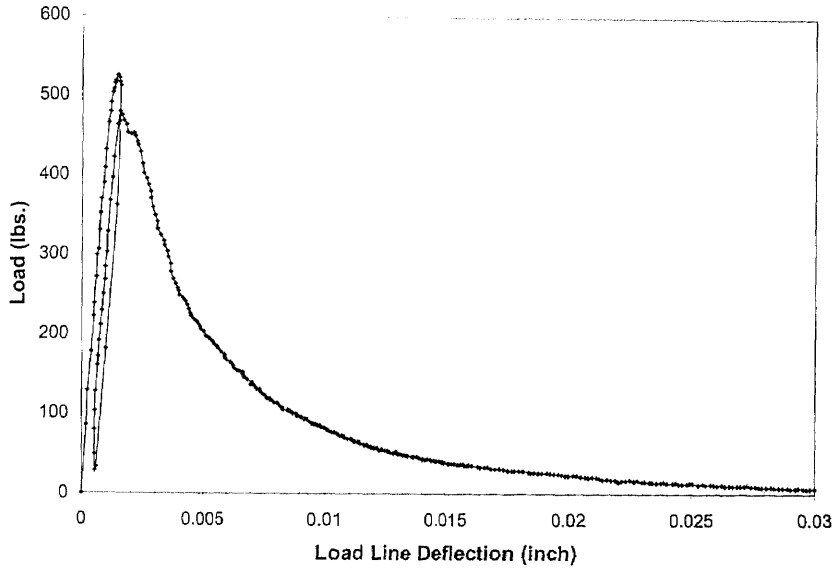

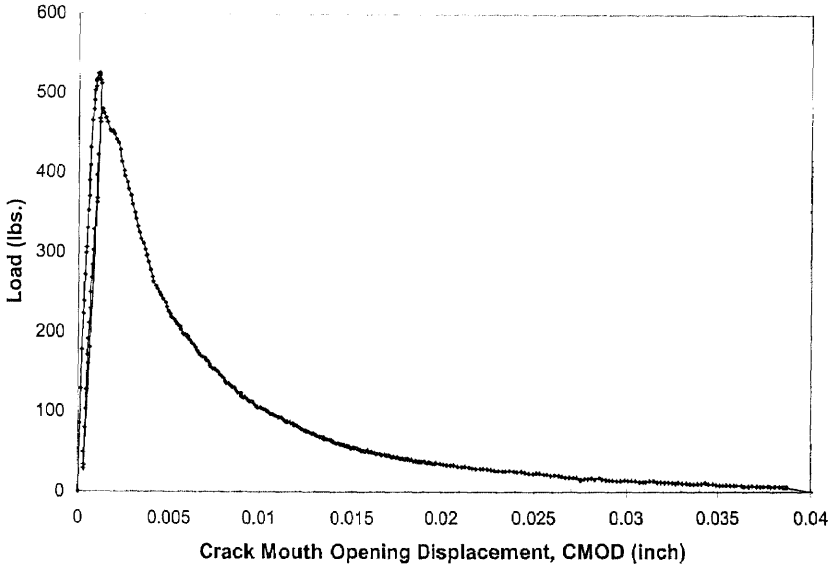

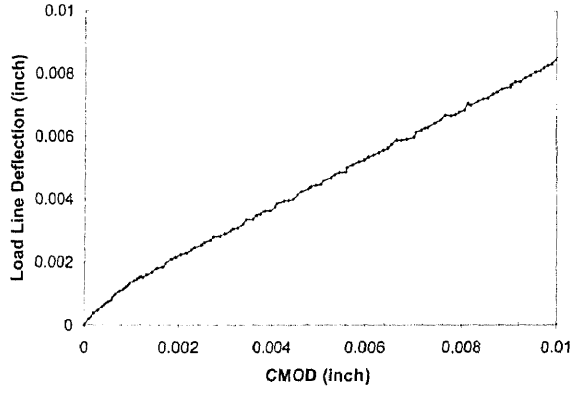

Figure B 4b Load-Deflection-CMOD Relationship of Fly Ash Concrete (15F25) (Specimen No.2)

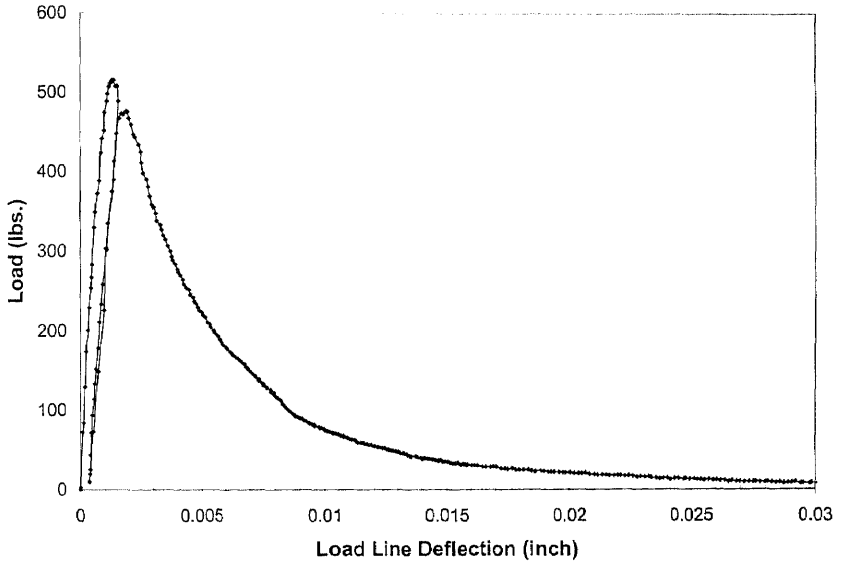

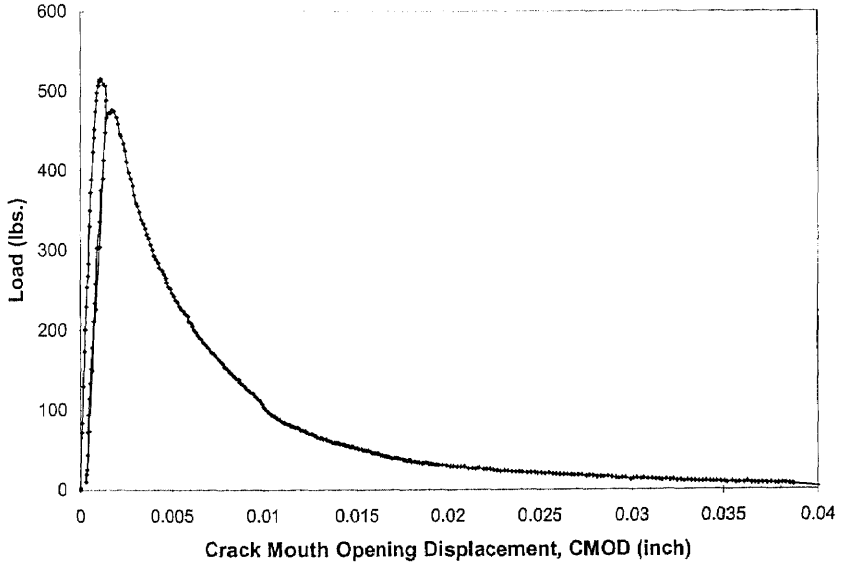

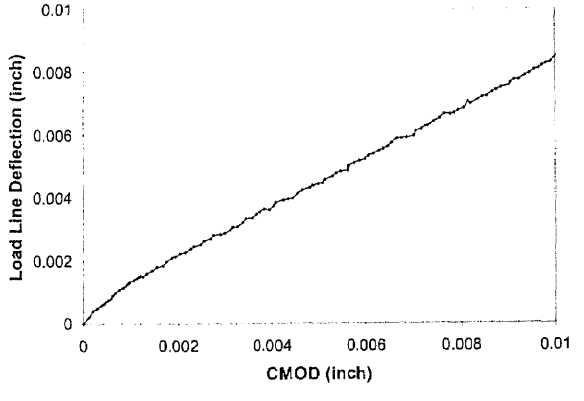

Figure B 4c Load-Deflection-CMOD Relationship of Fly Ash Concrete (15F25) (Specimen No.3)

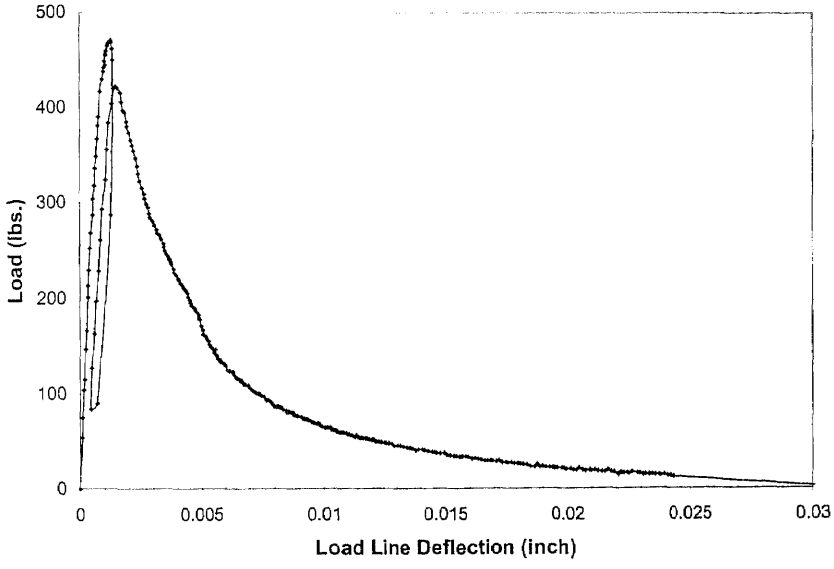

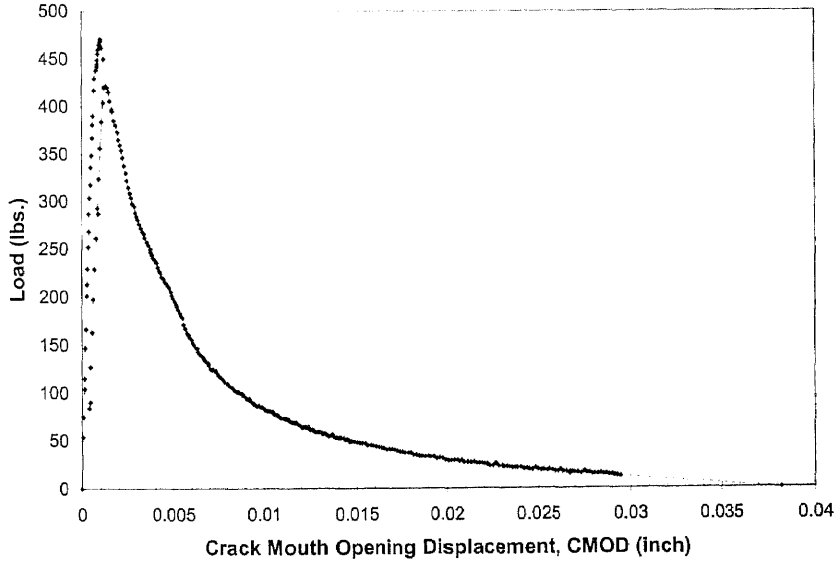

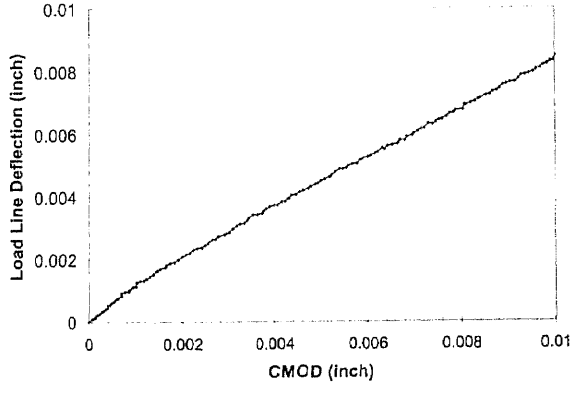

Figure B 5a Load-Deflection-CMOD Relationship of Fly Ash Concrete (16F25) (Specimen No.1)

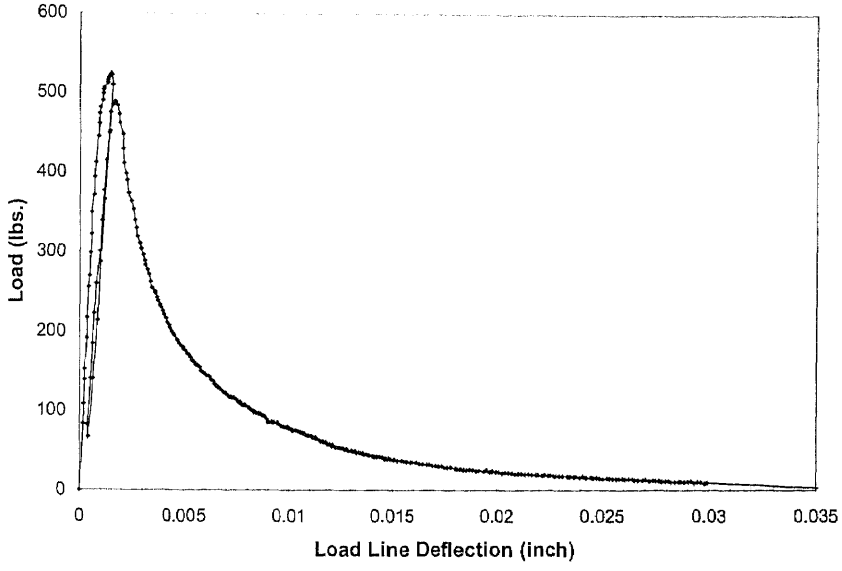

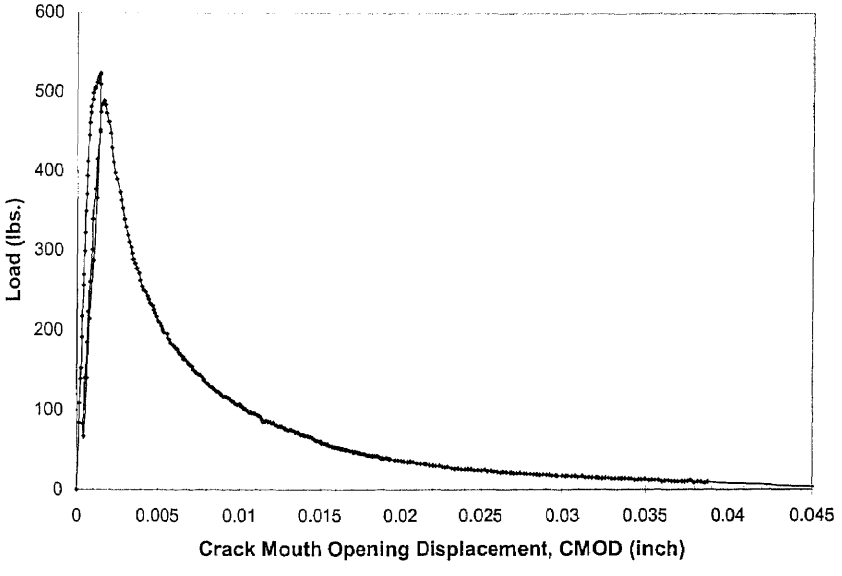

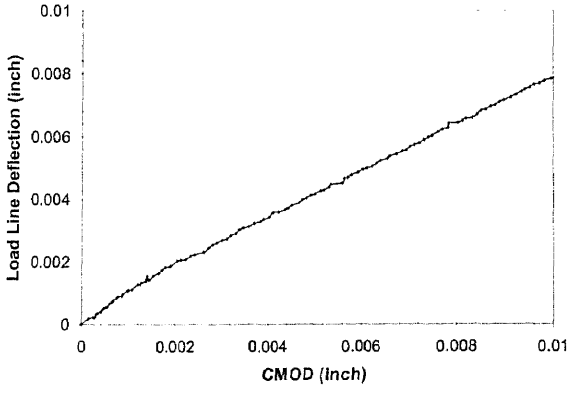

Figure B 5b Load-Deflection-CMOD Relationship of Fly Ash Concrete (16F25) (Specimen No.2)

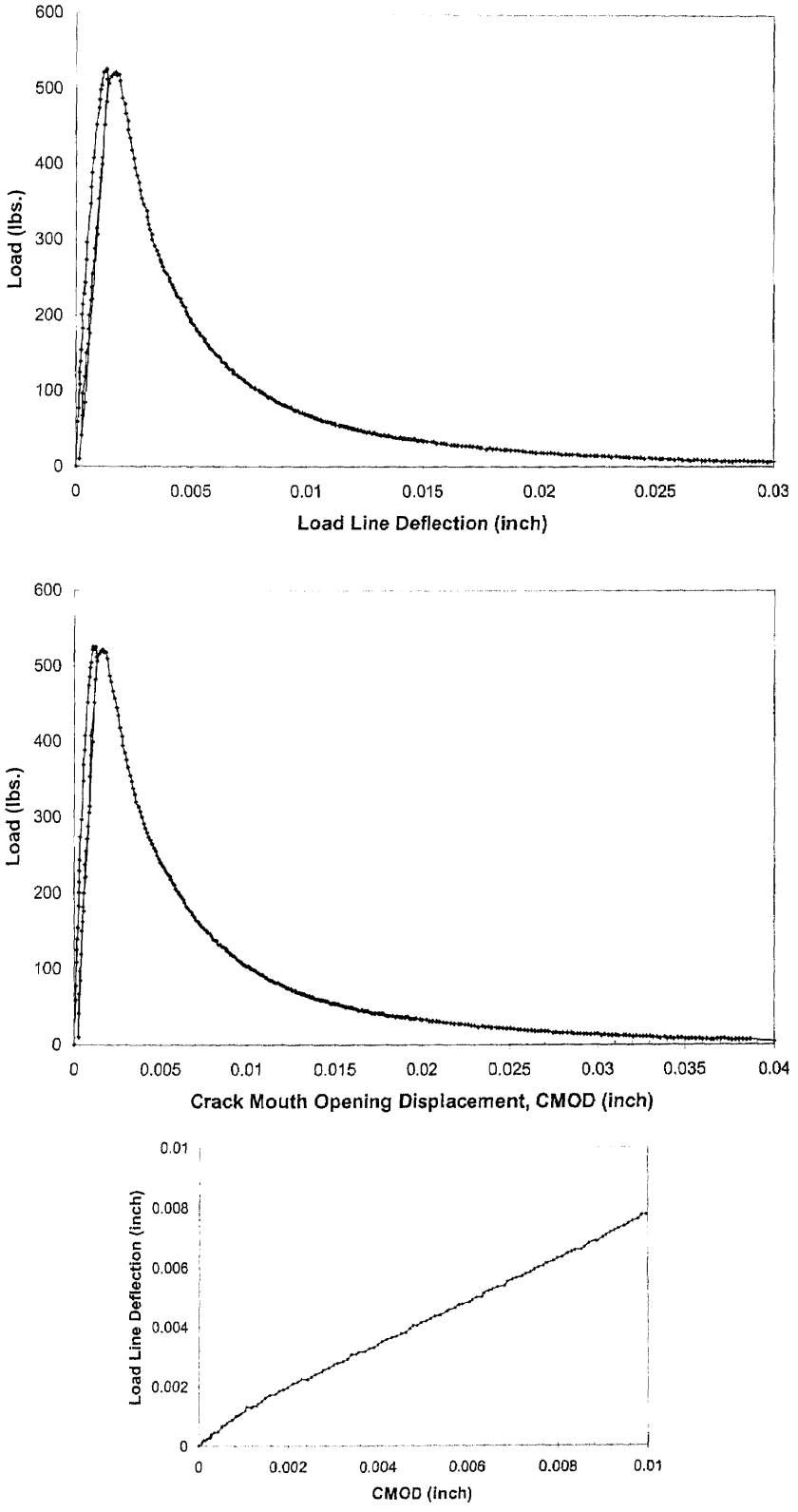

Figure B 5c Load-Deflection-CMOD Relationship of Fly Ash Concrete (16F25) (Specimen No.3)

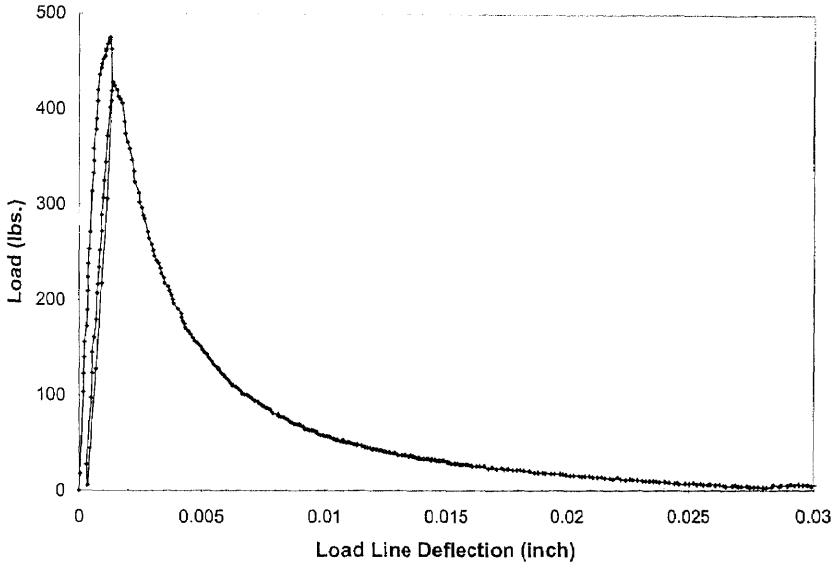

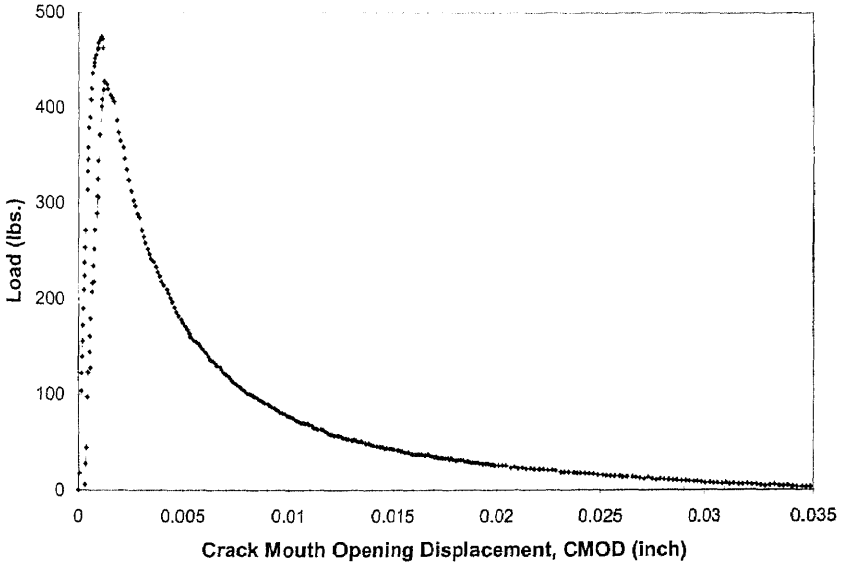

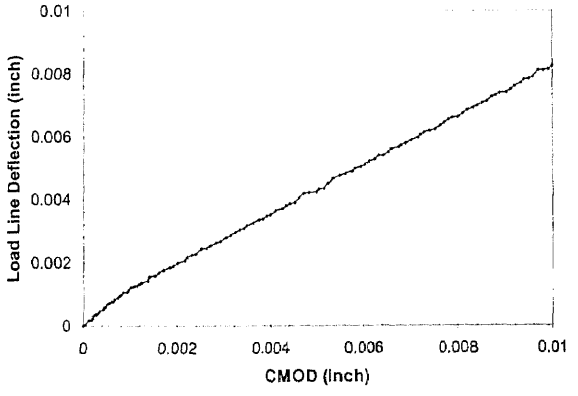

Figure B 6a Load-Deflection-CMOD Relationship of Fly Ash Concrete (18F25) (Specimen No.1)

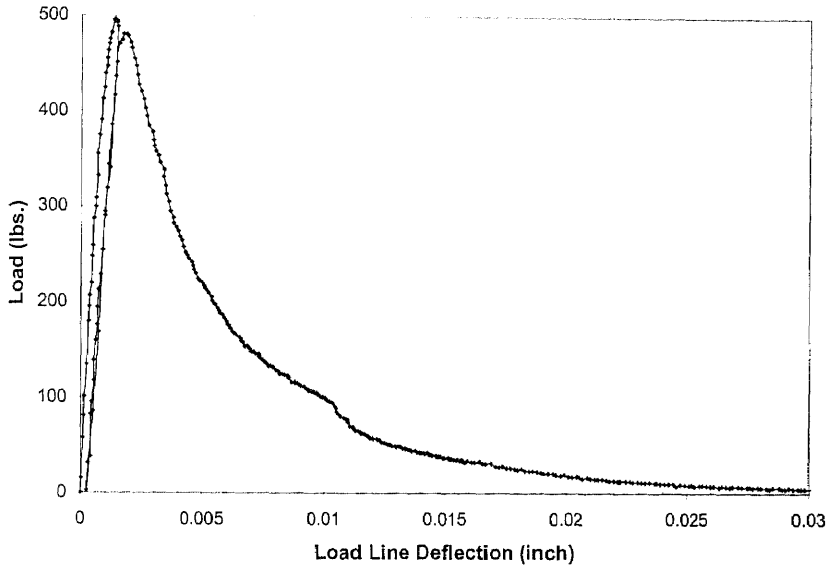

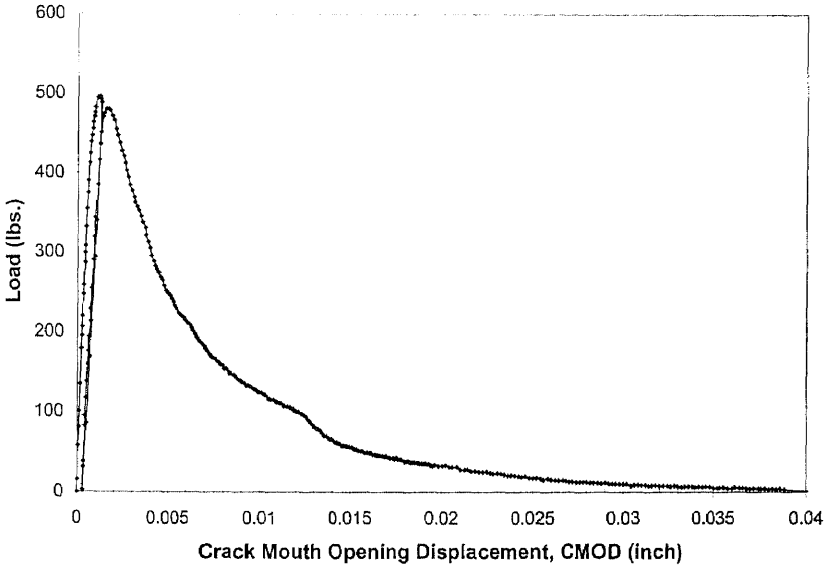

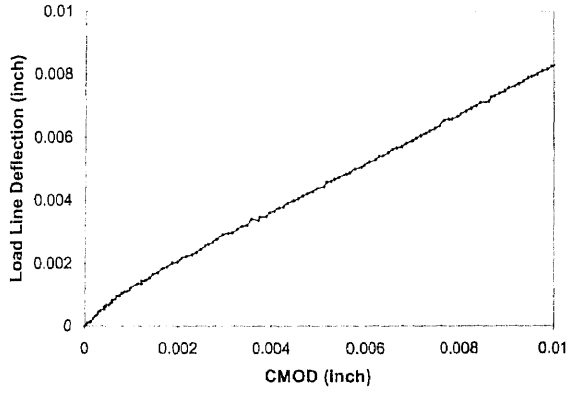

Figure B 6b Load-Deflection-CMOD Relationship of Fly Ash Concrete (18F25) (Specimen No.2)

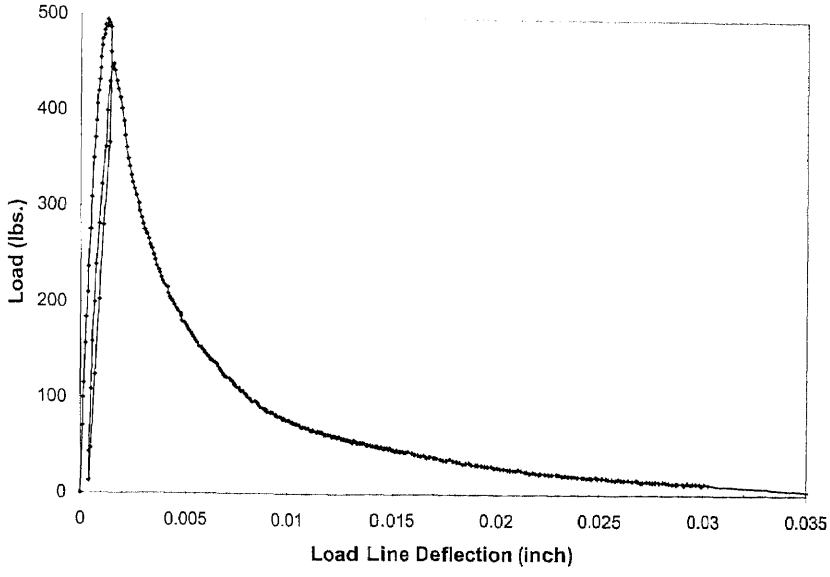

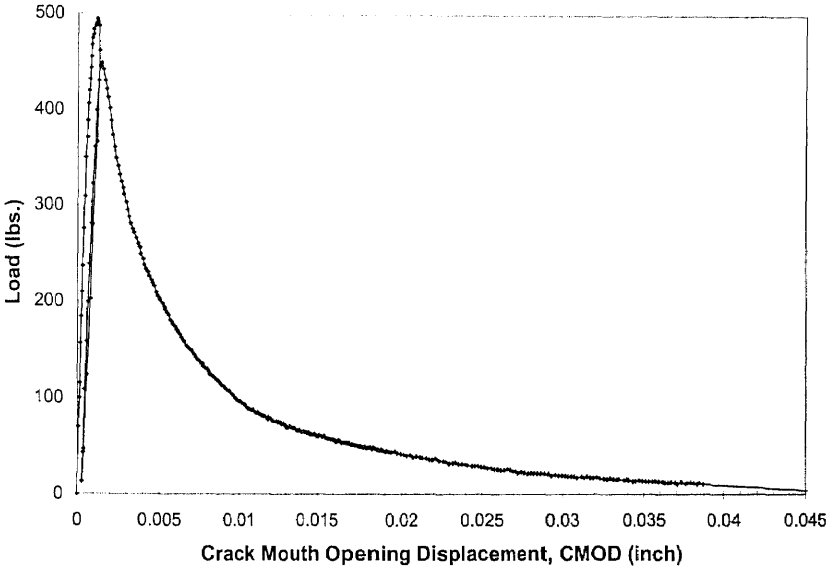

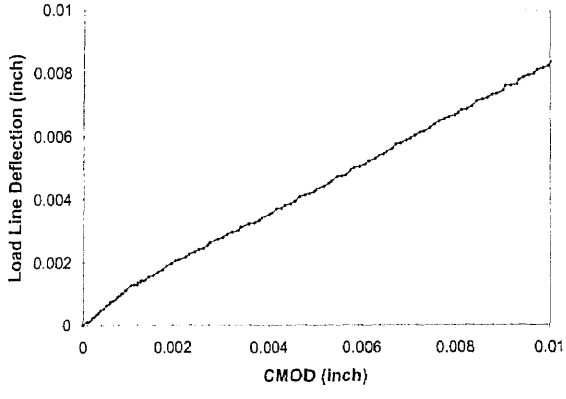

Figure B 6c Load-Deflection-CMOD Relationship of Fly Ash Concrete (18F25) (Specimen No.3)

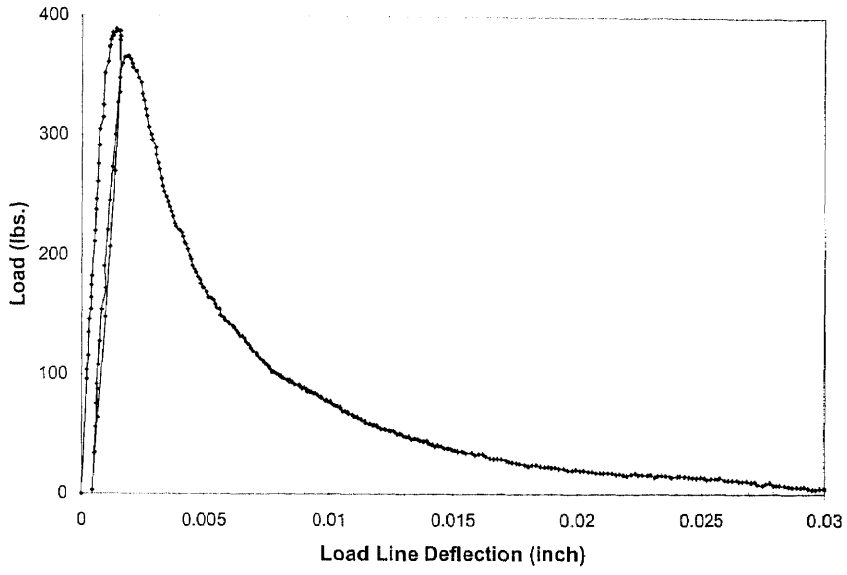

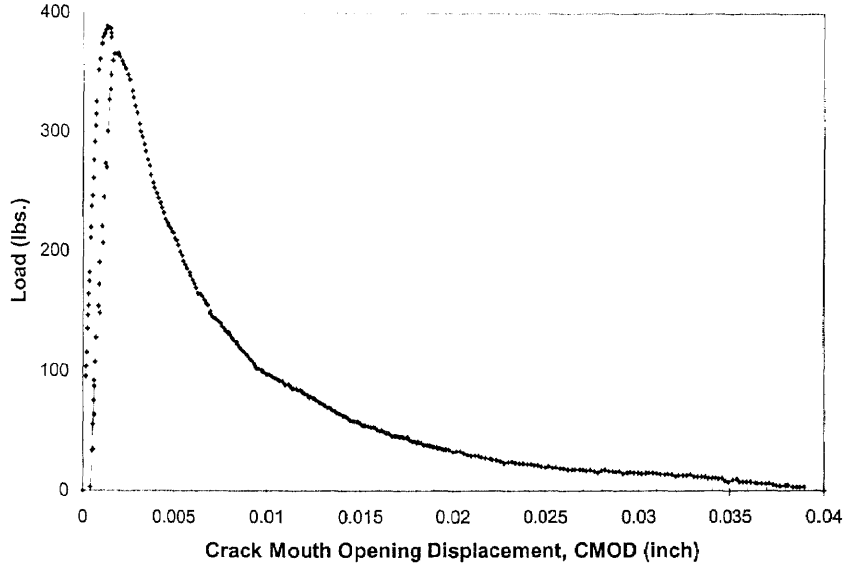

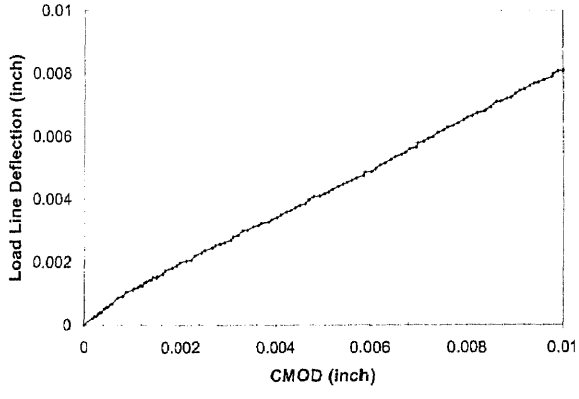

Figure B 7a Load-Deflection-CMOD Relationship of Fly Ash Concrete (18C25) (Specimen No.1)

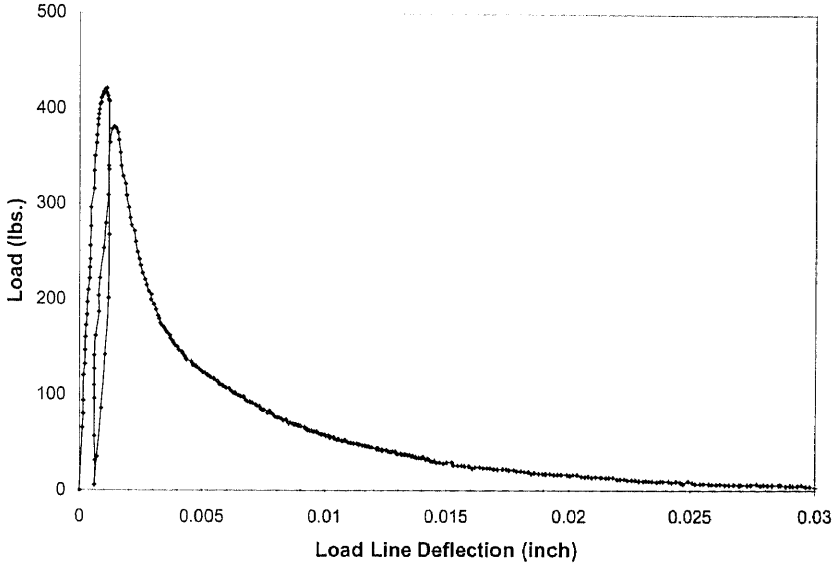

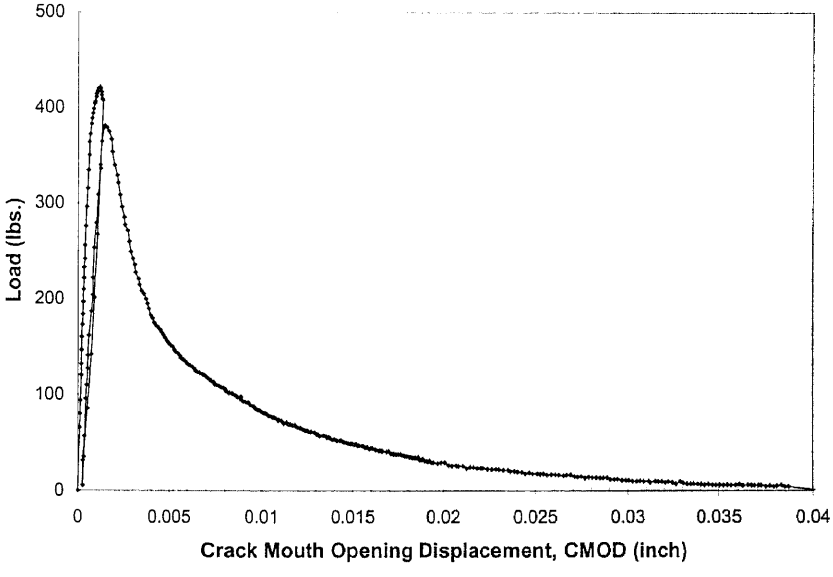

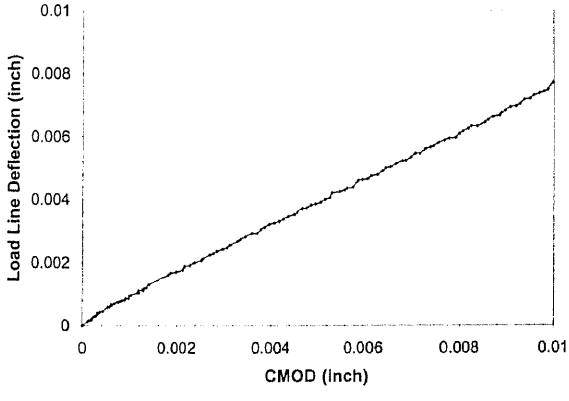

Figure B 7b Load-Deflection-CMOD Relationship of Fly Ash Concrete (18C25) (Specimen No.2)

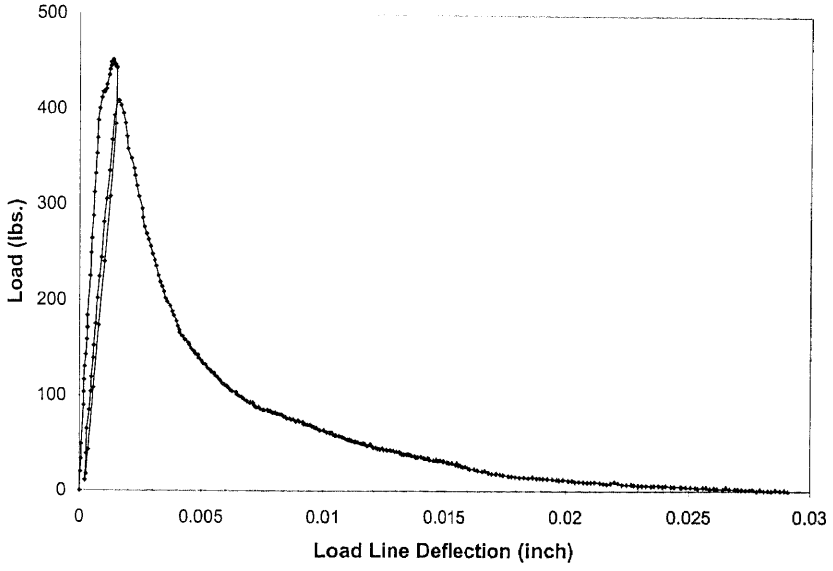

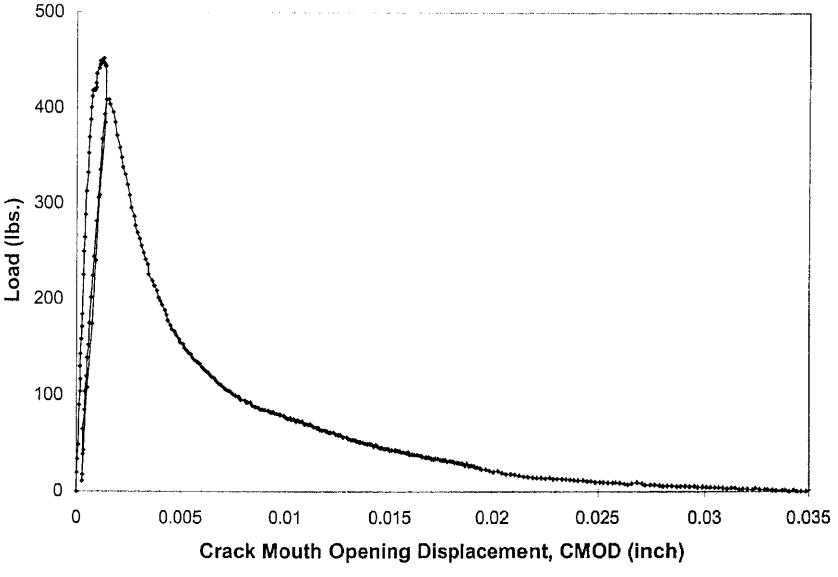

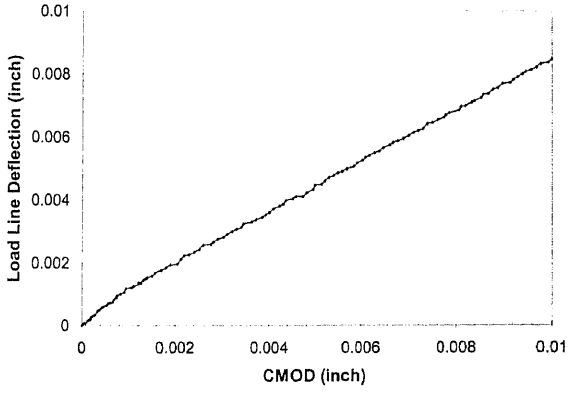

Figure B 7c Load-Deflection-CMOD Relationship of Fly Ash Concrete (18C25) (Specimen No.3)

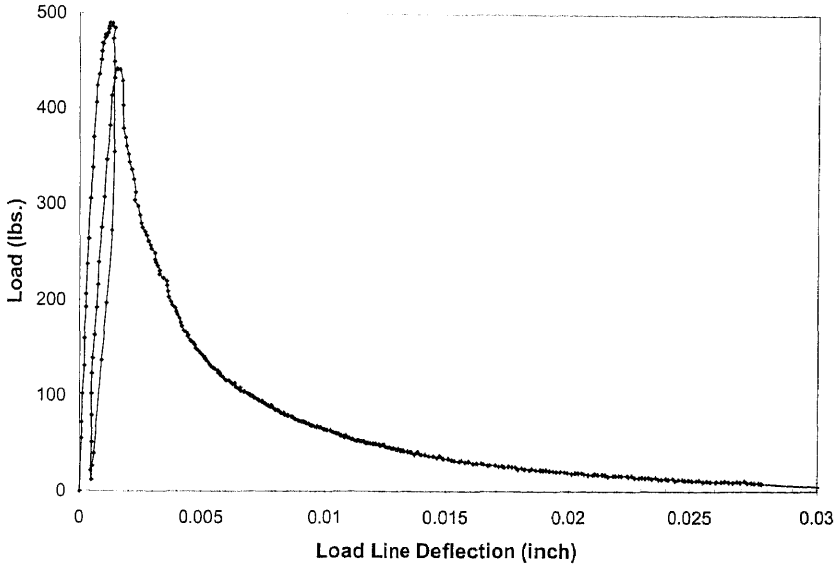

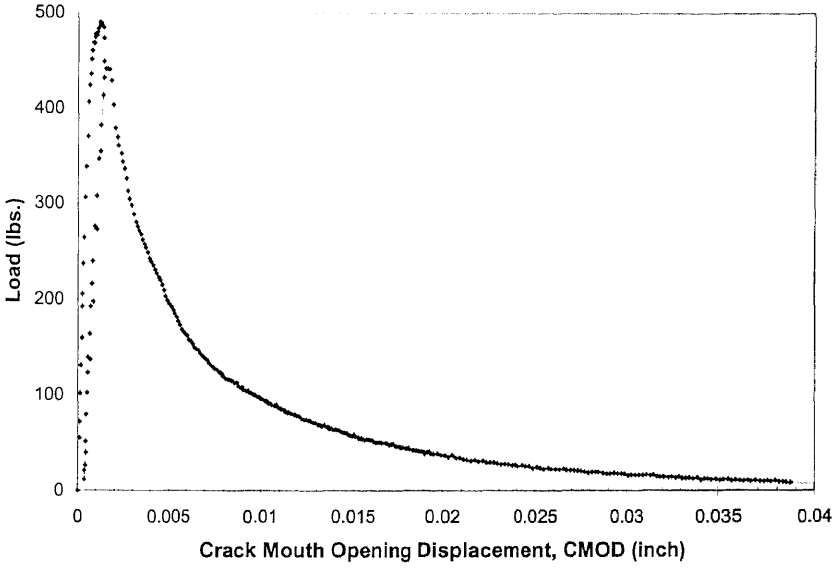

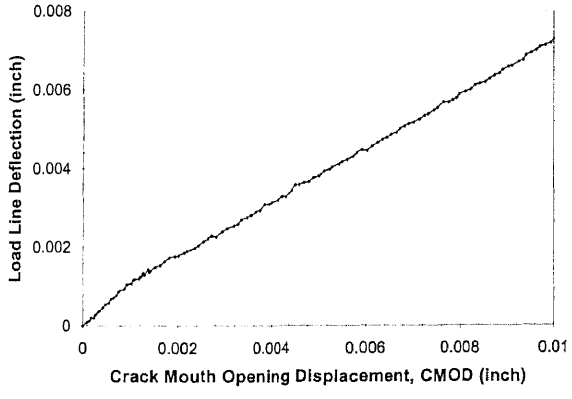

Figure B 8a Load-Deflection-CMOD Relationship of Fly Ash Concrete (MO25) (Specimen No.1)

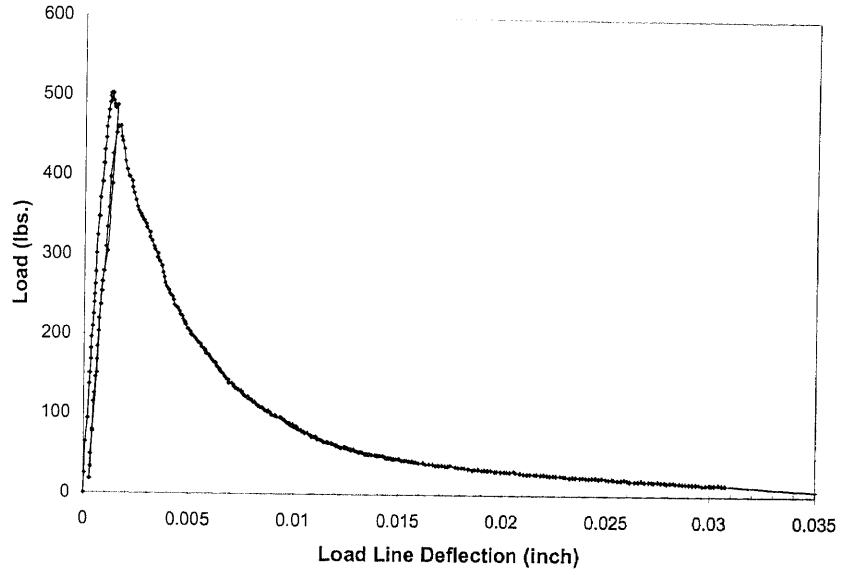

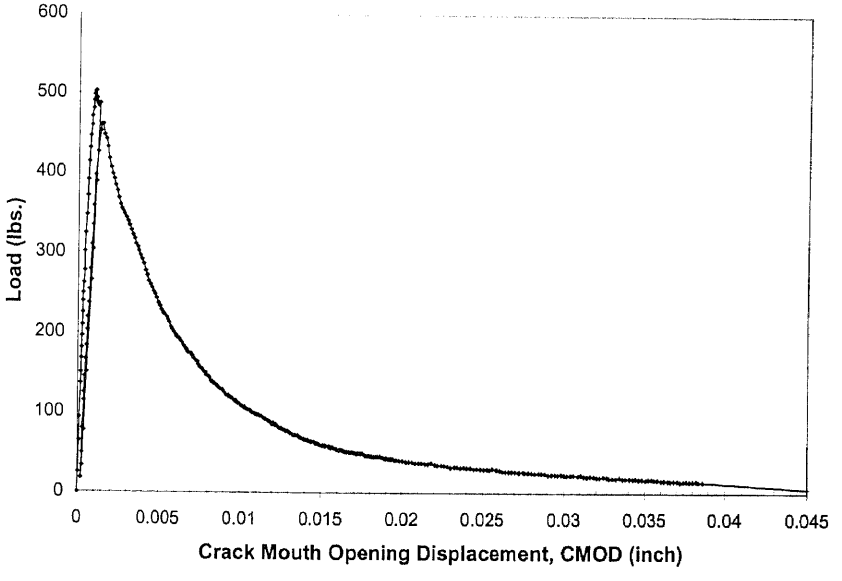

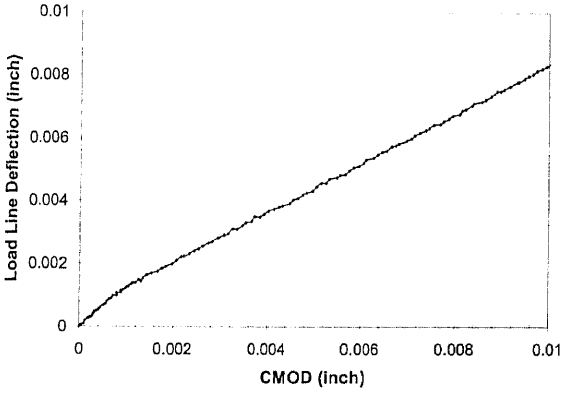

Figure B 8b Load-Deflection-CMOD Relationship of Fly Ash Concrete (MO25) (Specimen No.2)

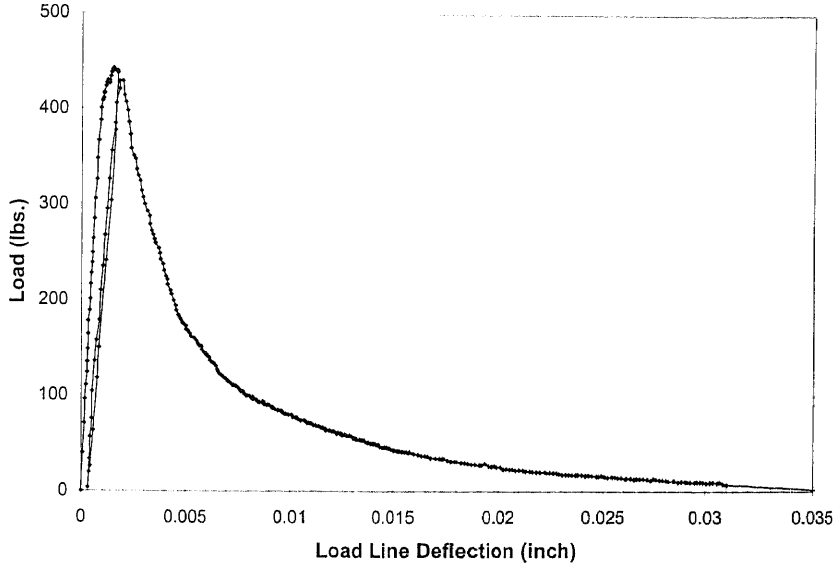

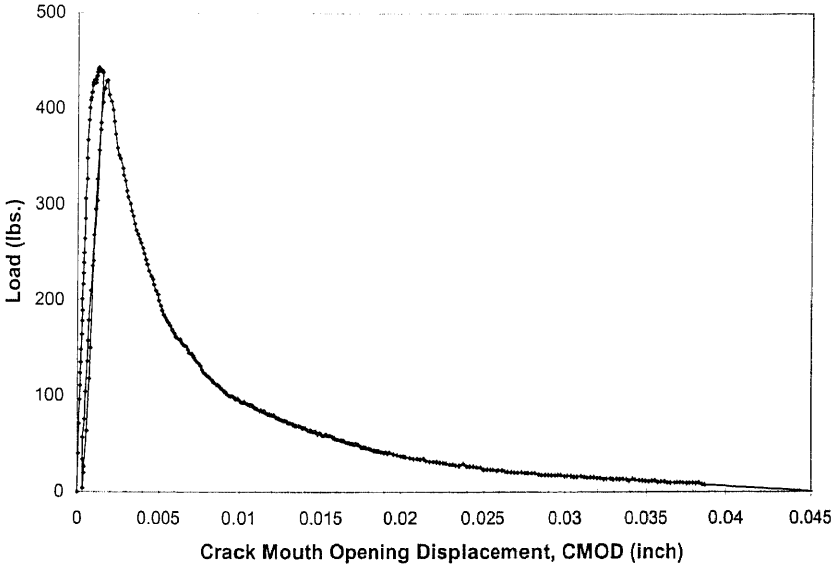

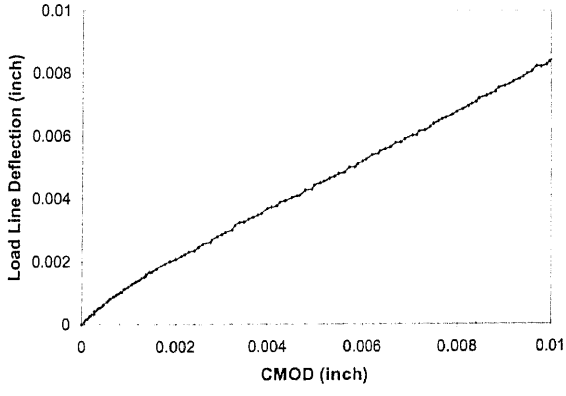

Figure B 8c Load-Deflection-CMOD Relationship of Fly Ash Concrete (MO25) (Specimen No.3)

APPENDIX C

ANALYTICAL RESULTS BY THE PROPOSED MODEL

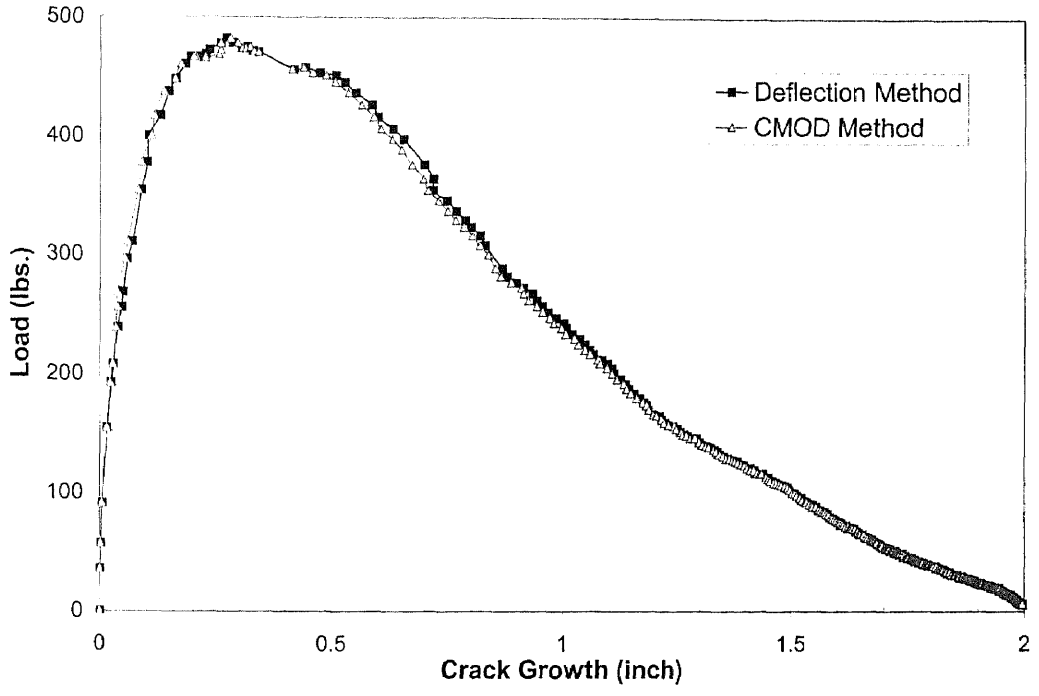

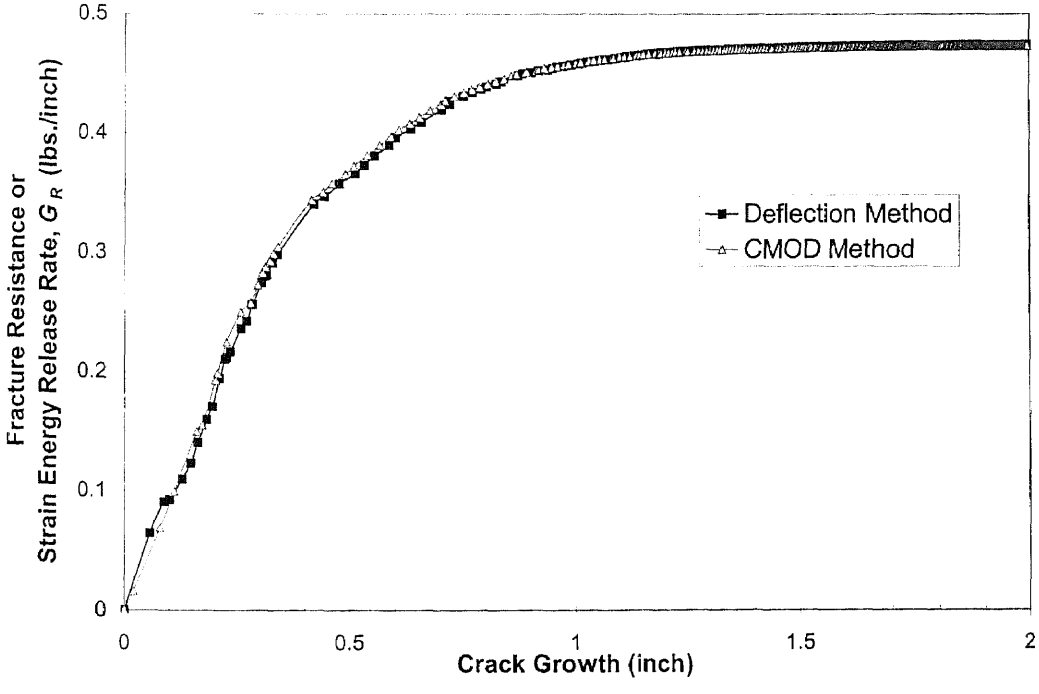

Figure C 1a Fracture Behavior of Control Concrete (CC) (Specimen No.1)

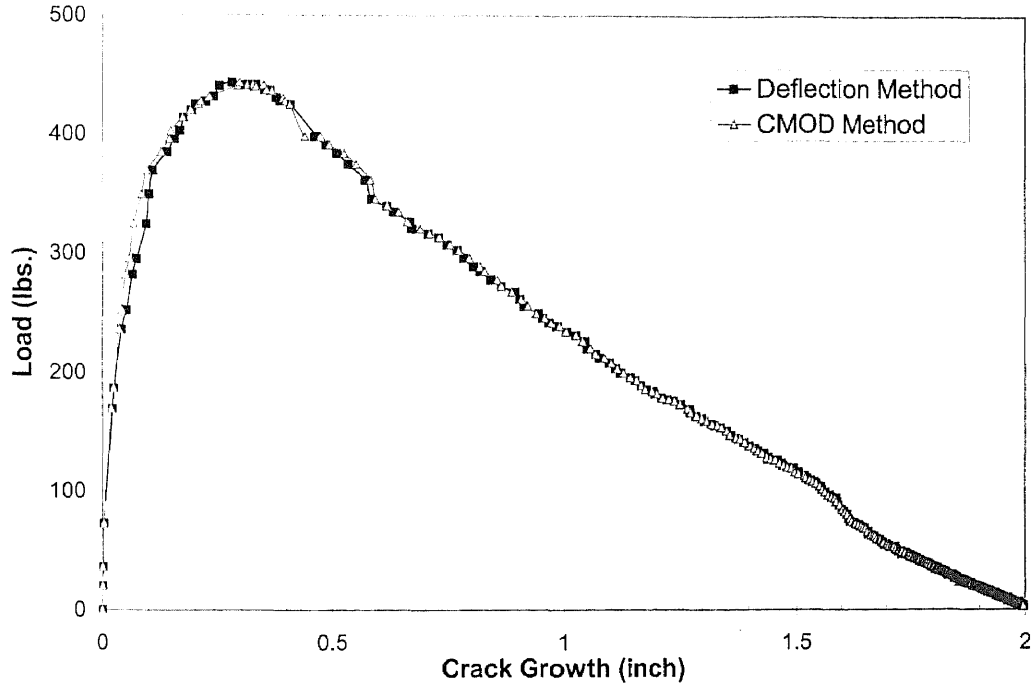

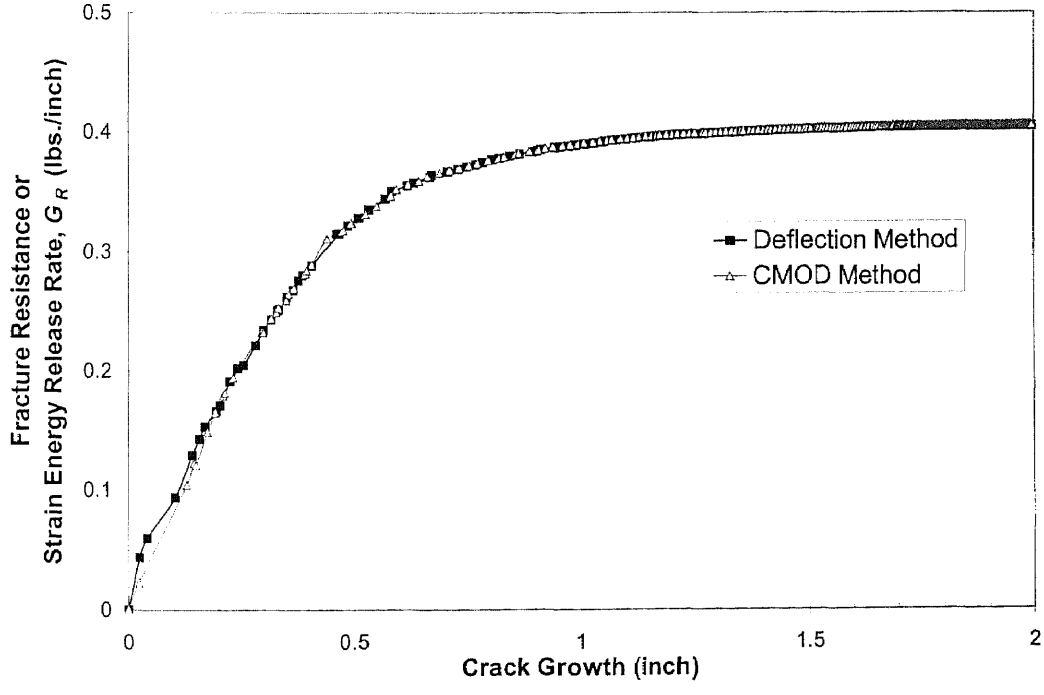

Figure C 1b Fracture Behavior of Control Concrete (CC) (Specimen No.2)

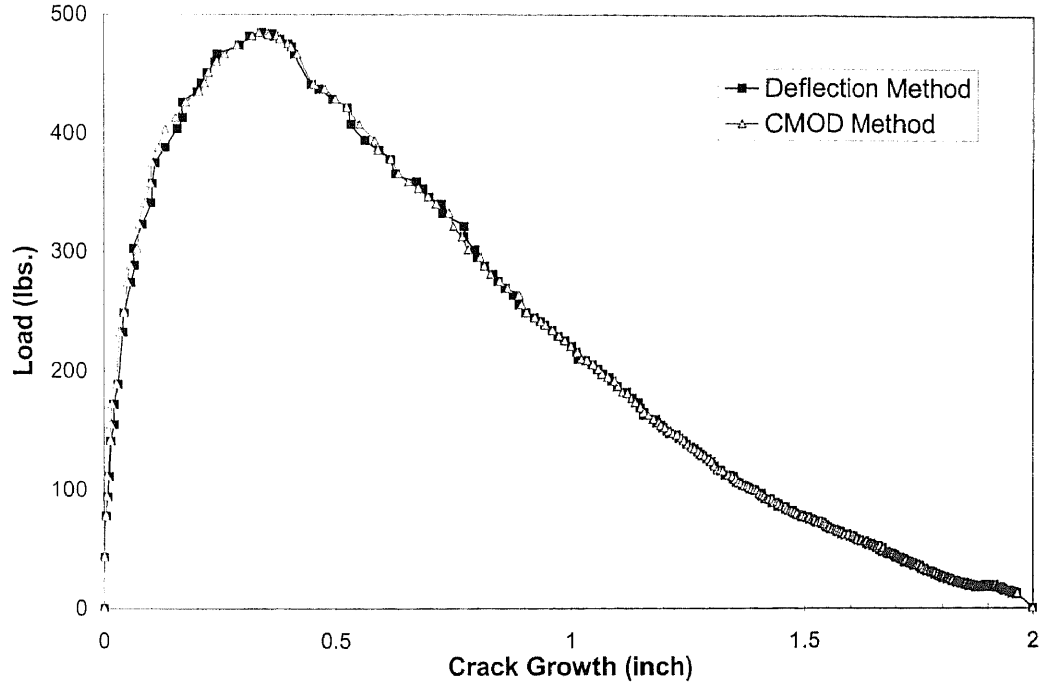

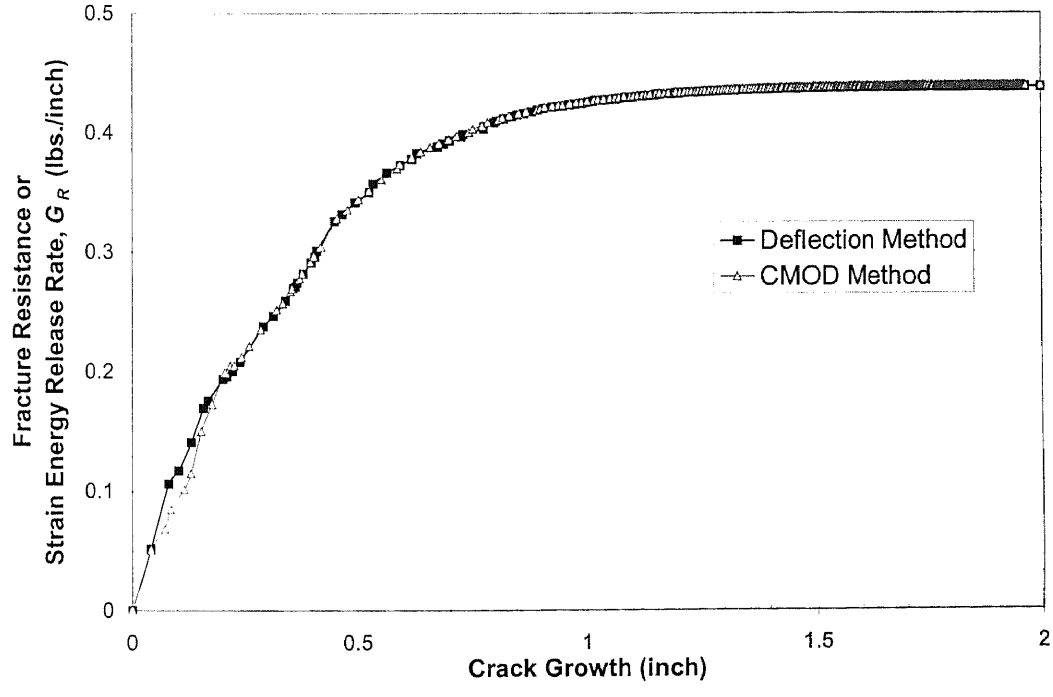

Figure C 1c Fracture Behavior of Control Concrete (CC)
(Specimen No.3)

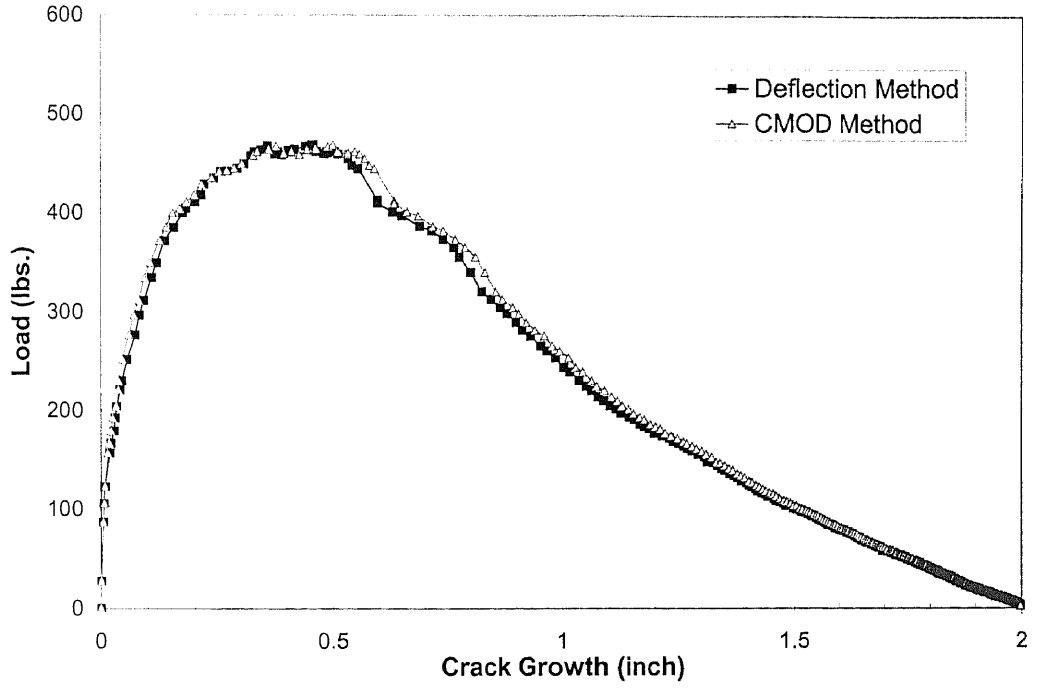

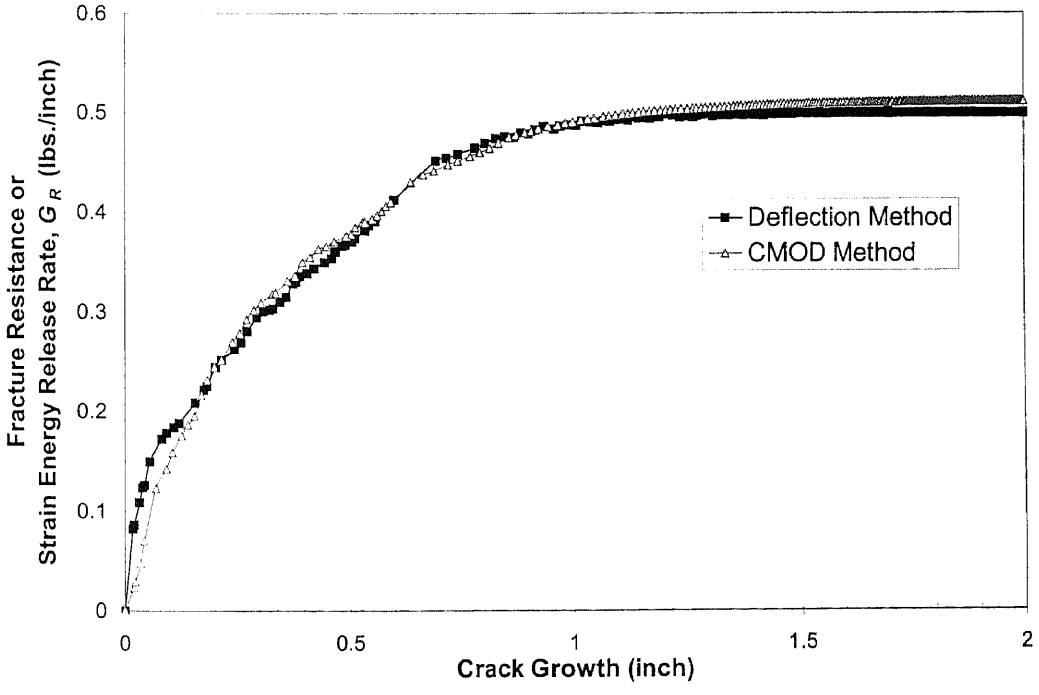

Figure C 2a Fracture Behavior of Silica Fume Concrete (SF) (Specimen No.1)

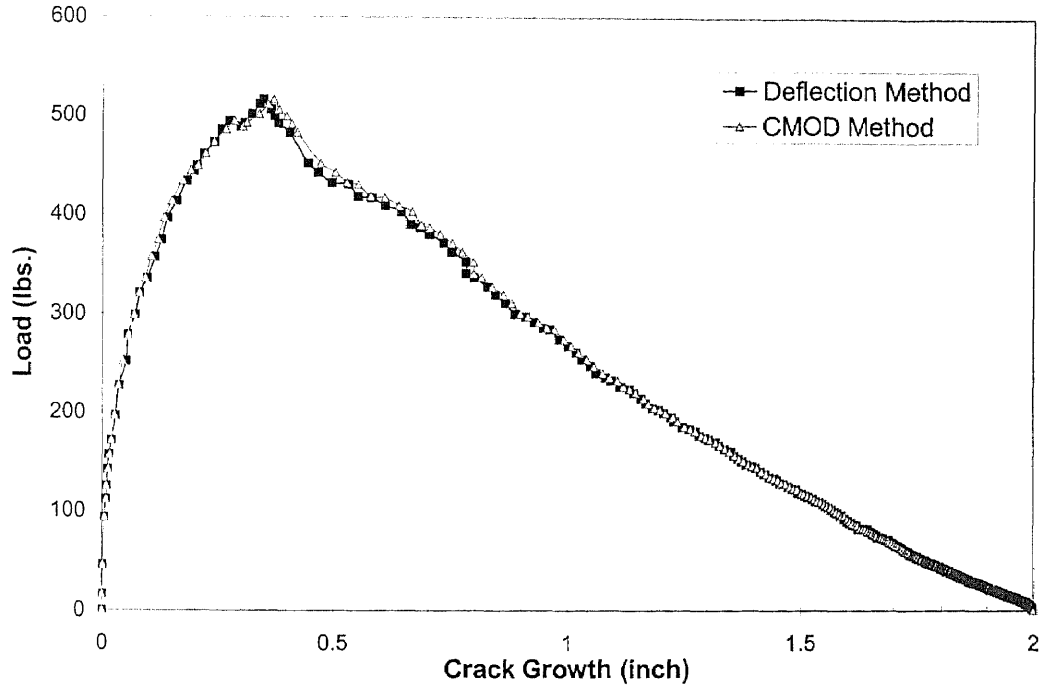

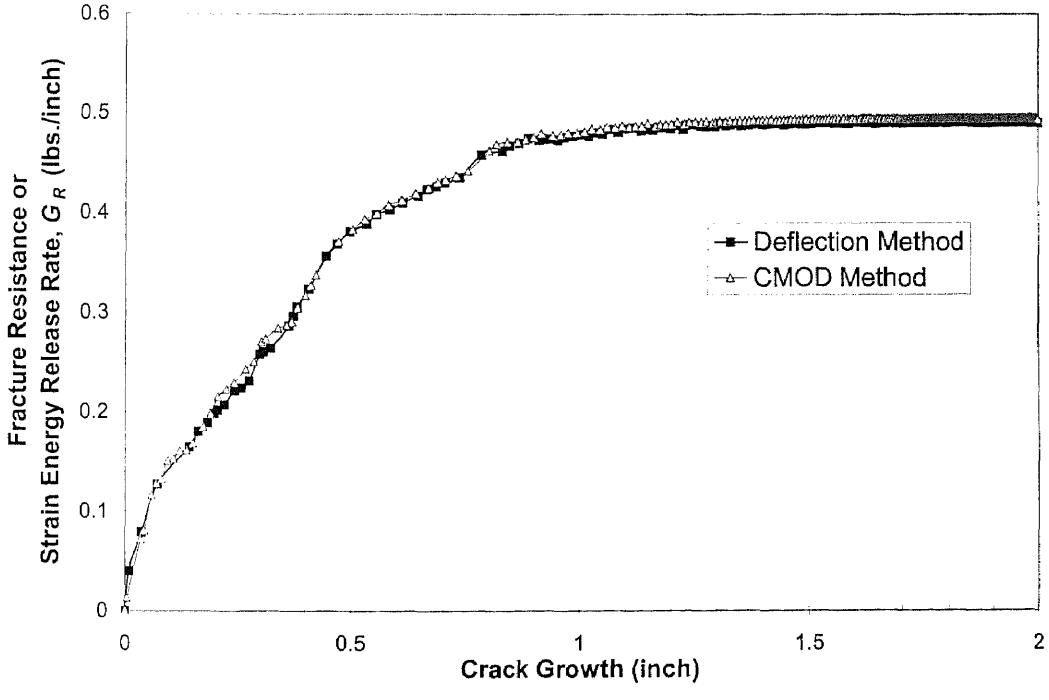

Figure C 2b Fracture Behavior of Silica Fume Concrete (SF) (Specimen No.2)

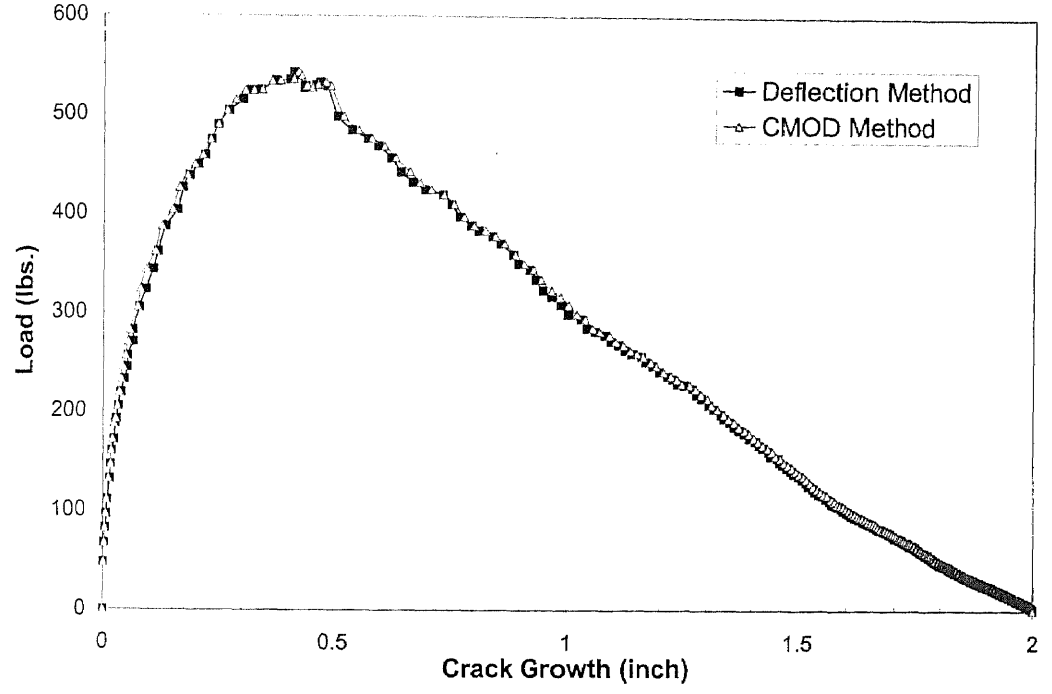

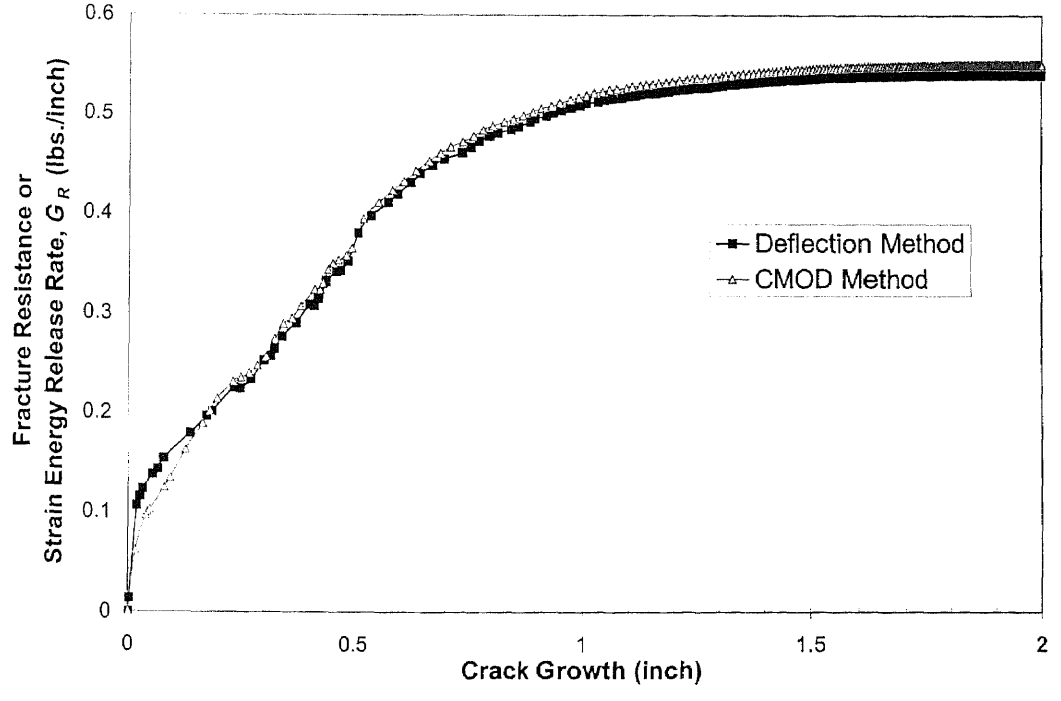

Figure C 2c Fracture Behavior of Silica Fume Concrete (SF) (Specimen No.3)

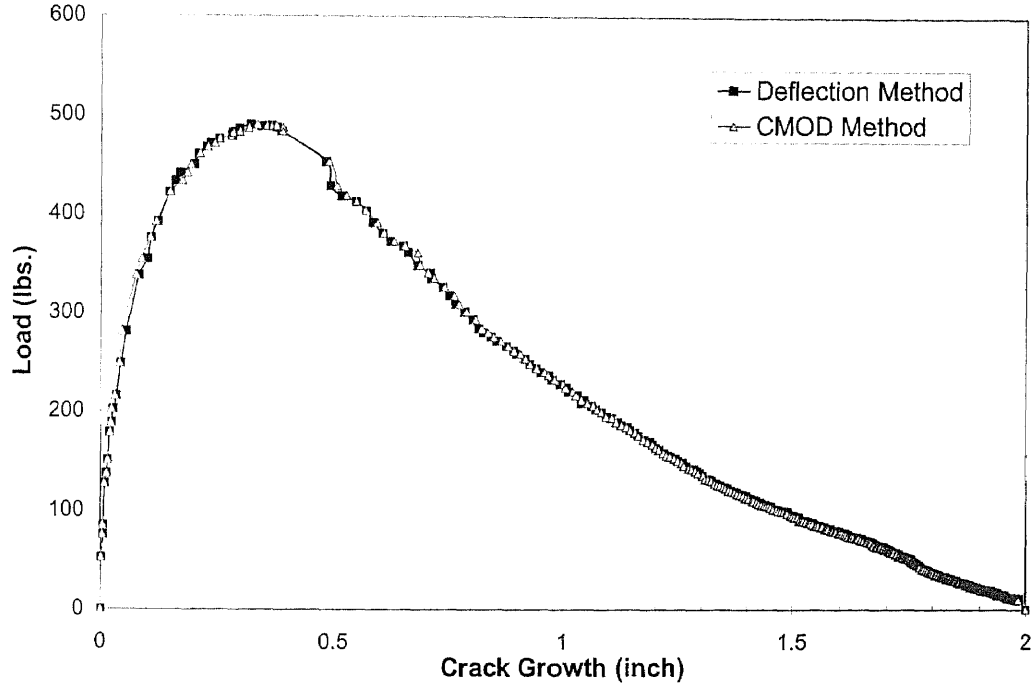

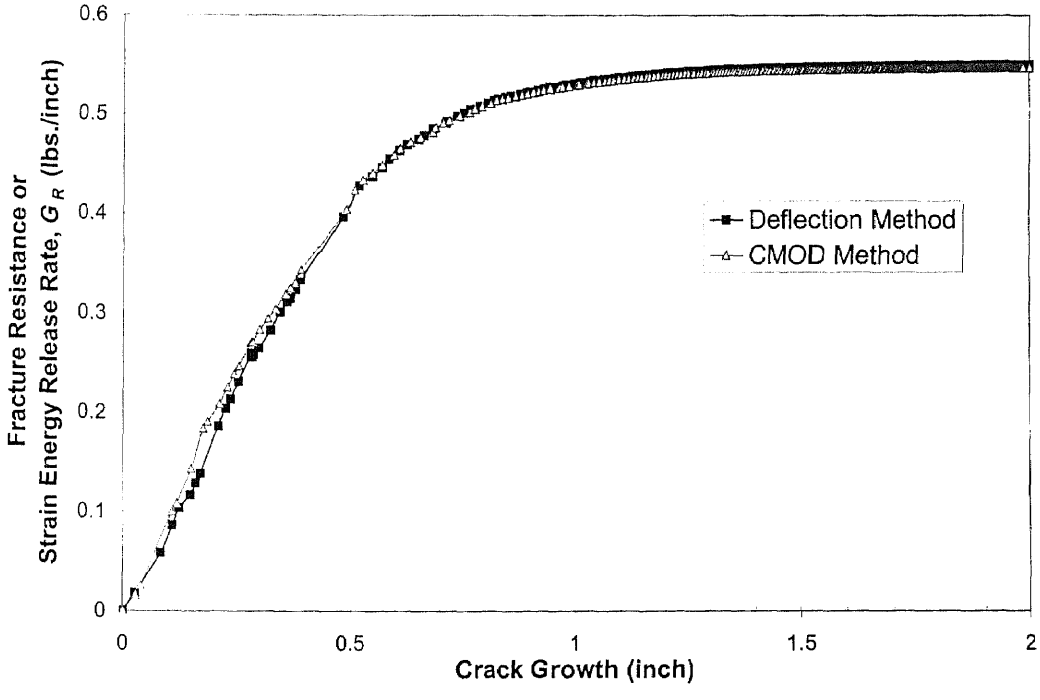

Figure C 3a Fracture Behavior of Fly Ash Concrete (13F25)
(Specimen No.1)

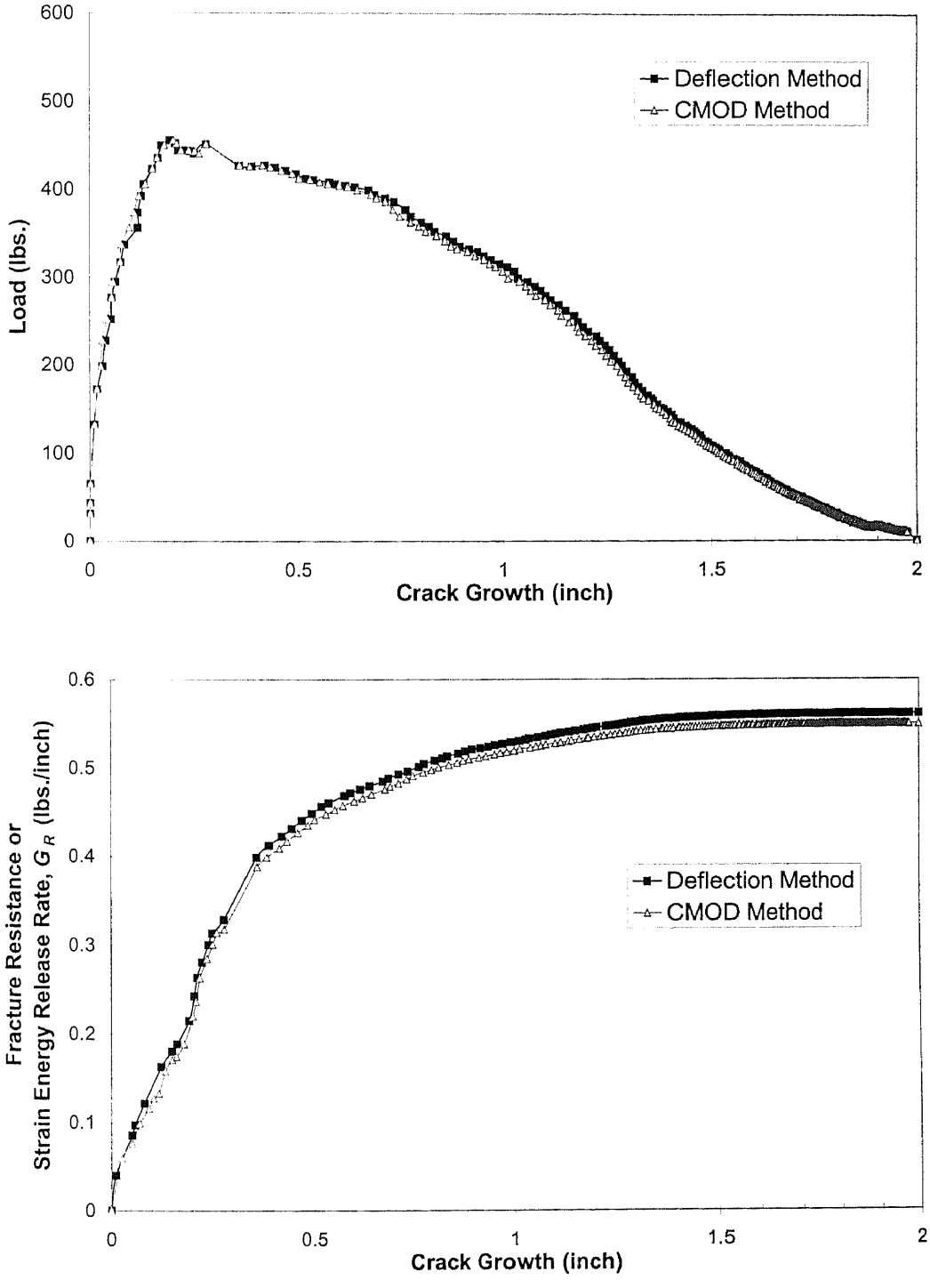

Figure C 3b Fracture Behavior of Fly Ash Concrete (13F25)
(Specimen No.2)

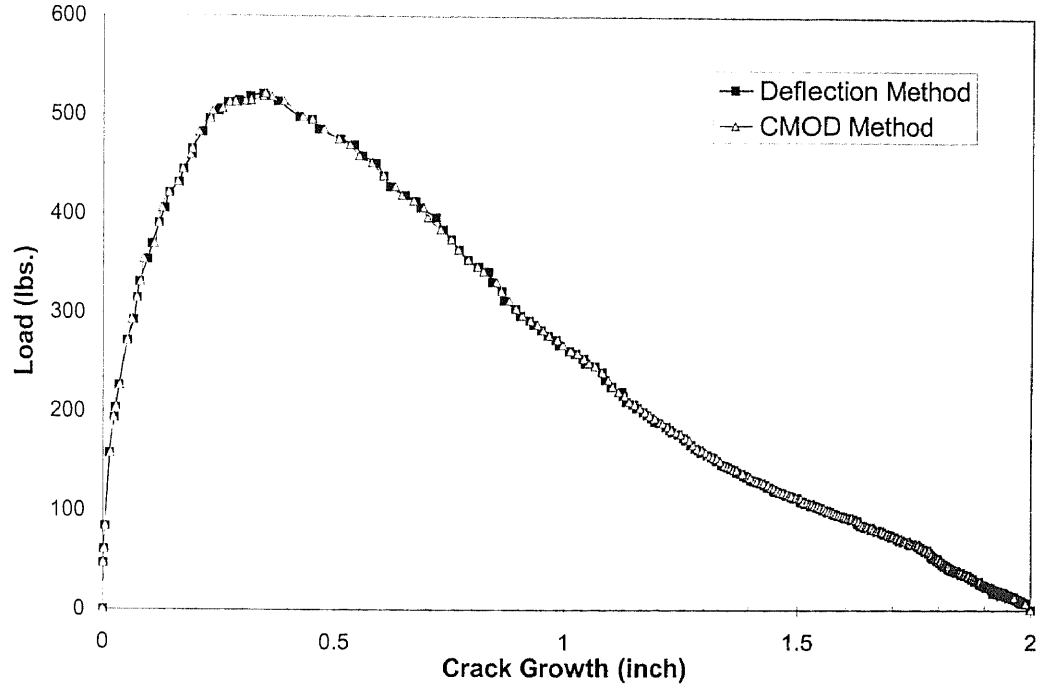

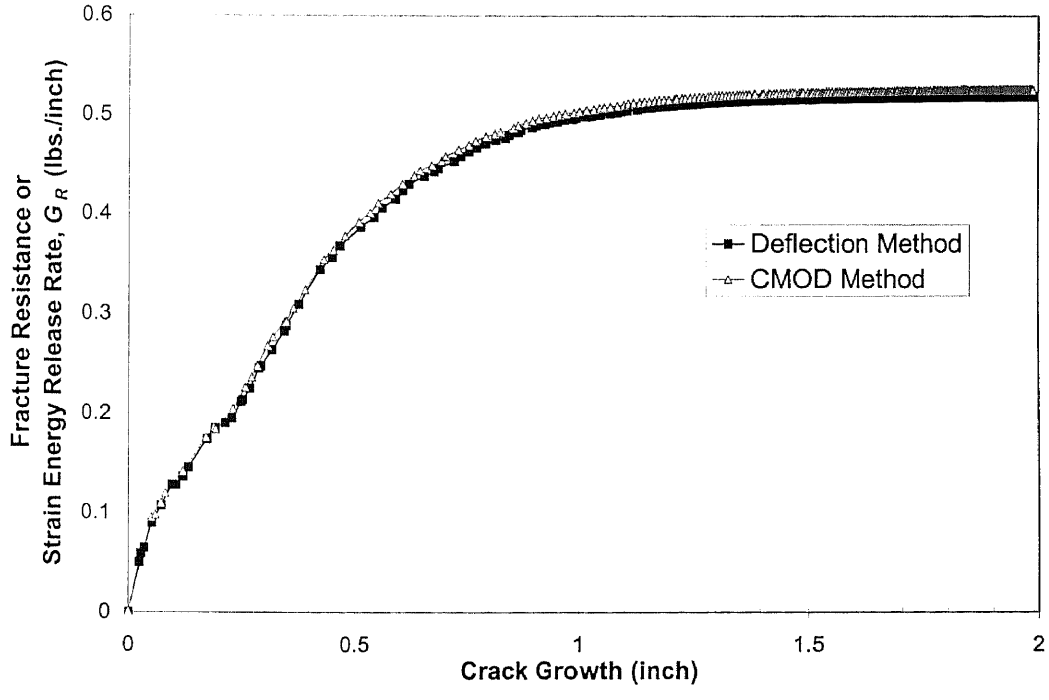

Figure C 3c Fracture Behavior of Fly Ash Concrete (13F25)
(Specimen No.3)

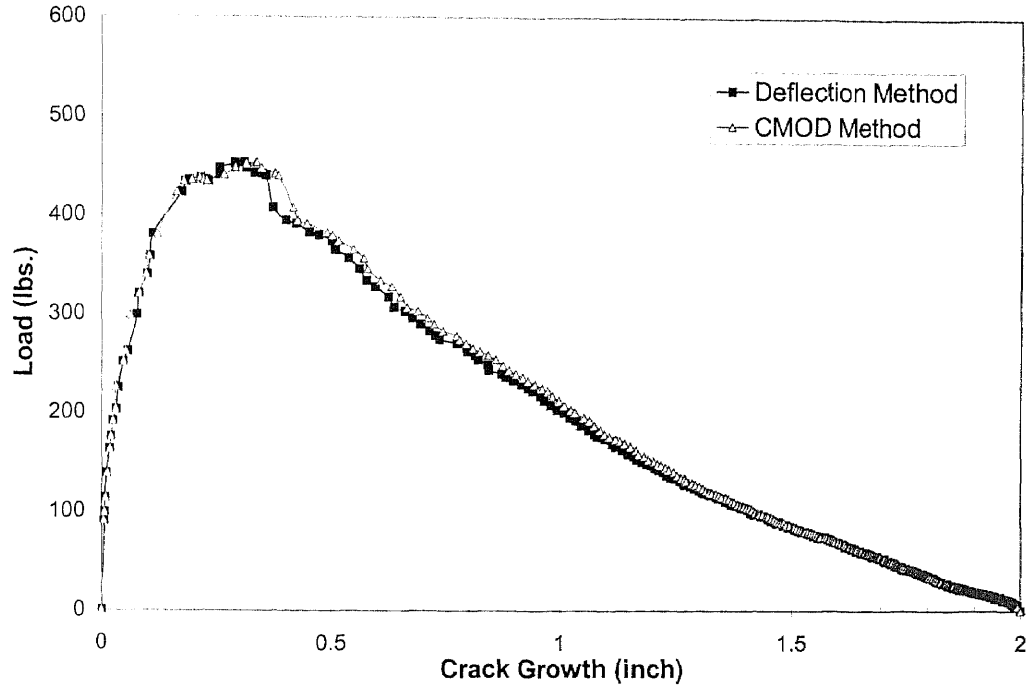

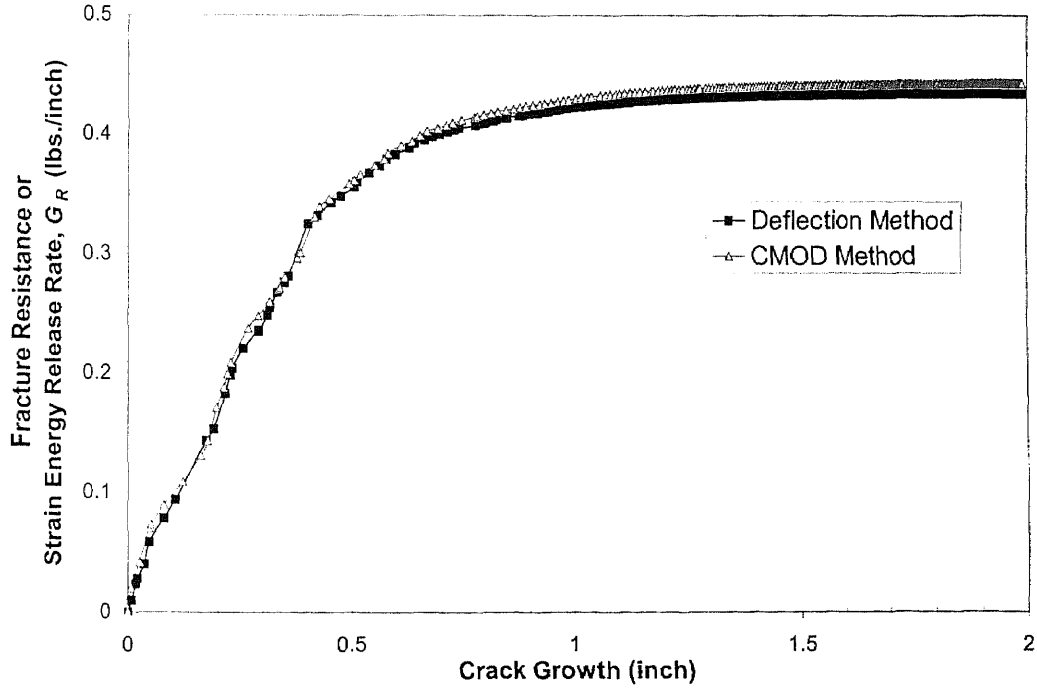

Figure C 4a Fracture Behavior of Fly Ash Concrete (15F25) (Specimen No.1)

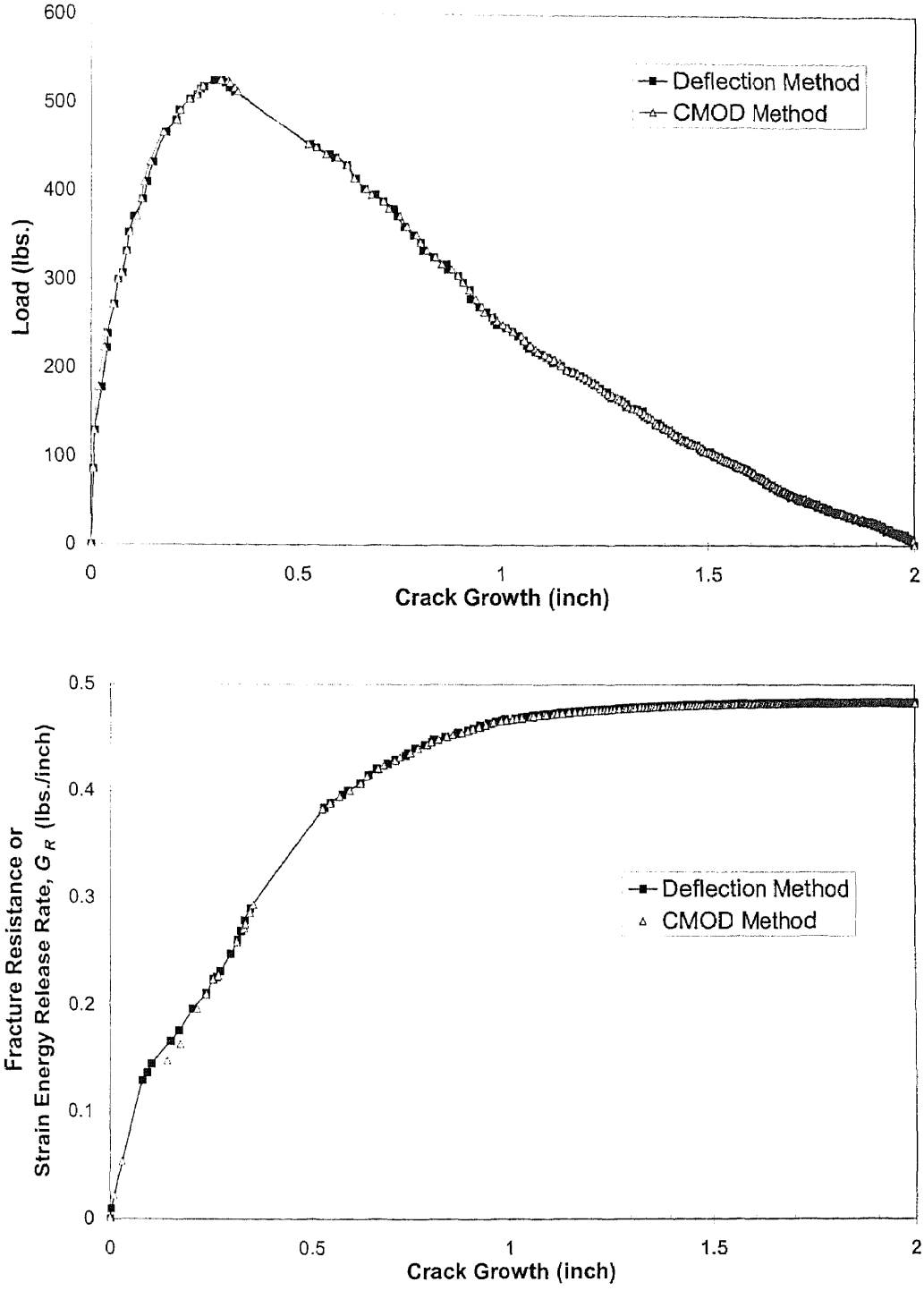

Figure C 4b Fracture Behavior of Fly Ash Concrete (15F25) (Specimen No.2)

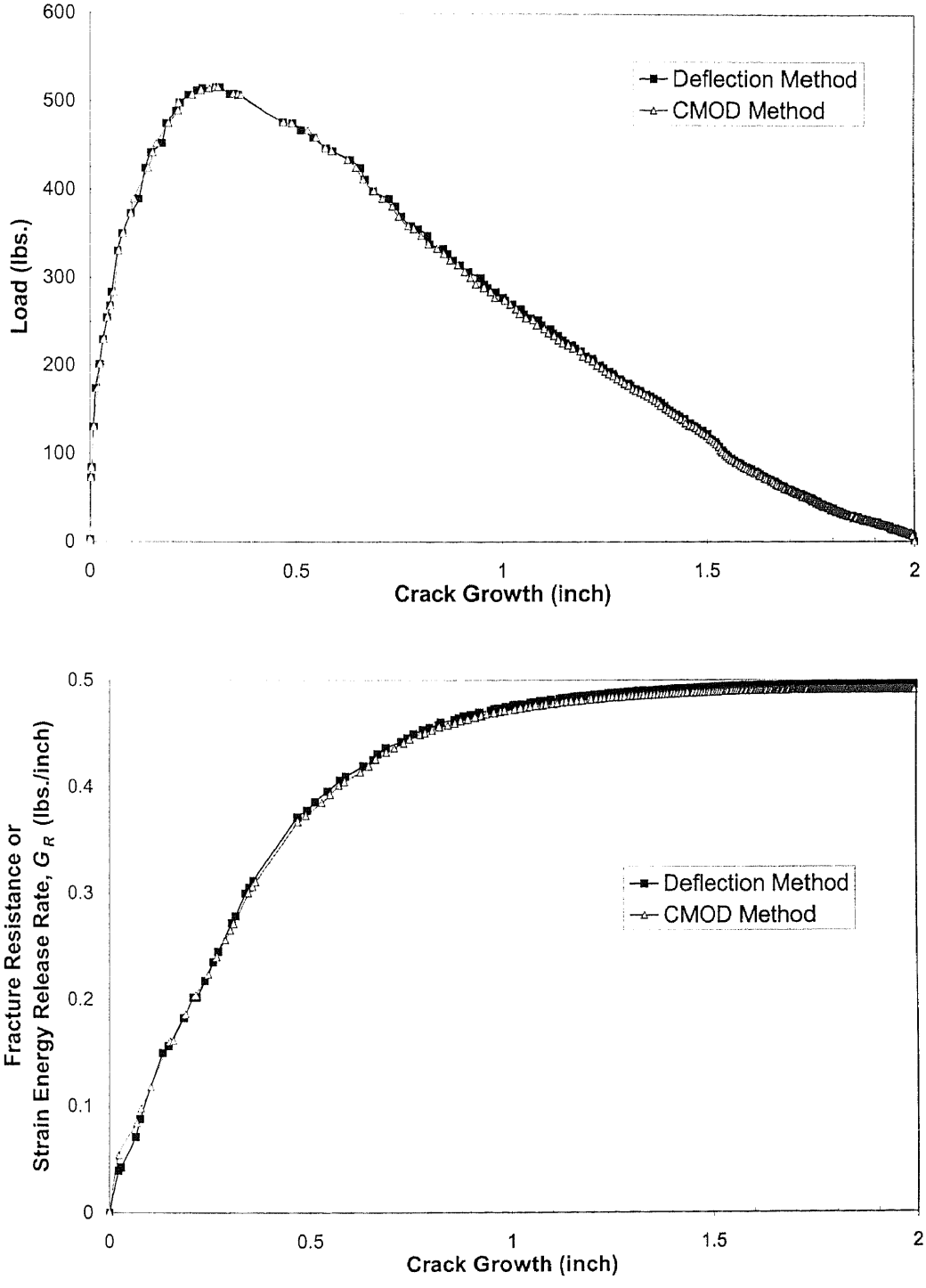

Figure C 4c Fracture Behavior of Fly Ash Concrete (15F25)
(Specimen No.3)

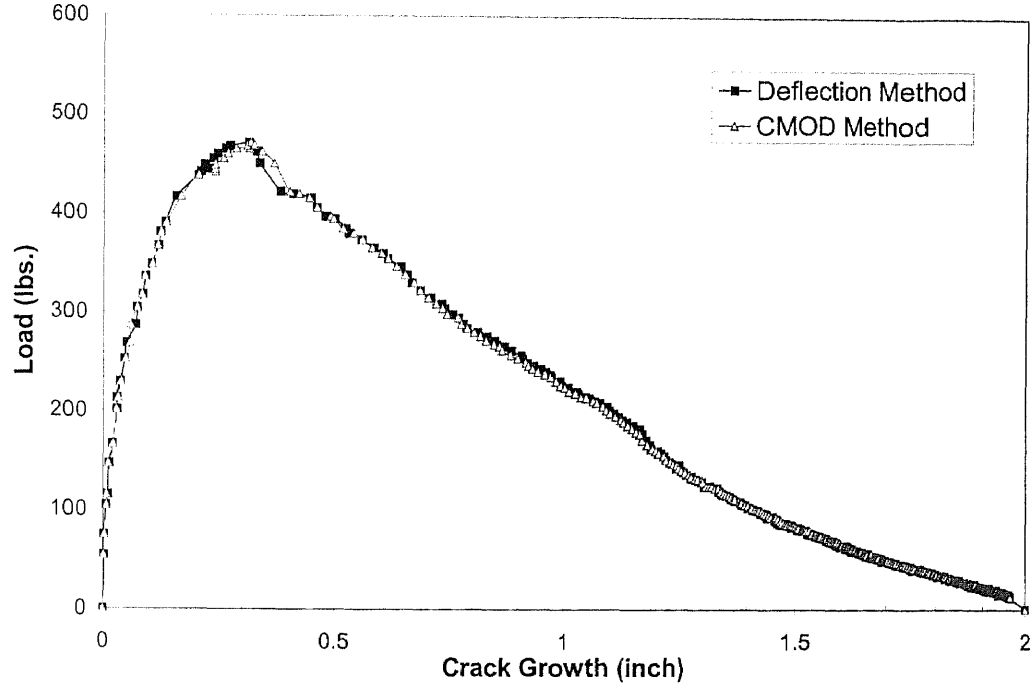

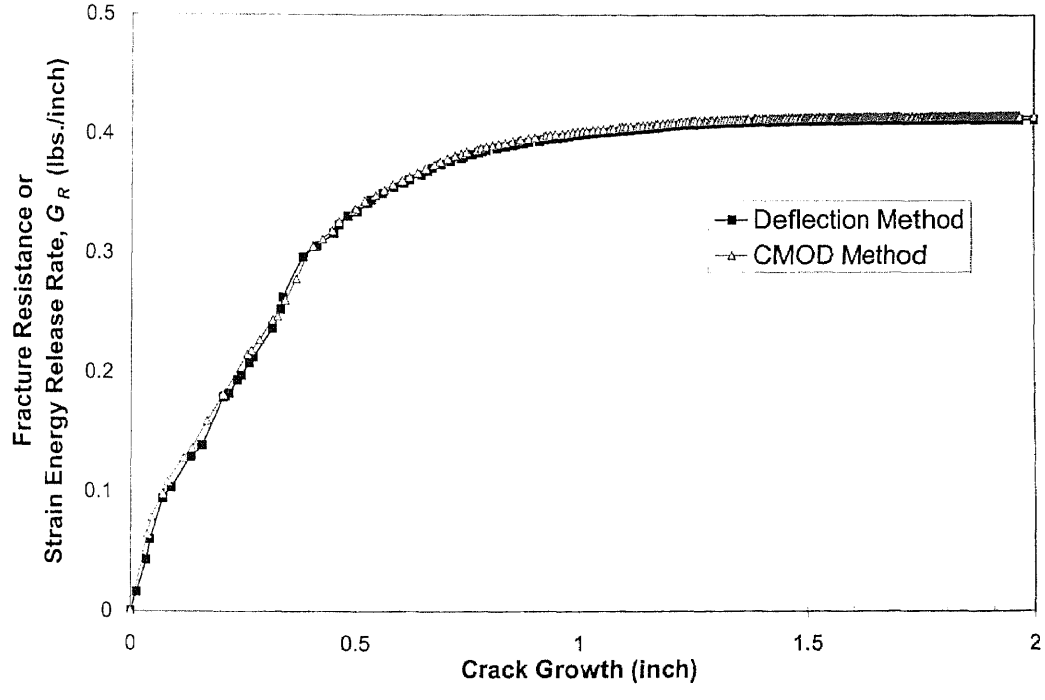

Figure C 5a Fracture Behavior of Fly Ash Concrete (16F25)
(Specimen No.1)

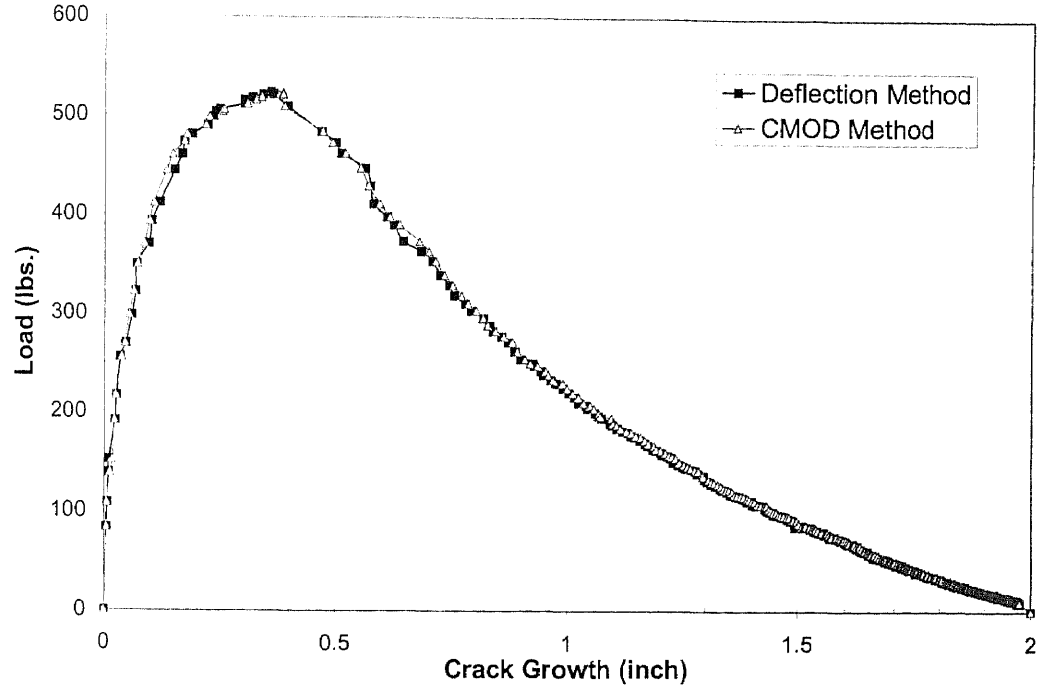

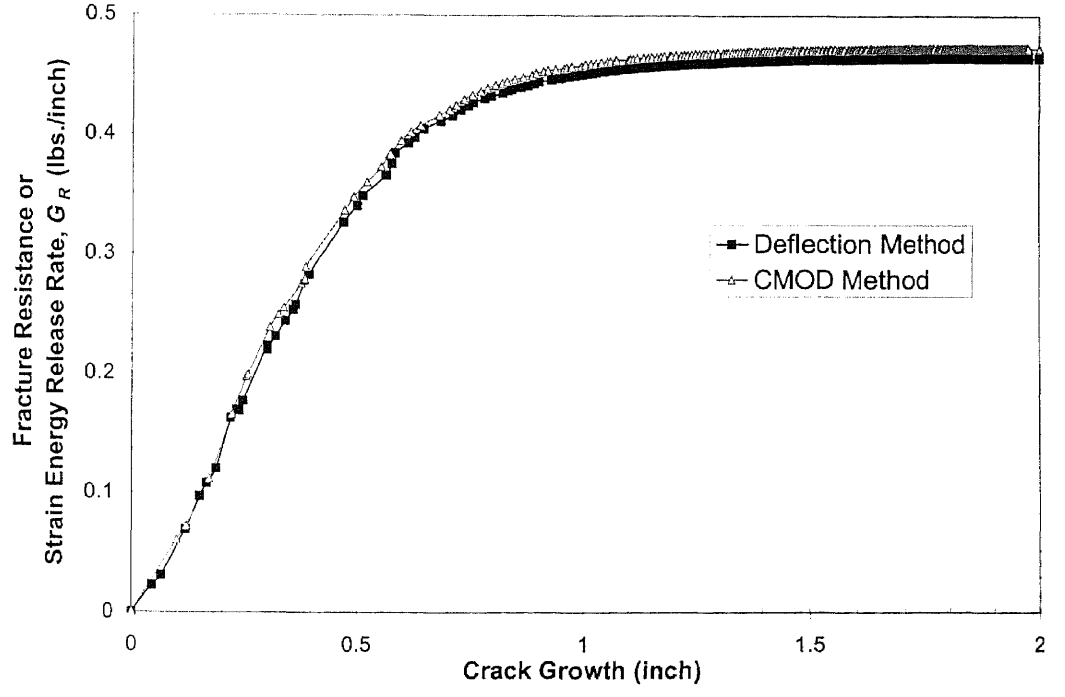

Figure C 5b Fracture Behavior of Fly Ash Concrete (16F25)
(Specimen No.2)

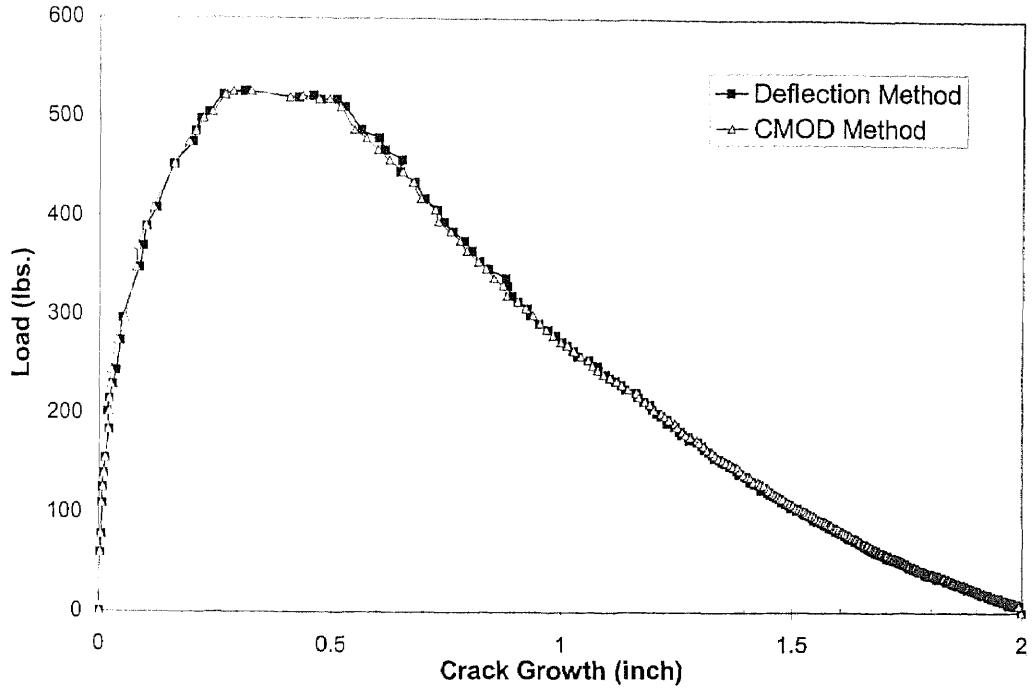

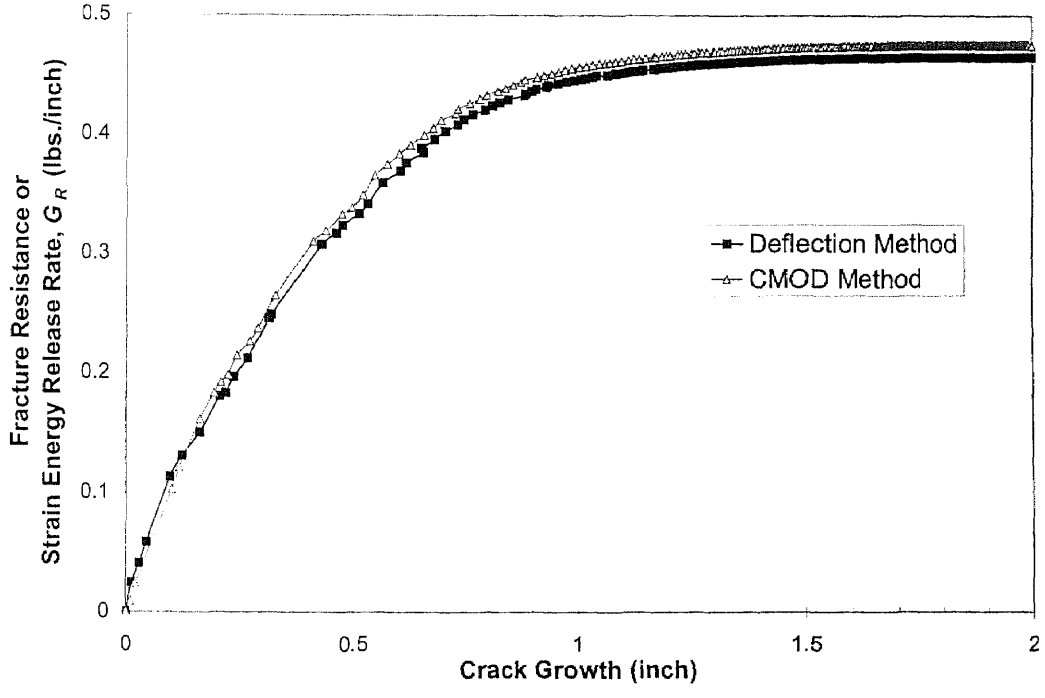

Figure C 5c Fracture Behavior of Fly Ash Concrete (16F25) (Specimen No.3)

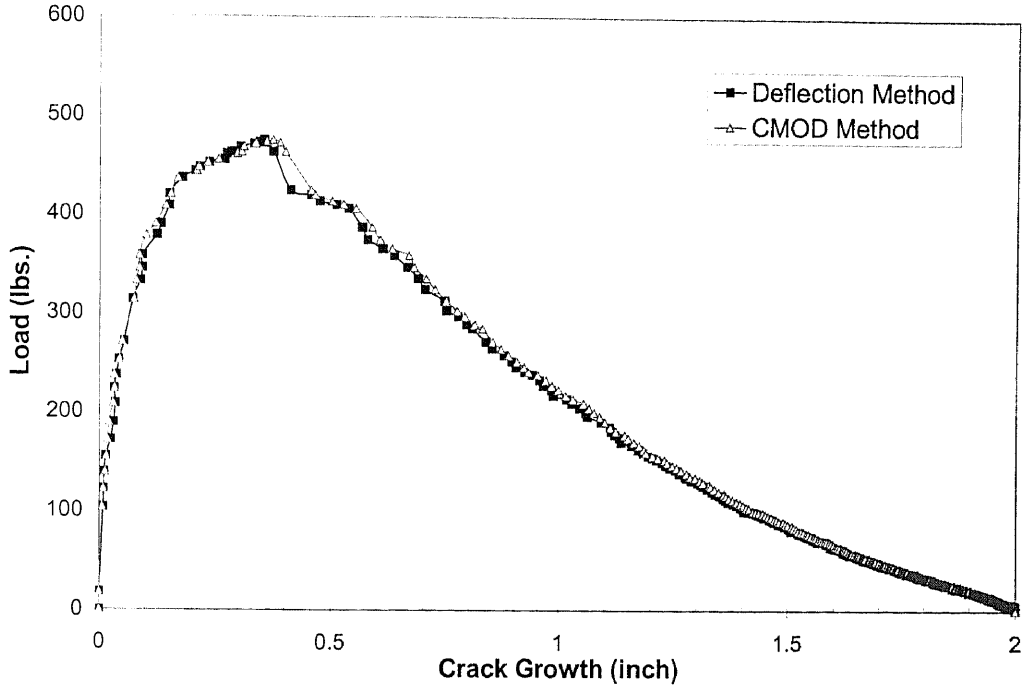

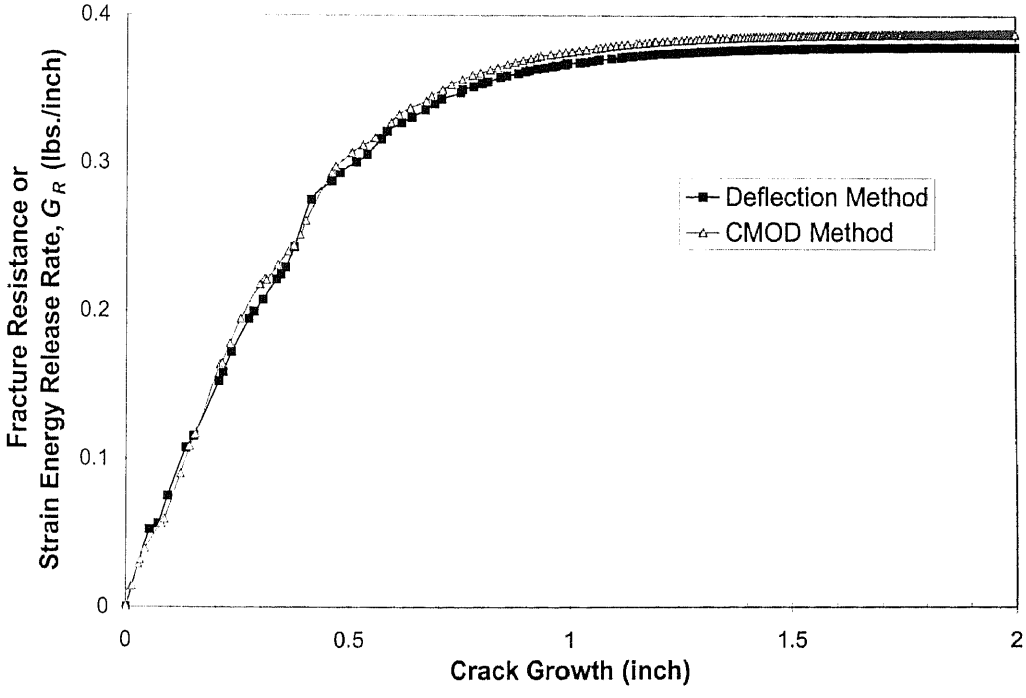

Figure C 6a Fracture Behavior of Fly Ash Concrete (18F25)
(Specimen No.1)

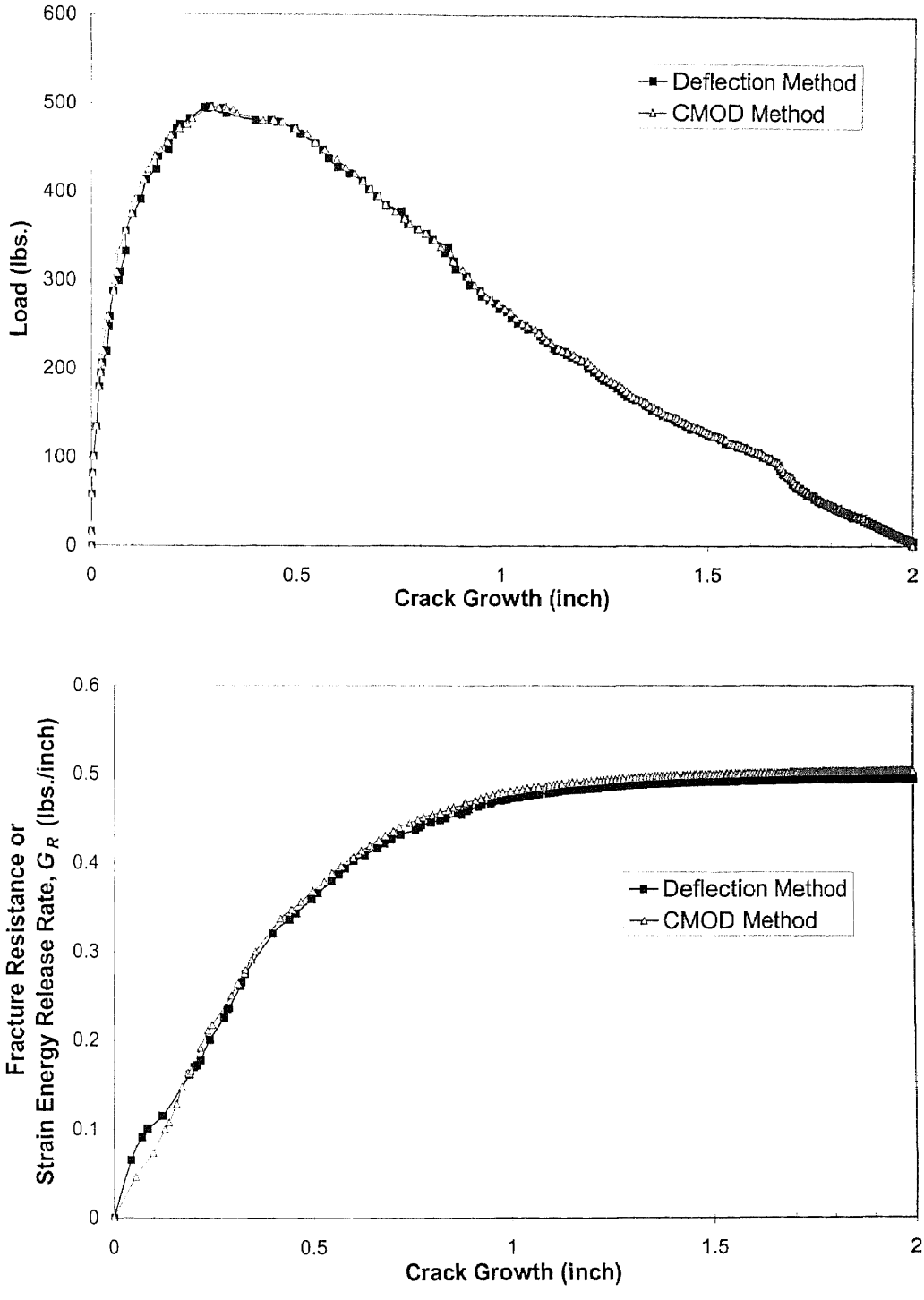

Figure C 6b Fracture Behavior of Fly Ash Concrete (18F25)
(Specimen No.2)

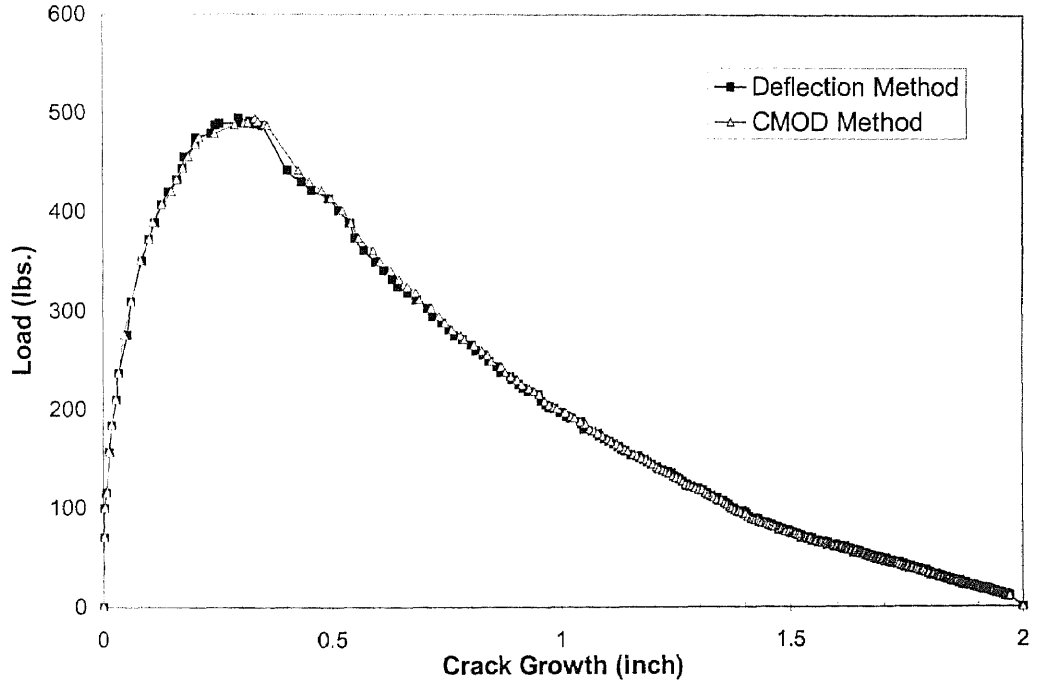

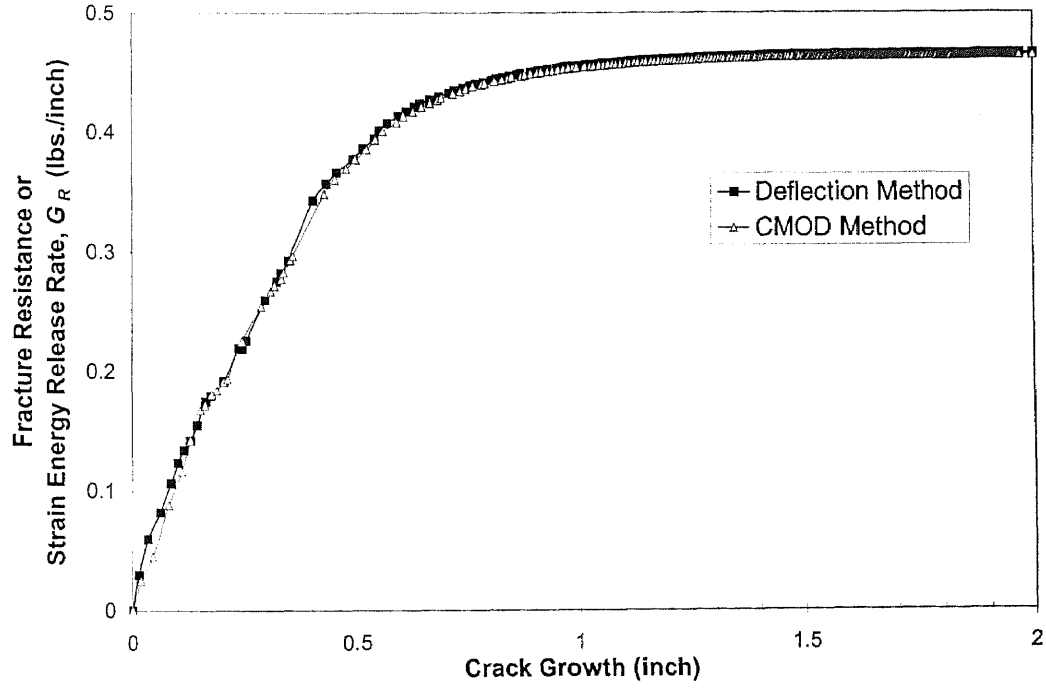

Figure C 6c Fracture Behavior of Fly Ash Concrete (18F25)
(Specimen No.3)

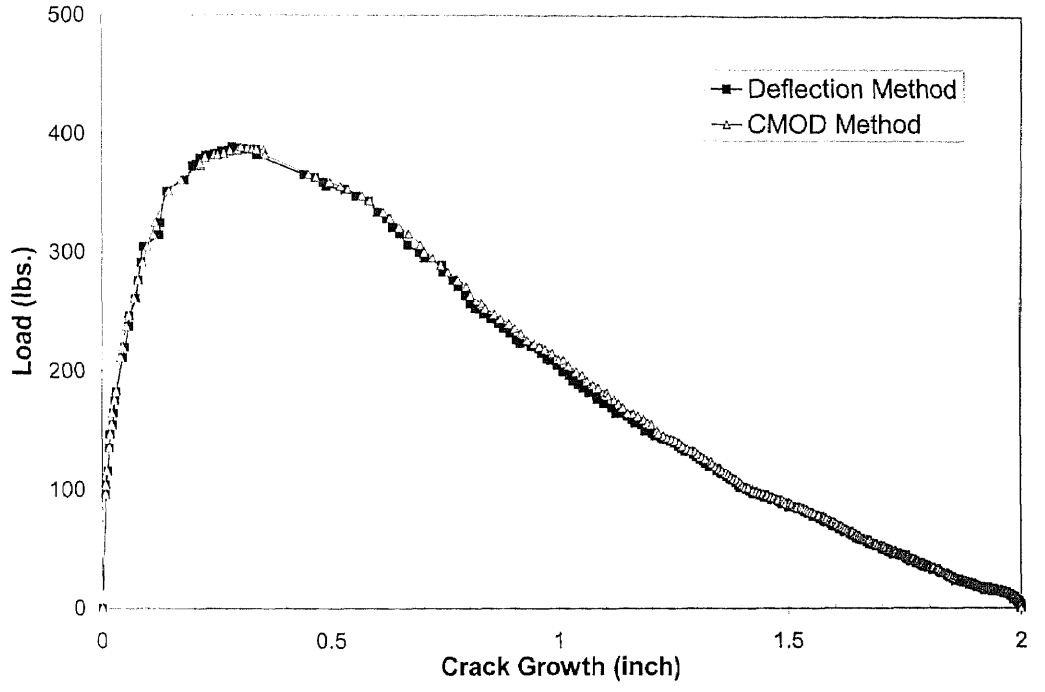

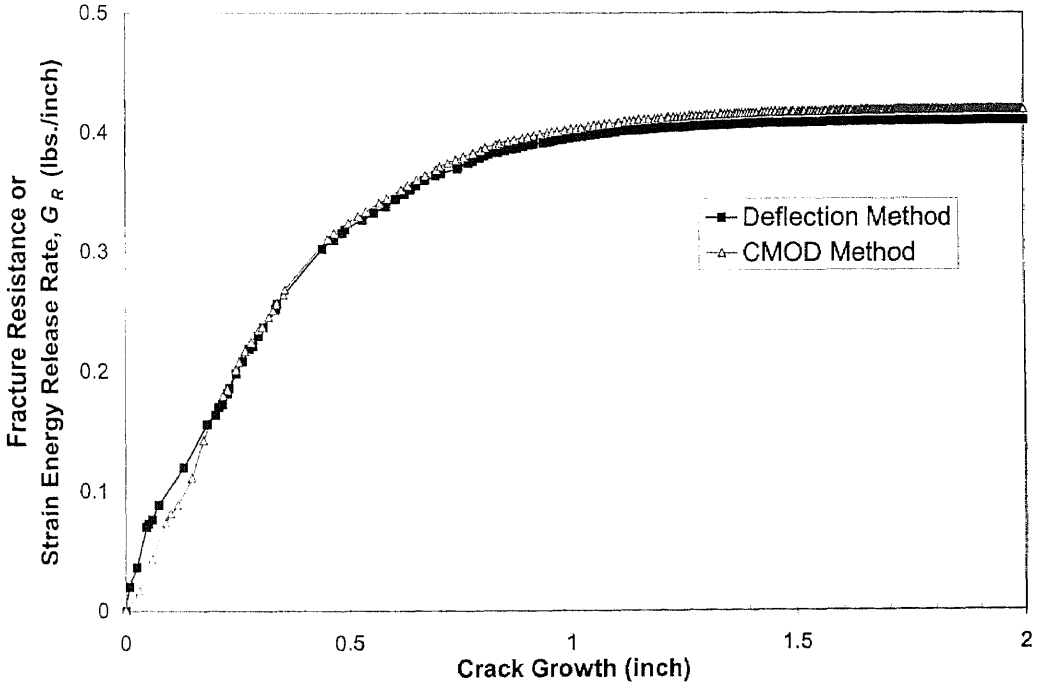

Figure C 7a Fracture Behavior of Fly Ash Concrete (18C25)
(Specimen No.1)

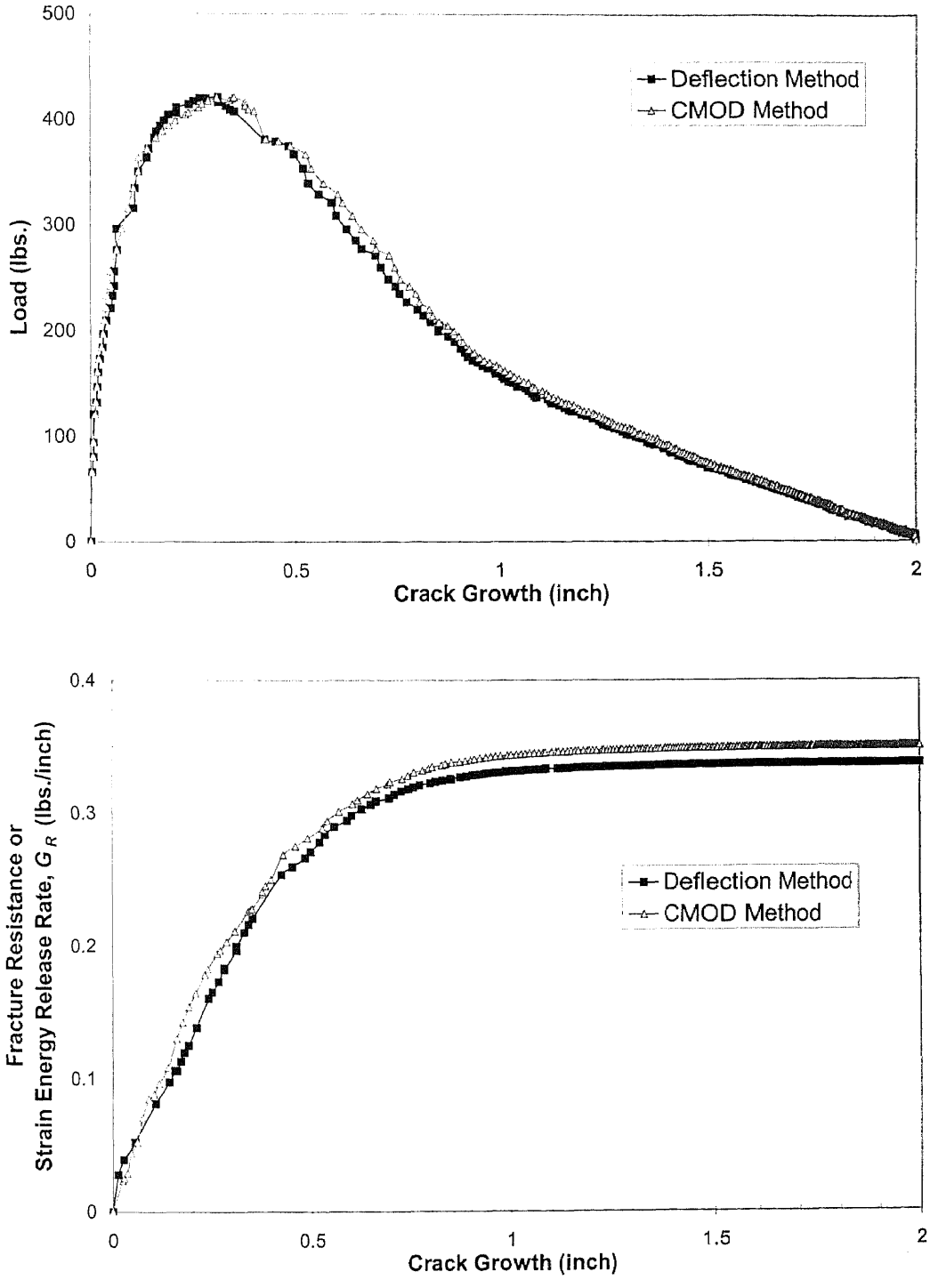

Figure C 7b Fracture Behavior of Fly Ash Concrete (18C25) (Specimen No.2)

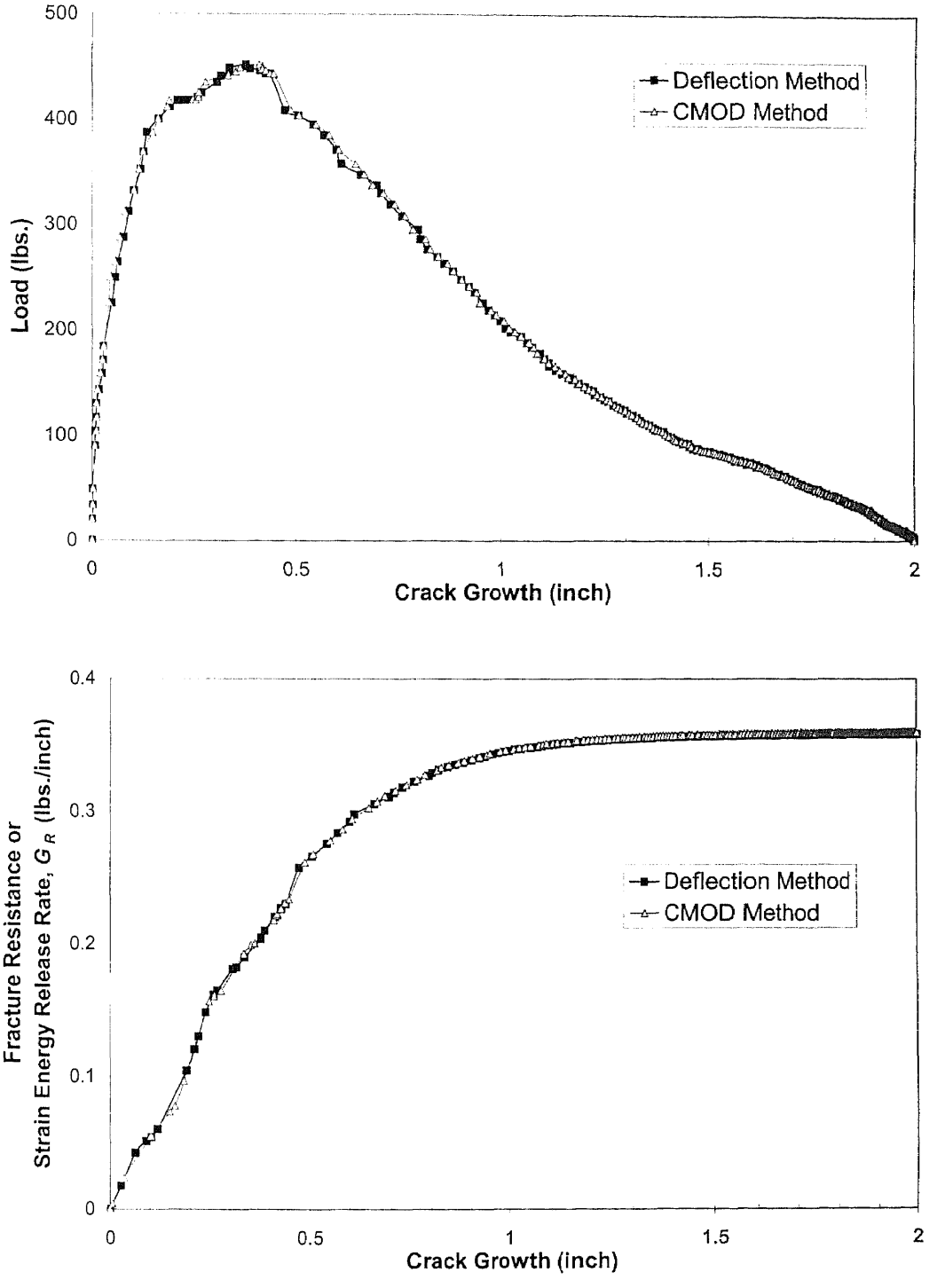

Figure C 7c Fracture Behavior of Fly Ash Concrete (18C25)
(Specimen No.3)

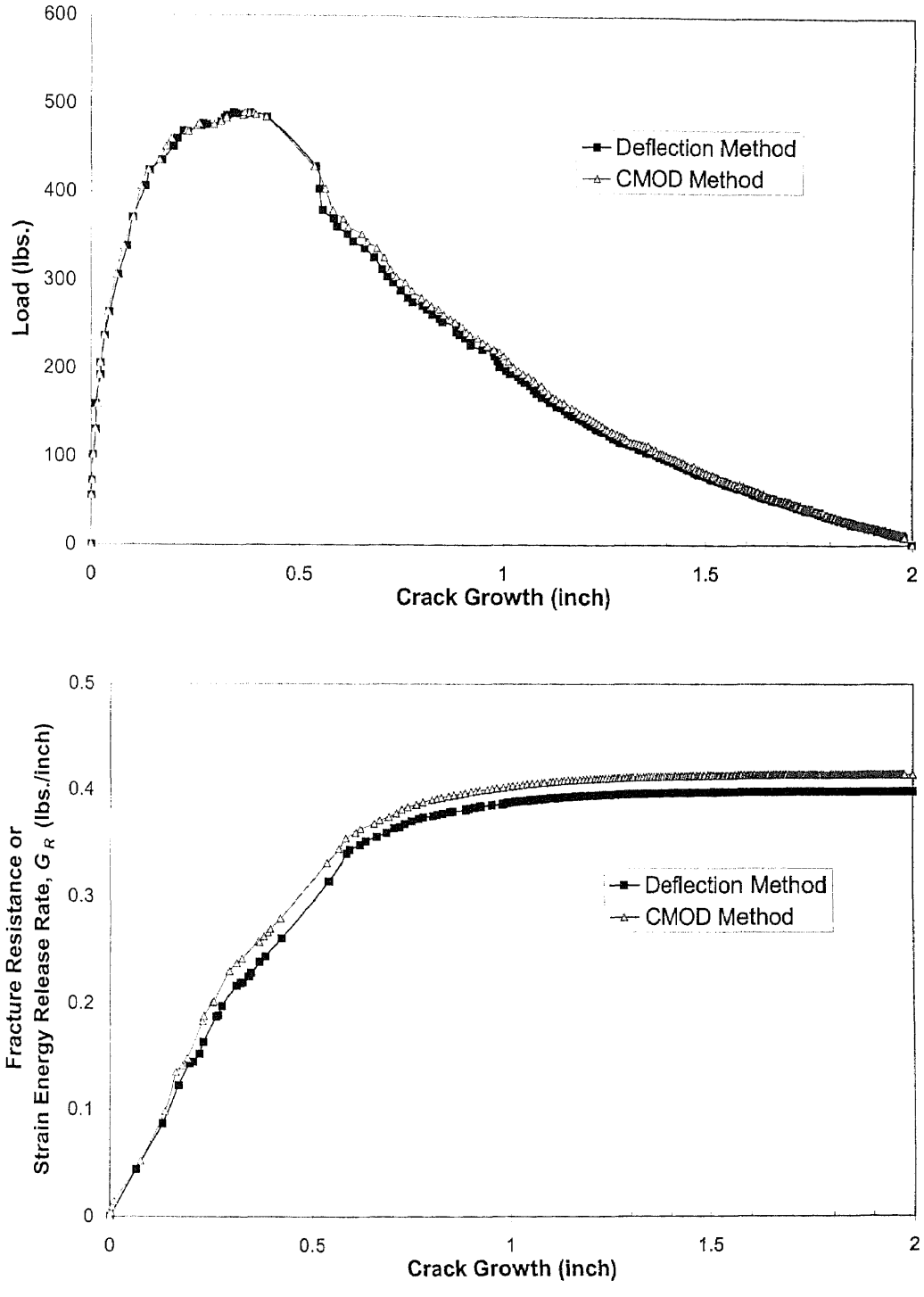

Figure C 8a Fracture Behavior of Fly Ash Concrete (MO25)
(Specimen No.1)

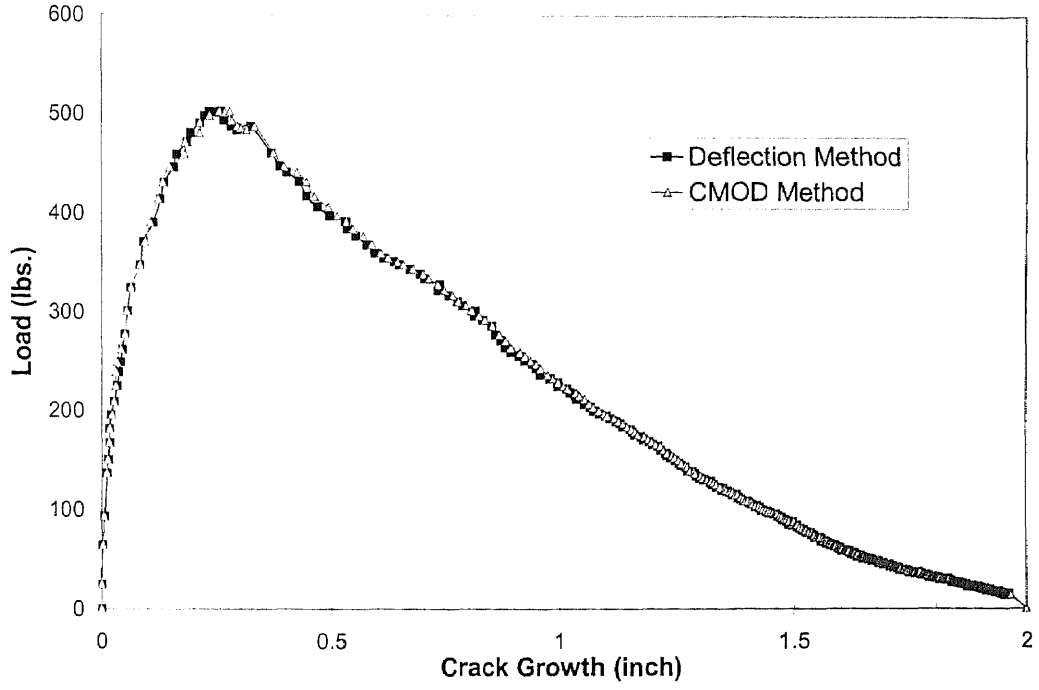

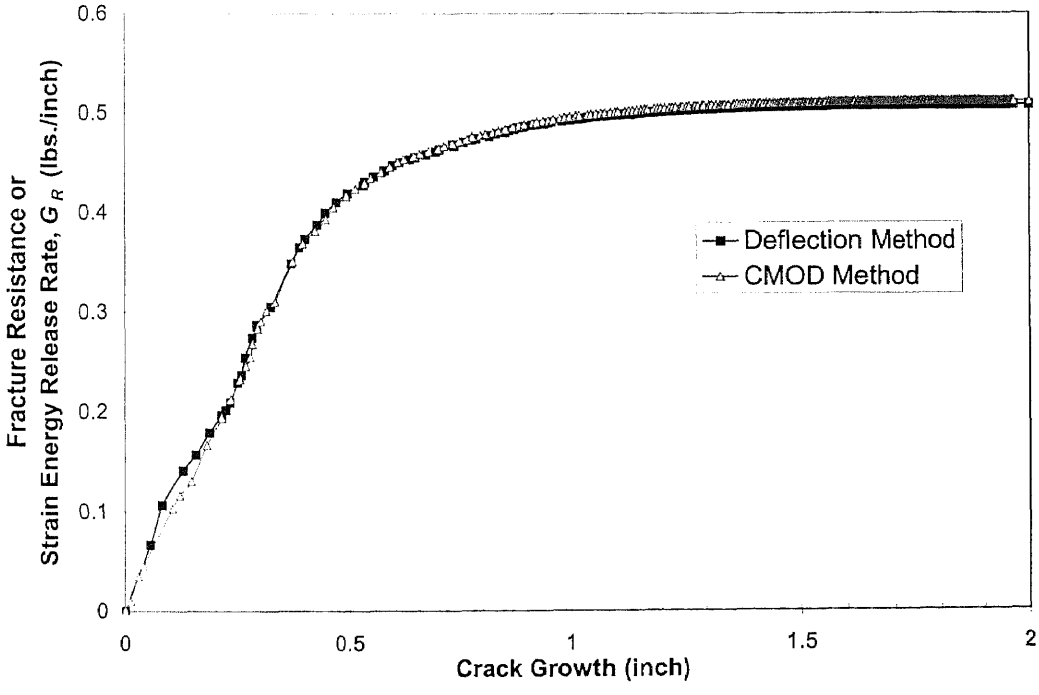

Figure C 8b Fracture Behavior of Fly Ash Concrete (MO25)
(Specimen No.2)

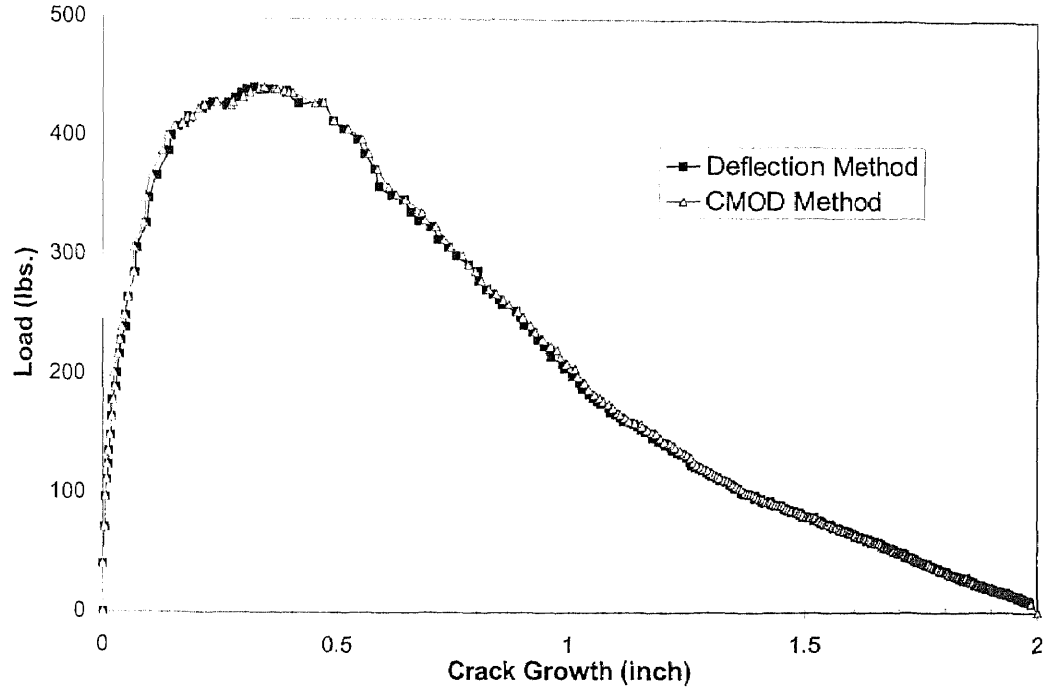

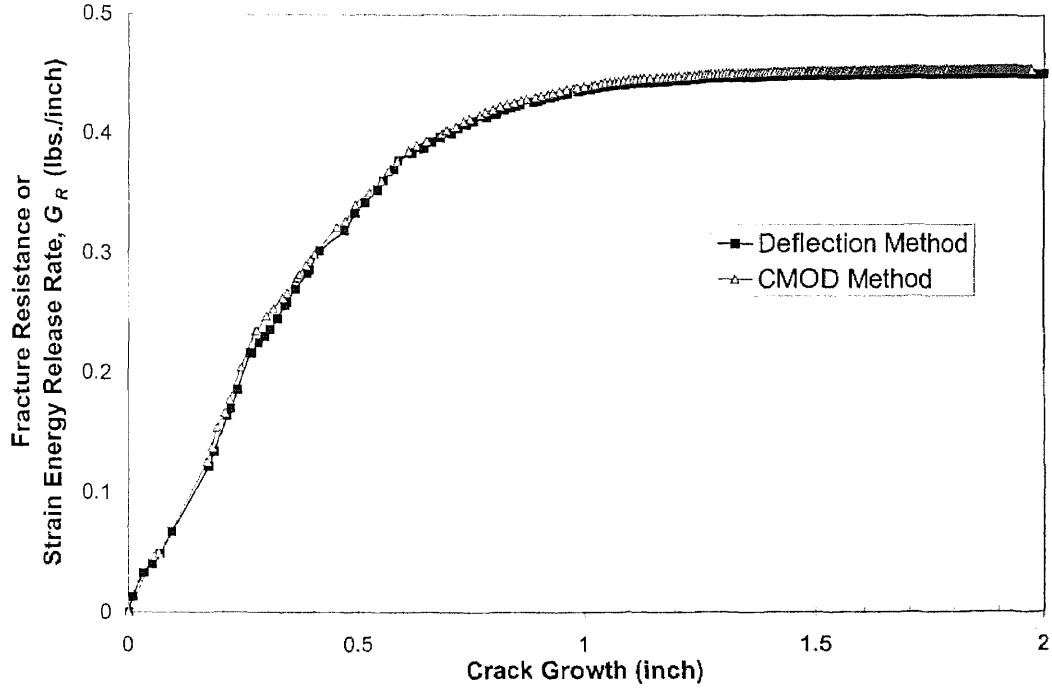

Figure C 8c Fracture Behavior of Fly Ash Concrete (MO25)
(Specimen No.3)

REFERENCES

ACI 318, 1994, "Building Code Requirements for Reinforced Concrete," *ACI Manual of Concrete Practice, Part 3*, American Concrete Institute, pp.318-83.

ACI 363, 1994, "State-of-the-Art Report on High Strength Concrte," *ACI Manual of Concrete Practice*, Part 1, American Concrete Institute, pp.363R-21.

Ahmed, A., and L. Sturble, 1994, "Effects of Microstructure on Fracture Behavior of Hardened Cement Paste," Microstructure of Cement-Based Systems: Bonding and Interfaces in Cementitious Materials, Vol. 370, *Materials Research Society*, pp. 99-106.

ASTM, 1994, "Concrete and Mineral Aggregate," *Annual Book of ASTM Standards*, Section 4, Vol. 04.02, American Society for Testing and Materials.

Bazant, Z. P., and B. H. Oh, 1988, "Crack Band Theory for Fracture of Concrete," *Materials and Structures*, Vol. 16, No. 93, pp. 155-177.

Bazant, Z. P., and M. T. Kazemi, 1988, "Determination of Fracture Energy, Process Zone Length and Brittleness Number from Size Effect, with Application to Rock and Concrete," *Report 88-7/498d* Center for Concrete and Geomaterials, Northwestern University, Evanston, Illinois.

Bentur, A., A. Goldman and M. D. Cohen, 1988, "Contribution of the Transition Zone to the Strength of High Quality Silica Fume Concrete," *Bonding in Cementitious Composites*, S. Mindess and S.P. Shah (eds.), Vol. 114, Materials Research Society, pp.97-104.

Bentur, A. and M. D. Cohen, "Effect of Condensed Silica Fume on the Microstructure of the Interfacial Zone in Portland Cement Mortars," *Journal of American Ceramic Society*, Vol. 70, No. 10, pp. 738-743.

Berry, E. E., and V. M. Malhotra, 1980, "Fly Ash for Use in Concrete-A Critical Review," *ACI Materials Journal*, Vol. 77, No. 2, pp. 59-83.

Broek, D., 1982, *Elementary Engineering Fracture Mechanics, 3rd ed.*, Martinus Nijhoff, Leyden, Netherlands.

Bumrongjaroen, W., 1999, "Utilization of Processed Fly Ash in Mortar," Ph.D. Dissertation, Department of Civil and Environmental Engineering, New Jersey Institute of Technology, Newark, New Jersey.

Buyukozturk, O., 1993, "Interface Fracture and Crack Propagation in Concrete Composites," *Micro-Mechanisms of Concrete and Cementitious Composites*, C. Huet (ed.), Presses Polytechniques et Universitaires Romandes, Rome, Italy, pp. 203-212.

Carrasquillo, R. L., A. H. Nilson and F. O. Slate, 1981, "Properties of High Strength Concrete Subjected to Short-Term Loads," *ACI Materials Journal*, Vol. 78, No. 3, pp. 171-178.

Chen, Z.Y., and J. G. Wang, 1987, "Effect of Bond Strength Between Aggregate and Cement Paste on the Mechanical Behavior of Concrete," *Bonding in Cementitious Composites*, S. Mindess and S.P. Shah (eds.), Vol. 114, Materials Research Society, pp. 41-47.

Cong, X. and S. Gong, D. Darwin and S. McCabe, 1992, "Role of Silica Fume in Compressive Strength of Cement Paste, Mortar and Concrete," *ACI Materials Journal*, vol. 89, No. 4, pp. 375-387.

De Larrard, F., 1989, "Ultrafine Particles for the Making of Very High Strength Concretes," *Cement and Concrete Research*, Vol. 23(3), pp. 161-172.

Fraay, A.L.A., J. M. Bigen and Y. M. De Haan, 1989, "The Reaction of Fly Ash in Concrete. A Critical Examination," *Cement and Concrete Research*, Vol. 19, No.2, pp. 235-246.

Francois, D., 1984, "Fracture and Damage Mechanics of Concrete," *Proceedings of the NATO Advanced Research Workshop on Application of Fracture Mechanics to Cementitious Materials*, Northwestern University, Illinois, U.S.A., pp. 141-156.

Giergiczny, Z. and A. Werysnka, 1989, "Influence of Fineness of Fly Ashes on Their Hydraulic Activity," *Fly Ash, Silica Fume, Slag, and Natural Pozzolans in Concrete, SP-114*, American Concrete Institute, Detroit, pp. 97-115.

Goldman, A. and A. Bentur, 1989, "Bond Effects in High-Strength Silica Fume Concrete," *ACI Materials Journal,* Vol. 86, No. 5, pp. 440-447.

Gopalaratanam V. S., S. Shah, G. B. Batson, M. E. Criswell, V. Ramakrishnan and M. Wecharatana, 1991, "Fracture Toughness of Fiber Reinforced Concrete," *ACI Materials Journal*, Vol. 88, No. 4, pp. 339-353.

Gopalaratnam V.S., and B. S. Ye, 1991, "Numerical Characterization of the Nonlinear Fracture Process in Concrete," *Engineering Fracture Mechanics*, Vol. 40, No.6, pp. 991-1006.

Griffith, A., 1920, "The Phenomenon of Rupture and Flow in Solids," *Philosophical Transactions, Series A*, Vol. 221, pp. 163-198.

Hillerborg, A., M. Modeer, and P.E. Petersson, 1976, "Analysis of Crack Formation and Crack Growth in Concrete by Means of Fracture Mechanics and Finite Elements," *Cement and Concrete Research*," Vol.6, pp. 773- 782.

Hsu, L.S. and C. T. Hsu, 1994, "Stress-Strain Behavior of Steel-Fiber High-Strength Concrete under Compression," *ACI Materials Journal*, Vol. 78, No. 3, pp. 171-178.

Hsu, T.T.C., and F. O. Slate, 1963, "Tensile Bond Strength between Aggregate and Cement Paste or Mortar," *Journal of the American Concrete Institute*, Vol. 60(4), pp. 465-486.

Irwin, G.R., 1957, "Analysis of Stresses and Strains Near the End of a Crack Transversing a Plate," *ASME Journal of Applied Mechanics*, Vol. 24, pp. 361-364.

Jaturapitakkul, C., 1993, "Utilization of Fly Ash in Concrete," Ph.D. Dissertation, Department of Civil and Environmental Engineering, New Jersey Institute of Technology, Newark, New Jersey.

Jenq, Y. S., and S. P. Shah, 1985a, "Two Parameter Fracture Model for Concrete," *Journal of Structural Engineering*, Vol. 112, No.1, ASCE, pp. 19-34.

Jenq, Y. S., and S. P. Shah, 1985b, "A Fracture Toughness Criterion for Concrete," Engineering Fracture Mechanics, Vol. 21, No.5, pp. 1055-1069

Kim, S. K., 1996, "The Constant Fracture Angle Model for Cementitious Materials", Ph.D. Dissertation, Department of Civil and Environmental Engineering, New Jersey Institute of Technology, Newark, New Jersey.

Lam, L., Y. L. Wong, and C. S. Poon, 1998, "Effect of Fly Ash and Silica Fume on Compressive and Fracture Behaviors of Concrete", *Cement and Concrete Research*, Vol. 28, No.2, pp. 271-283.

Langley, W.S., G. G. Carette, and V. M. Malhotra, 1989, "Structural Concrete Incorporating High Volumes of ASTM Class F Fly Ash, *ACI Materials Journal*, Vol. 86, No.5, pp.507-514.

Lee, K. M., O. Buyukozturk, and A. Oumera, 1992, "Fracture Analysis of Mortar Aggregate Interfaces in Concrete," *Journal of Engineering Mechanics (ASCE)*, Vol. 118(10), pp. 2031-2047.

Lee, K. M., O. Buyukozturk, and Y. Kitsutaka, 1994, "The Role of Interface Fracture Toughness in Cracking Behavior of High Strength Concrete", *Interface Fracture and Bond, SP-156*, American Concrete Institute, pp. 69-84.

Mindess, S., 1987, "Bonding in Cementitious Composites: How Important Is It," *Bonding in Cementitious Composite*, S. Mindess and S. P. Shah (eds.), Vol. 114, Materials Research Society, pp. 3-20.

Mindess, S., 1994, "Mechanical Properties of the Interfacial Transition Zone," *Interface Fracture and Bond, SP-156*, American Concrete Institute, pp. 1-10.

Navalurkar, R., 1996, "Fracture Mechanics of High Strength Concrete Members," Ph.D. Dissertation, Department of Civil and Environmental Engineering, New Jersey Institute of Technology, Newark, New Jersey.

Navalurkar, R., C.T. T. Hsu, S. K. Kim, and M. Wecharatana, 1999, "True Fracture Energy of Concrete," *ACI Materials Journal*, Vol.96, No. 2, pp. 213-225.

Neville, A.M., *Properties of Concrete*, 1983, 3rd, Pitman Publishing Inc, London, England

Petersson, P. E., 1980a, "Fracture Energy of Concrete: Method of Determination," *Cement and Concrete Research*, Vol. 10, pp. 78-89.

Petersson, P. E., 1980b, "Fracture Energy of Concrete: Practical Performance and Experimental Results," *Cement and Concrete Research*, Vol. 10, pp. 78-89.

Petersson, P. E., 1981, "Crack Growth and Development of Fracture Zones in Plain Concrete and Similar Materials," *Report TVBM-1008*, Division of Building Materials, Lund Institute of Technology, Lund, Sweden.

Popovics, S., 1987, "Attempts to Improve the Bond between Cement Paste and Aggregate," *Materials and Structures*, Vol. 20, No. 115, RILEM, pp. 32-38.

Ratanalert, S., and M. Wecharatana, 1989, "Evaluation of Existing Fracture Models in Concrete," *Fracture Mechanics Application to Concrete, SP-118*, American Concrete Institute, pp. 113-146

Regourd, M., 1985, "Microstructure of High Strength Cement Based Materials," *Very High Strength Cement-Based Materials*, J.F. Young (ed.), Vol. 42, Materials Research Society, pp. 3-17.

RILEM, TC50-FMC Fracture Mechanics of Concrete, 1985, "Determination of Fracture Energy of Mortar and Concrete by Means of Three-Point Bend Tests on Notched Beams," *Materials and Structures*, Vol. 18, pp. 285-296.

RILEM, TC89-FMT Fracture Mechanics of Concrete Test Methods, 1990, "Determination of Fracture Parameters (K^s_{IC} and $CTOD_C$) of Plain Concrete Using Three-Point Bend Tests," *Materials and Structures*, Vol. 23, pp. 457-460.

Rosenberg, A. M., M. Arnold, and J. M.Gaidis, 1989, "New Mineral Admixture for High-Strength Concrete, *Concrete International*, Vol. 11, No.4, pp. 31-36.

Scholer, C.F., 1967, "Role of Mortar-Aggregate Bond in Strength of Concrete," *Highway Research Record*, Vol. 210, pp. 108-117.

Scrivener, K. L., A. K. Crumbie, and P. L. Pratt, 1988, "A Study of the Interfacial Region between Cement Paste and Aggregate in Concrete," *Bonding in Cementitious Composite*, Vol. 114, Material Research Society, pp. 77-86.

Scrivener, K. L., and A. M. Gartner, 1988, "Microstructural Gradients in Cement Paste around Aggregate Particles," *Bonding in Cementitious Composite*, Vol. 114, Material Research Society, pp. 77-86.

Shah, S. P., 1990, "Fracture Toughness of High-Strength Concrete," *ACI Materials Journal*, Vol. 87, No. 3, pp. 260-265.

Strubel, L., J. Skalny, and S. Mindess, 1980, "A Review of the Cement-Aggregate Bond," *Cement and Concrete Research*, Vol.10, pp. 277-286.

Tada, H., C. Paris, and G. R. Irwin, 1985, *The Stress Analysis of Cracks Handbook*, Del Research Corporation, Hellertown, Pennsylvania.

Utika, K. and Ishii, M., 1991, "A Fundamental Study on Applicability of Classified Fly Ash for Use as a High Strength Concrete Admixture," *Proceeding: Ninth International Ash Use Symposium,* Vol. 1, EPRI GS-7162, pp. 4-1 to 4-14.

Westergaard, H. M., 1939, "Bearing Pressures and Cracks," *ASME Journal of Applied Mechanics*, Vol.61: pp. A49-A53.

Windslow, D. N., M. Cohen, D. P. Bentz, K. A. Snyder, and E. J. Garboczi, 1994, "Percolation and Pore structure in Mortars and Concrete," *Cement and Concrete Research*, Vol. 24, No.1, pp. 25-36.

Wu, K., and J. Zhou, 1987, "The Influence of the Matrix-Aggregate Bond on the Strength and Brittleness of Concrete," *Bonding in Cementitious Composites*, S. Mindess and S.P. Shah (eds.), Vol. 114, Materials Research Society, pp.29-34.

Wu, X., D. Li, X. Wu, and M. Tang, 1987, "Modification of the Interfacial Transition Zone between aggregate and Cement Paste," *Bonding in Cementitious Composites*, S. Mindess and S.P. Shah (eds.), Vol. 114, Materials Research Society, pp.35-40.

Zhang, M. H., 1995, "Microstructure, Crack Propagation, and Mechanical Properties of Cement Pastes Containing High Volumes of Fly Ashes," *Cement and Concrete Research*, Vol. 25, No. 6, pp. 1165-1178.